



CHARLES PANKOW
FOUNDATION

Building Innovation through Research

Defining Structurally Acceptable Properties of High-Strength Steel Bars through Material and Column Testing

PART II: COLUMN TESTING REPORT

The University of Texas at Austin

Drit Sokoli

Albert Limantono

Wassim M. Ghannoum

Sponsored by:

The Charles Pankow Foundation

The Concrete Reinforcing Steel Institute

The American Concrete Institute's Concrete Research Council

February 3, 2017

**Defining Structurally Acceptable Properties
of High-Strength Steel Bars through Material and Column Testing**

CPF Research Grant Agreement #05-14
Funded by
CHARLES PANKOW FOUNDATION
P.O. Box 820631

Vancouver, Washington 98682
Co-funded by
The Concrete Reinforcing Steel Institute, and
The American Concrete Institute's Concrete Research Council

Principal Investigator: Dr. Wassim M. Ghannoum

Graduate Research Assistants: Drit Sokoli
Chase Slavin
Albert Limantono

Industry Support:

Industry Champions: Mike Mota, VP Engineering, CRSI
Ron Klemencic, Chairman and CEO, MKA

Advisory Panel: Dominic Kelly, SGH
Andrew Taylor, KPFF
Loring Wyllie, Degenkolb

Acknowledgements

This project was made possible by funding from the Charles Pankow Foundation, the Concrete Reinforcing Steel Institute, and ACI's Concrete Research Council. The steel and fabrication donated by CMC, NUCOR Steel Inc. Seattle, and MMFX are gratefully acknowledged.

Abstract

Economic, environmental, and constructability incentives are fueling the demand for higher strength reinforcing steel in concrete construction, particularly in highly congested seismic designs. In response, steel mills in the United States are developing high-strength reinforcing bar (HSRB) that can be used in seismic as well as non-seismic applications. However, different manufacturers are achieving higher strengths using different techniques (i.e., micro-alloying, quenching, etc.), leading to HSRB having differing mechanical properties. Such differences have raised questions about what the minimum acceptable mechanical properties should be for HSRB to achieve acceptable structural performance in various members and for various loading types. An experimental program was undertaken to assess the influence of the tensile-to-yield strength (T/Y) ratio and ductility of HSRB on the behavior of concrete columns under cyclic lateral loading. Four column tests were conducted in this study that was part of a broader research effort aimed at setting the minimum acceptable T/Y ratios and elongations in new ASTM specifications for seismic grade 80 and 100 reinforcing bars. Three of the specimens were reinforced with grade 100 bars produced by different manufacturers and therefore having different mechanical properties. The fourth column was reinforced with conventional grade 60 ASTM A706 bars. Column specimens were tested under constant axial load and reverse cyclic lateral loading of increasing amplitude until fracture of longitudinal bars. Conclusions are drawn with respect to the effects of the higher strength reinforcement on the seismic performance of concrete columns, strain demands on reinforcing bars, plasticity spread, and energy dissipation. In this report, HSRB are defined as those having a yield strength in excess of 80 ksi (or grade 80 and higher).

Table of Contents

1.	Introduction.....	17
1.1	Motivation.....	17
1.2	Objectives and Scope.....	19
1.3	Organization.....	21
2.	Background.....	22
2.1	Metallurgy.....	22
2.1.1.	Micro-alloying.....	22
2.1.2.	Quenching and Tempering.....	24
2.1.3.	Proprietary Combination of Alloying and Micro Structure Manipulation.....	24
2.1.4.	Cold Working.....	25
2.2	Low-Cycle Fatigue.....	25
2.3	Relevant Experimental Studies with HSRB.....	29
2.3.1	Introduction.....	29
2.3.2	Experimental Programs.....	30
2.3.3	Summary.....	37
2.4	Strain Demands in Longitudinal Reinforcing Bars.....	38
2.4.1	Experimental Evidence.....	38
2.4.2	Estimating Strain Demands in Longitudinal Reinforcement.....	38
2.4.3	Strain Demands and Tension Shift due to Shear/Inclined Cracks....	39

2.5	Ductility, Plasticity Spread, and Strain Demands	41
2.5.1	Plastic Hinge Length Models	41
2.5.2	Discussion on Past Work and Needs for HSRB	56
3.	Experimental Program	57
3.1	Specimen Design	57
3.2	Materials	62
3.2.1	Concrete.....	62
3.2.2	Reinforcing steel.....	63
3.3	Specimen Fabrication.....	68
3.4	Instrumentation	71
3.5	Test Setup and Procedure.....	73
4.	Experimental Results	75
4.1	Data Processing.....	75
4.1.1	Deformation Measurements	76
4.1.2	Strain Measurements	78
4.1.3	Damage Evaluation.....	79
4.1.4	Behavioral Milestones	80
4.2	Test Results for CH100.....	82
4.2.1	General Behavior.....	83
4.2.2	Deformation Components.....	90
4.2.3	Strain History.....	92

4.2.4	Strain Profile.....	94
4.2.5	Crack Widths.....	95
4.2.6	Buckling History.....	97
4.2.7	Energy Dissipation.....	99
4.3	Test Results for CL100.....	100
4.3.1	General Behavior.....	101
4.3.2	Deformation Components.....	108
4.3.3	Strain History.....	110
4.3.4	Strain Profile.....	112
4.3.5	Crack Widths.....	113
4.3.6	Buckling History.....	115
4.3.7	Energy Dissipation.....	117
4.4	Test Results for CM100.....	118
4.4.1	General Behavior.....	119
4.4.2	Deformation Components.....	126
4.4.3	Strain History.....	128
4.4.4	Strain Profile.....	130
4.4.5	Buckling History.....	133
4.4.6	Energy Dissipation.....	135
4.5	Test Results for CH60.....	136

4.5.1	General Behavior.....	137
4.5.2	Deformation Components.....	143
4.5.3	Strain History.....	145
4.5.4	Strain Profile.....	147
4.5.5	Crack Widths	148
4.5.6	Buckling History.....	150
4.5.7	Energy Dissipation	153
5.	Discussion on Experimental Results.....	154
5.1	General Behavior	154
5.2	Moment Strength - Envelope Behavior	159
5.2.1	Moment Strength.....	159
5.2.2	Envelope Response.....	161
5.3	Cyclic Behavior	163
5.4	Strain Demands and Plasticity Spread	169
5.4.1	Maximum Strain Demands in the Longitudinal Bars.....	170
5.4.2	Strains over Height in the Longitudinal Bars	176
6.	Summary and Conclusions	182
6.1	Summary.....	182
6.2	Conclusions.....	183
	Appendix A.....	191
	Appendix B.....	205

Appendix C	209
References.....	211

List of Figures

Figure 1:	Number of half cycles to failure with: (a) total strain (Kunnath et. al., 2004); (b) lateral drift ratio (Kunnath et. al., 1999).....	26
Figure 2:	Results from Brown and Kunnath (2004) overlaid with data from grade 60 #8 bars produced by Manufacturer I (Slavin and Ghannoum, 2015) 28	
Figure 3:	Debonding of longitudinal reinforcement effect on strain in longitudinal bars (Berry and Eberhard, 2007).....	39
Figure 4:	The distribution of longitudinal bar tension forced at end region of the member affected by shear-induced inclined cracking	40
Figure 5:	Flexural deformation calculations	42
Figure 6:	Elevation and cross-sectional view of the reinforcement in columns ...	60
Figure 7:	Typical stress-strain curves for the longitudinal reinforcement used in each specimen	66
Figure 8:	Typical stress-strain curves for the longitudinal reinforcement used in each specimen.....	68
Figure 9:	Steel cage assembly and strain gauge installation	69
Figure 10:	Column casting process	70
Figure 11:	Strain gauge installation process (Sokoli, 2014)	72
Figure 12:	Column CL100 at the end of the test.....	74
Figure 13:	Deformation components in a concrete member (from Sokoli et. al., 2014)	77
Figure 14:	Behavioral milestones naming and corresponding marker.....	80
Figure 15:	CH100 – measured lateral displacement at every captured frame.....	82
Figure 16:	CH100 – applied axial load ratio at every captured frame	82
Figure 17:	CH100 – lateral response.....	83

Figure 18:	CH100 – cracking pattern (up) and measured largest principal strains (down) at several drift ratio targets.....	86
Figure 19:	CH100 – base and top moment vs. drift ratio.....	87
Figure 20:	CH100 – last cycles response.....	89
Figure 21:	CH100 – pictures of fractured and buckled bars.....	89
Figure 22:	CH100 – deformation components.....	91
Figure 23:	CH100 – strain gauge L17NW (top north-western corner) recording at the interface between the column and top footing.....	93
Figure 24:	CH100 –column-end bar strain gauge recordings at each drift target and calculated average.....	93
Figure 25:	CH100 – longitudinal reinforcement strain demands over height at drift targets.....	94
Figure 26:	CH100 – average values of largest flexural crack widths at drift targets.....	96
Figure 27:	CH100 – width of one of the two largest flexural cracks.....	96
Figure 28:	CH100 – longitudinal bar buckling.....	98
Figure 29:	CH100 – rotation at a distance 9 inches from the base.....	98
Figure 30:	CH100 – dissipated energy at drift targets for each cycle.....	99
Figure 31:	CL100 – measured lateral displacement at every captured frame.....	100
Figure 32:	CL100 – applied axial load ratio at every captured frame.....	100
Figure 33:	CL100 – lateral response.....	102
Figure 34:	CL100 - cracking pattern (up) and measured largest principal strains (down) at several drift ratio targets.....	104
Figure 35:	CL100 - base and top moment vs. drift ratio.....	105
Figure 36:	CL100 – last cycles response.....	107
Figure 37:	CL100 – pictures of fractured and buckled bars at the end of the test.....	107

Figure 38:	CL100 – deformation components	109
Figure 39:	CL100 – strain gauge L4NE (bottom north-eastern corner) recording at the interface between the column and bottom footing.....	111
Figure 40:	CL100 –column-end bar strain gauge recordings at each drift target and calculated average.....	111
Figure 41:	CL100 – longitudinal reinforcement strain demands over height at drift targets.....	112
Figure 42:	CL100 - average values of largest flexural crack widths at drift targets.....	114
Figure 43:	CL100 – width of one of the two largest flexural cracks.....	114
Figure 44:	CL100 –longitudinal bar buckling.....	116
Figure 45:	CL100 – rotation at a distance 9 inches from the base	116
Figure 46:	CL100 – dissipated energy at drift targets for each cycle.....	117
Figure 47:	CM100 – measured lateral displacement at every captured frame	118
Figure 48:	CM100 – applied axial load ratio at every captured frame.....	118
Figure 49:	CM100 – lateral response	119
Figure 50:	CM100 - cracking pattern (up) and measured principal strains (down) at drift targets.....	121
Figure 51:	CM100 - base and top moment vs. drift ratio	123
Figure 52:	CM100 – last cycles response.....	125
Figure 53:	CM100 – pictures of fractured and buckled bars at the end of the test	125
Figure 54:	CM100 – deformation components	127
Figure 55:	CM100 – strain gauge L4SW (top south-western corner) recording at the interface between the column and top footing.....	129
Figure 56:	CM100 – column-end bar strain gauge recordings at each drift target and calculated average.....	129

Figure 57:	CM100 – longitudinal reinforcement strain demands over height at drift targets.....	130
Figure 58:	CM100 - average values of largest flexural crack widths at drift targets.....	132
Figure 59:	CM100 – width of one of the two largest flexural cracks	132
Figure 60:	CM100 –longitudinal bar buckling.....	134
Figure 61:	CM100 – rotation at a distance 9 inches from the base.....	134
Figure 62:	CM100 – dissipated energy at drift targets for each cycle	135
Figure 63:	CH60 – measured lateral displacement at every captured frame.....	136
Figure 64:	CH60 – applied axial load ratio at every captured frame	136
Figure 65:	CH60 – lateral response.....	137
Figure 66:	CH60 - cracking pattern (up) and measured principal strains (down) at drift targets.....	139
Figure 67:	CH60 - base and top moment vs. drift ratio.....	140
Figure 68:	CH60 – last cycles response	142
Figure 69:	CH60 – picture of fractured and buckled bars.....	142
Figure 70:	CH60 – deformation components.....	144
Figure 71:	CH60 – strain gauge L4NW (bottom north-western corner) recording at the interface between the column and top footing.....	146
Figure 72:	CH60 –column-end bar strain gauge recordings and calculated average.....	146
Figure 73:	CH60 – longitudinal reinforcement strain demands over height at drift targets.....	147
Figure 74:	CH60 - average values of largest flexural crack widths at drift targets	149
Figure 75:	CH60 – width of one of the two largest flexural cracks	149
Figure 76:	CH60 – rotation at a distance 9 inches from the base.....	151

Figure 77:	CH60 –longitudinal bar buckling	152
Figure 78:	CH60 – dissipated energy at drift targets for each cycle	153
Figure 79:	Lateral response of CH100 and CL100 with milestones (filled markers for CH100, hollow marker for CL100)	156
Figure 80:	Average backbone of the response for each column	162
Figure 81:	Hysteresis loops of columns pushed to a drift ratio of 3.0%	165
Figure 82:	Hysteresis loops of all columns pushed to the first cycles to a drift ratio of 3.0%	165
Figure 83:	Cumulative dissipated energy at drift targets: first cycle (left); second cycle (right)	166
Figure 84:	Cumulative dissipated energy (CDE) as a fraction of M_{ns} (left) and M_{nm} (right)	168
Figure 85:	Typical stress-strain curve for longitudinal reinforcement used in each specimen	169
Figure 86:	Average strain demands in longitudinal reinforcement at drift targets for all column	171
Figure 87:	Average strain demands in longitudinal bars at column ends at various drift targets [CH100 & CL100]	173
Figure 88:	Average strain demands in longitudinal bars at column ends at various drift targets [CH100 & CL100]	173
Figure 89:	Average strain demands in longitudinal reinforcement at drift targets [CH100; CL100 & CH60]	175
Figure 90:	Average strain demands after removing the length of the yield plateau at drift ratios beyond yield (0.6% for CH60 and 1.5% for CH100 and CL100) [CH100; CL100 & CH60]	175
Figure 91:	Spread of inelastic strains on the longitudinal bars of CH100 and CL100	177
Figure 92:	Spread of inelastic strains on the longitudinal bars of CH100, CL100, and CH60	178

Figure 93: Spread of inelastic strains on the longitudinal bars of all specimens: a) yield strain in CM100 calculated with 0.2% offset rule; b) yield strain in CM100 taken at a stress of 100 ksi180

Figure 94: Average strain in longitudinal reinforcement over column and foundation spans at different drift ratios181

List of Tables

Table 1:	Summary of material coefficients for fatigue life equations for #8 bars (Slavin and Ghannoum, 2015).....	28
Table 2:	Summary of column reinforcement details.....	59
Table 3:	Assumed properties of reinforcing bars used for designing specimens..	61
Table 4:	Sectional analysis results	62
Table 5:	Concrete mix design quantities.....	62
Table 6:	Concrete compressive strengths of columns at day of column testing (ksi) 63	
Table 7:	Average results from tension tests on sample #6 bars (minimum of three tests per bar type).....	66
Table 8:	Average results from tension tests on sample #4 bars	68
Table 9:	Loading protocol.....	74
Table 10:	CH100 - behavioral milestones.....	84
Table 11:	CH100 – deformation components as percentage of total.....	91
Table 12:	CL100 - behavioral milestones.....	102
Table 13:	CL100 - deformation components as percentage of total.....	108
Table 14:	CM100 - behavioral milestones.....	120
Table 15:	CM100 - deformation components as percentage of total.....	127
Table 16:	CH60 - behavioral milestones.....	138
Table 17:	CH60 - deformation components as percentage of total.....	144
Table 18:	Summary of behavioral milestones for all four specimens.....	155
Table 19:	Flexural strength of columns evaluated using ACI 318-14 procedures and measured experimentally	160

Table 20: Ratios of measured to calculated moment strengths.....160

List of Equations

Equation 1: Fatigue life modeling with strain range as the dependent variable.....	27
Equation 2: Fatigue life modeling with fatigue life as the dependent variable.....	27
Equation 3: Calculation of ultimate lateral drift.....	41
Equation 4: Equivalent plastic hinge length (Baker and Amarakone, 1964).....	43
Equation 5: Plastic rotation (Baker and Amarakone, 1964).....	43
Equation 6: Coefficient accounting for applied axial load (Baker and Amarakone, 1964).....	43
Equation 7: Ultimate concrete compressive strain (Mattock, 1965).....	46
Equation 8: Calculation of ultimate rotation (Mattock, 1965).....	46
Equation 9: Ultimate rotation (Corley, 1966).....	47
Equation 10: Equivalent ultimate curvature.....	48
Equation 11: Equivalent plastic hinge length rotation (Priestley and Park, 1987).....	49
Equation 12: Equivalent plastic hinge length rotation (Paulay and Priestley, 1992).....	49
Equation 13: Analytical calculation of ultimate rotation.....	51
Equation 14: Equivalent plastic hinge length for cyclic loading (Panagiotakos and Fardis, 2001).....	51
Equation 15: Equivalent plastic hinge length for monotonic loading (Panagiotakos and Fardis, 2001).....	52
Equation 16: Equivalent plastic hinge length for cyclic loading (Restrepo et. al., 2006)	53
Equation 17: Yield spread coefficient - α - (Restrepo et. al., 2006).....	53
Equation 18: Strain penetration contribution to plastic rotation (Restrepo et. al., 2006).....	54
Equation 19: Strain penetration coefficient - β - (Restrepo et. al., 2006).....	54

Equation 20: Equivalent plastic hinge length equation form (Berry et. al., 2008).....55

Equation 21: Equivalent plastic hinge length equation (Berry et. al., 2008).....55

Equation 22: Equivalent plastic hinge length equation to be used in design (Berry et. al., 2008)55

Equation 23: Crack-width calculation using data from GVIS.....79

1. Introduction

1.1 MOTIVATION

The use of higher strength reinforcing bars in concrete construction has the potential to reduce bar congestion especially in seismic designs. Economic and environmental considerations also contribute to the demand for higher strength reinforcement. Recently, the reinforcing bar industry adopted a grade 80 steel that satisfies the ASTM A706 (ASTM A706/ A706M – 16a, 2016) standard. Several mills across the country are able to produce this steel grade, making it available to the structural engineering community. High-strength reinforcing bars (HSRB) with yield strength of 80 ksi and higher are currently under development in the U.S. for seismic as well as non-seismic applications. However, the HSRB being developed have varying mechanical properties. None of these bars are able to match the benchmark mechanical properties of the benchmark grade 60 bars, with each high-strength variant diverging from benchmark behavior in different ways. Structural engineers and steel mills are currently trying to strike the best balance between needed and feasible properties for high-strength reinforcing bars. High strength reinforcing bars (HSRB) are defined in this report as reinforcing bars having yield strength of 80 ksi or more.

Current code limits on the strength of reinforcing steel, combined with a lack of understanding of the effects of higher strength steel on the performance of concrete members, are hindering progress in structural designs. Many of today's limits on strength of concrete reinforcing steel have been enforced since the 1950s. The 1956 version of the ACI 318 building code (ACI 318, 1956) set the yield-strength limit on reinforcement at 60 ksi, increasing it from 40 ksi. In the 1971 version of the ACI 318 code, an 80 ksi limit was placed for gravity systems (ACI 318, 1971). To this date, the limit remains at 80 ksi for

non-seismic systems except for shear, which has to be designed using maximum yield strength of transverse reinforcement of 60 ksi. For seismic design, the limit currently remains at 60 ksi (ACI 318, 2014). Grade 100 steel was recently allowed in the ACI building code but only for confinement design.

Performance concerns that have maintained the code limits on the strength of reinforcing steel span a wide range of behavioral aspects. An increase in steel strength in reinforcing bars is associated with an increase in strain at yield, and often with a reduction in the fracture elongation, the tensile-to-yield strength ratio, and the length of the yield plateau. Certain production techniques can also lead to HSRB that do not exhibit a well-defined yielding point.

For a given bar size, higher strength steel implies larger tensile and compressive forces. Larger tensile forces for the same bar size result in an increase in bond demands and the forces at bar hooks or heads. On the other hand, larger compressive forces for the same bar size can increase bar buckling susceptibility given the same lateral bracing. There is also evidence that the tensile-to-yield strength ratio affects the spread of plasticity in reinforced concrete members and a low value of the ratio can produce higher strain concentrations in bars at cracks (Macchi et al. 1996, Aoyama, H. 2001, NEHRP 2013, Sokoli and Ghannoum 2016). Strain concentrations in the longitudinal reinforcement in turn can reduce member ductility and cause premature bar fracture. When compared to regular strength grade 60 bars, potentially larger strain demands coupled with lower fracture elongations in HSRB, have also raised concerns about their cyclic fatigue performance in concrete structures subjected to seismic demands.

Limited comparative experimental data exist on the behavior of variants of high-strength reinforcing steel in concrete structures. New experimental data is needed to assess

the implication of using different types of high-strength reinforcement in concrete structures and allow the relaxation of code restrictions on the strength of reinforcing bars. However, benchmark structurally desirable properties need to be defined and specified in material standards for HSRB before the bulk of the experimental studies can be undertaken. This would allow for all testing to be done with the steels satisfying the specifications that will be adopted in the design codes.

1.2 OBJECTIVES AND SCOPE

A two-part study was undertaken to help define both feasible and structurally acceptable mechanical properties of HSRB. The study focused particularly on the seismic behavior and applications of HSRB. The first part of the study was completed in 2015 and quantified the mechanical properties, particularly the low-cycle life of the HSRB under development in the U.S. (Slavin and Ghannoum, 2015). The study highlighted the wide range of fatigue life of HSRB under development, indicating that the fatigue performance of HSRB can far exceed or be far below benchmark grade 60 performance. The study also identified possible means by which production techniques can be upgraded to improve the fatigue performance of HSRB. The second part of the study, presented in this report, consists of a targeted structural testing program aimed at uncovering any major issues in the performance of HSRB in concrete members, as well as provide necessary data to set material specifications for the new HSRB. A recent study by Sokoli and Ghannoum (2016) indicated that HSRB can experience up to twice the strain demands as compared to their grade 60 counterparts in seismic applications. This finding, coupled with the wide range of fatigue performance of HSRB uncovered in the first part of this study, raised concerns about the possibility of having premature fracture of longitudinal HSRB in concrete members under seismic excitations.

The experiments were designed to impart large tensile strains and a large number of cycles on longitudinal bars. Therefore, longitudinal bars were expected to experience fatigue induced fracture of the longitudinal bars. Of particular interest was quantifying the effects of the shape of the stress-strain curve and the tensile-to-yield (T/Y) strength ratio of high-strength longitudinal bars on the behavior of concrete columns and the strain demands in the longitudinal bars.

Four columns were tested in this study. Three columns were reinforced with grade 100 longitudinal and transverse bars obtained from three steel manufacturers. The three types of HSRB used in this study were produced using the three main production techniques in the United States for HSRB. The fourth specimen was reinforced with grade 60 ASTM A706 bars (ASTM A706/ A706M – 16a, 2016).

One column in the series was reinforced with HSRB having a relatively high T/Y ratio of 1.27 (a relatively high value for grade 100 bars produced using the micro-alloying process). The second column utilized steel bars having a relatively low T/Y ratio of 1.16 (a relatively high value for grade 100 bars produced using the tempering and quenching process). The third column was reinforced with grade 100 ASTM A1035 (ASTM 1035/ A1035M – 16b, 2016) steel bars, which exhibit no clear yield point and possess rounded stress-strain relations with a pronounced inelastic hardening behavior. The last specimen, reinforced with grade 60 A706 (ASTM 706/ A706M – 16, 2016) steel, delivered benchmark behavior for comparison with HSRB behaviors. Since the T/Y ratio and ultimate elongation are coupled properties in HSRB, i.e., increasing one decreases the other, the bars used in this project targeted specific T/Y ratios at the high end of production capabilities and the maximum attainable elongations at those T/Y ratios. Hoops in the

columns were fabricated using standard bend diameters currently specified for grade 60 bars in ACI 318-14 (2014).

1.3 ORGANIZATION

Chapter 2 presents relevant background information related to the applications of HSRB in seismic designs. This chapter focuses also on several equivalent plastic hinge models that give insight into factors concentrating plastic deformations and associated strain demands. Chapter 3 describes in detail the experimental program, including the design and fabrication of the specimens, instrumentation, and the testing setup and protocol. In Chapter 4, detailed results are presented for each test individually, while Chapter 5 compares the behaviors of all columns and highlights the influence of bar mechanical properties. Chapter 6 summarizes the study's conclusions.

2. Background

This chapter provides a brief summary of the leading manufacturing methods currently used to produce HSRB. Background information on the low-cycle fatigue behavior of steel reinforcing bars is also presented. The discussion focused on possible implications related to the use of high strength steel in concrete columns, while also presenting past research on relevant behavioral aspects of reinforced concrete columns. Special focus is given to research looking into deformation concentrations and strain demands in plastic hinge regions of concrete columns.

Limited number of studies were found that treated the topic of strain demands in longitudinal bars directly, while none were available for the new HSRB under development. This study is the first to investigate the effect of the tensile-to-yield (T/Y) ratio and shape of the stress-strain curve on the behavior of concrete columns.

2.1 METALLURGY

Earlier attempts at increasing the yield strength of reinforcing bars focused on increasing the carbon and manganese content in steel alloys. These methods can successfully increase the yield strength of steel bars but have the drawback of significantly reducing the elongations at fracture. The four main methods of strengthening steel reinforcing bars that are currently used in the industry are: micro-alloying, quenching and tempering, a proprietary combination of alloying and micro structure manipulation, and cold working.

2.1.1. Micro-alloying

Micro-alloying can produce a marked yield point and a T/Y ratio larger than that from quenched and tempered steels (on the order of 1.25 for grade 100 reinforcing bars). Micro-alloying is the process of producing high-strength steel by adding small amounts of

vanadium (V), titanium (Ti), or niobium (N) to form a “solid solution”. The micro-alloying method consists of two strengthening mechanisms: grain refinement and precipitation. Grain refinement strengthening occurs by producing a very fine grain size generated by pinning the planar defects (grain boundaries) through thermos-mechanical processing (rolling). Furthermore, the pinning of planar defects causes the intermetallic carbides to be dispersed through the ferrite grains, which further raises the yield strength of the material. This mechanism is called precipitation strengthening. Titanium micro-alloying contributes to precipitation strengthening. However, titanium has a strong tendency to combine with oxygen, sulfur, and nitrogen, which makes it difficult to control the strengthening effects. Niobium micro-alloying in reinforcement production requires a high degree of control on rolling temperatures, which makes it more challenging to use for high-strength reinforcement production.

Vanadium is a strong carbide former and vanadium carbides precipitates have the highest austenite solubility compared to niobium and titanium (Gladman, 1997). Adding vanadium increases yield strength due to grain size refinement and precipitation of carbides and nitrides. Precipitation of second phase particles within the grain’s crystal lattices impedes the movement of dislocations throughout the grain. This process makes the resulting dislocations move around the precipitates or through them. Enhancing nitrogen in vanadium-contained bars increases the precipitation of particles, which produces higher yield strength. Furthermore, vanadium-nitrogen micro-alloying eliminates the adverse effects of strain aging on other properties of steel (Caifu, 2010; Erasmus and Pussegoda, 1978; Restrepo-Posada et al., 1994). Alloyed bars, particularly those produced with vanadium, have a relatively large T/Y ratio, on the order of 1.2 to 1.4 for grade 80 or higher

bars. However, at grade 100, the fracture elongation of alloyed bars currently ranges from 9 to 14% and can be lower than that of tempered and quenched bars.

2.1.2. Quenching and Tempering

Quenching produces high-strength bars from inexpensive carbon steel. This process consists of rapid cooling of the steel after it has been heated to the austenitic phase, resulting in a hard and brittle material. The remaining heat at the core of the bar modifies the microstructure and decreases the hardness while increasing the ductility of the material. This process is called tempering. As a result, quenched and tempered bars have a softer more ductile center and a harder brittle shell. Quenching and tempering typically produces large gains in yield strength but relatively modest gains in tensile strength. Therefore, the T/Y ratio of such bars can be relatively low and on the order of 1.10 to 1.15 for grade 100 bars. On the other hand, fracture elongation of tempered and quenched bars tends to be larger than that of micro-alloyed bars.

2.1.3. Proprietary Combination of Alloying and Micro Structure Manipulation

The proprietary combination of alloying and micro structure manipulation method has been patented by MMFX (MMFX Technologies Corporation, 2012). This process involves manipulating the microstructure of steel to obtain the desired mechanical properties and strength. The process generates bars with stress-strain relations that do not have a well-defined yield point, exhibit a relatively high T/Y ratio, but have relatively low fracture elongations (in the order of 6%). The MMFX steel bars satisfy the ASTM A1035 specifications (ASTM A1035/A1035M-16a, 2016). ACI 318-14 (2014) allows for the use of A1035 grade 100 bars in confinement applications.

2.1.4. Cold Working

Cold working is the method used to strengthen metal by enforcing plastic deformation. The strengthening occurs due to additional dislocations and movements generated within the crystal structure of the material. When two or more of these internal dislocations meet, increased resistance to plastic deformations occurs, which contributes to the gain in strength. However, this method reduces the ductility of the material. Cold working also eliminates the yield plateau. This method may result in an increase in the yield strength, but it reduces both ductility and the ratio of the tensile-to-yield (T/Y) strength. For these reasons, this method is not used in producing high-strength steel bars for seismic applications.

2.2 LOW-CYCLE FATIGUE

Brown and Kunnath (2004) performed low-cycle fatigue tests on typical longitudinal-bar sizes; #6, #7, #8, and #9. All the bars tested satisfied ASTM A615 (ASTM A615 / A615M - 16) grade 60 specifications. Bars were cycled at constant strain amplitudes varying between 1.5% to 3.0%. The strains were measured over the entire span of the coupons, which was selected as 6 times the bar diameter (d_b). The strain amplitudes measured were based on the average strains across the entire clear span. The tests concluded that the number of half cycles to failure of the reinforcing bars decreases exponentially as the strain amplitude increased (Figure 1a). When tested at large strain amplitudes, the larger diameter bars also appeared to be prone to failure at fewer half cycles than smaller bars.

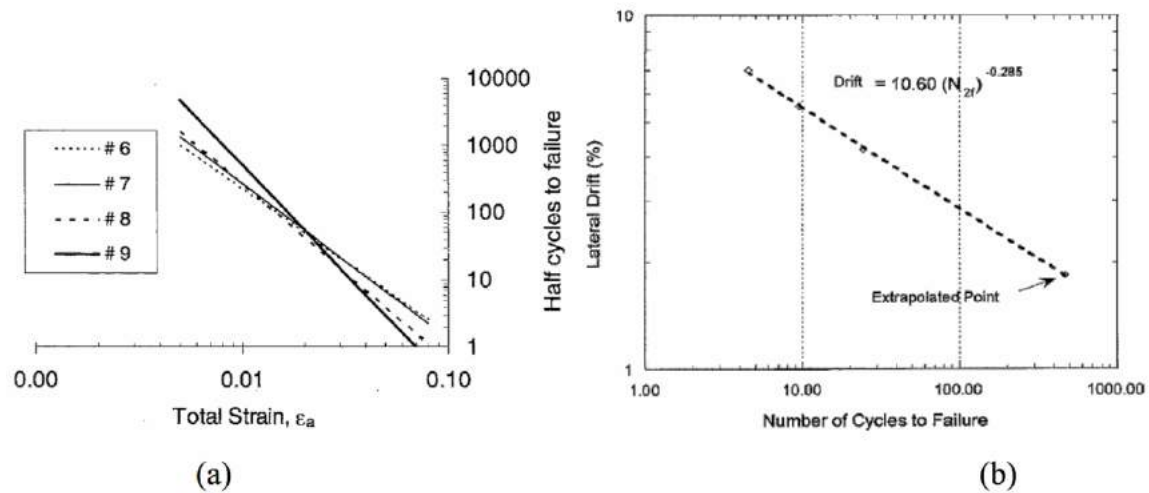


Figure 1: Number of half cycles to failure with: (a) total strain (Kunnath et. al., 2004); (b) lateral drift ratio (Kunnath et. al., 1999)

Previous research on cumulative seismic damage of circular bridge columns (Kunnath et al., 1999) also focused on fatigue life of the columns. Four quarter-scale circular columns were tested in constant drift cycles of 2%, 4%, 5.5%, and 7% lateral drift ratio respectively. The test results demonstrated that the number of half cycles to failure decreased exponentially (Figure 1b).

Low-cycle fatigue tests were recently performed on newly developed high-strength reinforcing bars as part of this larger study (Slavin and Ghannoum, 2015). The reinforcing bars tested were classified as grade 60 ASTM A706, grade 80 ASTM A706, grade 80 ASTM A615, and grade 100 (without specification). Test results showed similar conclusions to previous research by Brown and Kunnath (2004), that half-cycles to fracture decreases exponentially as the total strain range increases. Equations for assessing the fatigue of bars given a specific strain amplitude were proposed (Equation 1, Equation 2 and Table 1). The “a”, “b”, “c”, “d” parameters are summarized in Table 1 for #8 reinforcing bars of varying grades, specifications, and clear-span gripping lengths. Figure

2 compares bar-test results for grade 60 #8 bars to previous research by Brown and Kunnath (2004). Slavin and Ghannoum (2015) concluded that the fatigue performance, defined in terms of the number of half-cycles to fracture and the total strain energy dissipation, was marginally poorer for HSRB than for grade 60 bars. However, high variability of fatigue performance was observed for HSRB, some could fracture at significantly fewer numbers of half-cycles than their grade 60 counterparts and others at much higher numbers. Over all the tests performed by Slavin and Ghannoum (2015), the average number of half-cycles to failure of the grade 100 bars was 91% of that for the grade 60 A706 bars.

Equation 1: Fatigue life modeling with strain range as the dependent variable

$$\textit{Total Strain Range} = a * (\textit{Half-Cycles to Failure})^b$$

Equation 2: Fatigue life modeling with fatigue life as the dependent variable

$$\textit{Half-Cycles to Failure} = c * (\textit{Total Strain Range})^d$$

Table 1: Summary of material coefficients for fatigue life equations for #8 bars (Slavin and Ghannoum, 2015)

Manufacturer	Grade	Clear Span	c	d
1	60	4db	5.14E-03	-2.87
		5db	5.92E-03	-2.77
		6db	7.92E-03	-2.59
	80	4db	2.48E-03	-2.97
		6db	6.60E-03	-2.43
	100	4db	2.40E-05	-4.62
5db		8.14E-05	-4.06	
6db		1.49E-04	-3.77	
2	60	4db	3.59E-04	-3.75
		5db	8.49E-04	-3.31
		6db	1.49E-03	-3.03
	100	4db	1.90E-06	-5.42
		5db	2.60E-06	-5.25
		6db	1.65E-05	-4.46

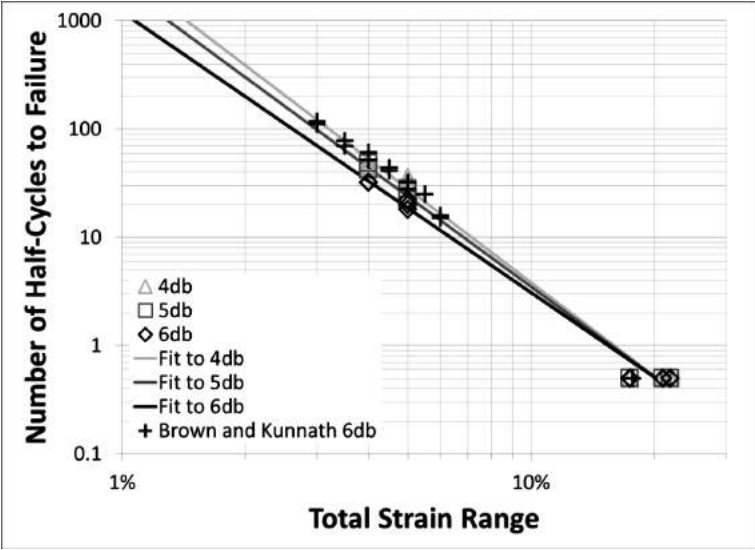


Figure 2: Results from Brown and Kunnath (2004) overlaid with data from grade 60 #8 bars produced by Manufacturer I (Slavin and Ghannoum, 2015)

2.3 RELEVANT EXPERIMENTAL STUDIES WITH HSRB

2.3.1 Introduction

The use of high-strength reinforcement may reduce member stiffness and lead to larger elastic deformations before yield, as less steel is utilized compared to lower strength steel alternatives. Bars with higher strength require longer straight, hooked, or anchored development lengths. Such increases in required lengths may influence member dimensions and steel congestion. Moreover, the shape of reinforcement's stress-strain curve influences the spread of plasticity within a plastic hinge region. The presence and the length of a yield plateau, the ratio of tensile-to-yield strength, and the total elongation at fracture are all important properties that affect the spread of plasticity and maintain strength through large inelastic rotations (Macchi et al., 1996; Aoyama, 2001; Rautenberg, 2011; Rautenber et al., 2012, 2013; Sokoli and Ghannoum, 2016). Increasing the strength of steel bars usually results in a relatively short yield plateau, if any. The steel specified in ASTM A1035 (ASTM A1035 / A1035 – 16b, 2016) has rounded stress-strain relations with no defined yielding point. The presence of a yield plateau can be consequential on strength estimates and deformation capacity of concrete members (ACI ITG-6R, 2010).

Bars with higher strength steel resist more load for a given bar size than bars with lower strength steel. Higher loads for the same cross-section increase the likelihood that high-strength bars will buckle unless restrained lengths are decreased in accordance with their strength. Restraint effectiveness depends on the spacing and stiffness of the transverse reinforcement as well as the absolute strain experienced by the longitudinal bars (Tanaka, 1990; Restrepo-Posada 1992; Moyer and Kowalsky, 2003). Absolute strain is the difference between the maximum tensile and compressive strain in a longitudinal bar during cyclic loading. As the use of high-strength longitudinal bars is explored, the re-

evaluation of the maximum permitted spacing and minimum cross-sectional area of transverse reinforcement may be needed.

2.3.2 Experimental Programs

Baker and Amarakone (1964)

Baker and Amarakone (1964) reported results from tests on concrete beams and columns aimed at assessing “the influence of grade of concrete or steel, percentage of steel, single loads and double loads, axial force, shear, transverse binding, and percentage of compression steel” on the inelastic distribution of rotations along member’s length. Two types of steel were used in this study, grade 40 mild steel with a well-defined yield plateau and what could be considered as grade 75 cold-worked steel having a curved continuous stress-strain curve, without a well-defined yielding point. The actual yield strength of the tension reinforcement varied from 37 to 85 ksi. Concrete strength varied from 2.5 to 6.5 ksi and the axial load varied from 16% to 120% of the gross sectional axial capacity. The authors also summarized the experimental work done in several research centers around the world on the same topic.

The authors developed equations discussed in Section 2.5.1 to calculate an equivalent plastic hinge length and maximum plastic rotation at peak strength. The equations highlight the influence of loading conditions, materials used, and sectional design on the distribution of plasticity in columns. Notably, Baker and Amarakone identified steel type and grade as a factor influencing plasticity spread. For higher strength reinforcement without a well-defined yielding point, the plastic hinge length was observed to be longer than for the mild steel. The authors concluded that the span length to depth

ratio did not have a major impact on the observed plasticity spread, but the moment gradient did.

Macchi et. al. (1996)

Twenty-seven small-scale columns with two different reinforcing steel properties were tested cyclically in single curvature by Macchi et.al. (1996). The first type of steel used, named A8, had yield strength of 87 ksi, T/Y ratio of 1.1, and uniform elongation of 0.08. The second type of steel used was Fe steel, with yield strength of 86 ksi, a T/Y ratio of 1.4, and a uniform elongation of 0.11. Specimens with varying cross sections and longitudinal and transverse reinforcement layouts were tested under three different loading protocols. Applied axial loads varied from 0 to 16% $A_g f'_c$ (where A_g = gross sectional area; f'_c = concrete compressive strength). In all cases, failure was observed due to longitudinal bar fracture. Specimens reinforced with A8 steel failed before completing the target loading protocol. In contrast, concrete columns reinforced with Fe steel failed in all cases after completing the target loading protocol. Authors concluded that premature failure of columns reinforced with A8 steel was mainly attributed to strain concentrations in longitudinal reinforcement and limited plasticity spread. Strain hardening, or the T/Y ratio, was observed to have a larger effect on the overall behavior of the members than fracture elongation values. The authors suggested that a T/Y ratio of 1.1 does not produce satisfactory lateral behavior, while bars with a T/Y of 1.15 to 1.2 can lead to satisfactory performances. However, the authors recommended a minimum T/Y ratio of 1.3 for seismic applications, which is close to the minimum specified T/Y ratio of 1.25 in ASTM A706 (ASTM A706 / A706M – 16, 2016). Also, the authors recommended a minimum fracture elongation of 8% for reinforcement used in columns which are to sustain inelastic deformations in regions of high seismicity. The authors observed that larger diameter bars

in concrete columns perform better under reverse loading. They argued that the lower bond strength between the bigger bars and the surrounding concrete allowed for the spread of plasticity over higher lengths.

Aoyama (2001)

Aoyama (2001) reported tests on beams reinforced with high-strength bars. Two different types of reinforcing steel were used in the study. The R90 steel had a relatively low T/Y ratio of 1.1, and the CR75 steel a higher T/Y ratio of 1.33. Failure occurred at an earlier loading stage in the beams with the steel having a low T/Y ratio due to longitudinal bar fracture at a lateral drift ratio of 5%. These failures were attributed to strain concentrations in the bars. The author concluded that a lower T/Y strength ratio results in substantially larger bar strains for the same lateral deformation.

Restrepo et. al. (2006)

Restrepo et. al. (2006) tested two 35%-scale circular cantilever bridge piers. Both units were reinforced with #5 longitudinal bars and butt-welded #3 hoops spaced at 1.56 inches. The longitudinal reinforcement in Unit 1 consisted of conventional grade 60 ASTM A706 steel with a strain at fracture of 10.5%, while Unit 2 was reinforced with steel with a round-shaped stress-strain curve, not exhibiting a defined yield point (akin to A1035 steel). The yield stress calculated through the 0.2% rule was 94 ksi for bars in Unit 2. The strain at fracture for these bars was 5.1%. The longitudinal reinforcement ratio for Unit 1 was 2.54%, while for Unit 2 it was 1.27%. The concrete compressive strength was 9.3 and 8.2 ksi, respectively for Unit 1 and 2. Self-consolidating concrete was used in this study, which was found not to affect the behavior of the columns. A compressive axial load on the order of 7.5% of the gross-sectional capacity was applied to both members while being pushed

by lateral quasi-static load.

Unit 1 sustained significant buckling and concrete crushing after completing 3 full cycles to a drift ratio of 5.5% and as it was being pushed to the first cycle to +7.5% drift ratio. Bars fractured at a drift ratio of -7.5%. In Unit 2, a hoop fracture occurred at a drift ratio of 3.1%. This resulted in longitudinal bars buckling in the subsequent cycles. The first longitudinal bar fractured at 4.5% drift ratio, which resulted in significant lateral strength loss.

The authors suggested the reduced residual drifts observed in members reinforced with HSRB without a yielding point in their stress-strain curve need to be taken advantage of in seismic design. Moreover, it was stated that HSRB with the described properties is very effective when used as transverse reinforcement to brace the longitudinal bars. The fact that these bars do not exhibit an “unrestricted yielding” coupled with the high strain hardening slope gives this type of reinforcement a clear edge over other alternatives commonly used at present.

Even though not explicitly reported in Restrepo et. al. (2006), the presented results suggest that the column reinforced with grade 100 A1035 bars dissipated significantly less energy within the hysteretic loops than the column reinforced with grade 60 bars.

Rautenberg et. al. (2011, 2012, 2013)

Rautenberg et al. (2011, 2012, 2013) reported tests on columns reinforced with steel satisfying ASTM A1035. The steel used had a yield strength around 120 ksi but no defined yield point, thus no yield plateau. These columns lost significant lateral-load capacity at a drift ratio of 4%. Rautenberg (2011) concluded that tests reinforced with high-strength steel without a yield plateau “have smaller drift capacities than columns reinforced with A706 60-ksi steel reinforcement with a yield plateau. The difference in drift capacity is attributed

to the difference in the shape of the stress-strain curves, which leads to differences in the distribution of curvature”. Additional comparative tests were reported in 2013 (Rautenberg et al., 2012, 2013). The type of high-strength steel used in this study was again A1035 (ASTM A1035 / A1035M – 16b, 2016) for the longitudinal reinforcement. It was found that a decrease in drift capacity of 10-50% occurred when A1035 grade 100 or 120 reinforcement was used compared with when A706 (ASTM A706 / A706M – 16, 2016) grade 60 steel was used.

Tallavali et al. (2014)

Tallavali et al. (2014) tested beams reinforced with SAS 670 longitudinal bars, and concluded: “Replacing conventional grade 60 longitudinal steel bars with reduced amounts of grade 97 high-strength steel bars provided nearly identical flexural strength and did not decrease the usable deformation capacity.”

Cheng and Giduquio (2014)

Cheng and Giduquio (2014) reported results from three cantilever flexural tests: Member SP1 was reinforced with conventional grade 60 flexural steel ($T/Y \sim 1.5$); SP2 with SD685 steel ($T/Y \sim 1.23$); and SP3 with A1035 steel ($T/Y \sim 1.26$). Members were tested under quasi static cyclic displacement. SP2 was found to spread plastic flexural rotations up to a height of $0.59d$ from base. Plastic rotations in SP3 were distributed up to a distance $0.89d$ from the base. Plastic rotations were not evaluated in SP1. Authors concluded that even though the T/Y ratio of the flexural reinforcement in SP2 and SP3 was very similar, members spread the plastic rotations over different heights. Therefore, the authors concluded that the T/Y ratio of the reinforcement does not significantly affect the plasticity spread in concrete members. Instead, they suggest that curvature distribution is

affected more by the location of the flexural cracks. Specimen SP2 had two major cracks concentrated at a distance less than $0.6d$ from the base, while specimen SP3 had more uniformly distributed cracks over a higher length. The observed curvature distribution also suggested that at a given lateral drift ratio, the tensile strain demands were higher in specimen SP2 than in specimen SP3. Both specimens failed at similar deformation levels by fracture of the longitudinal reinforcement.

Cheng and Giduquio (2014) observed a lower energy dissipation in members reinforced with A1035 (ASTM A1035 / A1035M – 16b, 2016) steel and attributed it to the lack of the yield plateau in this type of reinforcing steel.

Barbosa et al. (2015)

Barbosa et. al., (2015) tested 4 circular half-scale bridge columns under quasi static lateral load. Columns were subjected to a constant axial load of 90 kips, corresponding to 5% of the nominal axial capacity. Members were reinforced with grade 60 (named G60 and G60-s) and 80 (named G80 and G80-s) A706 steel. A Specified concrete compressive strength of 4 ksi was used in all specimens. G60 and G80 had a moment-shear span ratio of 6, while G60-s and G80-s had a moment-shear span ratio of 3. Shear stresses were in the order of $1.7 \sqrt{f'_c}$ for G60 and G80 columns, and $3.4 \sqrt{f'_c}$ for G60-s and G80-s (in psi units). The four columns were designed to achieve similar nominal moment capacities. Columns reinforced with grade 80 steel achieved similar moment strengths, maximum lateral displacement, and curvature ductility to the ones reinforced with grade 60. All columns achieved similar maximum lateral drift capacities on the order of 6% of their clear span and displacement ductilities larger than 4.0. Members failed in flexure due to the longitudinal bars buckling followed by bar fracture. The energy dissipated by columns reinforced with grade 80 bars was lower than that of columns reinforced with grade 60

bars. The difference was attributed to the difference in lateral stiffness and the fact that the member reinforced with higher strength steel had less steel in its section. The length of the yield plateau did not seem to have had a detrimental effect on the amount of energy dissipated by each member.

Sokoli and Ghannoum (2016)

Sokoli and Ghannoum (2016) performed reversed cyclic tests on three columns designed for the same flexural strength but with different grades of reinforcing bars (grade 60, grade 80 and grade 100). Except for the bar strength, all other parameters were kept nominally identical for all three columns. Columns were designed with a concrete compressive strength of 4 ksi. Columns had a shear span-to-depth ratio of 2.7, and shear stresses on the order of $9.6 \sqrt{f'_c}$ (in psi units). The three members were subjected to a constant axial load of 370 kips, which corresponded to approximately 30% of the gross axial capacity. Columns reinforced with grade 60 and grade 80 bars showed comparable lateral behavior, achieving similar maximum lateral displacements beyond drift ratios of 5.5% (drift ratio = lateral drift divided by column clear span). These two columns failed in shear and subsequently their axial load carrying capacity degraded. CS100 failed in a bond-splitting mode, with bond degradation starting at a drift ratio of 1.5%. The column developed its peak strength, but lost lateral strength as debonding progressed. The authors recommended reducing the available anchorage length of longitudinal bars by the distance over which concrete is damaged in the plastic hinge regions of concrete columns in Special Moment Frames. These columns also exhibited different strain demands in the longitudinal bars, with higher strength bars experiencing higher strain demands at the same drift levels. In these tests, Grade 100 longitudinal bars experienced as much as 100% larger strains than grade 60 bars at the same drift levels.

2.3.3 Summary

In conclusion, the available experimental data have demonstrated that reinforcing steel bars with higher values of the T/Y ratio are preferred in seismic applications. Longitudinal bars with a relatively high T/Y ratio allow plasticity to spread farther in regions of yielding, which in turn reduces significantly the elongation and fatigue demands on bars. The effects of having a yield plateau remain unclear as some research indicates that its absence could result in decreasing drift capacity. Columns with HSRB were found to dissipate less energy than members of equivalent strength reinforced with grade 60 bars. Data are mixed on whether HSRB reduce the ductility capacity of concrete members compared to grade 60 A706 (ASTM A706 / A706M – 16, 2016) bars.

2.4 STRAIN DEMANDS IN LONGITUDINAL REINFORCING BARS

2.4.1 Experimental Evidence

Macchi et. al. (1996) and Aoyama (2001) both suggested that a lower T/Y ratio contributes to strain concentrations in the longitudinal reinforcement strain. They concluded that a lower T/Y ratio leads to higher strain demands at a given drift ratio. Sokoli and Ghannoum (2016) reported that columns reinforced with grade 80 and 100 bars exhibit significantly larger strain demands than their counterpart reinforced with grade 60 bars. Grade 80 longitudinal bars sustained about 65% larger strains at all drift levels than those of the grade 60 longitudinal bars. The column reinforced with grade 100 bars sustained bond splitting failure. However, maximum strains in the grade 100 longitudinal bars were found to be 25% higher than in grade 80 bars and 100% higher than in the grade 60 bars at a given drift level prior to bond degradation. The T/Y ratio was smaller for the higher-strength steel used in the three columns of this study, with grade 100 steel having a T/Y of 1.26, grade 80 a T/Y of 1.34, and grade 60 a T/Y of 1.41.

2.4.2 Estimating Strain Demands in Longitudinal Reinforcement

Previous research (Berry and Eberhard, 2007) attempted to predict the average strain in longitudinal bars of bridge circular columns over the height of the member at distances of $(0-D/2)$ and $(D/2-D)$ from column ends; with D being the section diameter. Berry and Eberhard (2007) stated that their model accurately predicts strains at low levels of column deformation, but is less accurate at higher levels as shown in Figure 3. The authors stated that the discrepancy was likely caused by debonding of the longitudinal reinforcement. Results from the study indicated that strains in the bars within the column span $D/2-D$ increased rapidly while those within $0-D/2$ decreased after the onset of spalling. Spalling and debonding of the longitudinal reinforcement was attributed to the

spreading of the strains along the column height rather than concentration at the section of highest moment.

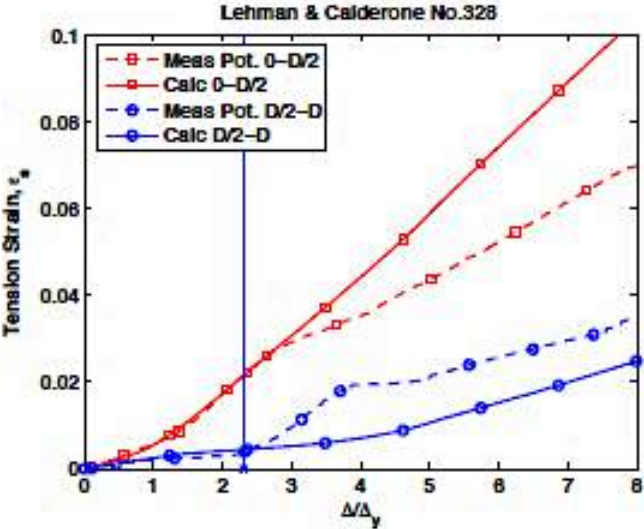


Figure 3: Debonding of longitudinal reinforcement effect on strain in longitudinal bars (Berry and Eberhard, 2007)

2.4.3 Strain Demands and Tension Shift due to Shear/Inclined Cracks

Shear stresses leading to inclined cracking have been demonstrated to shift the tension force in longitudinal bars over a distance of about the section depth from the point of peak flexural demand. This shift effectively increases the tension in the bars within that distance. This leads to higher strains from what are predicted based on the moment diagram from sectional analysis. Park and Paulay (1975) explained that shear/inclined crack near the end region of concrete members could potentially spread the yielding of longitudinal bar over considerable length of the member. When the flexural reinforcement has yielded, shear/inclined cracks increase in width and less shear can be transferred by either aggregate interlock or dowel action. As a result, a larger portion of the shear force will have to be transferred across the compression zone through a truss mechanism that pulls on the

longitudinal bars in tension at the location they intersect the inclined cracks (Figure 4). This hypothesis was corroborated experimentally with strain gauge readings (Wight, 2016). Therefore, large shear forces can potentially increase tension forces away from the end of a column, which possibly can lead to less strain concentrations at the section of highest moment.

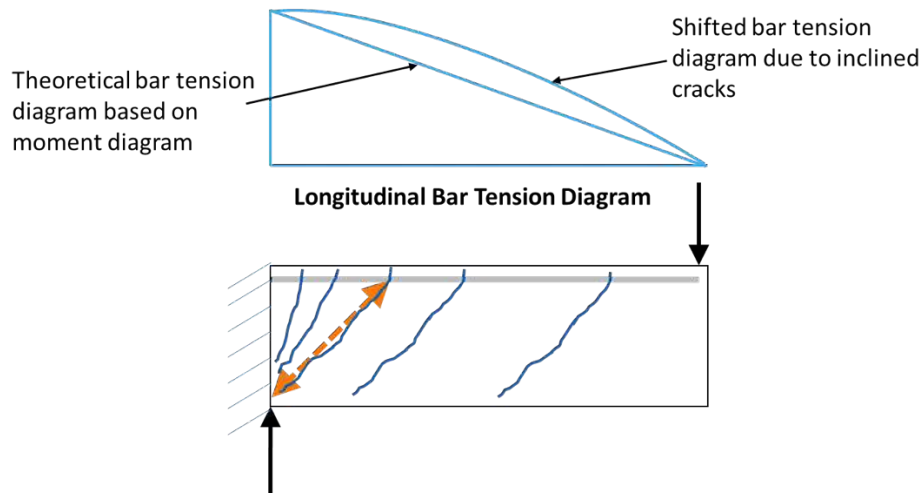


Figure 4: The distribution of longitudinal bar tension forced at end region of the member affected by shear-induced inclined cracking

2.5 DUCTILITY, PLASTICITY SPREAD, AND STRAIN DEMANDS

Past research exploring concentration of deformations in hinge regions of concrete columns has mainly focused on evaluating a plastic hinge length that is associated with a limiting curvature, from which a drift capacity at failure is estimated. The following sections provide an overview of some relevant models and their formulations that give insight into factors concentrating plastic deformations and associated strain demands in concrete members. A discussion about model limitations with respect to HSRB is also presented.

2.5.1 Plastic Hinge Length Models

The ultimate lateral drift, Δ_u , provides a measure of the ductility of a concrete member at a given failure, which is defined differently in different works (i.e., crushing of the concrete core, hoop fracture, bar buckling, bar fracture, etc.) Typically, inelastic deformations are estimated through rotational deformations of idealized plastic hinges that are given an equivalent length (l_p^*) and ultimate curvature (Ψ_u^*) at which failure is considered to occur (Figure 5). Often, the behavior of plastic hinges is idealized as having a constant inelastic curvature over the equivalent plastic hinge length. Loss of lateral strength occurs when an associated limiting ultimate curvature is reached. Member drift capacity is then estimated by adding inelastic lateral drifts to elastic drifts (Δ_y), by integrating the constant curvature (difference between curvature at elastic limit and the ultimate curvature = $\Psi_u^* - \Psi_y$) over the equivalent plastic hinge length (l_p^*) (Equation 3 for a cantilever member).

Equation 3: Calculation of ultimate lateral drift

$$\Delta_u = \Delta_y + l_p^*(\varphi_u^* - \varphi_y)\left(l - \frac{l_p^*}{2}\right)$$

Several models have been proposed to estimate an equivalent plastic hinge length and the associated ultimate curvature at failure (i.e., Baker and Amarakone, 1964; Mattock, 1965, 1967; Corley, 1966; etc.). These empirical models typically provide a lower-bound estimate of the plastic hinge length and associated drift capacity. Some of the most widely recognized models specify an ultimate concrete compressive strain from which an ultimate curvature can be calculated using sectional analysis (i.e., Baker and Amarakone; 1956; Mattock, 1964; Corley, 1966, etc.). The inherent assumption in these models is that failure, often defined at a certain loss in lateral strength, occurs due to damage of the concrete core. The following provides a summary of some of the most prominent plastic hinge models.

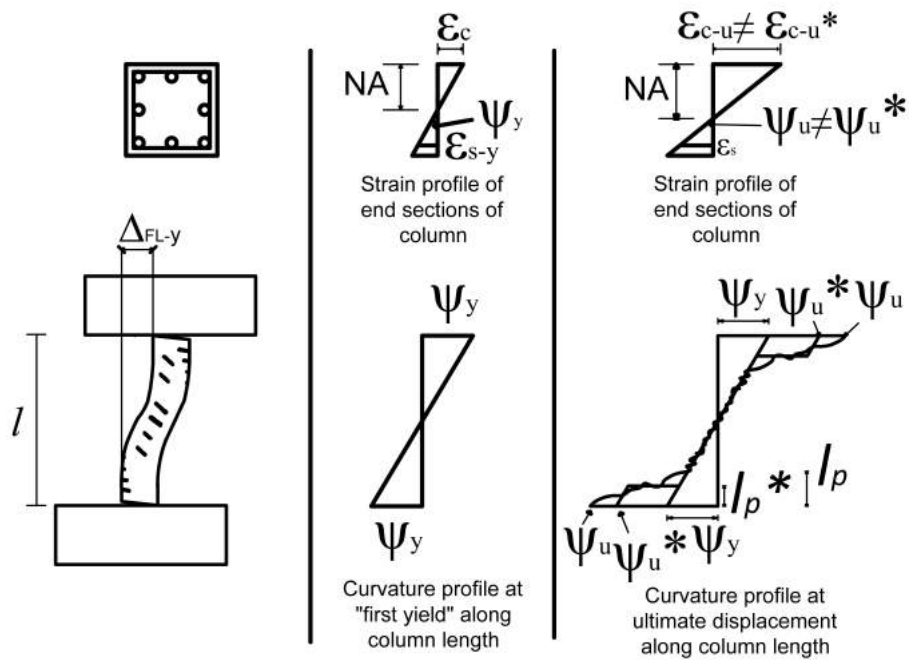


Figure 5: Flexural deformation calculations

Baker (1956); Baker and Amarakone (1964)

In his 1956 publication (Baker, 1956), Baker concluded that an equivalent plastic hinge length for columns could be assumed to range between $0.5h$ and h , where h is the height of the section in the direction of loading. In a second publication by Baker and Amarakone (1964), results from tests on concrete beams and columns were presented (see section 2.3.2). This work aimed to assess “the influence of grade of concrete or steel, percentage of steel, single loads and double loads, axial force, shear, transverse binding, and percentage of compression steel” on the inelastic distribution of rotations along member’s length. Two types of steel were used in this study, grade 40 mild steel with a well-defined yield plateau and what could be considered as grade 75 cold-worked steel having a curved continuous stress-strain curve, without a well-defined yielding point.

The authors developed the following equations to calculate an equivalent plastic hinge length and maximum plastic rotation at peak strength:

Equation 4: Equivalent plastic hinge length (Baker and Amarakone, 1964)

$$l_p^* = k_1 k_2 k_3 \left(\frac{z}{d}\right)^{1/4} d$$

Equation 5: Plastic rotation (Baker and Amarakone, 1964)

$$\theta_p = 0.8 \left(\frac{e_{cu} - e_{ce}}{c}\right) l_p^*$$

Equation 6: Coefficient accounting for applied axial load (Baker and Amarakone, 1964)

$$k_2 = 1 + 0.5 \frac{P}{P_u}$$

where:

- k_1 accounts for the type of the tension reinforcement, and is equal to 0.7 for the grade 40 mild steel and 0.9 for the grade 75 cold-worked steel.
- k_2 defined by Equation 6, accounts for the axial load
- k_3 accounts for the influence of concrete compressive strength and is equal to 0.6 for concrete cube strength of 6 ksi and 0.9 for concrete cube strength of 2 ksi. Linear interpolation is to be used for values that fall within that range.
- z (in.) was defined as the distance of the critical section to the point of contra-flexure
- d is the effective depth of the cross-section
- θ_p is the maximum permissible plastic rotation at the critical section
- e_{cu} is the maximum concrete compressive strain at ultimate strength taken as (0.0035)
- e_{ce} is the maximum concrete compressive strain at yield (taken as 0.002)

Equation 4 predicts an equivalent plastic hinge length which falls between $0.4d$ and $2.4d$ considering the “broad range of structural members” used in practice. Equation 4 also indicates the influence of loading conditions, materials used, and sectional design on the distribution of plasticity in columns. Notably, Baker and Amarakone identified steel type and grade as a factor influencing plasticity spread. For higher strength reinforcement without a well-defined yielding point, the plastic hinge length was observed to be longer than for the mild steel. The factor k_1 , accounting for the type of reinforcement used, is 28% larger for the cold-worked steel. The authors concluded that the span-length-to-depth ratio did not have a major impact on the observed plasticity spread, but the moment gradient did.

The ultimate plastic rotation and plastic hinge length proposed models were related to a fixed value of the maximum compressive strain in the outermost fiber of the section. The calculated maximum plastic rotations were found to vary significantly, because the ultimate strain in concrete varies and does not have a set maximum value.

Mattock (1964)

Mattock (1964) presented results from tests on simply supported beams loaded monotonically to failure. These tests were carried to assess “the influence of several variables on the moment-curvature relationships for reinforced concrete section adjacent to a support, and on the total rotational capacity of hinging regions adjacent to a support.” In this study, rotational capacity was assumed to be reached when the section develops its flexural strength. Tension controlled (under-reinforced) beams were reinforced for tensile stresses with #6 bars having yield strengths of 47 ksi and 60 ksi, well-defined yielding points, and a relatively long yield plateau. The amount of tension reinforcement varied from about 1% to 3% of the effective sectional area. The compression reinforcement used had yield strengths of 50 and 70 ksi. 4 and 6 ksi concrete was used in the specimens. The ratio between the span from maximum to zero moment to the effective depth varied from 2.5 to 10. The proposed model was based on the moment gradient and difference between the tension and compression reinforcement ratios (reinforcement index), to predict the ultimate displacement ductility of concrete beams.

In his study, Mattock concluded that “for a given reinforcement index and depth of beam, the ultimate curvature at mid-span decreases as the distance from point of maximum moment to point of zero moment increases.” In line with the work from Baker and Amarakone (1965), Mattock suggested that the variation in the concrete maximum compression strain varies with the distance between point of zero and maximum moment. Mattock proposed a formula to calculate the maximum concrete compressive strain based on the distance between the point of zero and maximum moment (z) (Equation 7).

Equation 7: Ultimate concrete compressive strain (Mattock, 1964)

$$\epsilon_{cu} = 0.003 + \frac{0.5}{z}$$

Conclusions were also drawn regarding the maximum curvature demands and plasticity spread. It was observed that inelastic deformations “do not concentrate at the section of maximum moment.” Therefore, plasticity spreads to a distance which is larger than $d/2$ from the section of maximum moment, where d is the effective depth of the tested members. The distance over which the plasticity spreads out was found to be depended on: “the ratio of the distance from the point of maximum moment to the point of zero moment to the effective depth of the section, and on the degree of flexural reinforcement of the section.” Plasticity spread was defined as the ratio between the inelastic rotation between points of maximum and zero moment (θ_{tu}) to the inelastic rotation in a distance half-the-depth from the point of maximum moment (θ_u) (Equation 8).

Equation 8: Calculation of ultimate rotation (Mattock, 1964)

$$\frac{\theta_{tu}}{\theta_u} = 1 + (1.14 \sqrt{\frac{z}{d}} - 1) \left[1 - \left(\frac{q - q'}{q_b} \right) \sqrt{\frac{d}{16.2}} \right]$$

where the term $\left(\frac{q - q'}{q_b} \right)$ accounts for the difference between tension and compression reinforcement in a section, accounting for strain hardening.

Corley (1966)

Corley built on the original work by Mattock, to come up with a rotational capacity model for reinforced concrete beams. Corley tested 40 simply supported beams under concentrated mid-span loads, while broadening the scope of the research to investigate the effect of confinement of concrete in compression and size effects on plasticity spread. The parameters that were varied in the test matrix were: width of the beams: 3, 9 and 12 in;

effective depth: 5 to 30 in.; span: 36 to 330 in; tension reinforcement index: 1% and 3%. The steel used was what can now be considered conventional grade 60 steel. Concrete with a specified compressive strength of 4 ksi was used in all specimens.

All tested beams were tension controlled with the longitudinal reinforcement yielding prior to concrete crushing in compression. Corley concluded that “the direct effect of size on rotational capacity is not significant.” However, the size may come into play when designing for transverse reinforcement. Considering that requirements for shear or confinement are usually governed by the depth of the member, a smaller width would lead to more transverse reinforcement being provided per unit volume. In return, more transverse reinforcement which provides confinement for the concrete, was found to lead to an increase in the maximum concrete compressive strain. Therefore, larger values of rotational capacity were attained for members with more transverse reinforcement. Corley went on to propose a new equation (Equation 9), which builds on the one given by Mattock (Equation 8). Equation 9 accounts for the contribution of the ratio of the volumetric quantity of the binding reinforcement to the volume of the concrete between 2 stirrups.

Similar to Mattock, Corley used the ratio between the inelastic rotation in the length between points of maximum and zero moment (θ_{tu}) to the inelastic rotation in a distance half-the-depth from the point of maximum moment (θ_u), to measure the plasticity spread (Equation 9).

Equation 9: Ultimate rotation (Corley, 1966)

$$\frac{\theta_{tu}}{\theta_u} = 1 + \frac{0.4 z}{\sqrt{d} d}$$

Arguing that the gathered results indicated a large scatter when relating the $\left(\frac{q-q'}{q_b}\right)$ term to the maximum rotation at ultimate load, Corley concluded that this variable can be overlooked when predicting the maximum plastic rotation.

Paulay and Priestley (1992)

Paulay, Park, and Priestley developed plastic hinge length equations that can be used to evaluate the drift capacity of concrete columns subjected to seismic load. In the equation, the ultimate curvature in a given section can be limited as desired, based on the maximum compressive strain of unconfined concrete ϵ_{cu} , which the authors suggest be taken as 0.004, or higher if accounting for the maximum compressive strain in a confined concrete core (ϵ_{cm}).

Equation 10: Equivalent ultimate curvature

$$\phi_u^* = \frac{\epsilon_c}{c_u}$$

where c_u is the neutral axis depth at ultimate curvature and ϵ_c can be taken as either ϵ_{cu} or ϵ_{cm} .

Their relations were calibrated to cyclic tests on columns and accounted for bar slip that occurs at member ends due to the strain penetration of longitudinal bars in adjacent anchoring regions. The authors found that bar size was the most influential parameter on plasticity spread, while axial load and the longitudinal reinforcement ratio were found to have limited influence. It should be noted that the columns considered in the calibration process had symmetric reinforcement layouts. The original plastic hinge length relation proposed by Priestley and Park (1987) for bridge piers was as follows:

Equation 11: Equivalent plastic hinge length rotation (Priestley and Park, 1987)

$$l_p^* = 0.008l + 6d_b$$

where d_b is the diameter of the reinforcing bar in tension.

Because the equation was empirically derived, it accounted for the effect shear on the crack pattern, and the tension-shift effect taking place in the member which leads to plasticity being spread over higher lengths.

In order to account for different grades of the reinforcing steel, Paulay and Priestley (1992) modified Equation 11 as follows:

Equation 12: Equivalent plastic hinge length rotation (Paulay and Priestley, 1992)

$$l_p^* = 0.008l + 0.15d_b f_{ye}$$

where f_{ye} is the yield stress of the reinforcing bar in tension. The above equation has to be larger or equal to $0.3d_b f_y$ in all cases. Equation 12 will lead to an equivalent plastic hinge length of $0.5h$ in most practical applications and indicates that higher strength reinforcement increases plasticity spread in columns.

Grimaldi and Zinaldi (2000)

Grimaldi and Zinaldi (2000) pointed out through analytical work the high dependency of the ultimate behavior of concrete members to the steel inelastic mechanical properties. The model they propose for the evaluation of an equivalent plastic hinge length and member ductility takes into account the plastic mechanical properties of the reinforcement.

Panagiotkos and Fardis (2001)

Panagiotakos and Fardis (2001) used a database of over 1012 tests of specimens representing “various types of reinforced concrete members” to develop a model which predicts their deformation at yield or failure. Failure was defined as “a clear change in the measured lateral force-deformation response: in monotonic loading a noticeable drop of lateral force after the peak (at least 15% of maximum force) is interpreted as failure; and in cyclic loading, failure is identified with a distinct reduction of the reloading slope, and the area of the hysteresis loops and the peak force, in comparison with those of the preceding cycle(s).” Most of these members (682) were symmetrically reinforced and can be representative of column members, tested with or without axial load. Hot-rolled ductile steel bars with a T/Y ratio of about 1.5 and fracture elongation of 15% were used 824 members. Heat-treated steel bars (i.e. tempcore steel) with a T/Y ratio of 1.2 and fracture elongation of 8% were used in 129 members. Brittle cold-worked steel bars having a T/Y of approximately 1.1 and fracture elongation of 4% were used in 59 members. The concrete compressive strength in these members varied from 2.2 ksi to 17 ksi. This model was calibrated to account for member’s geometric and mechanical characteristics.

In order to predict the “ultimate chord rotation”, 875 monotonic or cyclic tests were used from the 1012 which were part of the study. All these specimens sustained flexural modes of failure. When developing the empirical model, different parameters were considered to express the plastic hinge length “in terms of their geometric characteristics, material properties and reinforcement, and axial and shear load levels.” The authors presented two approaches, but here only the analytical approach based on curvature and plastic hinge length is presented as it is more relevant to the discussion. In this model, the effects of shear, strain penetration and tension stiffening were considered.

The approach taken by Panagiotakos and Fardis involves a plastic hinge length over which a constant ultimate inelastic curvature is applied. By re-arranging the terms in Equation 3, Equation 13 provides the ultimate rotation for a cantilever member:

Equation 13: Analytical calculation of ultimate rotation

$$\theta_u = \varphi_y \frac{l}{3} + l_p^*(\varphi_u^* - \varphi_y)(l - \frac{l_p^*}{2})$$

In Equation 13, Panagiotakos and Fardis recommend evaluating the ultimate and yield curvatures based on principles of sectional analysis, while accounting for different possible scenarios, such as failure of the section due to bar fracture in tension or concrete crushing in compression. Given that the confined core concrete is able to accommodate at least 80% of the full moment capacity of the “full but unconfined section”. The ultimate strain of unconfined concrete was recommended to be taken as 0.004.

The equation proposed by the authors to compute the plastic hinge length is based on Equation 12 developed by Paulay and Priestley (1992). After studying all the “relevant element variables”, Panagiotakos and Fardis agreed with taking the plastic hinge length of a cantilever member as a linear function of the length of the member itself and $d_b f_y$. They modified Equation 12 by adopting a best fit to the data from 875 tests, to come up with Equation 14 and Equation 15, for cyclic ($l_{p,cy}^*$) and monotonic ($l_{p,mon}^*$) loading cases, respectively:

Equation 14: Equivalent plastic hinge length for cyclic loading (Panagiotakos and Fardis, 2001)

$$l_{p,cy}^* = 0.12l + 0.0146\alpha_{sl}d_b f_{ye}$$

Equation 15: Equivalent plastic hinge length for monotonic loading (Panagiotakos and Fardis, 2001)

$$l_{p,mon}^* = 1.5 l_{p,cy}^* = 0.18l + 0.0216\alpha_{sl}d_b f_{ye}$$

where α_{sl} is a zero-one variable, being equal to one if slippage of the tension reinforcement is allowed, and zero if not allowed. The equations above use the metric system, with f_y being in MPa.

The authors compared the calculated drift capacities based on plastic hinge lengths from Equation 12, Equation 14 and Equation 15 (based on the type of test, cyclic or monotonic) in conjunction with ultimate rotations from Equation 13 with the experimental results. All three equations used to calculate the plastic hinge length predicted similar values, “suggesting little sensitivity” to the model used to predict an equivalent plastic hinge length. In all cases, the scatter of the predictions remained large, and although trends could be identified, the use of a single equation to predict the plastic hinge length for all types of members was deemed sufficient.

Restrepo et. al (2006)

The authors used Equation 12 (by Paulay and Priestley, 1992) to predict the ultimate displacement of the two columns they tested (see Section 2.3.2) for more details on the experiments). They calculated a similar ultimate curvature for Unit 1 as the one measured during the test. However, the experimental ultimate displacement was 56% greater than the theoretical prediction. For Unit 2, the predicted ultimate curvature was about 50% of the measured value. However, the measured ultimate displacement was 80% of the theoretical prediction. The authors suggested that these discrepancies come as a result of under-prediction of the equivalent plastic hinge length of circular columns from Equation 12. It was observed that the spread of plasticity in Unit 2 went higher than one

column diameter from the base. Based on the above-mentioned observations, the authors went on to modify Equation 12, while keeping the same form:

Equation 16: Equivalent plastic hinge length for cyclic loading (Restrepo et. al., 2006)

$$l_p^* = \alpha l + \beta d_b f_{ye} \leq 2\beta d_b f_{ye}$$

where

- α was defined as the yield spread coefficient
- β was defined as the strain penetration coefficient

In line with Paulay and Priestley (1992), the authors went on to idealize the equivalent plastic hinge length of a column as a function of the length of the shear span and a fixed base rotation due to bar-slip. The authors backtracked “yield spread coefficient”, α , from the equivalent of Equation 3 or Equation 13 in the displacement form. The derived formula used to calculate coefficient α at a given lateral displacement was as follows:

Equation 17: Yield spread coefficient - α - (Restrepo et. al., 2006)

$$\alpha = 1 - \sqrt{1 - 2 \frac{\delta_{fle} - (\frac{M}{M_y} \phi'_y) l^2}{\phi_p l^2}}$$

where:

- δ_{fle} is the flexural deformation component
- M is the bending moment
- M_y is the bending moment at first yield
- ϕ'_y is the curvature at first yield of the longitudinal reinforcement
- ϕ_p is the plastic curvature

The strain penetration coefficient was derived by equating the equivalent plastic hinge length due to the strain penetration to the base rotation (θ_f) divided by the base curvature (ϕ):

Equation 18: Strain penetration contribution to plastic rotation (Restrepo et. al., 2006)

$$\beta f_{ye} d_b = \frac{\theta_f}{\phi}$$

Therefore, the strain penetration coefficient, β , is:

Equation 19: Strain penetration coefficient - β - (Restrepo et. al., 2006)

$$\beta = \frac{\theta_f}{\phi f_{ye} d_b}$$

The above equations were both calibrated for S.I. units. The idea behind the model proposed by Restrepo et. al. (2006), is that coefficients α and β vary with the curvature ductility demand. This concept is justified arguing that the spread of plasticity is a gradual process, something that Paulay and Priestley (1992), among others, did not try to capture in their models. However, Restrepo et. al. (2006), found that the strain penetration coefficient, β , is “fairly independent” of the curvature ductility demand. The coefficients Restrepo et. al. (2006) derived for the tested specimens, both coefficients came out higher than the ones suggested by Paulay and Priestley (1992), meaning that the later model underestimated the plastic hinge length of circular columns and ultimately the displacement ductility.

Berry et. al (2008)

Berry et. al. (2008) also modified Equation 12 for circular bridge columns based on a database of thirty-seven tests. The spacing of the spiral pitch was less than $6d_b$ in all cases, so all the tested members were well confined. The equation proposed by Berry et.al. (2008) was of the form:

Equation 20: Equivalent plastic hinge length equation form (Berry et. al., 2008)

$$l_p^* = \gamma_1 D + \gamma_2 l + \gamma_3 \frac{d_b f_{ye}}{\sqrt{f'_c}}$$

In a slightly different approach, Equation 20 accounts for the contribution of the concrete compressive strength in the bond strength between the concrete and the reinforcing steel, when calculating the strain penetration contribution to the plastic hinge length. The authors calculated parameters $\gamma_1, \gamma_2, \gamma_3$, by considering two different approaches: one aiming to minimize the error (Equation 21) and the second to be used in design (Equation 22).

Equation 21: Equivalent plastic hinge length equation (Berry et. al., 2008)

$$l_p^* = 0.0375l + 0.01 \frac{d_b f_{ye}}{\sqrt{f'_c}}$$

Equation 22: Equivalent plastic hinge length equation to be used in design (Berry et. al., 2008)

$$l_p^* = 0.05l + 0.008 \frac{d_b f_{ye}}{\sqrt{f'_c}}$$

The above equations were both calibrated for imperial units. The authors found that there was a correlation between the diameter (D) and the length (l) of the cantilever columns with the plastic hinge length. Therefore, the term D was omitted from the above equations.

2.5.2 Discussion on Past Work and Needs for HSRB

The work described above presents attempts to predict the deformation capacity and ductility of concrete members through lumped plasticity models. The models presented exhibit relatively large errors between estimates of plastic hinge lengths and ultimate curvatures, and measured quantities. The crude estimates of the maximum concrete compressive strain or ultimate curvatures at failure and the simplified assumptions about the variation of inelastic curvatures over the plastic hinge length have contributed to those errors. Another major factor contributing to the large errors is the fact that none of the traditional models treat explicitly the effects of the shape of the steel stress-strain relation or the loading histories and numbers of cycles that columns sustain. Lumping modes of failure or ignoring some other modes of failure in the analysis is also a source of error.

In most models treating the seismic deformation capacity of columns, failure is defined at a loss of 20% of the lateral-load carrying capacity, which implies that the models are mostly calibrated to a gradual core-damage mode of failure. Fracture of longitudinal bars was not treated explicitly, thus omitting the effects of the fracture elongation and fatigue life of longitudinal reinforcement from the models. However, with the more brittle HSRB, fracture of longitudinal bars can become a more influential parameter defining the deformation capacity of concrete members. This is particularly true if strain demands on HSRB are higher than those on grade 60 bars and the fatigue life of HSRB does not match that of grade 60 bars (Sokoli and Ghannoum, 2016; Slavin and Ghannoum, 2015).

3. Experimental Program

Four concrete columns were designed, built, and tested as part of this experimental program. The column specimens were:

- CH100: reinforced with grade 100 longitudinal and transverse bars having a relatively high (H) tensile-to-yield (T/Y) ratio. The steel used in this column was produced using the micro-alloying process (Section 2.1.1).
- CL100: reinforced with grade 100 longitudinal and transverse bars having a relatively low (L) T/Y ratio. The steel used in this column was produced primarily using the quenching and tempering process (Section 2.1.2).
- CM100: reinforced with grade 100 longitudinal and transverse bars satisfying the ASTM A1035 (ASTM A1035 / A1035M – 16b, 2016) standard. The steel used in this column was produced using the MMFX proprietary process (MMFX Technologies Corporation, 2012) (Section 2.1.3).
- CH60: reinforced with grade 60 longitudinal and transverse bars satisfying the ASTM A706 (ASTM A706 / A706M-16, 2016) standard and having a typical T/Y ratio for that grade.

3.1 SPECIMEN DESIGN

Columns were designed to impart large strain demands on longitudinal bars. This was done to investigate the effect of steel grade and mechanical properties on fracture fatigue life of the longitudinal bars and plasticity spread in the hinge regions. A relatively low compressive axial load ratio of 15% was applied to all columns, not compressing enhance strain demands on longitudinal bars,. The axial load ratio is defined here as the axial load divided by the gross section area and measured concrete compressive strength. Relatively low shear stresses were also targeted, below $4\sqrt{f'_c}$ (in psi units), to minimize the

beneficial effects of the tension-shift phenomenon caused by inclined cracking on the spread of plasticity (Section 2.4.3). By keeping shear stresses low, plasticity spread is more reliant on the ability of the longitudinal reinforcement to accommodate deformation demands, theoretically providing the worst-case scenario for strain concentrations in longitudinal bars.

All columns reinforced with grade 100 steel were designed to have almost identical flexural capacities and associated shear demands. In CH60 the same diameter longitudinal bars were used as in grade 100 columns, leading to a lower flexural strength and associated shear stress. This was done as previous research has shown that the variation of bar sizes can influence the strain demands directly (Sokoli and Ghannoum, 2016). The only difference between grade 100 columns was the steel manufacturing process, which led to differing bar stress-strain relations. The post-yield hardening behavior and elongation capacities were the main differences between these types of steel.

Columns were designed to be tested in symmetric double-curvature with zero rotations at both top and bottom. They were designed to be 2/3 scale models of prototype columns. As such, the selected clear cover of columns was one inch. Column specimens had a clear height of 108 in. and cross-sectional dimensions of 18x18 in. (Figure 6). The shear span-to-depth ratio (a/d ratio) for this geometry was 3.4 for all columns (where a = shear span = half the clear length of the column and d = the effective depth of the section measured from the centroid of the outermost layer of steel to the compression face of the section). Columns framed into two end-blocks in which the longitudinal bars were anchored using standard ACI 318-14 hooks. Columns did not contain any splices and satisfied the seismic provisions for Special Moment Frames of ACI 318-14. All columns were designed assuming an expected concrete compressive strength of 5 ksi.

The reinforcing details of columns are presented in Table 2. The longitudinal steel ratios (ρ_l = ratio of the area of distributed longitudinal reinforcement to gross concrete area perpendicular to that reinforcement, (ACI 318-14, 2014) and the transverse reinforcement ratios (ρ_t = ratio of area distributed transverse reinforcement to gross concrete area perpendicular to that reinforcement, (ACI 318-14, 2014) are also presented for all columns in Table 2. All columns had 8 #6 longitudinal bars distributed evenly along all four faces (Figure 6; Table 2). The transverse reinforcement at each level consisted of a #4 seismic hoop and two #4 seismic cross-ties as defined in ACI 318-14. Transverse reinforcement spacing was 3.5 in. center-to-center, or $4.7 d_b$, for specimens reinforced with grade 100 longitudinal bars (with d_b = diameter of the longitudinal bars). This spacing is lower than the maximum required by ACI 318-14 (2014) for columns in Special Moment Frames ($6 d_b$) and closer to the $5 d_b$ spacing recommended in NIST GCR 13-917-30 (2014) when grade 80 and higher longitudinal bars are used. Transverse reinforcement in CH60 was spaced at 4.5 in. center-to-center, which corresponds to a spacing of $6 d_b$, which satisfies ACI 318-14 seismic provisions. All longitudinal and transverse bars for all specimens were bent to current ACI 318-14 bend radii. Design calculations and checks are presented in Appendix A1. Detailed construction drawings for all columns can be found in Appendix A2.

Table 2: Summary of column reinforcement details

	CH100	CL100	CM100	CH60
Longitudinal reinforcement	8 #6 $\rho_l = 1.1\%$	8 #6 $\rho_l = 1.1\%$	8 #6 $\rho_l = 1.1\%$	8 #6 $\rho_l = 1.1\%$
Transverse reinforcement in end regions	3 legs #4 @ 3.5in $4.7 d_b$	3 legs #4 @ 3.5in $4.7 d_b$	3 legs #4 @ 3.5in $4.7 d_b$	3 legs #4 @ 4.5in $6 d_b$

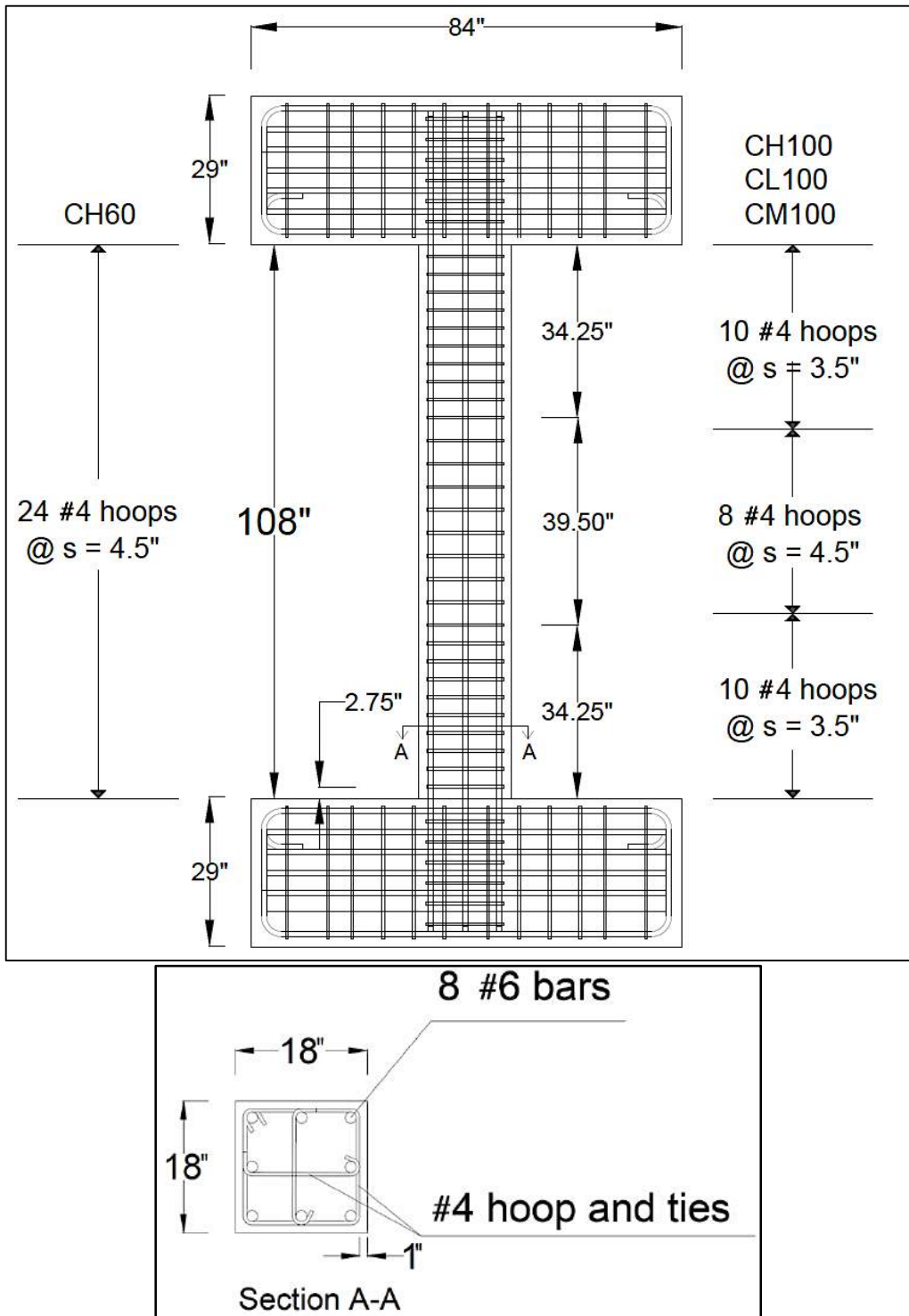


Figure 6: Elevation and cross-sectional view of the reinforcement in columns

Sectional analyses were performed at the design stage using specified material properties and accounted for a compressive axial load $P = 0.15 A_g f'_c$, where A_g is the gross sectional area of the cross-section and f'_c is the measured concrete compressive strength at the day of testing. The assumed steel properties for the first two tests are presented in Table 3. The concrete compressive strength was assumed to be 5.0 ksi.

Table 3: Assumed properties of reinforcing bars used for designing specimens

Steel Type	f_{ya}^i (ksi)	f_{ua}^i (ksi)	ϵ_{ya}^i	ϵ_{ua}^i
Grade 100 CH100; CM100; CL100	104	128	0.0034	0.09
Grade 60 CH60	64	90	0.0022	0.12

ⁱ Symbols used at the header refer to the assumed properties of the longitudinal bars used for design calculations only; f_{ya} is the assumed yield strength; f_{ua} is the assumed ultimate strength; ϵ_{ya} is the assumed strain at yield; ϵ_{ua} is the assumed strain at fracture.

This resulted in columns reinforced with grade 100 steel having about the same expected plastic moment strength (M_{pr}) of 4420 kip-in, and a corresponding peak shear demand (V_e) of 83 kips (Table 4). The plastic moment strength was obtained as the peak moment strength by fiber-section analysis using OpenSees (2016) while accounting for the maximum concrete compressive strain of confined concrete through the Mander et al. (1988) model. For CH60 the peak moment capacity was estimated to be 3525 kip-in. The expected peak shear stress (V_e/bd where b = width of section) was therefore estimated at about $3.9 \sqrt{f'_c}$ (in psi units) for columns reinforced with grade 100 steel and $3.1 \sqrt{f'_c}$ for CH60. The moments due to secondary $P\Delta$ (where P is the axial load in kips and Δ is the lateral displacement of the member in inches) effects were expected to increase to 18% of the primary moment capacities (M_{pr}) at a lateral drift ratio (ratio of the lateral displacement to the length of the columns) of 6% for CH100, CL100, and CM100 (Table 4). Secondary moments were expected to amount to a more significant percentage of the lower primary moments of specimen CH60 (22%).

Table 4: Sectional analysis results

Column	M_{pr} (kips-in)	V_e (kips)	$\frac{V_e}{bd\sqrt{f'_c}}$ (psi)	$P\Delta/M_{pr}$ @ drift ratio		
				2%	4%	6%
Grade 100	4490	83	3.9	0.06	0.13	0.18
Grade 60	3525	65	3.1	0.08	0.15	0.22

3.2 MATERIALS

3.2.1 Concrete

The columns and footings supporting them had the same concrete mix design. The concrete mix had a specified compressive strength of 5 ksi and a seven-inch slump. River gravel was used in both cases, with a specified maximum aggregate size of 1 in. Mix design quantities are presented in Table 5.

Table 5: Concrete mix design quantities

Material	Design Quantities
Type 1 cement	423 lb/yd ³
Fly ash – Class F	141 lb/yd ³
Sand	1343 lb/yd ³
1" max. river gravel aggregate	1950 lb/yd ³
Water	29.0 gal/yd ³
HRWR	28.2 oz/ yd ³

Cylinders with a four-inch diameter were prepared for each cast and stored near their respective specimen to cure in the same environmental conditions. Concrete cylinders were left in plastic containers and covered with a plastic sheet for the same duration as formwork was left on the specimens. Concrete cylinders were removed from the plastic containers the same day the formwork was removed.

Concrete cylinders from each cast were tested in compression to define compressive properties of the material. Four-inch diameter concrete cylinders were tested in compression at 7, 14, 21 and 28 days in accordance with ASTM C39 procedures. Cylinders from each column cast were also tested at the same day each column was tested. Day-of-testing compressive strengths are presented in Table 6. The remainder of the concrete material testing data is given in Appendix B1. The average measured concrete compressive strengths at the day of testing for all columns were within 12% from the specified strength of 5 ksi.

Table 6: Concrete compressive strengths of columns at day of column testing (ksi)

	Cylinder 1 (ksi)	Cylinder 2 (ksi)	Cylinder 3 (ksi)	Average (ksi)
CH100	5.17	5.24	5.21	5.21
CL100	5.30	5.08	5.11	5.16
CM100	5.60	5.50	5.63	5.58
CH60	4.48	4.69	4.54	4.57

3.2.2 Reinforcing steel

Sample reinforcing bars from the same heat as the steel used in the columns were also tested in tension. Three of the columns were reinforced with grade 100 steel bars sourced from three different manufacturers. These manufacturers use different approaches in producing the high strength steel bars. Manufacturer 1 provided the reinforcing bars for

column CH100 and produces HSRB mainly through micro-alloying as described in Section 2.1.1. Manufacturer 2 provided the steel bars for column CL100 and achieves higher strength steel mainly by quenching and tempering (Section 2.1.2). Grade 100 reinforcement produced by Manufacturer 3 satisfied the ASTM A1035 specifications and was used in column CM100. This reinforcement is a low-carbon steel that is produced under a controlled-rolling production process (Section 2.1.3). The grade 100 reinforcing bars used in these tests had tensile to yield strength ratios at the high end of what is achievable for each production technique. The fourth column was reinforced with conventional grade 60 ASTM A706 steel. Transverse bars were sourced from the same manufacturer and were of the same grade as the longitudinal bars of the same column.

In order to identify the material properties of the steel bars, monotonic tension tests were performed conforming to the procedures specified in *ASTM A370 – Standard Methods and Definitions for Mechanical Testing of Steel Products* and *ASTM E8 – Standard Test Methods for Tension Testing of Metallic Materials*. The complete force-strain response of a bar was recorded during each monotonic test. Stresses were calculated as the bar force divided by the nominal bar area. All strains used to generate bar stress-strain relations were measured over an 8-inch gauge length as specified in ASTM A370. The material properties obtained include: the modulus of elasticity, the yield strength, the tensile strength, the tensile-to-yield strength ratio, the uniform strain, and the fracture strain. The modulus of elasticity was measured as the slope of the initial elastic region of the stress-strain curve. Yield stress was calculated by the 0.2% offset method as detailed in ASTM E8. The ultimate tensile strength was measured as the maximum stress recorded in a test. The tensile-to-yield strength ratio was taken as the ratio of the ultimate tensile strength to the yield strength. Uniform strain is defined as the strain reached at tensile

strength and immediately prior to the initiation of necking. Since the stress-strain curve can be assumed to be nearly flat in this region, the uniform strain was taken, in accordance with ASTM E8, as the middle point of the range of strains that led to stresses of at least 99.5% of the ultimate tensile strength. Fracture strain was measured just prior to loss of load-carrying capacity and, therefore, includes both the plastic and the elastic components of strain.

The mean measured mechanical properties for the longitudinal reinforcing bars (#6 bars) are presented in Table 7. Typical stress-strain curves from #6 bars from each column are plotted in Figure 7. Grade 100 steel stress-strain curves from Manufacturers 1 and 2 had a similar shape, with a well-defined yield plateau (Figure 7). The grade 100 longitudinal bars of CH100 had a lower yield and higher tensile strength than those in CL100, which lead to a higher average T/Y ratio of 1.27 for CH100 bars as compared to 1.16 for CL100 bars. The longitudinal bars of CH100 had a yield strength that was only 6% smaller than that of the bars in CL100. The difference in tensile strength was even smaller, with CH100 longitudinal bars having a tensile strength that was only 3.3% larger than that of the CL100 bars. The differences in fracture elongation (11.5% vs. 12.8%) and uniform elongation (7.6% vs. 8.6%) were small, with bars having the lower T/Y ratio exhibiting larger fracture and uniform strain values (Table 7). Uniform elongations, defined as the strains at peak stress, were extracted for stress-strain data in accordance with ASTM E8 (ASTM E8 / ASTM E8M – 16a, 2016). The bars with the lower T/Y ratio had a noticeably longer yield plateau. Manufacturer 3 produced a reinforcing steel having a rounded shape stress strain curve, without a defined yield point. The measured yield strength and strain for these bars were obtained using the 0.2% offset strain method (ASTM A1035 / A1035M – 16b, 2016; ACI 318-14, 2014). The uniform elongation for the #6 bars

in CM100 was on average 35% lower than the uniform elongation of #6 bars in CH100 and 43% lower than for bars in CL100. The conventional grade 60 A706 reinforcement used in specimen CH60 had a significantly higher T/Y ratio compared to the specimens with grade 100 reinforcement; 1.45 for grade 60 vs. 1.27, 1.16, and 1.27 for grade 100 bars in CH100, CL100, and CM100, respectively. Grade 60 bars had higher ductility as well when compared to grade 100 bars.

Table 7: Average results from tension tests on sample #6 bars (minimum of three tests per bar type)

Specimen	Yield Strength (ksi)	Tensile Strength (ksi)	Tensile to Yield Strength Ratio (T/Y)	Elastic Strain Limit (%)	Uniform Elongation (%)	Fracture Elongation (%)
CH100	100.0	127.2	1.27	0.32	7.6	10.4
CL100	106.4	123.4	1.16	0.45	8.6	12.5
CM100	124.2	157.4	1.27	0.63	4.9	9.8
CH60	64.4	93.3	1.45	0.24	11.8	17.6

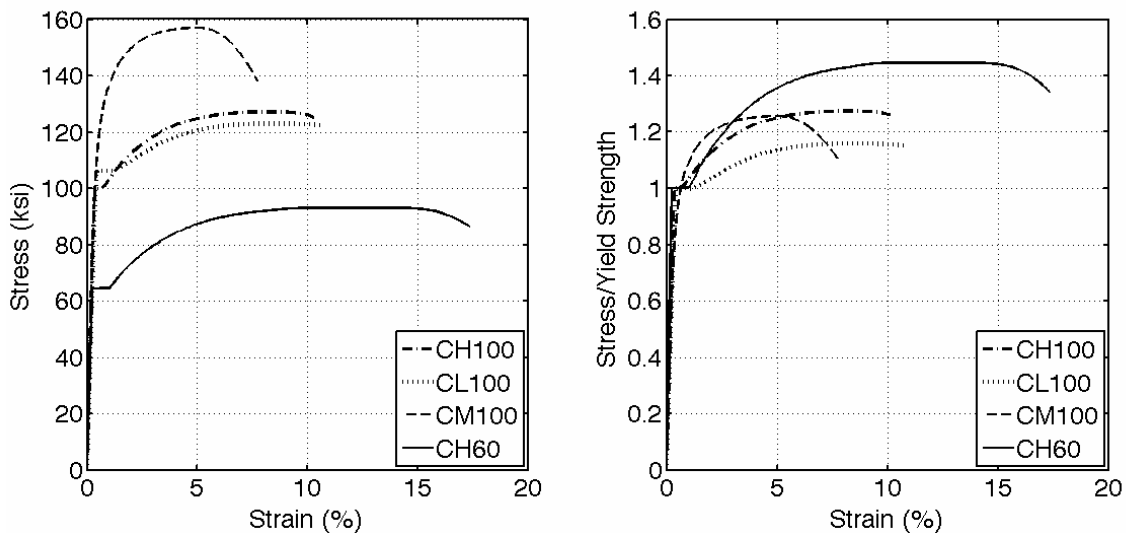


Figure 7: Typical stress-strain curves for the longitudinal reinforcement used in each specimen

The mean measured mechanical properties for the transverse reinforcing bars (#4 bars) are presented in Table 8. Typical stress-strain curves from #6 bars from each column are plotted in Figure 8. The steel used as transverse reinforcement in CL100 can be classified as grade 80 steel, considering its low (84.6 ksi) yield strength. The average T/Y ratio of this steel was 1.18, as compared to 1.21 for CH100 bars. The hoops of CH100 had a yield strength that was 20% higher than that of the hoops used in CL100. The difference in tensile strength was even larger, with CH100 longitudinal bars having a tensile strength that was only 23.2% larger than that of the CL100 bars. The differences in fracture elongation (11.5% vs. 12.8%) and uniform elongation (8.0% vs. 9.0%) were small, with hoops having the lower T/Y ratio also exhibiting lower fracture and uniform strain values (Table 8). Manufacturer 3 produced a reinforcing steel having a rounded shape stress strain curve, without a defined yield point. The measured yield strength and strain for these bars were obtained using the 0.2% offset strain method (ASTM A1035 / A1035M – 16b, 2016; ACI 318-14, 2014). The yield strength estimated with the above-mentioned method, resulted in #4 bars used as transverse reinforcement in CM100 having a yield strength 39% higher than the #4 bars in CH100, and 66% higher than those in CL100. The uniform elongation for the #4 bars in CM100 was on average 48% lower than the uniform elongation of #4 hoops in CH100 and 41% lower than for hoops in CL100. The conventional grade 60 A706 reinforcement used in specimen CH60 had a significantly higher T/Y ratio compared to the specimens with grade 100 reinforcement; 1.40 for grade 60 vs. 1.21, 1.18, and 1.22 for grade 100 bars in CH100, CL100, and CM100, respectively. Grade 60 bars had higher ductility as well when compared to grade 100 bars. The remainder of the concrete material testing data is given in Appendix B2.

Table 8: Average results from tension tests on sample #4 bars

Specimen	Yield Strength (ksi)	Tensile Strength (ksi)	Tensile to Yield Strength Ratio (T/Y)	Elastic Strain Limit (%)	Uniform Elongation (%)	Fracture Elongation (%)
CH100	101.1	122.7	1.21	0.35	9.0	12.8
CL100	84.6	99.6	1.18	0.32	8.0	11.5
CM100	140.5	171.1	1.22	0.60	4.7	8.6
CH60	68.5	95.8	1.40	0.22	9.9	12.4

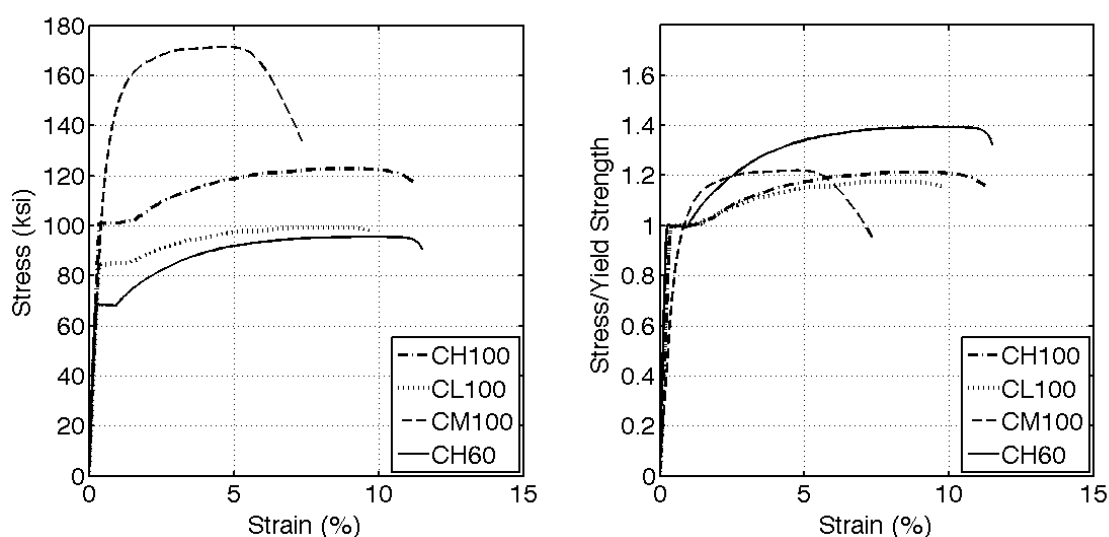


Figure 8: Typical stress-strain curves for the longitudinal reinforcement used in each specimen

3.3 SPECIMEN FABRICATION

Columns were cast in an upright position in three stages, simulating a typical construction sequence. The bottom footing and column cage were tied together and placed in steel forms (Figure 9; Figure 10). The bottom footing was cast first and the concrete surface at the interface with the column was roughened. The bottom footing was allowed to cure for several days before casting the column concrete. The top footing cage was then placed in the forms along with PVC pipes that created holes in order to enable the

attachment to the loading frame and for lifting. More than 28 days were allowed for each concrete column to cure before testing.

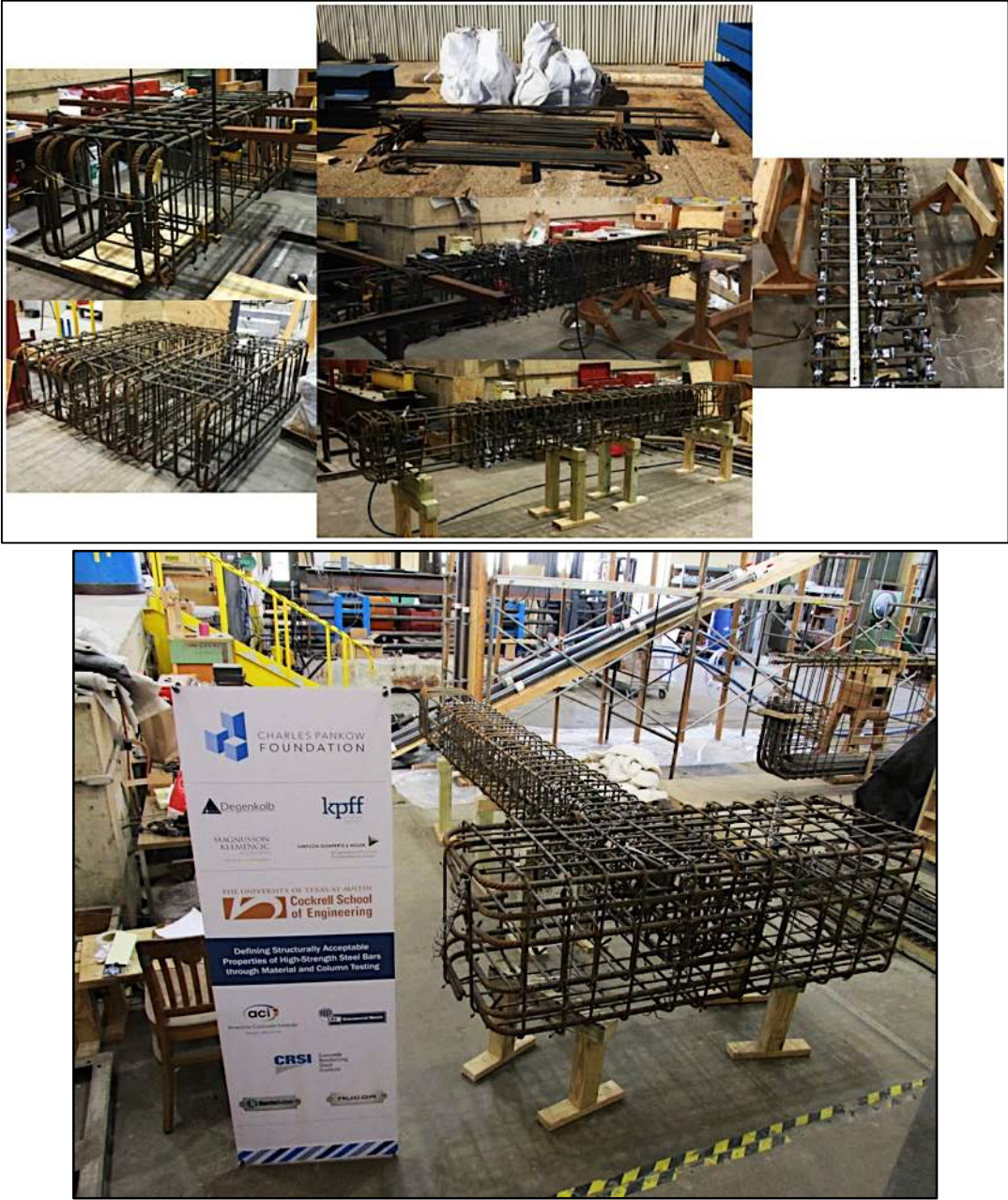


Figure 9: Steel cage assembly and strain gauge installation



Figure 10: Column casting process

3.4 INSTRUMENTATION

Columns and test setup were instrumented to measure the applied loads, distributed deformations of the specimens, strains and crack widths on the concrete surface, and strains in the longitudinal and transverse reinforcing bars. Two linear potentiometers were used to measure column lateral drifts during the test. A digital image correlation (DIC) system developed by the research team was used to measure column surface deformations (Sokoli et al. 2014). The vertical movement of the steel frame at the point of connection with the horizontal actuator was also measured using a Linear Voltage Displacement Transducer (LVDT). Data from this LVDT were used to triangulate the vertical position of the horizontal actuator when evaluating system force equilibrium.

Strain gauges were installed on the four corner bars at each column end, along four longitudinal bars within the footings and plastic hinge regions, as well as on the seven lower column hoops. Strain gauge installation followed manufacturer recommended procedures. Steel bars were ground to achieve a smooth surface at the location of a gauge. Great care was taken not to reduce bar cross-section in the grinding process. The cleared surface was then treated by removing any grease or dirt and was lightly polished with an abrasive #120 paper and wiped with acetone. CN-Y (Cyanoacrylate) adhesive was used to glue the gauges to the bar. After allowing for curing time, the gauge was wrapped with several protective layers as seen in Figure 11. Redundancy in strain gauge instrumentation allowed the omission of questionable measured strain data in when analyzing the results.

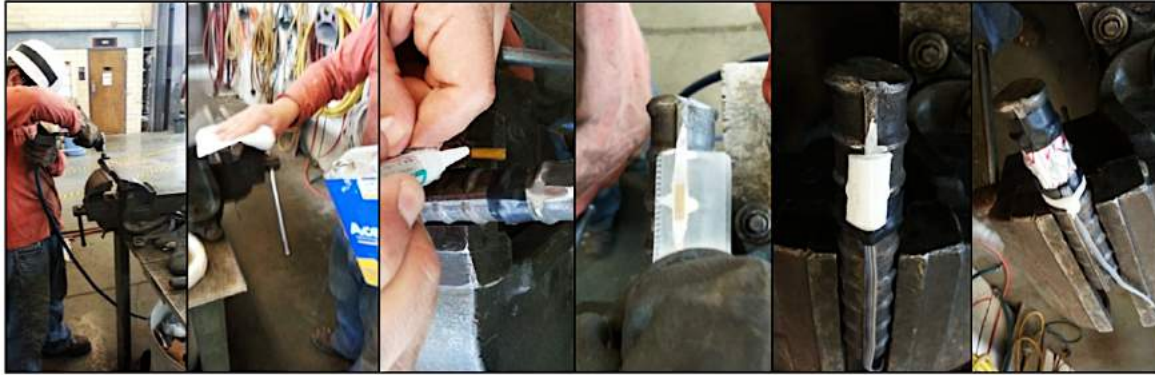


Figure 11: Strain gauge installation process (Sokoli, 2014)

A novel optical measurement system, dubbed the Ghannoum Vision System (GVIS), was used to measure the three-dimensional movement of paper targets glued on the west surface of the tested specimens. This system used two high-resolution cameras, digital image correlation (DIC), and triangulation software developed by the research team (Sokoli et. al., 2014). The system tracks target locations in each recorded frame using a Digital Image Correlation algorithm. A calibration procedure adjusts for lens distortion and provides the necessary extrinsic and intrinsic camera parameters for the three-dimensional triangulation of target locations. The system is able to resolve surface strains on the order of 10^{-4} over a field of view of 120 in. and a gauge length of 2.5 in., which were the parameters used in this study. The GVIS recorded image frames at an approximate frame rate of 0.75 Hz during all tests.

3.5 TEST SETUP AND PROCEDURE

Figure 12 illustrates the test setup and instrumentation used in this study. The specimens were tested under symmetric double curvature with fixed rotation boundary condition at the top and bottom. Specimens were post-tensioned to the strong floor using sixteen 1.25 in. diameter steel rods, which were stressed to a combined 600-kip force. The steel test frame was connected to the specimens through the top footings using eight 1.5 in. diameter steel rods, which were post-tensioned to 75 kips each. Two pedestals were used at top and bottom of the column's footings to fit the columns in the test frame and have the mid span of the column specimens at the same elevation as the horizontal actuator. Grout was used between all contact surface concrete surfaces to avoid stress concentration at the interfaces and facilitate specimen leveling. Three braces were used to prevent out-of-plane movement of the steel test frame and test specimens.

The setup consisted of three MTS actuators each having a 215-kip capacity in tension and 330-kip capacity in compression. The two vertical actuators (Figure 12) applied a constant compressive load which equaled $0.15 A_g f'_c$ in all columns, where f'_c was the concrete compressive strength measured at the day the corresponding column was tested. A third – horizontal – actuator pushed the columns in uni-directional quasi-static cyclic loading. The estimated self-weight of the top footing and hardware was accounted for when calculating the axial compression force that was applied by each actuator. The resulting axial loads applied at the bottom of each column were: 252 kips for CH100, 252 kips for CL100, 263 kips for CM100, and 232 kips for CH60.



Figure 12: Column CL100 at the end of the test

The lateral loading protocol imposed by the horizontal actuator to both columns consisted of two lateral displacement cycles at increasing displacement increments selected per FEMA 461 recommendations (Table 9). All tests were carried in displacement control under low loading rates. A control scheme developed at Ferguson Structural Engineering Laboratory ensured that the steel test frame remained level during testing and an applied the desired constant axial load.

Table 9: Loading protocol

Loading stage	1	2	3	4	5	6	7	8	9	10	11	12
Drift Ratio	0.2%	0.3%	0.4%	0.6%	0.8%	1.0%	1.5%	2.0%	3.0%	4.0%	5.5%	7.0%

4. Experimental Results

This chapter presents an overview of the test results for each of the large-scale column tests. Post processing of the collected data is explained. The general behavior of each column is summarized and results regarding deformation components, strain demands, bar buckling history, energy dissipation and damage accumulation are presented. A comparative analysis between all specimens and a more detailed discussion of test results is provided in Chapter 5.

4.1 DATA PROCESSING

Unless otherwise stated, the presented deformation data were measured using the Ghannoum Vision System (GVIS). The system used two cameras which recorded frames simultaneously at an average rate of 0.75 Hz. A script then ran through all the images extracting the image pixel coordinates of each target glued on the surface of the specimens. Targets were placed in a rectangular mesh spaced at 2.75 inches' center-to-center. Two-dimensional coordinates from each camera were then triangulated to produce the three-dimensional location of every target at each captured frame. Targets lost for short periods were linearly interpolated over the missing frames until the GVIS system recaptured the target. Targets permanently lost due to concrete spalling were ignored after being lost. The relatively low level of shear stress resulted in low damage in the column and at least 93% of targets remained on the column surface for the duration of all four experimental tests.

Frame data from the GVIS system were synchronized with the data gathered by the data acquisition system (DAQ) (i.e., strain gauge, load cell, and displacement transducer data). For column CH100, 22,757 frames were recorded by the end of the test, for CL100 20,859 frames, for CM100 22,680 frames, and for CH60 24,726 frames. Due to the large

number of data points gathered, the recordings from the GVIS and DAQ were smoothed by applying a 15-point moving average.

At the beginning of each test, the steel loading frame was leveled such that its weight was fully carried by the vertical actuators. Strain gauge readings and deformation quantities were zeroed at that stage. In all tests, positive drift values imply movement of the columns to the right (or the South direction) in images recorded by the optical measurement system.

Applied column forces (shear and axial) and moments were computed using large-deformation equilibrium accounting for the location and inclination of all three actuators. The free-body diagram and the static equilibrium equations are shown in Appendix C.

4.1.1 Deformation Measurements

The lateral drift (Δ_T - Figure 13) of each column was obtained by averaging the horizontal displacements of all available targets on the top footing and subtracting from them the average horizontal displacement of all available targets on the bottom footing. While the bottom footing did not slide during the test, this procedure removed any footing deformations from the column deformation data. In subsequent discussions, the term drift ratio refers to the lateral drift of a column divided by the clear span of the members (108 in.). Energy dissipated by columns in each cycle of every drift target were calculated from the area under the lateral drift versus average top and bottom column moment curves. The start of a cycle was taken as the point at which the column passed through the zero-lateral drift going from negative to positive drift (north-to-south).

The total lateral drift (Δ_T) of each column can be divided into three deformation components: flexural (Δ_{FL}), shear (Δ_{SH}), and bar-slip (Δ_{BS}) deformations (Figure 13).

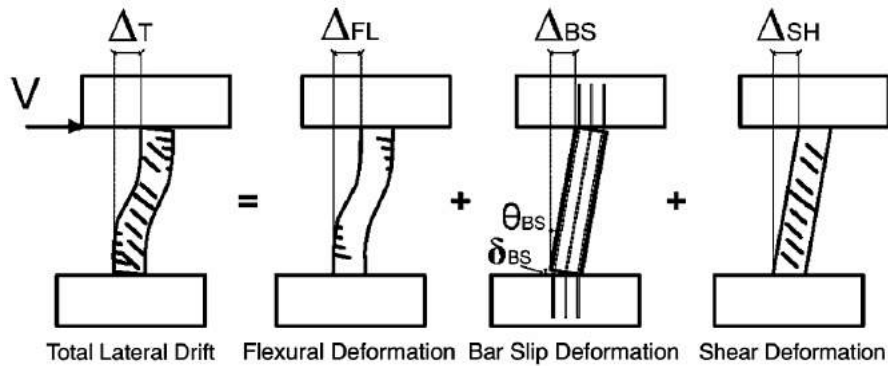


Figure 13: Deformation components in a concrete member (from Sokoli et. al., 2014)

Deformation components exhibit an essentially bilinear force-deformation relation at low demands, linear to first cracking and then linear to up to initiation of inelastic behavior at larger demands. Deformation components are sometimes coupled to the extent that one component entering the inelastic behavioral range may cause other components to exhibit an inelastic behavior. For example, as inelastic flexural deformations increase, so do shear deformations governed by expanding flexure-shear cracks.

Target displacement data from the GVIS were used to get rotations, curvatures, and deformation components over the height of the specimens, as described in Sokoli (2014) and Sokoli et. al. (2014). A linear regression line was fit through each horizontal row of seven targets. Sectional rotations along column height were computed at each frame as the change in the slope of each target line with respect to the initial slope of the line prior to loading. Curvature profiles along column height were evaluated as the difference in angle of rotation between two target rows divided by the measured distance between the rows. Flexural deformations were evaluated from target displacement values by integrating those curvatures over the height of the column. The slip of column longitudinal bars from adjacent members causes rigid body rotations of the column about the interface between

the column and the adjacent members. Lateral drifts generated by bar slip at the level of each target row were derived by multiplying the average rotation of the row of targets at column ends by the height of the target row considered. It is to be noted that at large deformations after concrete cover crushing, the measured bar slip becomes less reliable due to debonding between the longitudinal bar and the concrete cover. Shear deformations along column height were extracted by subtracting the lateral drifts due to flexure and bar-slip from the total column lateral drift at each row of targets. The end result was the deconstruction of column drifts into three deformation components.

4.1.2 Strain Measurements

Given sufficiently high resolution, such as that achieved by the GVIS system, measurements of three-dimensional movements of known locations (i.e., targets) on a test specimen can be used to calculate surface material-strains. The GVIS can resolve surface strains to within 10^{-4} for a field of view of about 8ft (2.44m) and a gauge length of about 2.75 in.; a strain resolution that is on the order of the cracking strain of concrete. The surface targets arranged in a rectangular mesh were used as nodal points for bilinear-strain quadrilateral elements. Assuming that strains varied linearly between targets, the following element strain were calculated: the x-directional or horizontal strains (ϵ_x), the y-directional or vertical strain (ϵ_y), and the principal strains (ϵ_1 = largest principal strain and ϵ_2 = smallest principal strain), as well as the angle of inclination of the principal strains were determined. DIC measurements of surface strains were also used to estimate internal transverse reinforcement strains (Sokoli et. al., 2014).

4.1.3 Damage Evaluation

Using GVIS surface-strain data, crack widths were estimated over the entire specimen surface, from which crack-width damage indices were evaluated. For a given frame, a crack was assumed to have formed within a quadrilateral surface-element when the element's maximum principal tensile strain (ϵ_1) exceeded an assumed cracking strain, $\epsilon_{cr}=f'_t/E_c=7.5/57000=1.3 \times 10^{-4}$ (with f'_t = concrete ultimate tensile strain, E_c = concrete modulus of elasticity, and their values based on provisions of ACI 318-14). After an initial crack formed in an element, the average elastic strain in adjacent uncracked concrete was assumed to be half the cracking strain. Thus, the crack width within surface elements can be calculated by subtracting half of the cracking strain from the maximum principal tensile strain and then multiplying the modified strain by the surface elements' length perpendicular to the crack (Equation 23). Since the surface elements are square, their lengths perpendicular to an inclined crack vary with crack inclination. An equivalent length ($L_{equiv.}$) was used for all crack inclinations to simplify the crack width evaluation procedure. The equivalent length was taken as the diameter of a circle of equivalent area to the square elements. The relation for crack width in each quadrilateral element is therefore given as:

Equation 23: Crack-width calculation using data from GVIS

$$w_c = (\epsilon_1 - \epsilon_{cr}/2) * L_{equiv.}$$

4.1.4 Behavioral Milestones

The damage progression in the column specimens is presented in this report through the following major behavioral milestones: first flexural cracking (FFC), first inclined cracking (FIC), first longitudinal reinforcement yielding (FLRY), cover splitting crack (CSC), the peak shear force (PSF), longitudinal bar buckling (LBB), and longitudinal bar fracture (LBF) points. In plots of moment vs. lateral drift ratio, the peak applied moment (PAM) is given instead of peak shear force. Figure 14 shows the markers used in subsequent plots for each behavioral milestone.

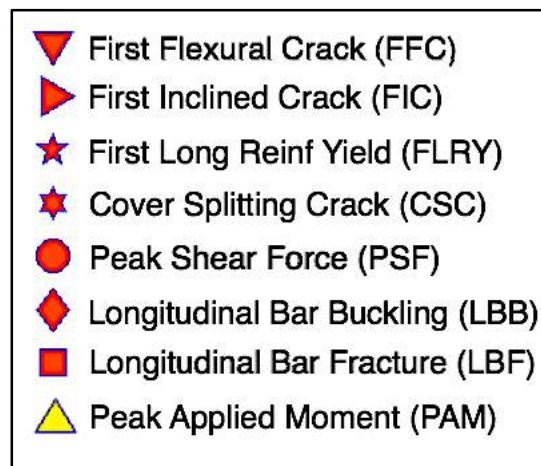


Figure 14: Behavioral milestones naming and corresponding marker

The yield strains of reinforcing bars were determined from material tests presented in Chapter 3. Yielding in longitudinal reinforcement was identified from strain gauges installed at the interfaces of the columns and footings where the demands were expected to be largest. First cracking was identified by monitoring the column surface for strain jumps above the concrete cracking strain, as described in Section 4.1.3. Flexural cracks were identified as having an angle of principal strain (ϵ_I) smaller than 25 degrees. Inclined

cracks were defined as cracks having an angle between 25°-65° based on the angle of principal strain (ϵ_1) from the horizontal line. The cover splitting crack was identified from surface x-direction (or horizontal) strains at column vertical edges in the plastic hinge regions. Bar buckling was identified from pictures taken at the end of each half-cycle. The exact point of initiation of bar buckling could therefore not be obtained while columns were being pushed laterally. Bar buckling markers are placed at the end of the half cycles during which buckling initiated. The transverse reinforcement did not yield in any of the specimens. All the columns maintained the prescribed axial load throughout the test, so no milestone related to axial load was introduced.

4.2 TEST RESULTS FOR CH100

Results for column CH100 are reported in this section. Specimen CH100 was reinforced with grade 100 longitudinal and transverse bars. The longitudinal bars had a relatively high (H) T/Y ratio of 1.27. These bars were produced using the micro-alloying process. As for all specimens, CH100 was tested under displacement-controlled quasi-static cyclic lateral loading. The recorded lateral displacement history is shown in Figure 15. An axial load of 242 kips was applied by the vertical actuators which together with the 10-kips self-weight of the top footing and testing frame resulted in an effective axial load of 14.8% $A_g f'_c$ ($A_g f'_c$ = gross sectional capacity; where A_g = gross sectional area and f'_c = concrete compressive strength at the day of column testing) (Figure 16). The axial load was kept constant throughout the test as shown in Figure 16.

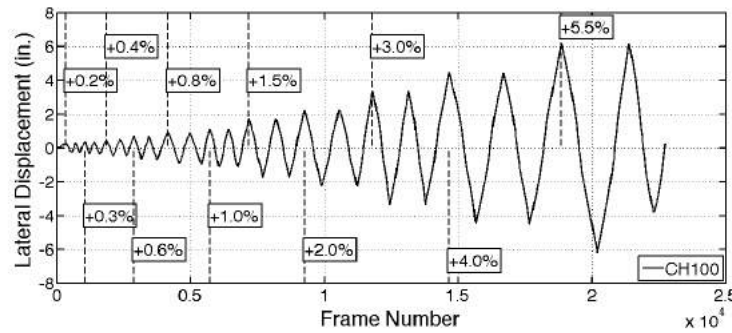


Figure 15: CH100 – measured lateral displacement at every captured frame

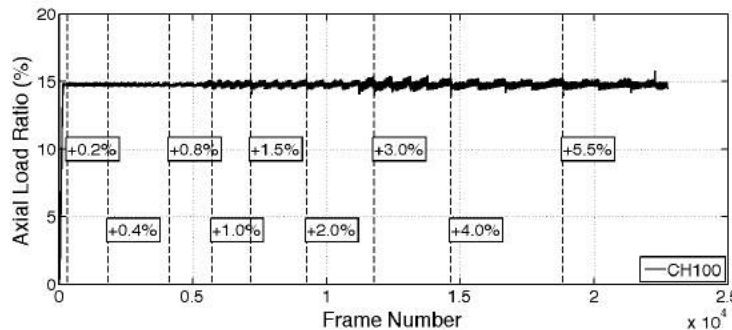


Figure 16: CH100 – applied axial load ratio at every captured frame

4.2.1 General Behavior

Prior to testing, no cracks were noticed on the specimen surface. The recorded lateral force versus drift ratio response of specimen CH100 is plotted in Figure 17. Table 10 summarizes the lateral force and drift values for all milestones for column CH100. The first flexural cracks formed at the end of the first cycle to +0.2% drift-ratio excursion (Figure 17, Figure 18). These cracks were noted through surface principal strains on the order of 0.002. The initial flexural cracks propagated closer to the centerline of the column leading to the formation of first inclined cracks at the end of the first half-cycle to a drift ratio of +0.6% (Figure 18).

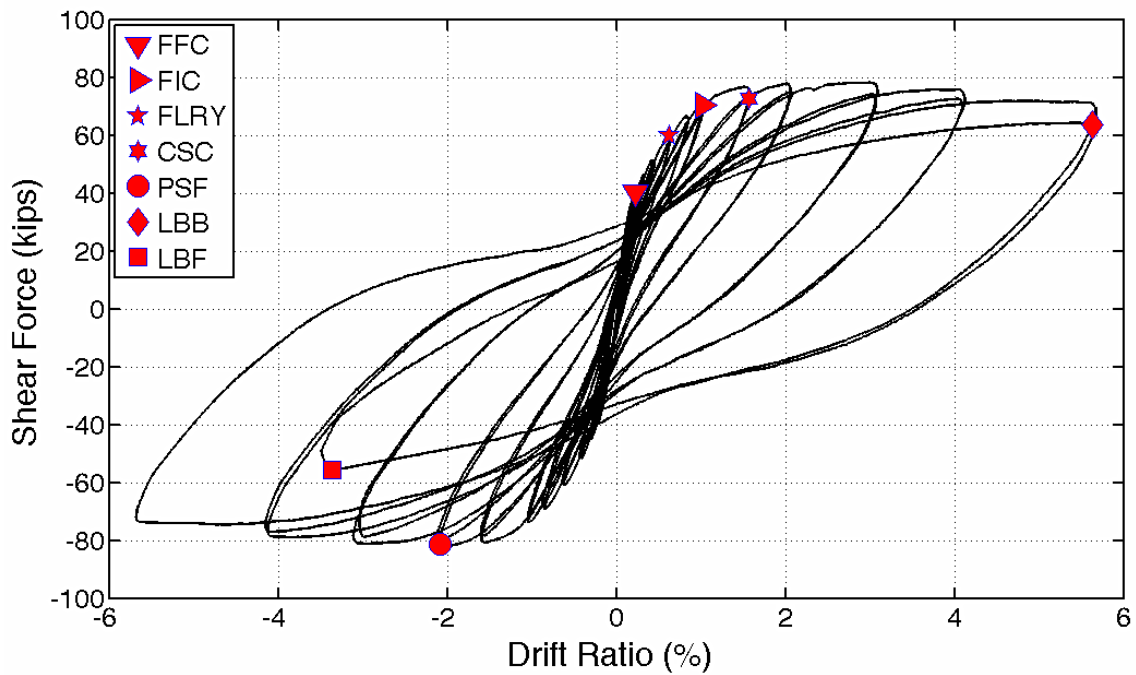


Figure 17: CH100 – lateral response

Table 10: CH100 - behavioral milestones

Milestone	Drift Ratio (%)	Lateral Load (kips)
First Flexural Crack	+0.2	+40.2
First Inclined Crack	+0.6	+60.4
First Long. Reinf. Yield	-0.8	-69.5
Cover Splitting Crack	+1.5	+72.8
Peak Shear Force	-2.0	-81.9
Long. Bar Buckling	+5.5	+64.3
Long. Bar Fracture	-3.6	-55.6

First yield in the longitudinal reinforcement was identified from strain gauge readings at the end of the first cycle to a drift ratio of +1.0%. At this point during the loading protocol, the initial flexural cracks opened wider and additional cracks formed closer to the column mid-height (Figure 18). The maximum applied shear-force of 81.9 kips was recorded at the end of first cycle to a drift ratio of -2.0%. Beyond that drift cycle, the lateral load diminished slightly, driven by second order axial load effects and the accumulation of damage such as concrete spalling. Top and base moments versus lateral drift ratio are plotted in Figure 19. As can be seen in the figure, peak moment strength occurred at a drift ratio of 2.0%. Gradual degradation of moment strength occurred beyond that drift due to accumulation of damage in concrete. During the second cycle to a drift ratio of +5.5%, initiation of longitudinal bar buckling was observed and was associated with a gradual loss in the moment capacity during that half cycle (Figure 17).

As the column was pushed to drift ratios of 3.0%, 4.0%, and 5.5%, increasing crushing and spalling of the concrete cover was observed. Two main flexural cracks formed in each column-end plastic hinge region. These cracks were 9.5 inches from the ends of the specimen and reached 0.15 in. by the end of the first cycle to a drift ratio of 5.5%. At the same drift ratio, vertical cracks at the location of the longitudinal reinforcement propagated 14 in. from column ends, indicating some de-bonding between the longitudinal bars and the surrounding concrete. These cracks initiated a drift ratio of 1.5% drift ratio, which corresponded to a curbing of the rate of increase in longitudinal bars strains with increasing drift ratios. This behavior is discussed in more details in Section 4.2.3.

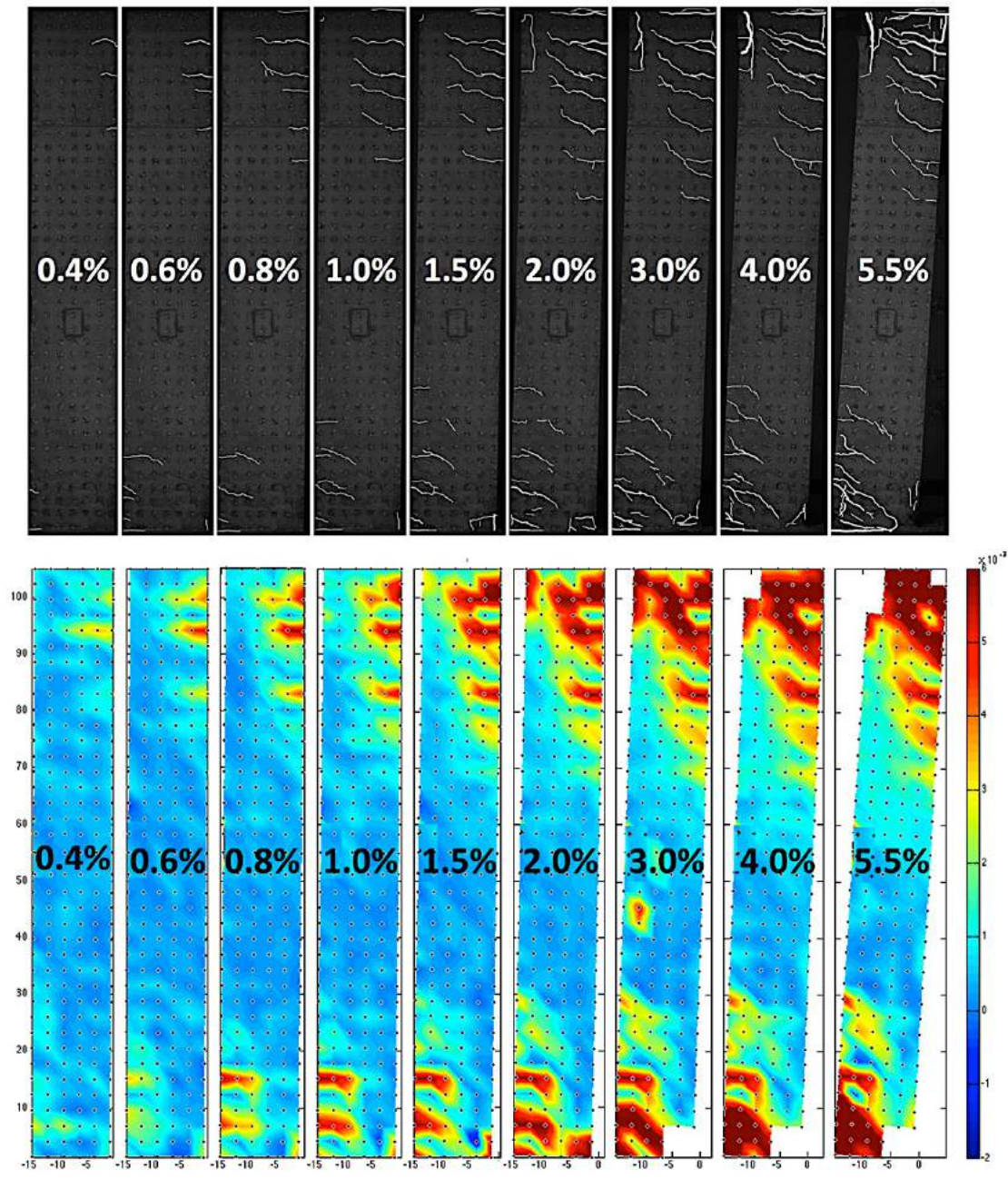


Figure 18: CH100 – cracking pattern (up) and measured largest principal strains (down) at several drift ratio targets

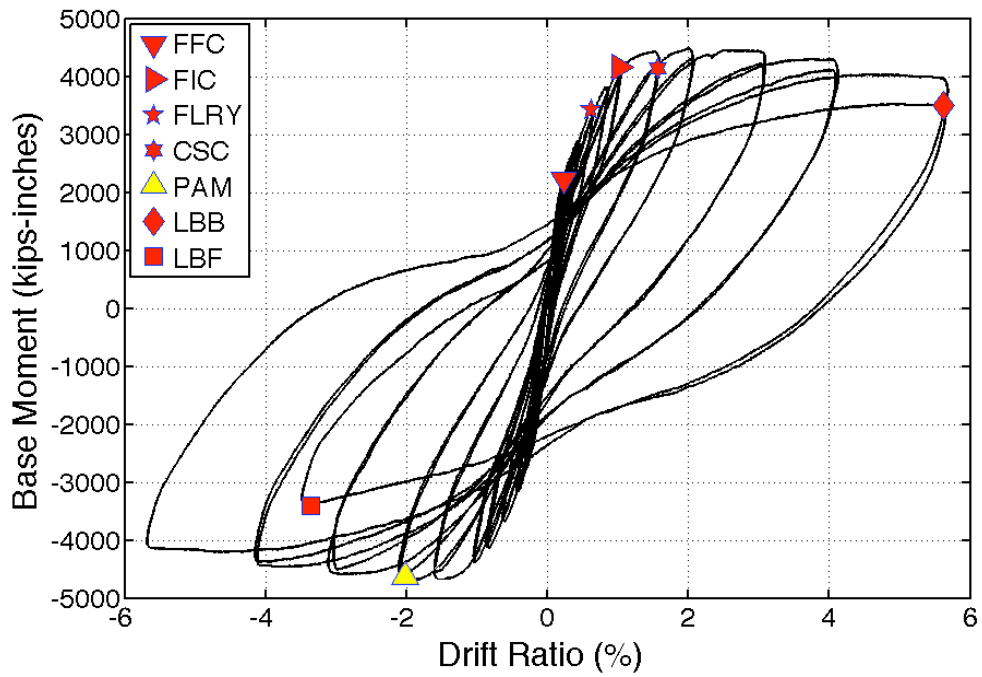
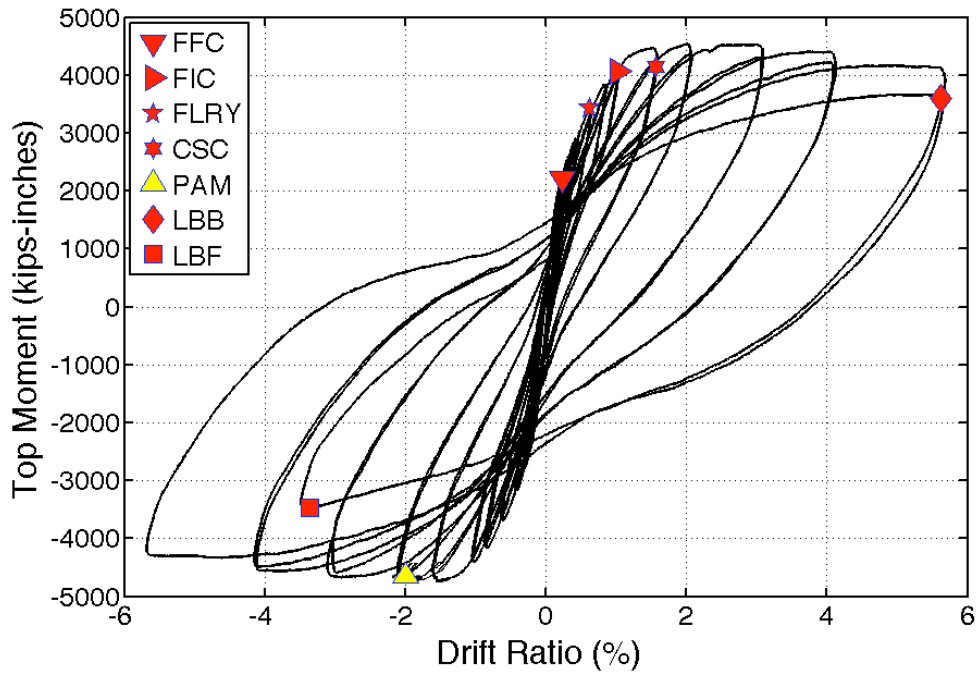


Figure 19: CH100 – base and top moment vs. drift ratio

The lateral load resistance of the column remained relatively stable and the column maintained axial load capacity past the first cycle to a drift ratio of +5.5% (Figure 20). During the second cycle to a drift ratio of +5.5%, the column experienced a 12% loss in moment resistance as compared to the previous half-cycle to the same drift target, and a 24% loss in moment resistance as compared to the peak lateral moment resistance. The significant loss in moment resistance was attributed to significant buckling of the longitudinal bars. By then, the cover concrete in the top and bottom plastic hinge regions had spalled to a distance of about 11.5 in. from column ends. As a result, on its way to completing two 5.5% drift cycles, one of the longitudinal bars fractured at the base of the column at a drift ratio of 3.6% (Figure 20; Figure 21). Just prior to first bar fracture, the column had lost 28% of its measured peak lateral moment resistance. The first bar fracture contributed to additional loss in lateral strength. Considering the considerable loss in lateral strength the test was stopped at this point. The column was able to carry the prescribed axial load throughout the test without showing signs of significant axial deformation even after longitudinal reinforcement fracture. It is noteworthy that the fractured bar was a middle bar. The 90-degree bend of the cross-tie restraining this bar had opened up significantly, during the previous half-cycle to a drift ratio of +5.5%, allowing the bar to buckle.

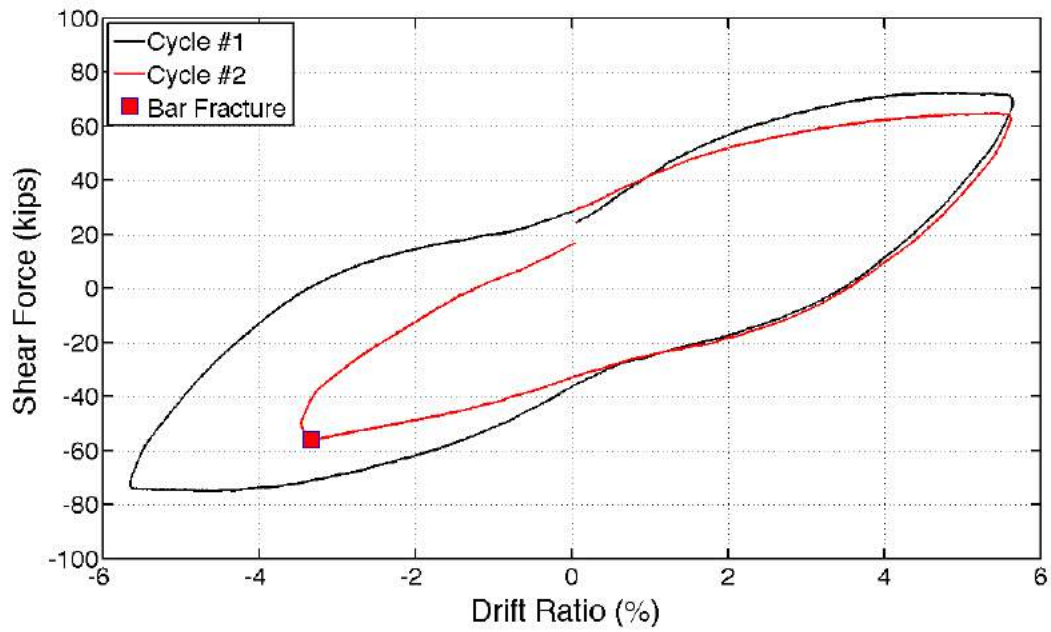


Figure 20: CH100 – last cycles response

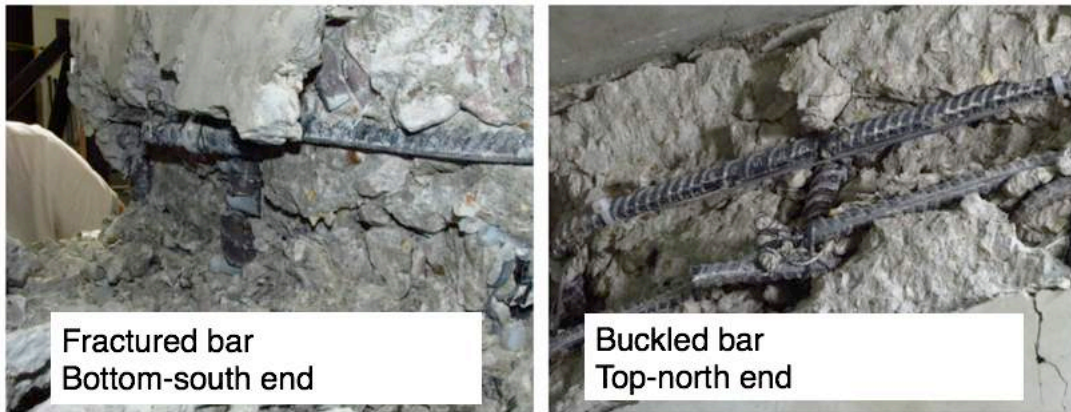


Figure 21: CH100 – pictures of fractured and buckled bars

4.2.2 Deformation Components

Flexural deformations contributed most to the column lateral drift throughout the test (Table 11; Figure 22). At higher drifts, the relative weight of flexural deformations lowered as the bar-slip component increased from about 30% of the total drift at low drift levels, to about 40% in the post-yield cycles. Possibly, the observed increase in recorded bar-slip contribution was due to debonding of the longitudinal reinforcement from the surrounding concrete at larger levels of concrete damage. This debonding of longitudinal bars due to concrete damage could have decoupled the bar deformations from measured concrete surface movements. Shear deformations increased in absolute value, but remained relatively low at around 5% of total drift throughout the test. The low amount of shear deformations was due to the applied shear stresses being relatively low. Results for deformation components were not reliable after cycles to a drift ratio of 4.0%.

Table 11: CH100 – deformation components as percentage of total

Total	Flexure	Bar-slip	Shear
0.2%	72.8%	24.1%	3.1%
0.3%	72.2%	23.9%	3.8%
0.4%	71.4%	24.9%	3.7%
0.6%	65.2%	30.4%	4.4%
0.8%	60.4%	35.1%	4.5%
1.0%	59.7%	35.9%	4.4%
1.5%	60.7%	34.8%	4.5%
2.0%	62.1%	33.4%	4.5%
3.0%	63.2%	32.1%	4.6%
4.0%	63.2%	33.4%	4.3%

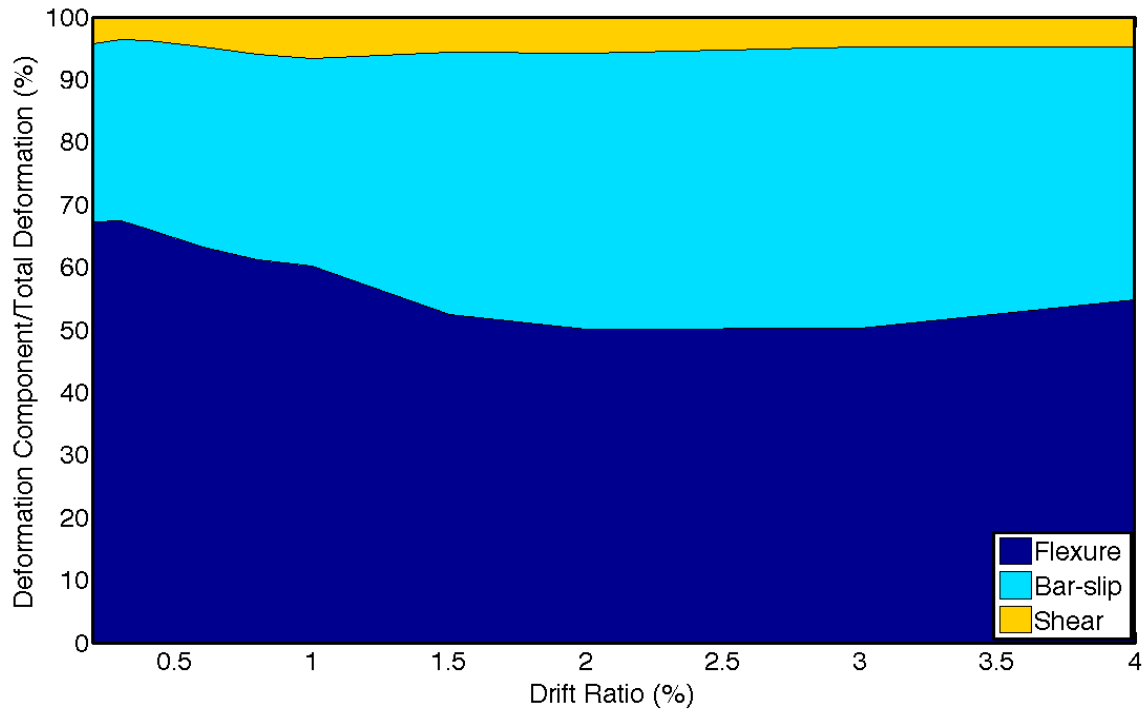


Figure 22: CH100 – deformation components

4.2.3 Strain History

Maximum strain demands were recorded at the interfaces between the column and footings. Figure 23 shows a typical strain versus lateral load response recorded on longitudinal bars at column ends. Figure 24 plots longitudinal bar tension strains at the end of each positive drift cycle target, measured at the top and bottom column interfaces with footings. The #6 bars used as longitudinal reinforcement in CH100 had a yield strain of 0.0032, as obtained from material testing. This strain was first reached at a drift ratio of +1.0% (Figure 24). After yield, the strain demands increased without significant increase in the lateral load. In general, strain demands of longitudinal bars were higher in the second cycle to the same drift target, with the difference increasing at higher drifts. This difference was however relatively small, and on the order of 5% of the strain value.

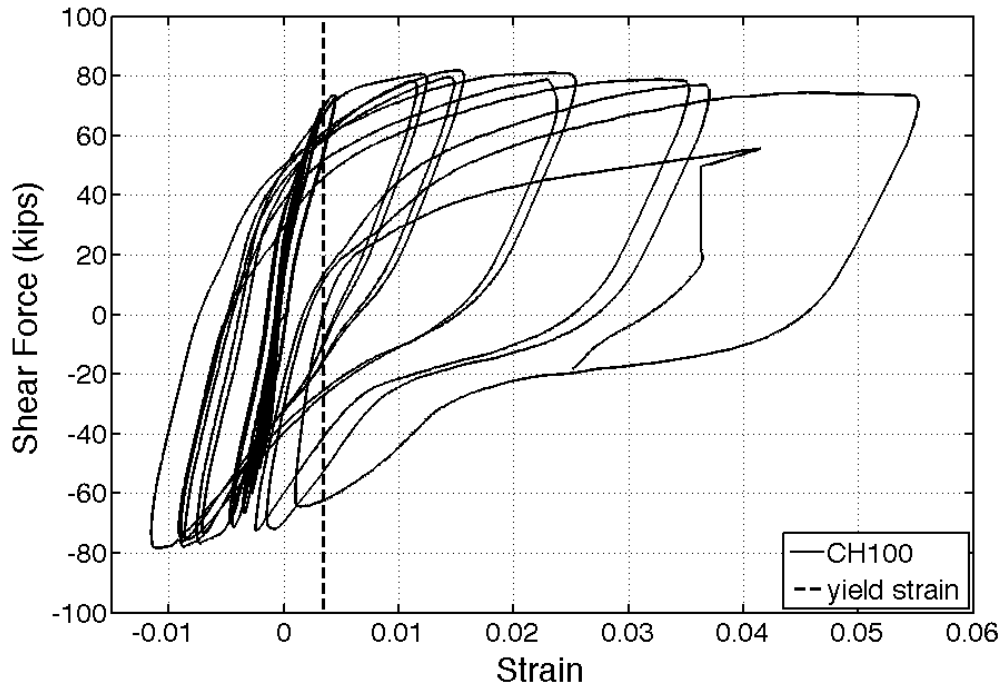


Figure 23: CH100 – strain gauge L17NW (top north-western corner) recording at the interface between the column and top footing

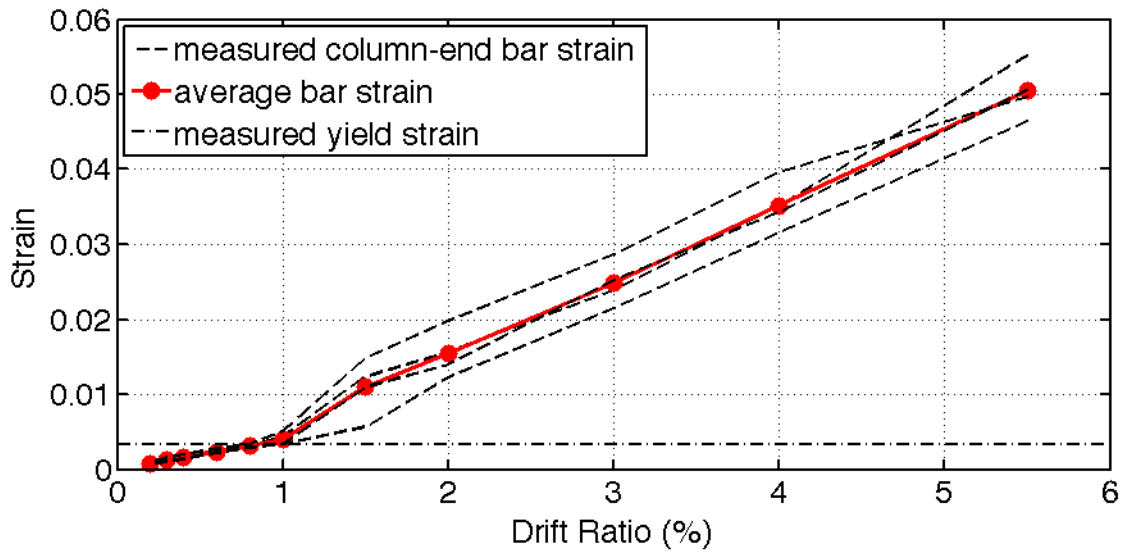


Figure 24: CH100 –column-end bar strain gauge recordings at each drift target and calculated average

4.2.4 Strain Profile

Strain readings over the height of the top part of the north-western longitudinal bar are given in Figure 25. As can be seen in Figure 25, once flexural yielding occurs, strains tended to concentrate at column ends. However, as the column was pushed past first yield to higher drift targets, inelastic strains were able to spread to 23 inches from the end of the column.

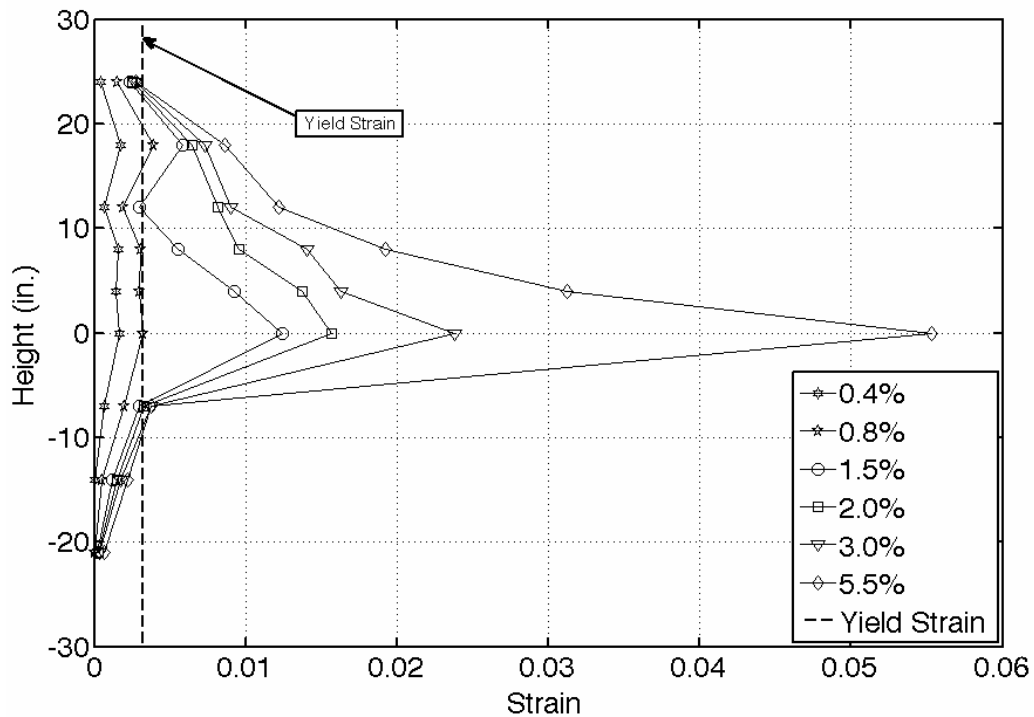


Figure 25: CH100 – longitudinal reinforcement strain demands over height at drift targets

4.2.5 Crack Widths

Data from the GVIS was used to monitor the widths of the major flexural cracks at first yield were monitored. These cracks were identified as having a width of 0.008 inches or larger at first yield. Considering that ACI 318-14 intends to limit crack widths to 0.016 inches during service loading, half of this value was used conservatively as a threshold at first yield for cracks of concern. Cracks within seven quadrilateral target elements were identified as satisfying the above-mentioned criteria for each drift direction; three at the bottom half of the member, and four in the upper part (Figure 18). The number of cracks was the same between the north and south faces of the member as the column was cycled. During the first half cycle to a positive drift (column being pushed south, i.e. right on the pictures), flexural crack widths were measured in the bottom-south and top-north sides of the member. Strain readings of the second elements in from the column vertical surfaces were used to calculate the reported cracks width values. This was done as the outermost targets in the plastic-hinge region were lost at high demands due to cover crushing. The average of these cracks is plotted in Figure 26 and identified as cracks occurring during “Half Cycle 1”. The same procedure was followed for other positive and negative drift half cycles for each drift target. At first yield, the average of all cracks was 0.012 inches. These cracks opened wider as the member was pushed passed yield. No significant difference in crack width was noticed between the successive half cycles in which the column was being pushed in the same direction. These critical cracks were all located within 16 inches from the ends of the member. As the column was pushed to higher drifts (past 2.0% drift ratio) two large flexural cracks formed at each end of the member, 9.5 inches from its ends. Figure 27 plots the width of one of these cracks as measured throughout the test.

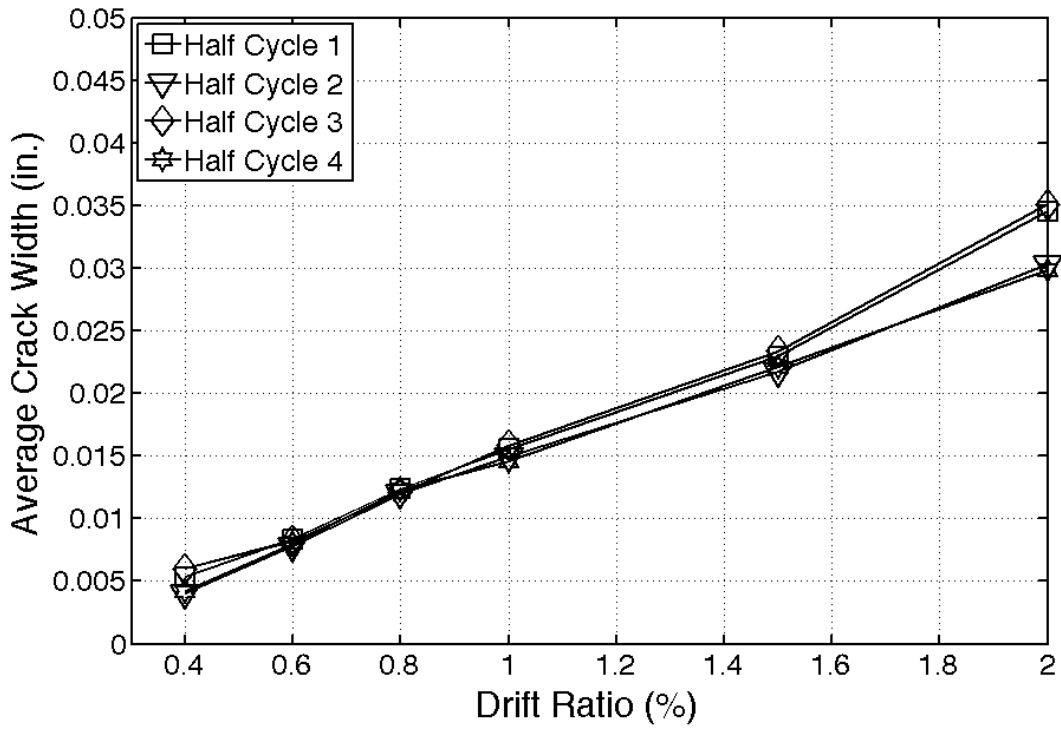


Figure 26: CH100 – average values of largest flexural crack widths at drift targets

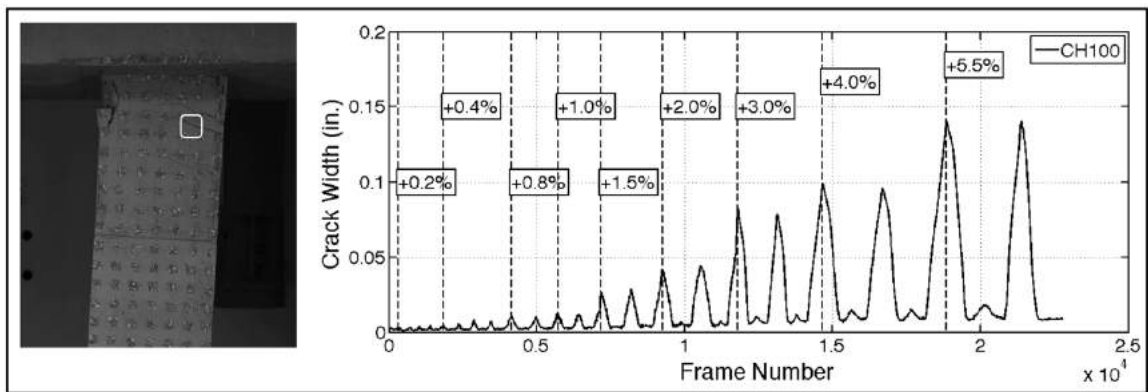


Figure 27: CH100 – width of one of the two largest flexural cracks

4.2.6 Buckling History

Buckling of the longitudinal reinforcement in CH100 was identified through the images taken at the end of each loading half-cycle. Buckling of the first longitudinal bars was observed at the second cycle to a drift ratio of +5.5% (Figure 28-left). The first bars to buckle were the middle bars that were restrained by the 90-degree hook of cross-ties, which opened up allowing the bar to buckle. At this point, the moment strength of the member had dropped by 28% as compared to the peak applied moment at the base. As the column was pushed back to a drift ratio of -5.5%, significant buckling took place, which led to the lateral strength of the member having decreased from peak by 32% at the onset of the first bar fracture. The rotation of the row of targets located 9 inches over the base, or the 4th target row from the end) of the column is plotted in Figure 29. The location of this row of targets corresponds to the first row of targets above the observed buckling location. The rotation at this location seems to not have captured the progression of buckling.

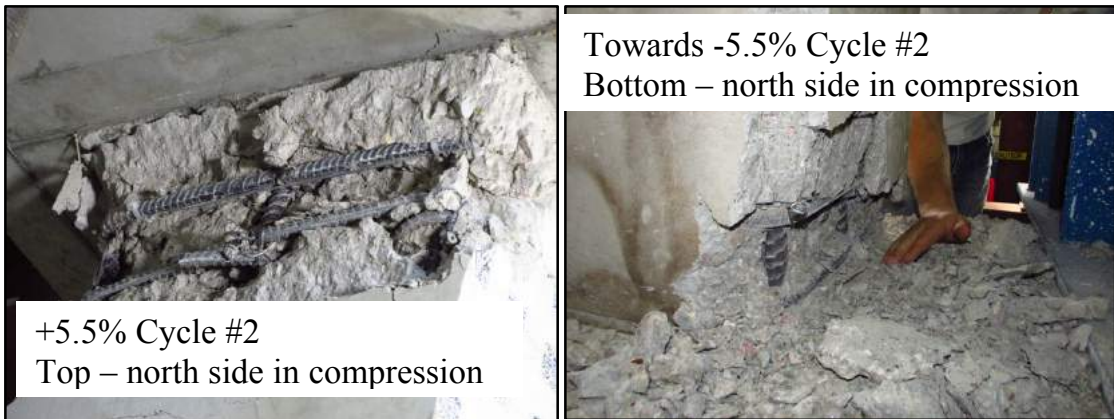


Figure 28: CH100 – longitudinal bar buckling

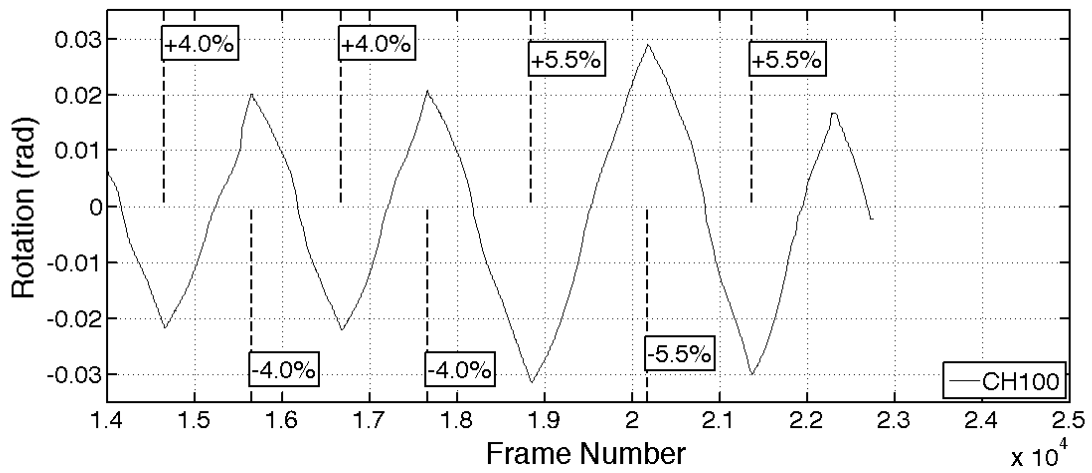


Figure 29: CH100 – rotation at a distance 9 inches from the base

4.2.7 Energy Dissipation

The dissipated energy, defined as the area under the average top and bottom moment versus lateral drift relation, is plotted in Figure 30 for each cycle. The average top and bottom moment was used to compute the dissipated energy as moment strength is more representative of column sectional strength, as opposed to lateral-load strength that is influenced by second order deformation effects. Prior to first yielding (drift ratio targets up to 0.8%) the amount of dissipated energy was similar between the two cycles at each target drift. As the column was pushed to higher drifts and damage accumulated, the difference in energy dissipation between the cycles increased. The difference between two consecutive post-yield cycles to the same drift ratio was in the range of 5 to 15%. The difference in cumulative dissipated energy between cycles at the end of the 4% drift ratio cycles was 10.7%.

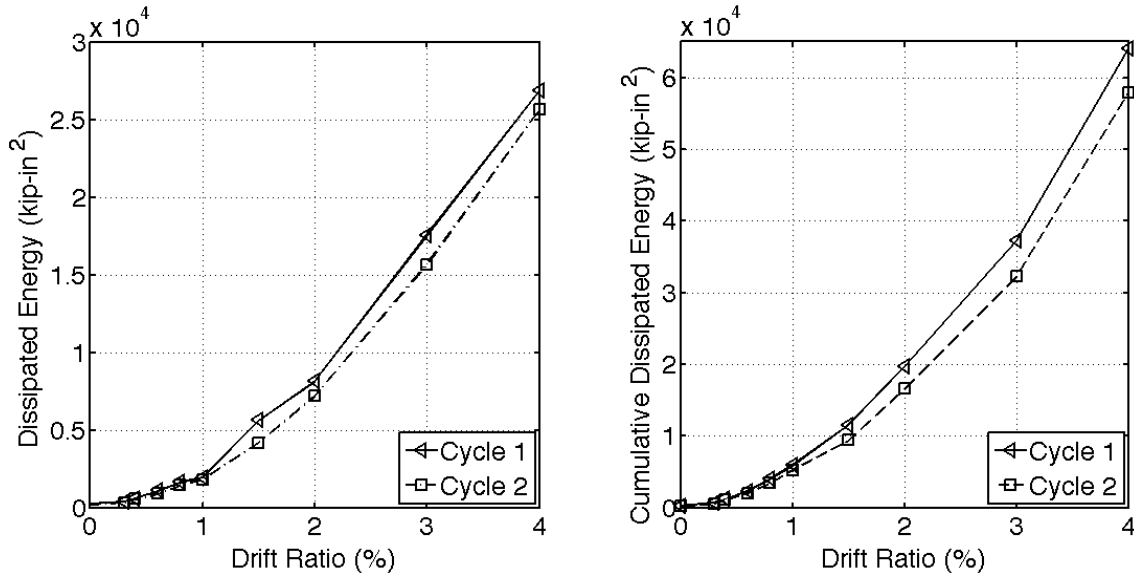


Figure 30: CH100 – dissipated energy at drift targets for each cycle

4.3 TEST RESULTS FOR CL100

Results from testing of column CL100 are reported in this section. Specimen CL100 was reinforced with grade 100 longitudinal and transverse bars with a relatively low (L) T/Y ratio of 1.16. These bars were produced primarily using the quenching and tempering process. Specimen CL100 was tested under displacement-controlled quasi-static cyclic lateral loading. The recorded lateral displacement history of specimen CL100 is illustrated in Figure 31. An axial load of 242 kips was applied by the vertical actuators to this specimen which together with the 10-kip self-weight of the top footing and testing frame resulted in an effective axial load of $\sim 14.9\% A_g f'_c$ after performing large-deformation equilibrium. The load was kept constant throughout the test as shown in Figure 32.

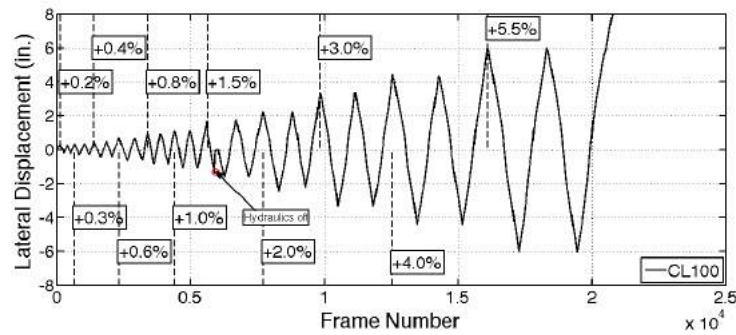


Figure 31: CL100 – measured lateral displacement at every captured frame

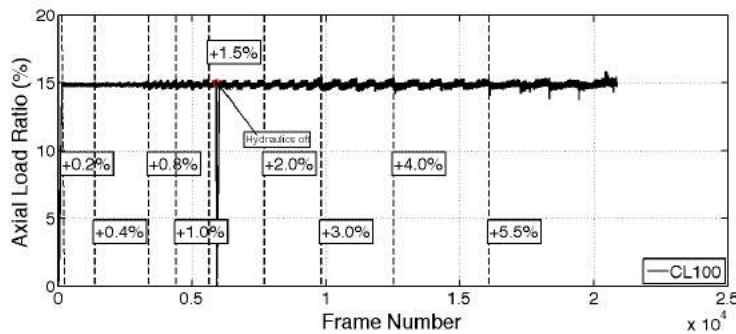


Figure 32: CL100 – applied axial load ratio at every captured frame

The loading protocol was disrupted during the test, as the specimen was being pushed towards the first half-cycle to a drift ratio of +1.5%. This took place at frame 5934 (Figure 31 & Figure 32), when the hydraulic system lost power. The column was reloaded axially and pushed to a drift ratio of +1.5% after being leveled. At the first cycle to a drift ratio of -2.0% the specimen was pushed 0.25 inches further than the target displacement. It is believed that these events did not affect the overall performance of the member.

4.3.1 General Behavior

Prior to testing, no cracks were noticed on the specimen surface. The recorded lateral force versus drift ratio response of specimen CL100 is plotted in Figure 33. Table 12 summarizes the lateral force and drift values for all milestones for column CL100. The first flexural cracks in column CL100 were visible at the end of the first cycle to +0.2% drift-ratio excursion (Figure 33; Figure 34). These cracks were noted through surface principal strain on the order of 0.002 (Figure 34). The initial flexural cracks propagated closer to the centerline of the column leading to the formation of first inclined cracks at the end of the first half-cycle to a drift ratio of +0.6% drift ratio (Figure 34).

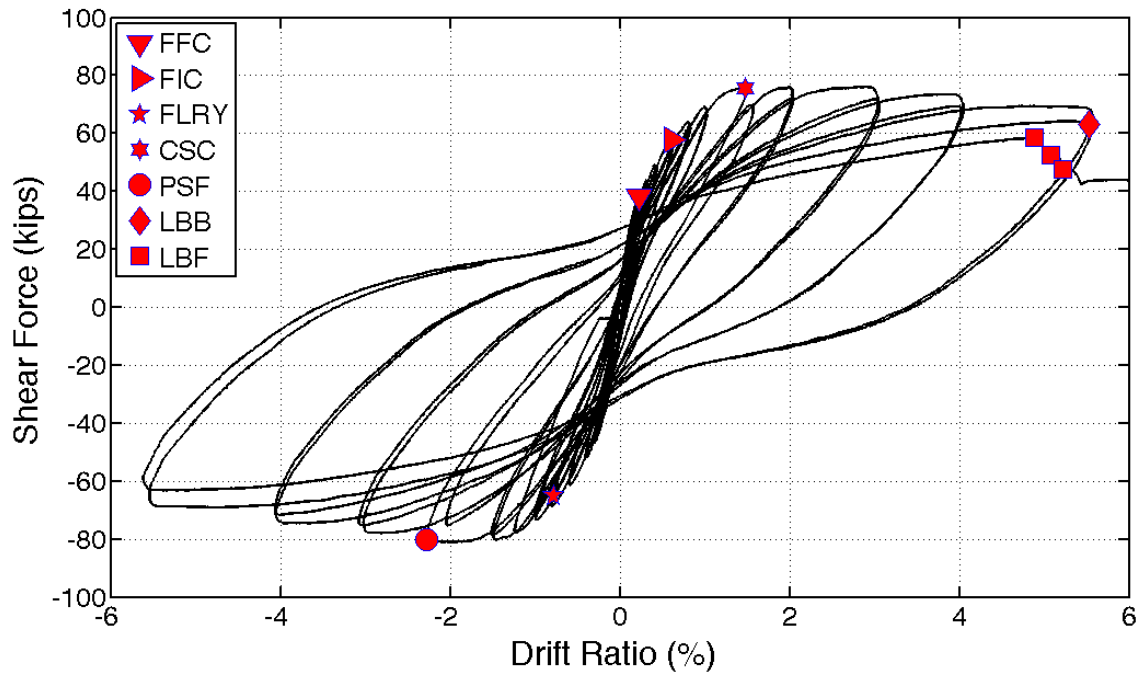


Figure 33: CL100 – lateral response

Table 12: CL100 - behavioral milestones

Milestone	Drift Ratio (%)	Lateral Load (kips)
First Flexural Crack	+0.2	+38.2
First Inclined Crack	+0.6	+57.8
First Long. Reinf. Yield	+1.0	+78.4
Cover Splitting Crack	+1.5	+79.4
Peak Shear Force	-2.0	-80.8
Long. Bar Buckling	+5.5	64.0
Long. Bar Fracture	+4.8	+58.6

First yield in the longitudinal reinforcement was identified from strain gauge readings at the end of the first cycle to a drift ratio of +1.0%. As the column was pushed to the first cycle towards +1.0% drift the initial flexural cracks opened wider and additional cracks formed closer to the column mid-height (Figure 34). The maximum applied shear force of 80.8 kips was recorded at the end of first cycle to a drift ratio of -2.0%. Beyond that drift cycle, the lateral load diminished slightly, driven by second order axial load effects and the accumulation of damage such as concrete spalling. Top and bottom moments versus lateral drift ratio are plotted in Figure 35. As can be seen in the figure, peak moment strength occurred at a drift ratio of -1.5%. Gradual degradation of moment strength occurred beyond that drift due to accumulation of damage in concrete. At the second cycle to a drift ratio of +5.5%, initiation of longitudinal bar buckling was observed and was associated with a steeper degrading slope in the moment versus drift plots

As the column was pushed to drift ratios of 3.0%, 4.0% and 5.5%, increasing crushing and spalling of the concrete cover was observed. CL100 showed similar cracking pattern to CH100, with two main flexural cracks in the order of 0.15 inches at each plastic hinge region. These cracks were 10 inches from the end of the specimen and reached a width of 0.15 in. by the end of the first cycle to a drift ratio of 5.5%. At the same drift ratio, vertical cracks at the location of longitudinal reinforcement propagated 14 in. from column ends, indicating some de-bonding between the longitudinal bars and the surrounding concrete. These cracks initiated at a drift ratio of 1.5%, which corresponded to a curbing of the rate of increase in longitudinal bars strains with increasing drift ratios. The behavior is discussed in more details in Section 4.3.3.

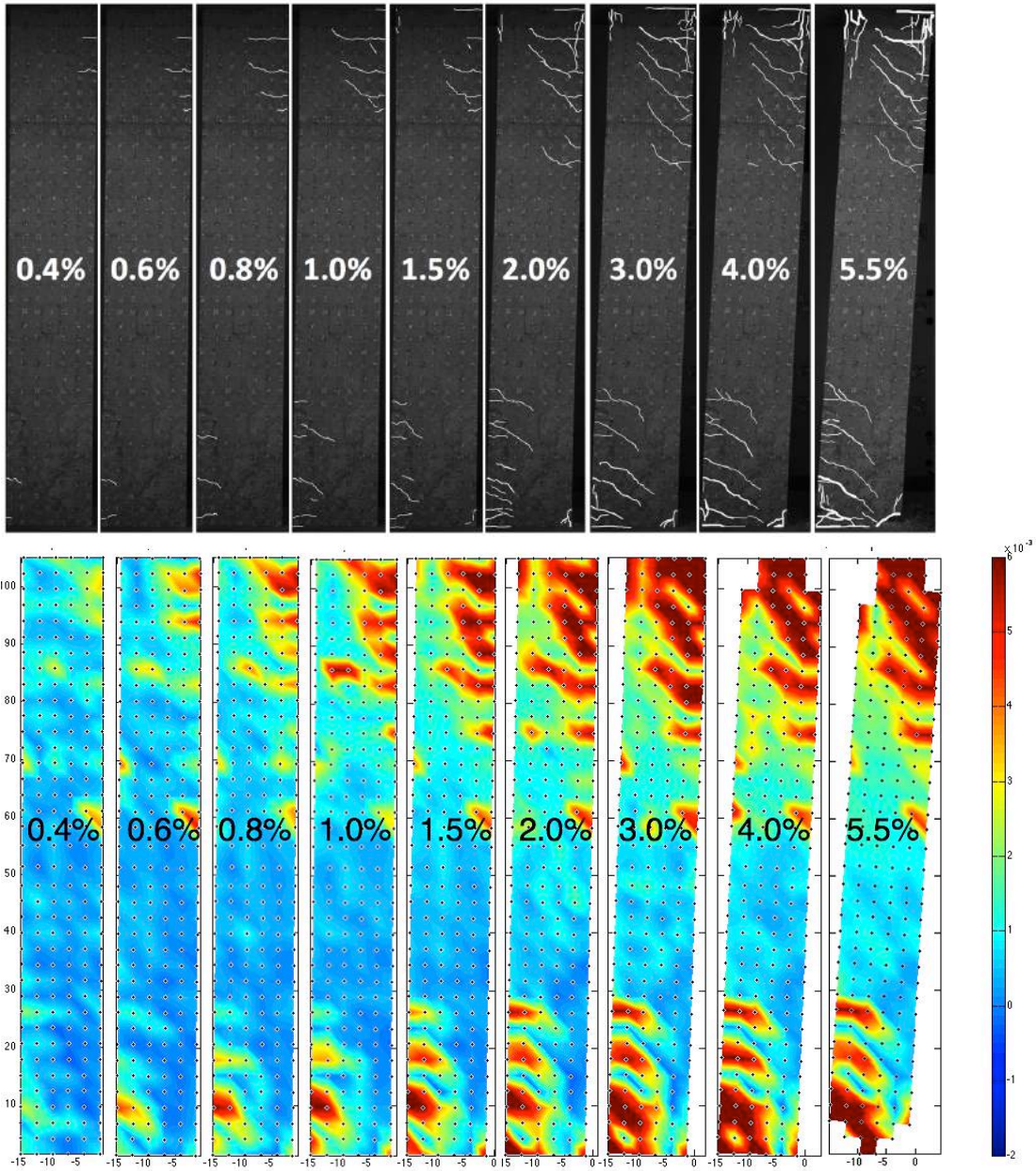


Figure 34: CL100 - cracking pattern (up) and measured largest principal strains (down) at several drift ratio targets

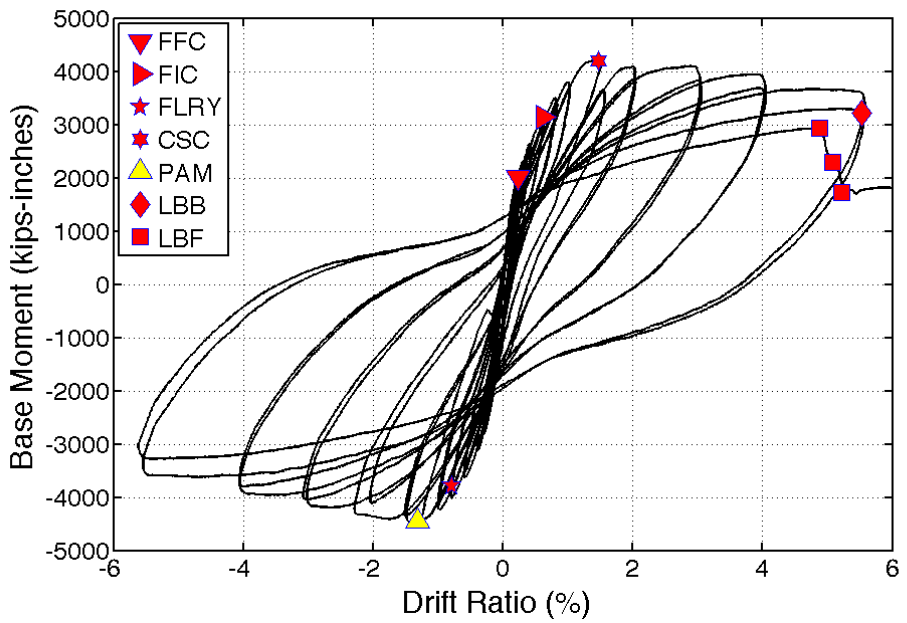
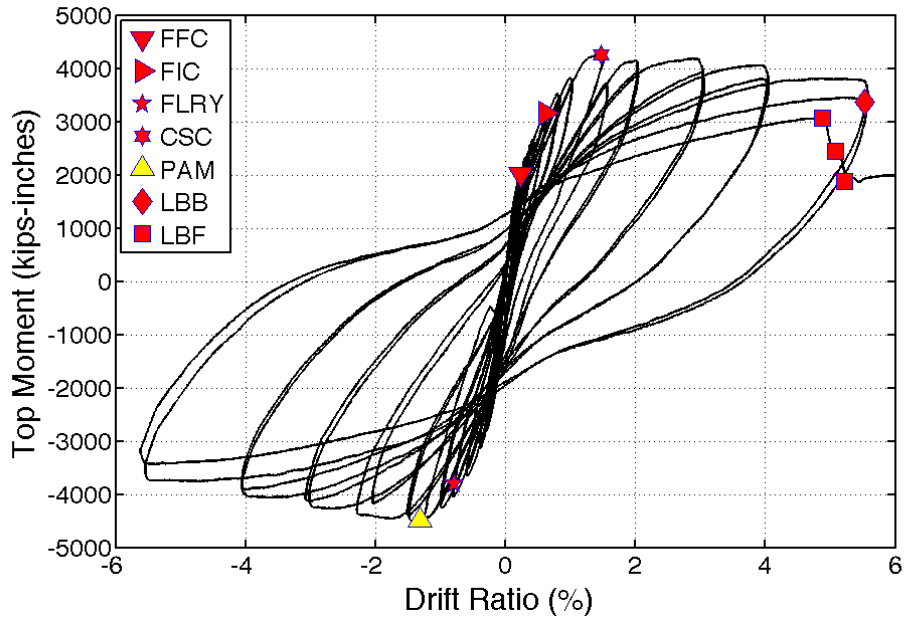


Figure 35: CL100 - base and top moment vs. drift ratio

The lateral load resistance of the column remained relatively stable and the column maintained axial load capacity past the first cycle to a drift ratio of 5.5% (Figure 36). During the second cycle to a drift ratio of +5.5%, the column experienced a 11% loss in moment resistance as compared to the previous half-cycle to the same drift target, or 29% loss as compared to the maximum peak moment resistance. This was due to significant buckling of longitudinal bars. By then, the cover concrete in the top and bottom plastic hinge regions had spalled to a distance of about 13 in. from column ends. The first 90-degree cross tie at the north-bottom face of the column had already opened up, contributing to the observed buckling. As a result, on its way to the first half-cycle to a drift ratio target of +7.0%, the first bar fractured at a drift ratio of 4.8% (Figure 36; Figure 37). Right before the first bar fractured, the lateral strength of the column was 34% lower as compared to the peak moment resistance (Figure 36; Figure 37). In an attempt to push the column towards a drift ratio of +7.0%, two more consecutive bar fractures occurred. The moment resistance at this point dropped below 50% of the peak moment resistance. The test was stopped after a fourth bar fractured at a drift ratio of +8.0%. The column was able to carry the prescribed axial load throughout the test without showing signs of significant axial deformation even after four-longitudinal reinforcement bars fractured.

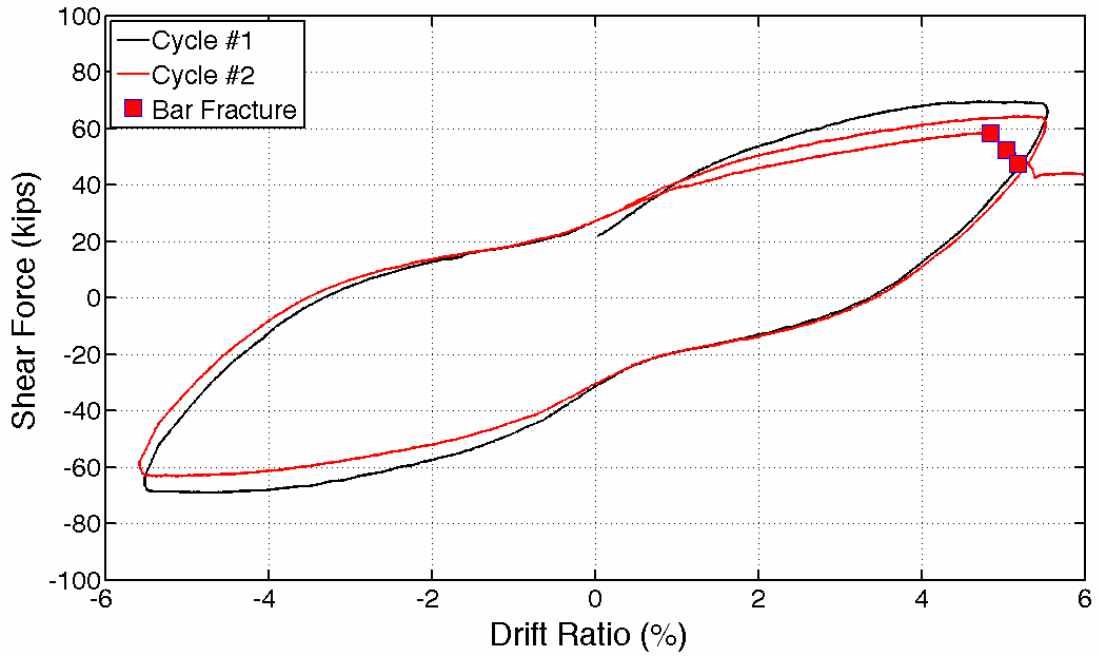


Figure 36: CL100 – last cycles response

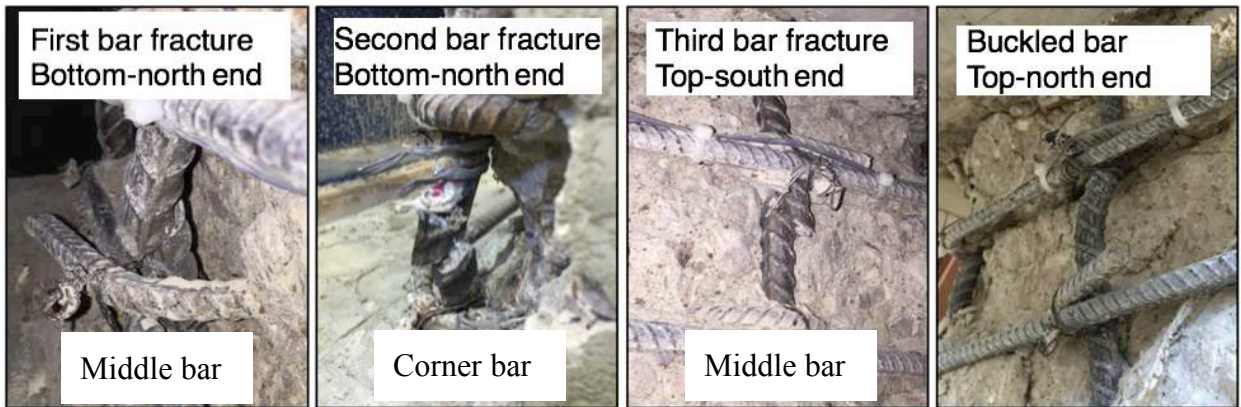


Figure 37: CL100 – pictures of fractured and buckled bars at the end of the test

4.3.2 Deformation Components

Flexural deformations contributed most to the column lateral drift throughout the test (Table 13; Figure 38). At higher drifts, the relative weight of flexural deformations lowered as the bar-slip component increased from about 20% of the total drift at low drift levels, to about 40% in the post-yield cycles. Possibly, the observed increase in recorded bar-slip contribution was due to debonding of the longitudinal reinforcement from the surrounding concrete at larger levels of concrete damage. This debonding of longitudinal bars due to concrete damage could have decoupled the bar deformations from measured concrete surface movements, from which bar-slip deformations were extracted. Shear deformations increased in absolute value, but remained relatively low at around 5% of total drift throughout the test. The low amount of shear deformations was due to the applied shear stresses being relatively low. Results for deformation components were not reliable after cycle to a drift ratio of 4.0%.

Table 13: CL100 - deformation components as percentage of total

Total	Flexure	Bar-slip	Shear
0.2%	74.0%	22.0%	4.0%
0.3%	68.7%	28.0%	3.3%
0.4%	67.9%	27.8%	4.2%
0.6%	64.7%	30.7%	4.6%
0.8%	63.9%	30.6%	5.5%
1.0%	62.7%	31.3%	6.0%
1.5%	52.0%	42.2%	5.8%
2.0%	53.9%	41.0%	5.0%
3.0%	54.6%	41.2%	4.3%
4.0%	55.8%	40.3%	3.9%

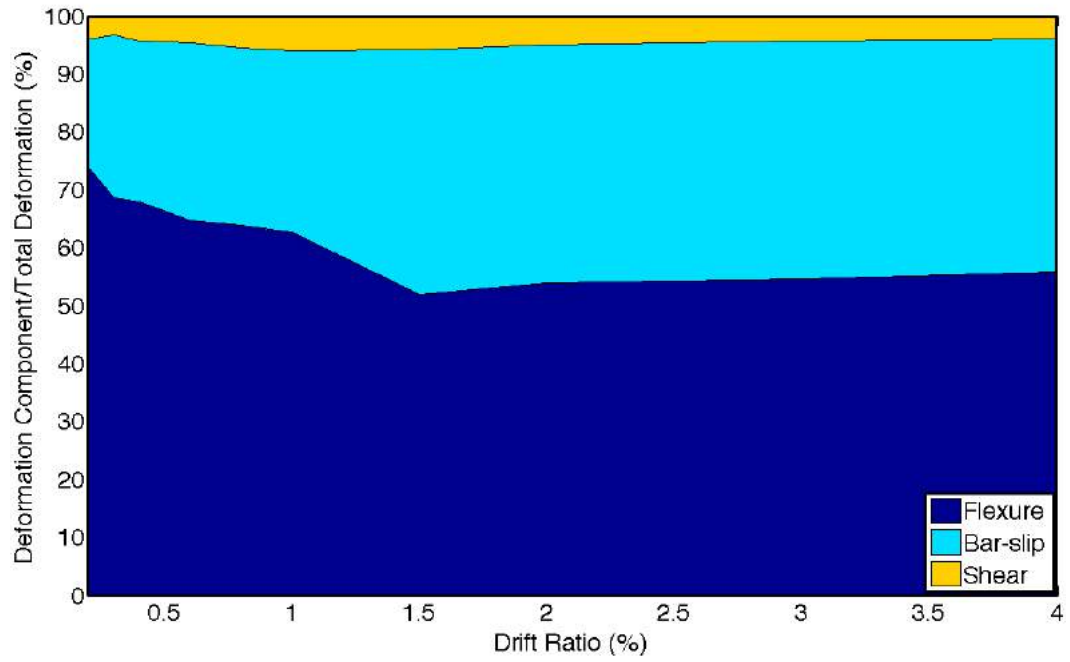


Figure 38: CL100 – deformation components

4.3.3 Strain History

Maximum strain demands were recorded at the interfaces between the column and footings. Figure 39 shows a typical strain versus lateral load response recorded on longitudinal bars at column ends. Figure 40 plots longitudinal bar tension strains at the end of each positive drift cycle target, measured at the top and bottom column interface with footings. The #6 bars used as longitudinal reinforcement in CL100 had a yield strain of 0.0032 as obtained from material testing. This strain was first reached at a drift ratio of -0.8%. However, the drift ratio of +1.0% was reported as the first yield, as an average between the available strain gauge recordings. After yield, the strain demands increased without significant increase in the lateral load. In general, strain demands on longitudinal bars were higher in the second cycle to the same drift target, with the difference increasing at higher drifts. This difference was however relatively small, and on the order of 5% of the strain value.

Strain gauge L4NE stopped recording right before the column was pushed to the first cycle to a drift ratio of 5.5%. The strain value at 5.5% drift ratio presented below was linearly interpolated. A linear behavior at these range of deformation demands was observed at all other measured strain data from other tests.

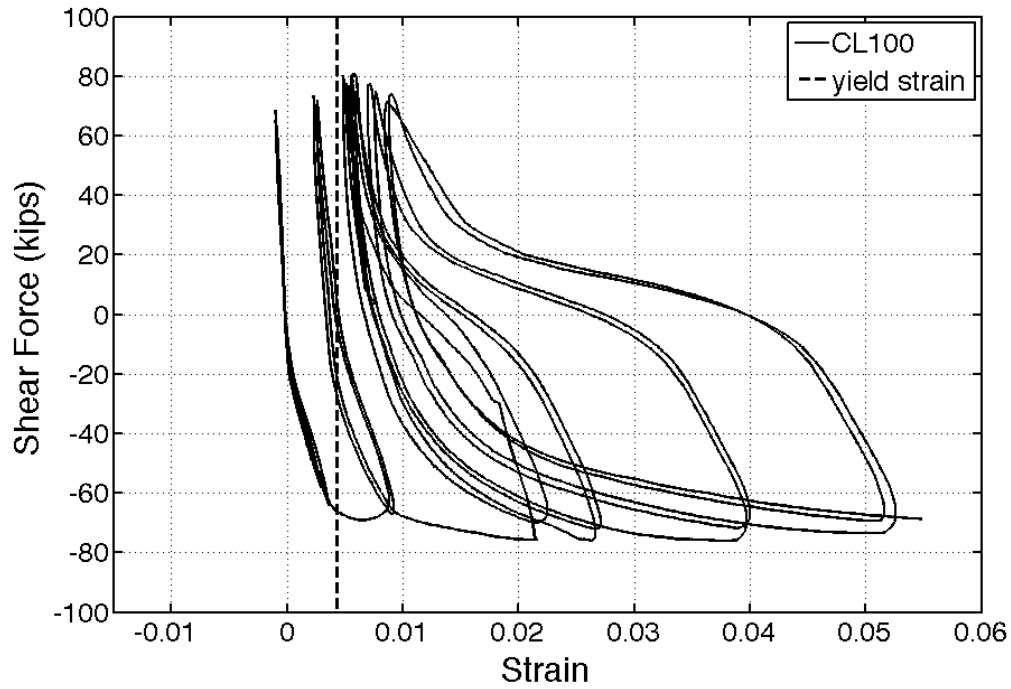


Figure 39: CL100 – strain gauge L4NE (bottom north-eastern corner) recording at the interface between the column and bottom footing

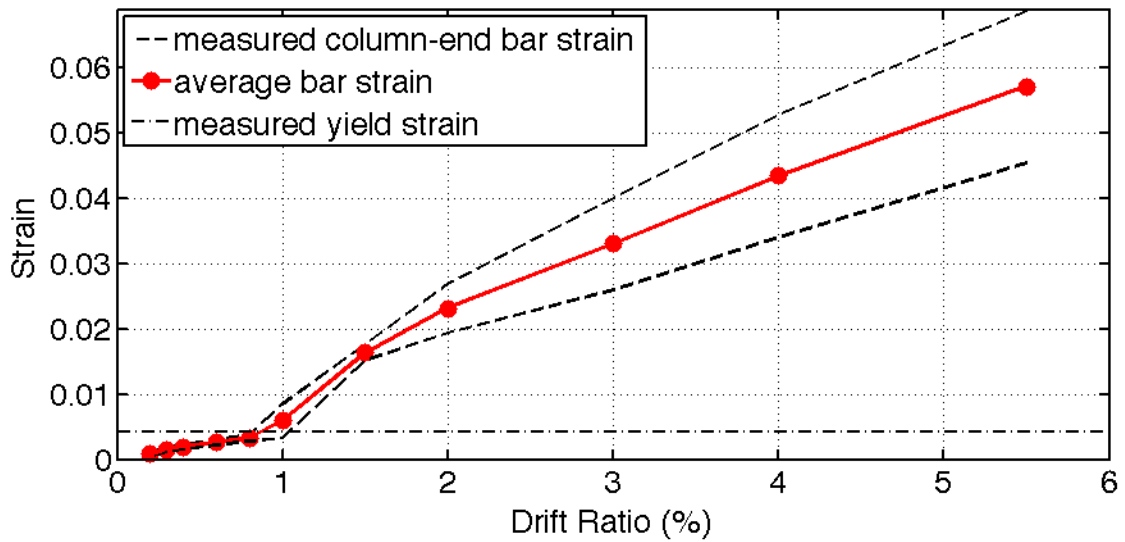


Figure 40: CL100 –column-end bar strain gauge recordings at each drift target and calculated average

4.3.4 Strain Profile

Strain readings over the height of the bottom south-western longitudinal bar are given in Figure 41. As it can be seen in Figure 41, once flexural yielding occurs, strains tended to concentrate at column ends. However, as the column was pushed past first yield to higher drift targets, inelastic strains were able to spread to 18 inches from the end of the column.

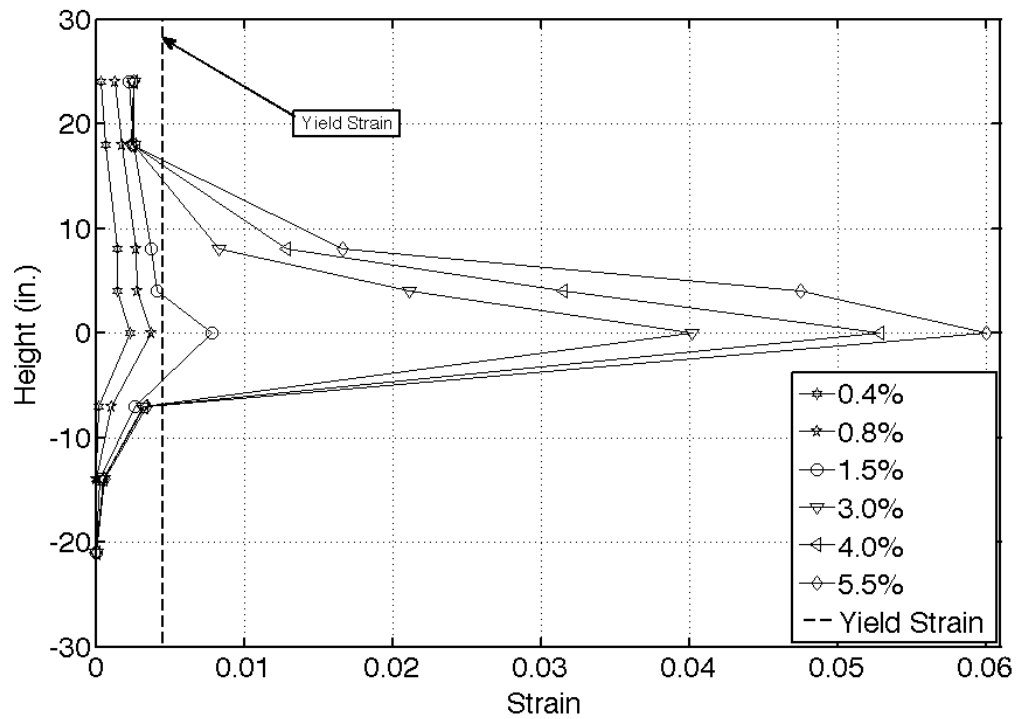


Figure 41: CL100 – longitudinal reinforcement strain demands over height at drift targets

4.3.5 Crack Widths

Data from the GVIS was used to monitor the widths of the major flexural cracks at first yield were monitored. Considering that ACI 318-14 intends to limit crack widths to 0.016 inches during service loading, half of this value was used conservatively as a threshold at first yield for cracks of concern. Cracks within nine quadrilateral target elements were identified as satisfying the above-mentioned criteria, for each drift direction; three at the bottom half of the member, and four in the upper part (Figure 34). Six cracks formed when the column was pushed to a negative drift (column being pushed north, i.e. left in the pictures), 3 at each end of the member. During the first half cycle to a positive drift (column being pushed south, i.e. right in the pictures), flexural crack widths were measured in the bottom-south and top-north sides of the member. Strain readings between the second elements in from the column vertical surfaces were used to calculate the reported cracks width values. This was done as the outermost targets in the plastic-hinge region were lost at high demands due to cover crushing. The average of these cracks is plotted in Figure 42 and identified as cracks occurring during “Half Cycle 1”. The same procedure was followed for other positive and negative drift half cycles for each drift target. At first yield, the average of all cracks was 0.014 inches. These cracks opened wider as the member was pushed passed yield. No significant difference in crack width was noticed between the successive half cycles in which the column was being pushed in the same direction. These critical cracks were all located within 18 inches from the ends of the member. As the column was pushed to higher drifts (past 2.0% drift ratio) two large flexural cracks formed at each end of the member, 9 inches from its ends. Figure 49 plots the width of one of these cracks as measured throughout the test.

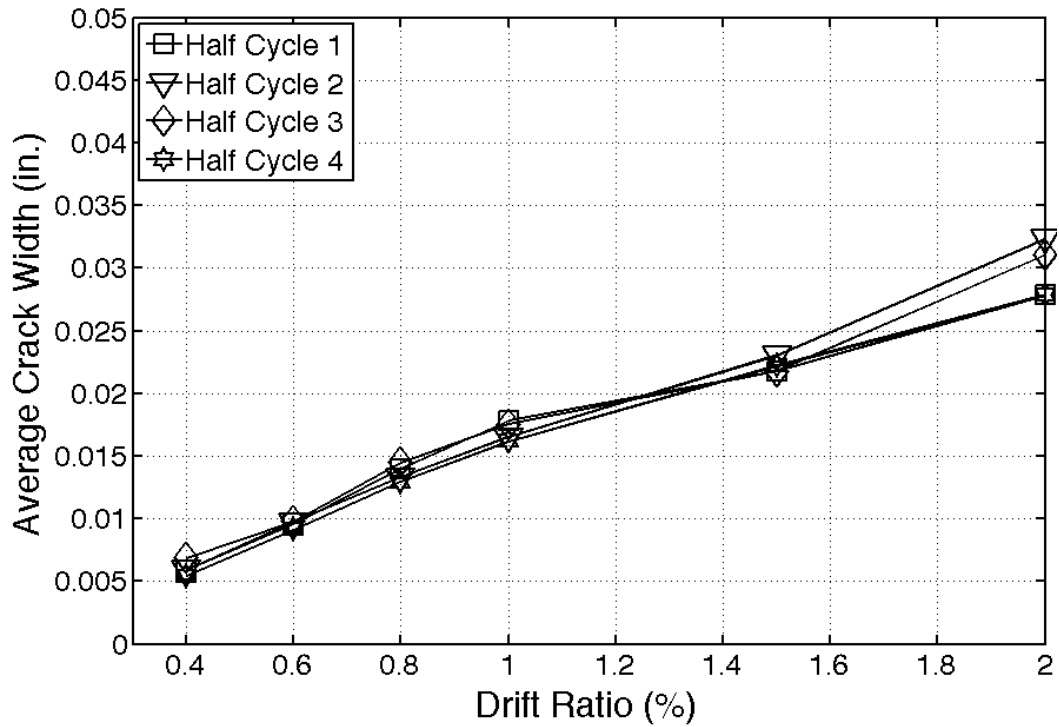


Figure 42: CL100 - average values of largest flexural crack widths at drift targets

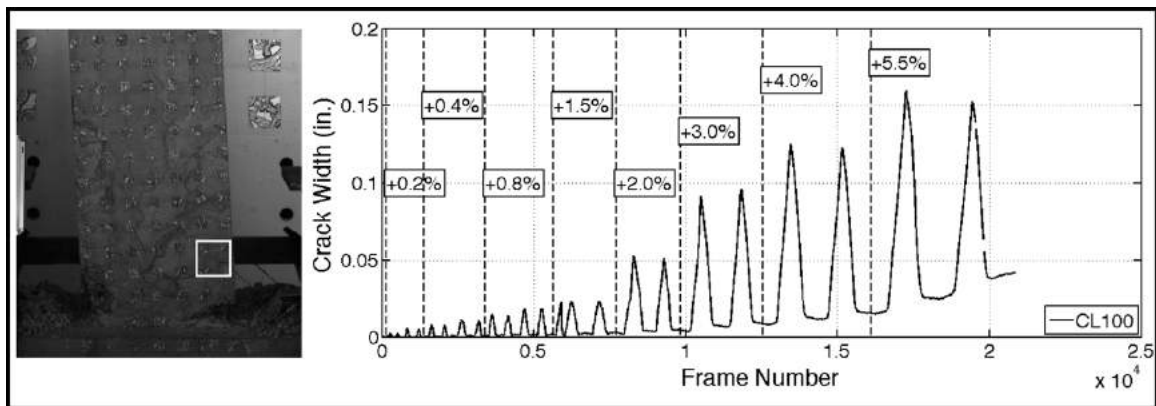


Figure 43: CL100 - width of one of the two largest flexural cracks

4.3.6 Buckling History

Buckling of the longitudinal reinforcement in CL100 was identified through the images taken at the end of each loading half-cycle. Buckling of the first longitudinal bars was observed at the second cycle to a drift ratio of +5.5% (Figure 44). The first bars to buckle were the middle bars that were restrained by the 90-degree hook of cross-ties, which opened up allowing the buckling. At this point, the moment strength of the member had dropped by 29% as compared to the peak applied moment at the base. As the column was pushed back to a drift ratio of -5.5%, significant buckling took place, which led to the lateral strength of the member having decreased by 34% at the onset of the first bar fracture. The rotation of the row of targets located 9 inches over the base, or the 4th target row from the end of the column is plotted in Figure 45. The location of this row of targets corresponds to the first row of targets above the observed buckling location. The rotation at this location seems to not have captured the progression of buckling.

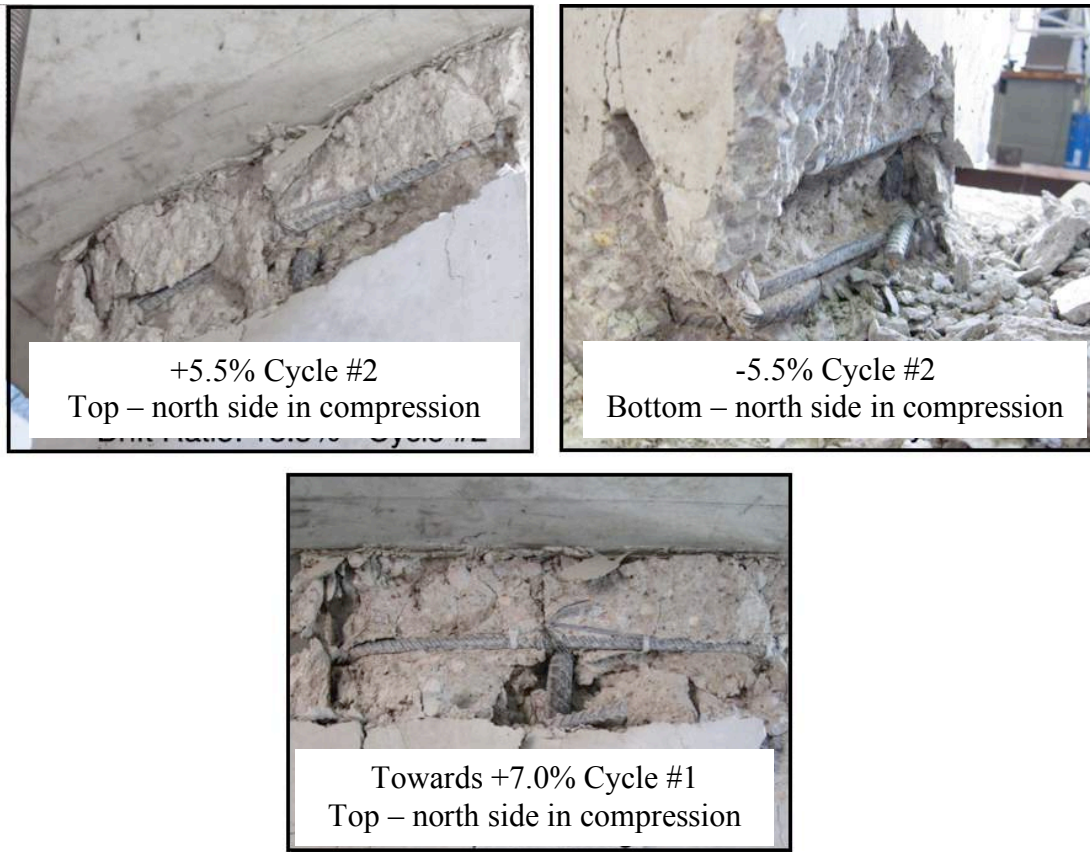


Figure 44: CL100 –longitudinal bar buckling

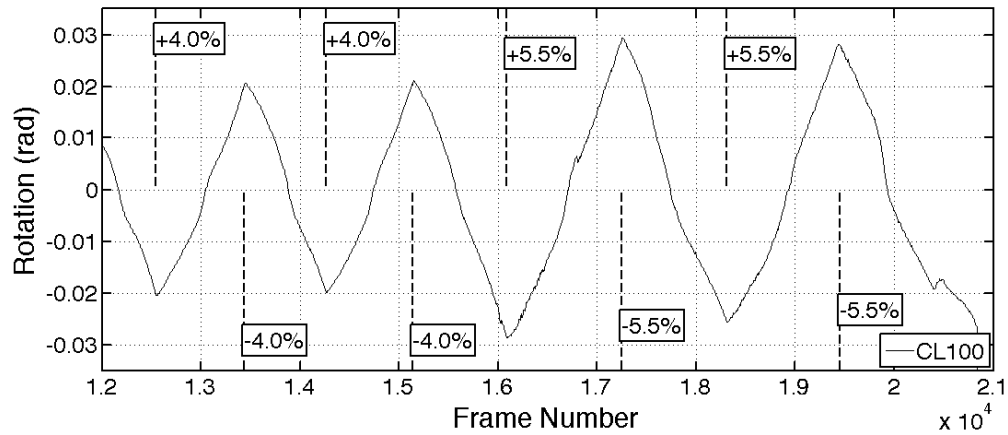


Figure 45: CL100 – rotation at a distance 9 inches from the base

4.3.7 Energy Dissipation

The dissipated energy, defined as the area under the average top and bottom moment versus lateral drift relation, is plotted in Figure 46 for each cycle. The average top and bottom moment was used to compute the dissipated energy as moment strength is more representative of column sectional strength, as opposed to lateral-load strength that is influenced by second order deformation effects. Prior to first yielding (drift ratio targets up to 0.8%) the amount of dissipated energy was similar between the two cycles at each target drift. As the column was pushed to higher drifts and damage accumulated, the difference in energy dissipation between the cycles increased. The difference in cumulative dissipated energy between cycles at the end of the 4% drift ratio cycles was 15.2%.

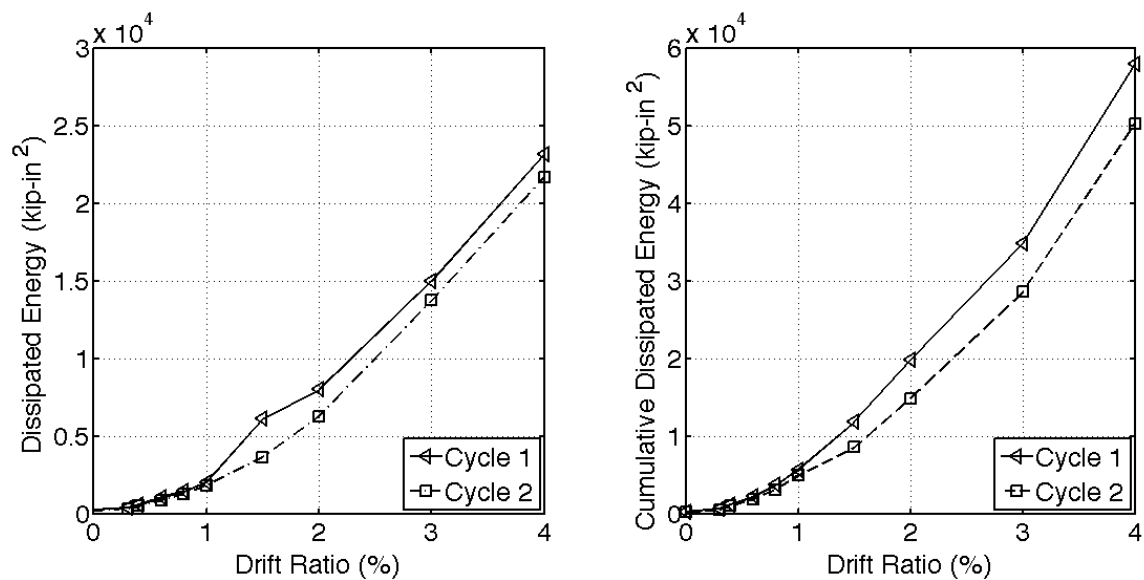


Figure 46: CL100 – dissipated energy at drift targets for each cycle

4.4 TEST RESULTS FOR CM100

Test results for column CM100 are reported in this section. Specimen CM100 was reinforced with grade 100 A1035 longitudinal and transverse bars. These bars were produced using the MMFX (M) proprietary process (2012). As for all specimens, CM100 was tested under displacement-controlled quasi-static cyclic lateral loading. The recorded lateral displacement history is shown in Figure 47. An axial load of 253 kips was applied by the vertical actuators which together with the 10-kips self-weight of the top footing and test frame resulted in an effective axial load of $15.0\% A_g f'_c$ (Figure 48). CM100 was loaded at $14.3\% A_g f'_c$ up to the first cycle to a drift ratio of 0.3% due to an input error (Figure 48). It is believed that this did not affect the overall performance of the test.

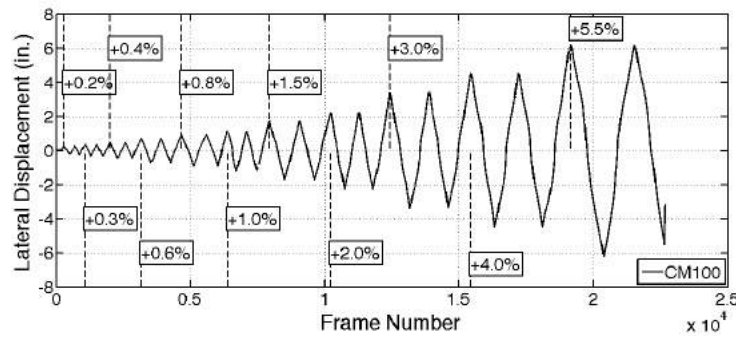


Figure 47: CM100 – measured lateral displacement at every captured frame

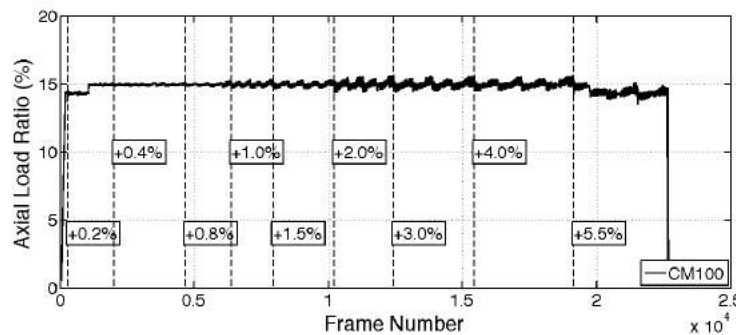


Figure 48: CM100 – applied axial load ratio at every captured frame

4.4.1 General Behavior

Prior to testing, no cracks were noticed on the specimen surface. The recorded lateral force versus drift ratio response of specimen CM100 is plotted in Figure 49. Table 14 summarizes the lateral force and drift values for all milestones for column CM100. The first flexural cracks in column CM100 were visible at the end of the first cycle to +0.2% drift-ratio excursion (Figure 49). These cracks corresponded to surface principal strains at the order of 0.002 (Figure 50). The initial flexural cracks propagated inside the centerline of the column leading to the formation of first inclined cracks (Figure 50 - 0.6%).

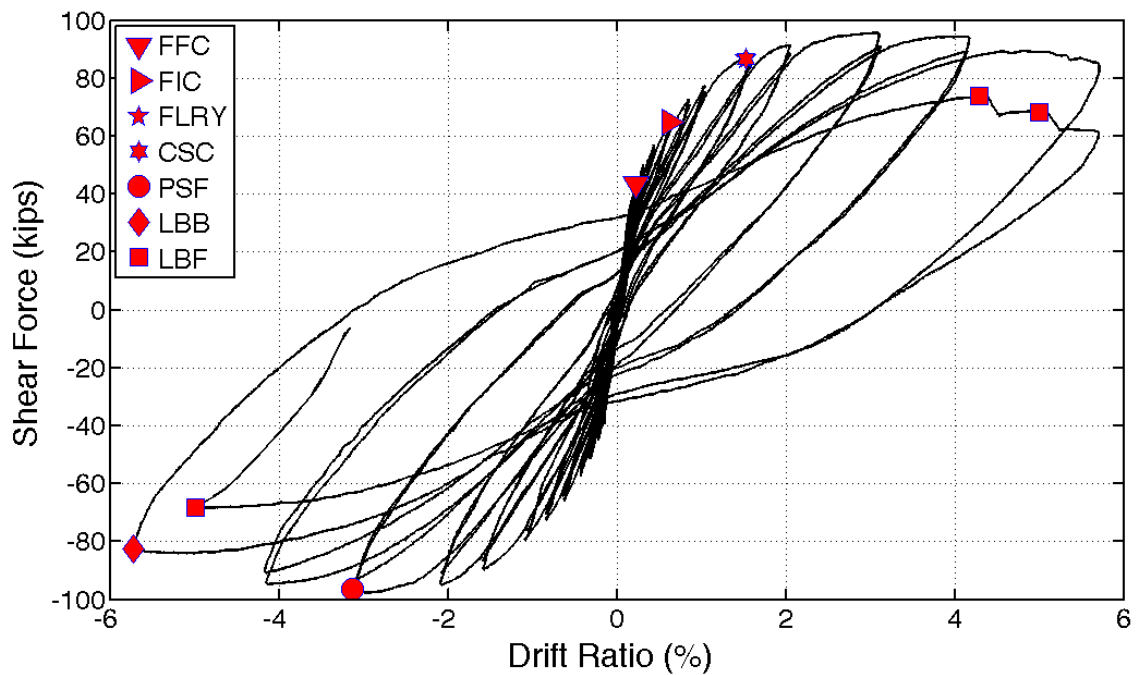


Figure 49: CM100 – lateral response

Table 14: CM100 - behavioral milestones

Milestone	Drift Ratio (%)	Lateral Load (kips)
First Flexural Crack	+0.2	+42.6
First Inclined Crack	+0.6	+65.2
First Long. Reinf. Yield	+1.5	+87.5
Cover Splitting Crack	+1.5	+87.5
Peak Shear Force	-2.9	-97.5
Long. Bar Buckling	-5.5	-80.6
Long. Bar Fracture	+4.3	-74.1

First yield in the longitudinal reinforcement was identified at a drift ratio of +1.5%, from strain gauge readings. The relatively high drift at first yield was attributed to the high yield strain of 0.0063 obtained from the 0.2% offset. The maximum applied shear-force of 97.5 kips was recorded at the end of first cycle to a drift ratio of -3.0%. Beyond that drift cycle, the lateral load diminished slightly, driven by second order axial load effects and the accumulation of damage such as concrete spalling.

Top and base moments versus lateral drift ratio are plotted in Figure 51. As can be seen, peak moment strength occurred at a drift ratio of 3.0% for the base moment, and 4.0% at the top moment. Gradual degradation of moment strength occurred beyond that drift due to accumulation of damage in concrete. During the first cycle to a drift ratio of -5.5%, initiation of longitudinal bar buckling was observed and was associated with a gradual loss in the moment capacity during that half cycle (Figure 52).

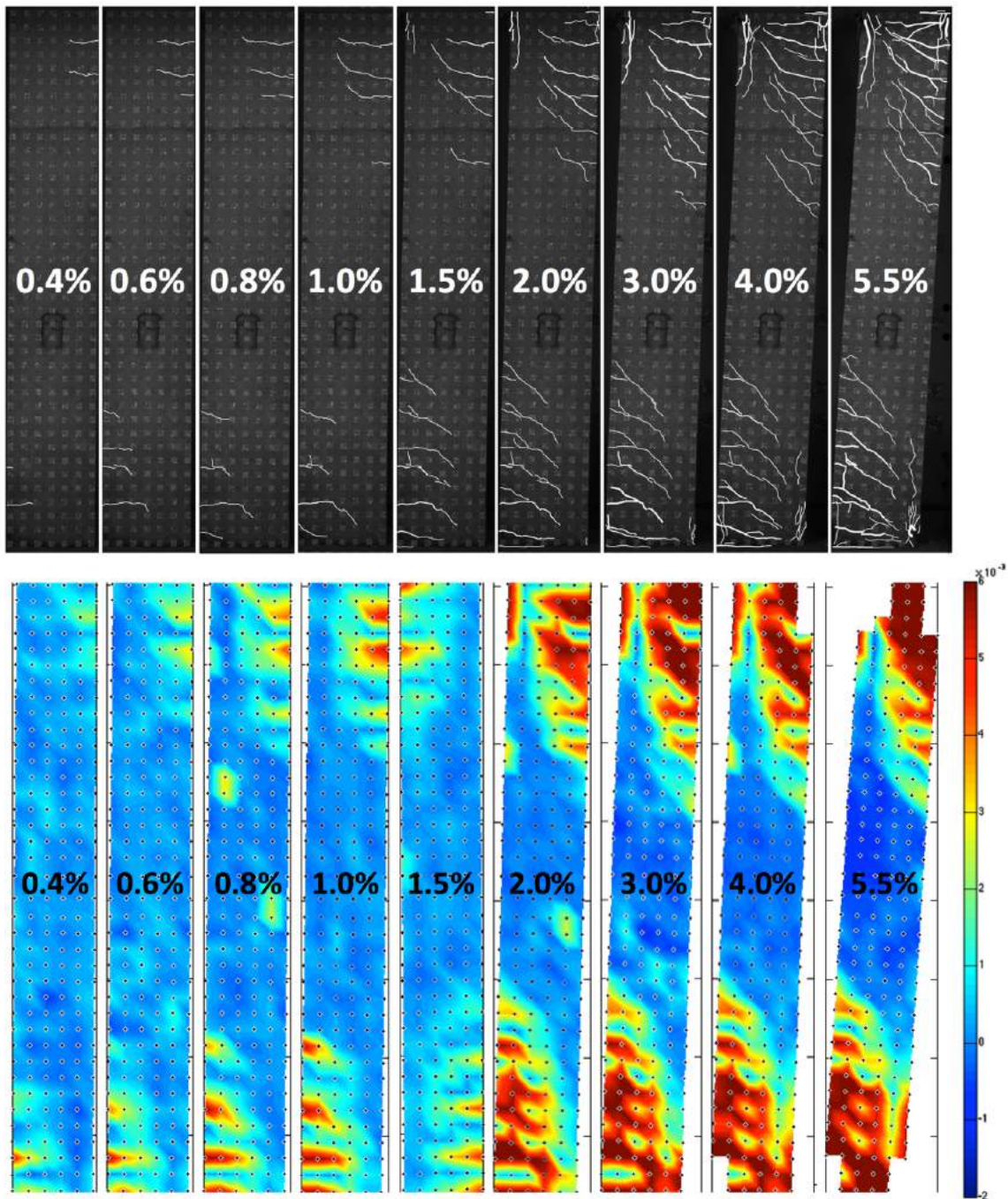


Figure 50: CM100 - cracking pattern (up) and measured principal strains (down) at drift targets

As the column was pushed to drift ratios of 4.0%, and 5.5%, increasing crushing and spalling of the concrete cover was observed. In contrast to specimens CH100 and CL100, specimen CM100 had smaller flexural cracks which spread over a larger height, up to 40 inches from its ends. Specimen CM100 formed more cracks with smaller widths when compared to the other specimens reinforced with grade 100 steel. Only one flexural crack had a width on the order of 0.15 inches at the end of the test, while other cracks were narrower than 0.1 inches. At the same drift ratio, vertical cracks at the location of the longitudinal reinforcement propagated up to 24 in. from column ends, indicating some debonding between the longitudinal bars and the surrounding concrete. These cracks initiated at a drift ratio of 1.5% drift ratio, which corresponded to a curbing of the rate of increase in longitudinal bars strains with increasing drift ratios. This behavior is discussed in more details in Section 4.4.3.

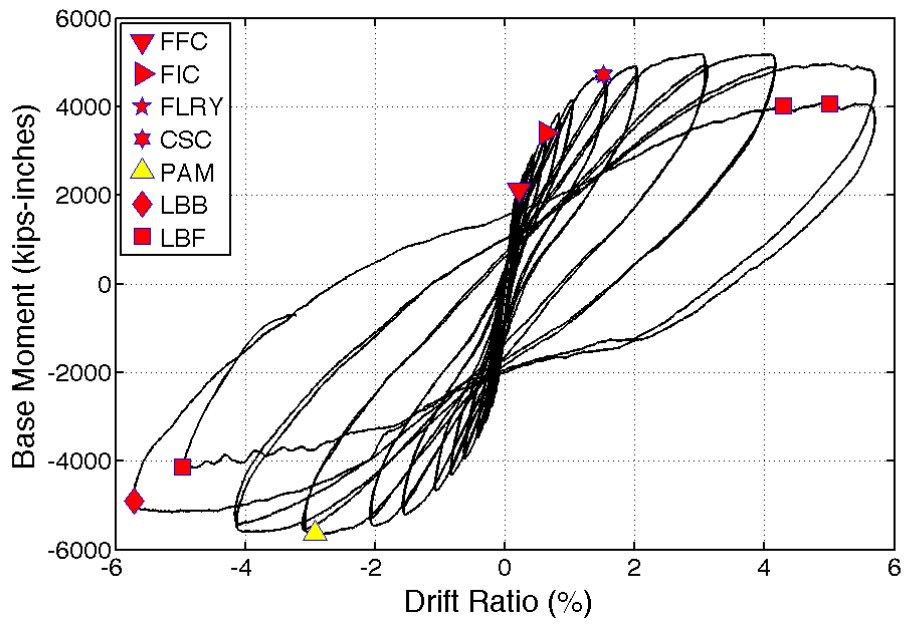
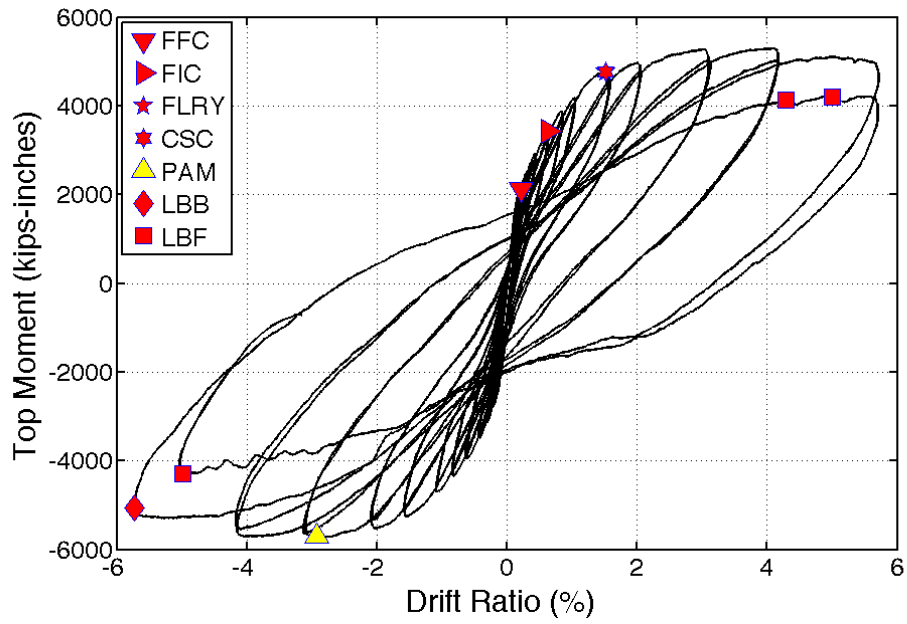


Figure 51: CM100 - base and top moment vs. drift ratio

The lateral load resistance of the column remained stable and the column maintained axial load capacity past the first cycle to a drift ratio of +5.5% (Figure 52). During the first cycle to a drift ratio of -5.5%, the column experienced only a 14% loss in moment strength as compared to the measured peak lateral moment resistance. By then, the cover concrete in the top and bottom plastic hinge regions had spalled to a distance of about 6 in. from column ends. On its way to the second cycle to +5.5% drift cycles, one of the corner longitudinal bars fractured at the base of the column at a drift ratio of 4.3% (Figure 52; Figure 53). Just prior to first bar fracture, the column had lost 29% of its measured peak moment resistance. The first bar fracture contributed to additional loss in lateral strength and a second bar fracture occurred shortly after, at a drift ratio of 5.0%. A third bar fractured at a drift ratio of -5.0% as the column was being pushed towards the completion of the second cycle to a drift ratio of 5.5%. The column was able to carry the prescribed axial load throughout the test without showing signs of significant axial deformation even after longitudinal reinforcement fracture.

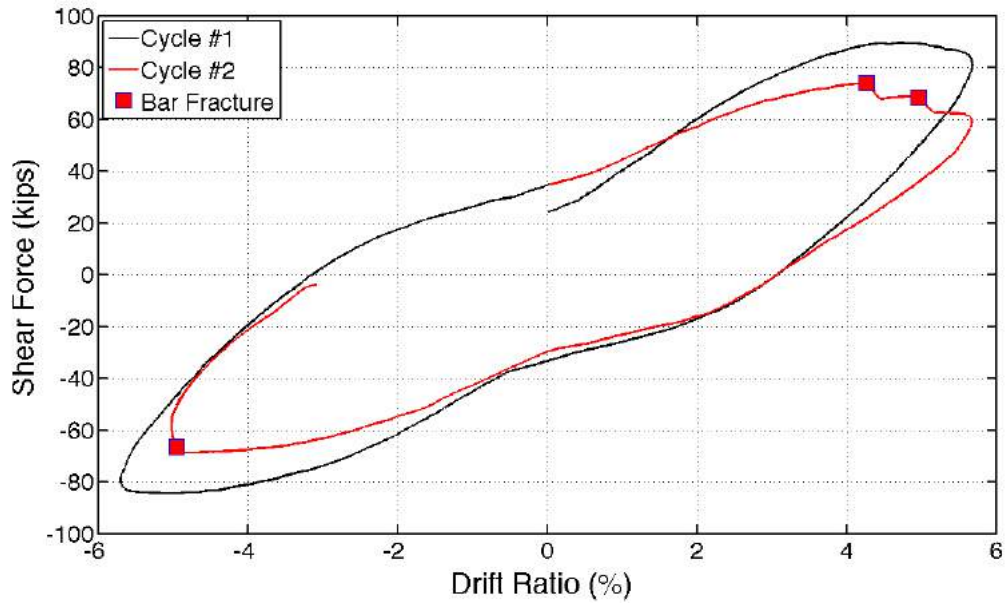


Figure 52: CM100 – last cycles response

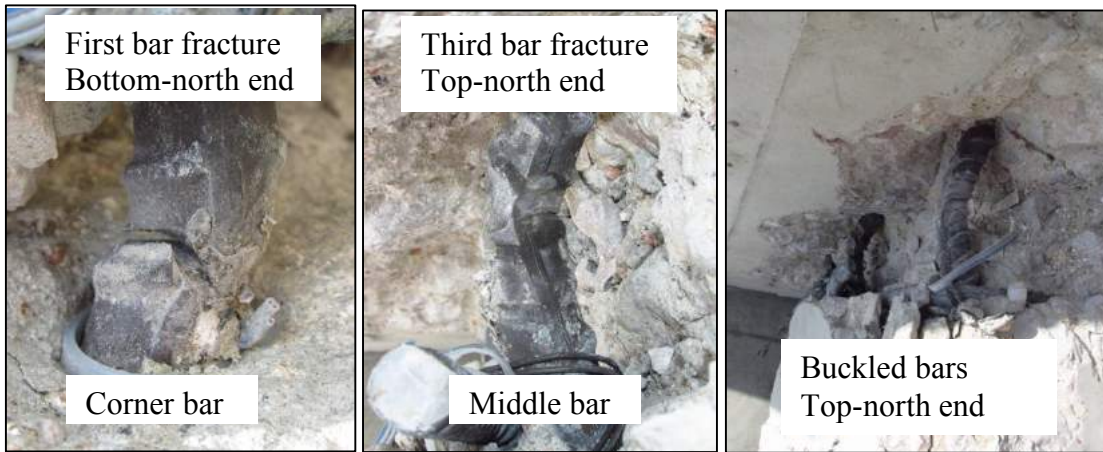


Figure 53: CM100 – pictures of fractured and buckled bars at the end of the test

4.4.2 Deformation Components

Flexural deformations contributed most to the column lateral drift throughout the test (Table 15; Figure 54). At higher drifts, the relative weight of flexural deformations lowered as the bar-slip component increased from about 25% of the total drift at low drift levels, to about 30% in the post-yield cycles. Possibly, debonding of the longitudinal reinforcement from the surrounding concrete at larger levels of concrete damage resulted in this observed increase in recorded bar-slip contribution. This debonding of longitudinal bars due to concrete damage could have decoupled the bar deformations from measured concrete surface movements, from which bar-slip deformations were extracted. Shear deformations increased in absolute value, but remained relatively low at around 7% of total drift throughout the test. The shear deformations were higher for specimen CM100, as compared to other specimens reinforced with grade 100. The higher shear deformations are attributed to the higher sectional strength due to the high yield strength of the #6 bars used in this specimen. Results for deformation components were not reliable after cycles to a drift ratio of 4.0%.

Table 15: CM100 - deformation components as percentage of total

Total	Flexure	Bar-slip	Shear
0.2%	72.6%	24.4%	3.9%
0.3%	72.4%	23.6%	4.0%
0.4%	71.4%	23.6%	5.0%
0.6%	69.4%	25.6%	5.1%
0.8%	67.0%	26.8%	6.2%
1.0%	65.9%	27.2%	6.9%
1.5%	63.6%	29.0%	7.5%
2.0%	62.4%	30.5%	7.2%
3.0%	63.2%	29.9%	6.9%
4.0%	60.7%	33.0%	6.2%

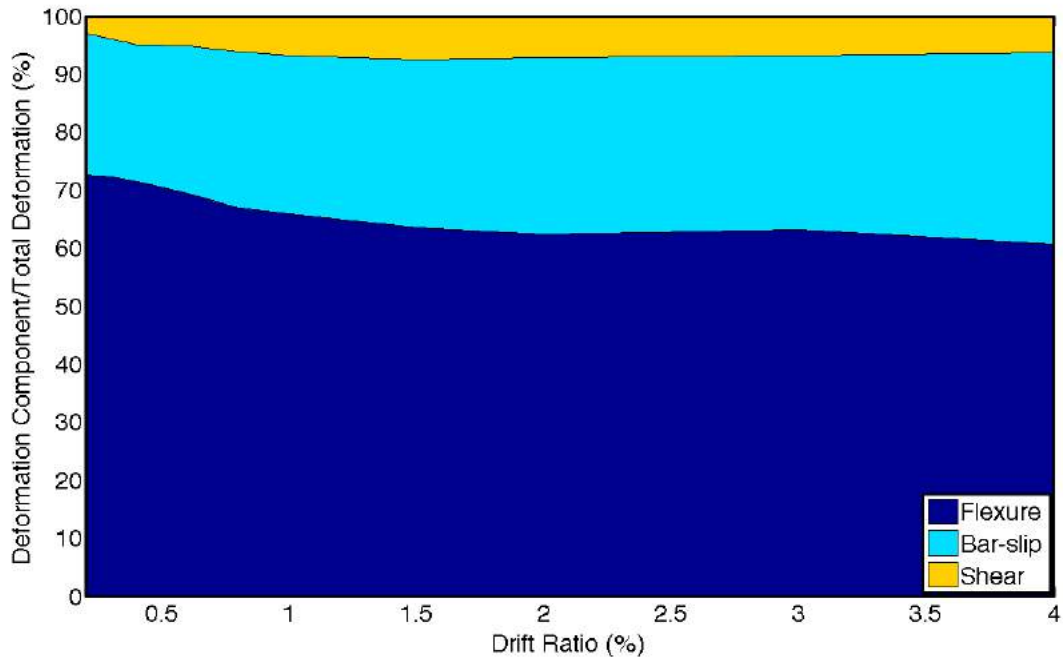


Figure 54: CM100 – deformation components

4.4.3 Strain History

Maximum strain demands were recorded at the interfaces between the column and footings. Figure 55 shows a typical strain versus lateral load response recorded on longitudinal bars at column ends. Figure 56 plots longitudinal bar tension strains at the end of each positive drift cycle target, measured at the top and bottom column interfaces with footings. The #6 bars used as longitudinal reinforcement in CM100 had a yield strain of 0.0063 as obtained from material testing. This strain was first reached at a drift ratio of 1.5% (Figure 55; Figure 56). After reaching a yield strain as computed with the 0.2% offset rule, the strain demands increased without significant increase in the lateral load. In general, strain demands on longitudinal bars were not much higher in the second cycle to the same drift target, and started to get noticed only at a drift ratio of 4.0%. This difference was however relatively small, and on the order of 5% of the strain value.

Three of the strain gauges showed in Figure 56 stopped recording right before the column was pushed to the first cycle to a drift ratio of 5.5%. The strain value at 5.5% drift ratio presented below was linearly interpolated.

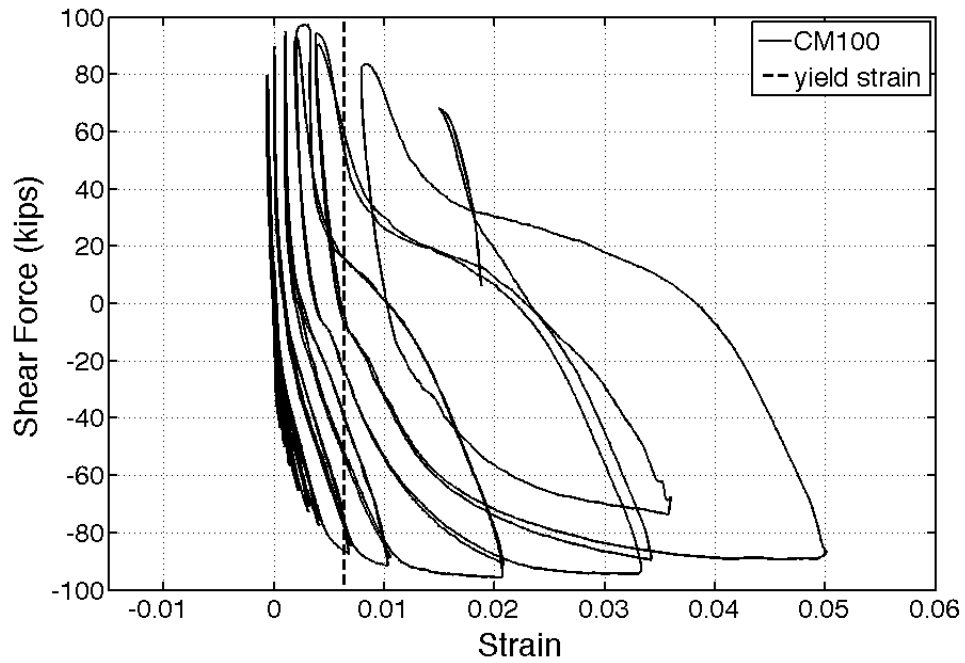


Figure 55: CM100 – strain gauge L4SW (top south-western corner) recording at the interface between the column and top footing

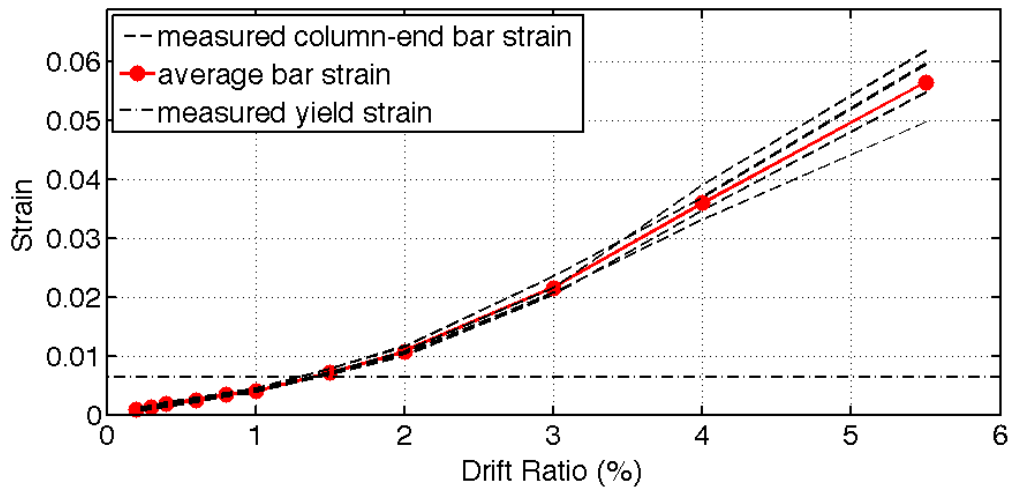


Figure 56: CM100 – column-end bar strain gauge recordings at each drift target and calculated average

4.4.4 Strain Profile

Strain readings over the height of north-eastern longitudinal bar are given in Figure 57. As it can be seen in Figure 57, as the column was pushed past the first yield to higher drift targets, the yielded length of the bar went up to 20 inches from the base of the column, as compared to 23 inches in specimen CH100. The strain demands between the first cycle to 4.0% drift and first cycle to 5.5% drift ratio were less than 3% (Figure 57).

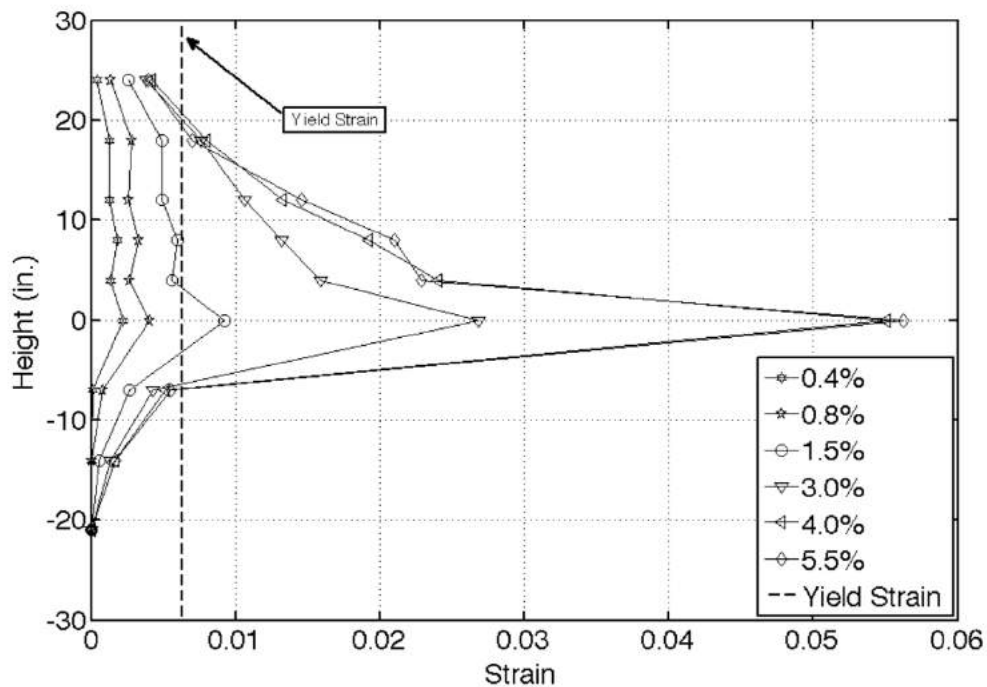


Figure 57: CM100 – longitudinal reinforcement strain demands over height at drift targets

Data from the GVIS was used to monitor the widths of the major flexural cracks at first yield were monitored. These cracks were identified as having a width of 0.008 inches or larger at first yield. Considering that ACI-318-14 intends to limit crack widths to 0.016 inches during service loading, half of this value was used conservatively as a threshold at first yield for cracks of concern. Cracks within nine quadrilateral target elements were identified as satisfying the above- mentioned criteria, for each drift direction; four at the bottom half of the member, and five in the upper part (Figure 50). Eight cracks formed when the column was pushed to a negative drift (column being pushed north, i.e. left in the pictures), four in each end of the member. During the first half cycle to a positive drift (column being pushed south, i.e. right in the pictures), flexural crack widths were measured in the bottom-south and top-north sides of the member. The average of these cracks is plotted in Figure 58 and identified as occurring during “Half Cycle 1”. The same procedure was followed for other positive and negative drift half cycles for each drift target. At 0.8% drift ratio, the average of all cracks was 0.015 inches, as compared to 0.012 inches in CH100 and 0.014 inches in CL100. The slightly larger measured width in CM100 is attributed to one of the cracks which contributed to the increased average crack width in one direction. This crack could have been considered an outlier, but no physical evidence was found to support such a determination. No significant difference in crack width was noticed between the successive half cycles in which the column was being pushed in the same direction. Figure 59 plots the width of one of the largest cracks as measured throughout the test. The width of this crack measured at one of the outermost strain-elements of the column, was 0.15 inches by the end of the first cycle to a drift ratio of 5.5%.

The largest crack-widths in CH100 and CL100 were measured one strain-element in from the column surface and were in the same range (i.e. 0.15 inches).

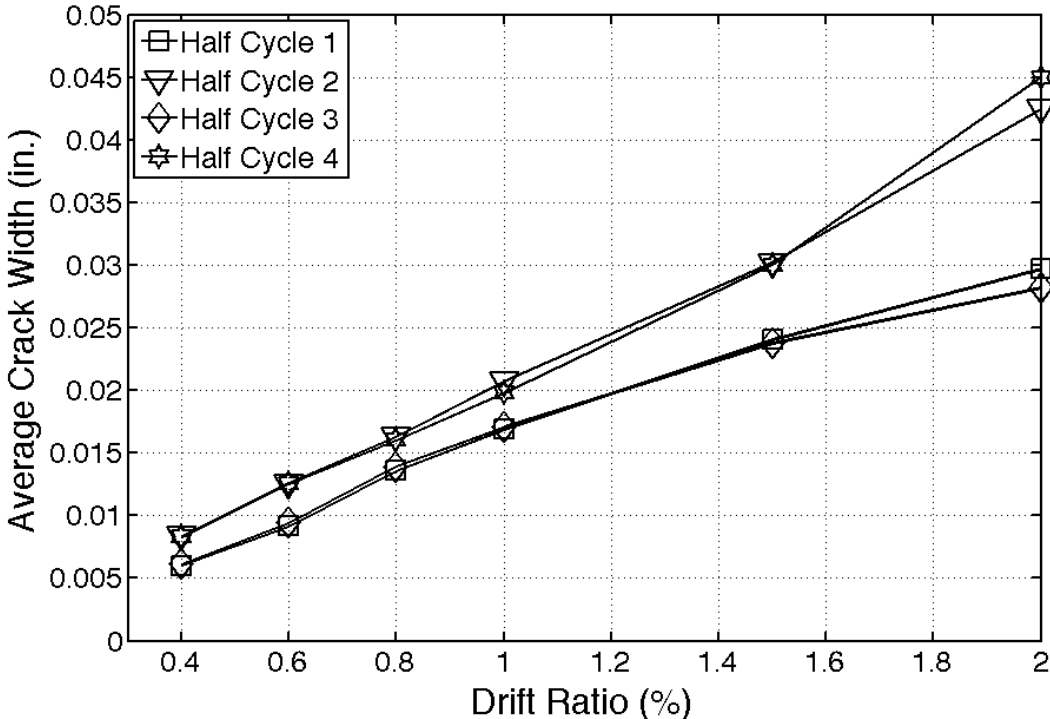


Figure 58: CM100 - average values of largest flexural crack widths at drift targets

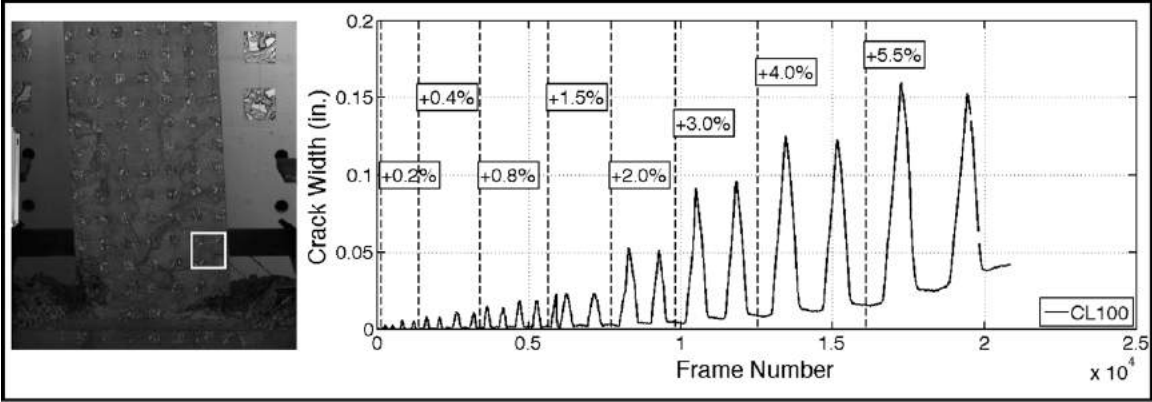


Figure 59: CM100 – width of one of the two largest flexural cracks

4.4.5 Buckling History

Buckling of the longitudinal reinforcement in CM100 was identified through the images taken at the end of each loading half-cycle. Buckling of the first longitudinal bars was observed at the first cycle to a drift ratio of -5.5% (Figure 60). At this point, the moment strength of the member had dropped by 14% as compared to the peak applied moment at the base. As the column was pushed back to a drift ratio of +5.5%, significant buckling took place, which led to the lateral strength of the member having decreased from peak by 29% at the onset of the first bar fracture. Contrary to other columns tested in this study, bends in the crossties in CM100 did not open up and buckling in the longitudinal bars was limited prior to their fracture.

The rotation of the row of targets located 9 inches over the base, or the 4th target row from the end of the column is plotted in Figure 61. The location of this row of targets corresponds to the first row of targets above the observed buckling location. The rotation at this location seems to not have captured the progression of buckling as most of the rotation in either direction was concentrated over this height.

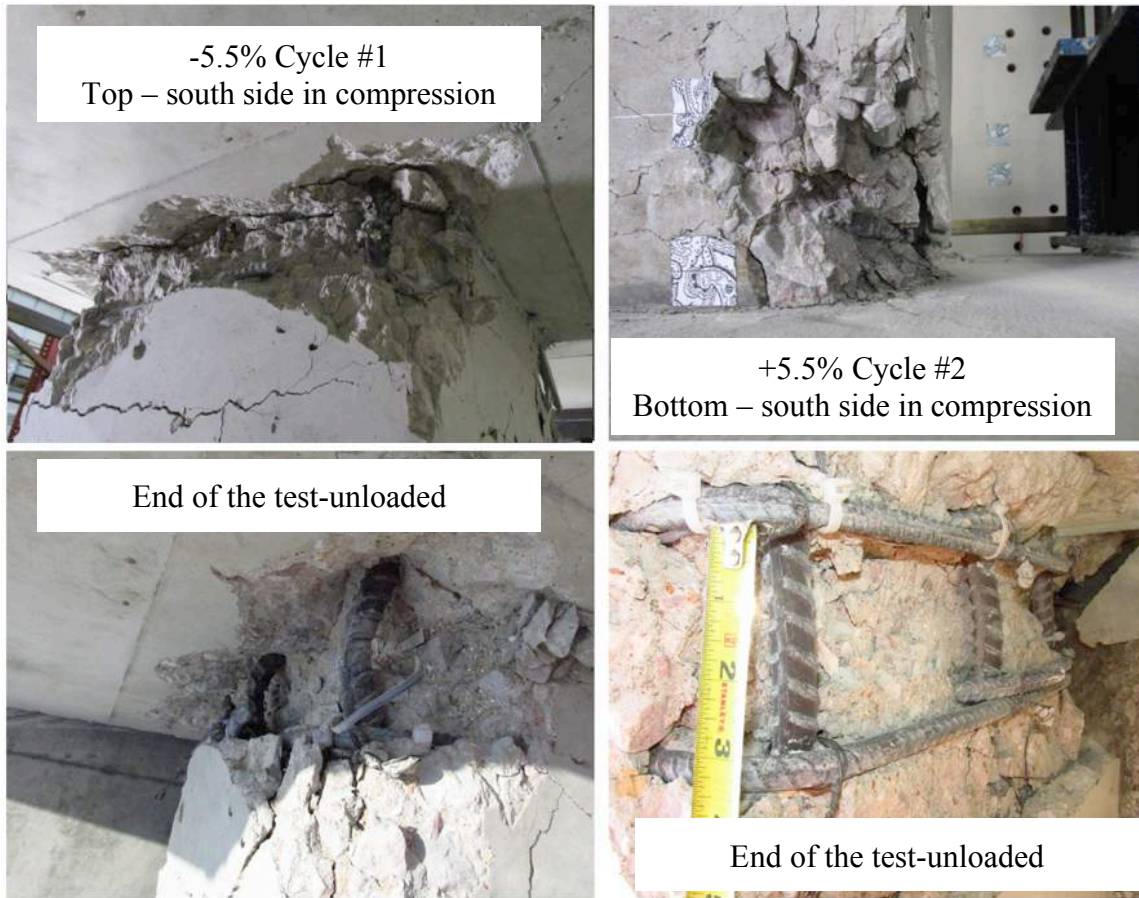


Figure 60: CM100 –longitudinal bar buckling

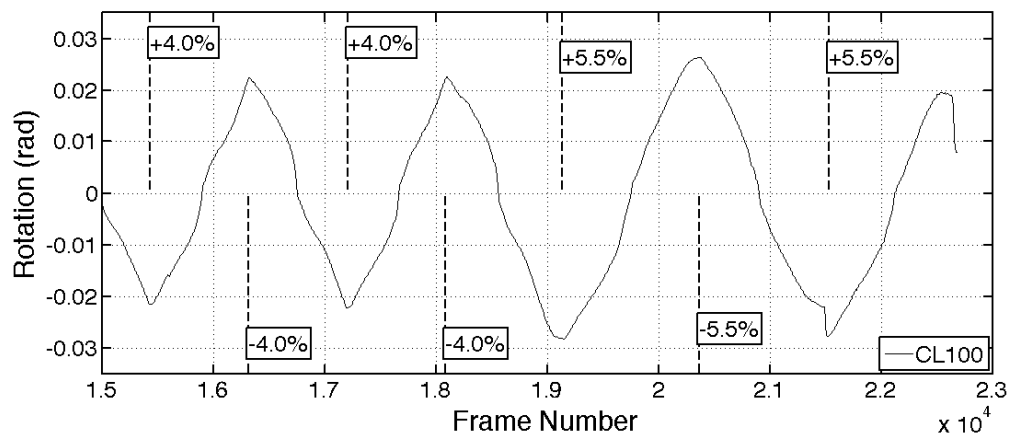


Figure 61: CM100 – rotation at a distance 9 inches from the base

4.4.6 Energy Dissipation

The dissipated energy, defined as the area under the average top and bottom moment versus lateral drift relation, is plotted in Figure 63 for each cycle. The average top and bottom moment was used to compute the dissipated energy as moment strength is more representative of column sectional strength, as opposed to lateral-load strength that is influenced by second order deformation effects. Prior to first yielding (drift ratio targets up to 0.8%) the amount of dissipated energy was similar between the two cycles at each target drift. As the column was pushed to higher drifts and damage accumulated, the difference in energy dissipation between the cycles increased. The difference between two consecutive post-yield cycles to the same drift ratio was in the range of 20 to 40%. The difference in cumulative dissipated energy between cycles at the end of the 4% drift ratio cycles was 22.4%.

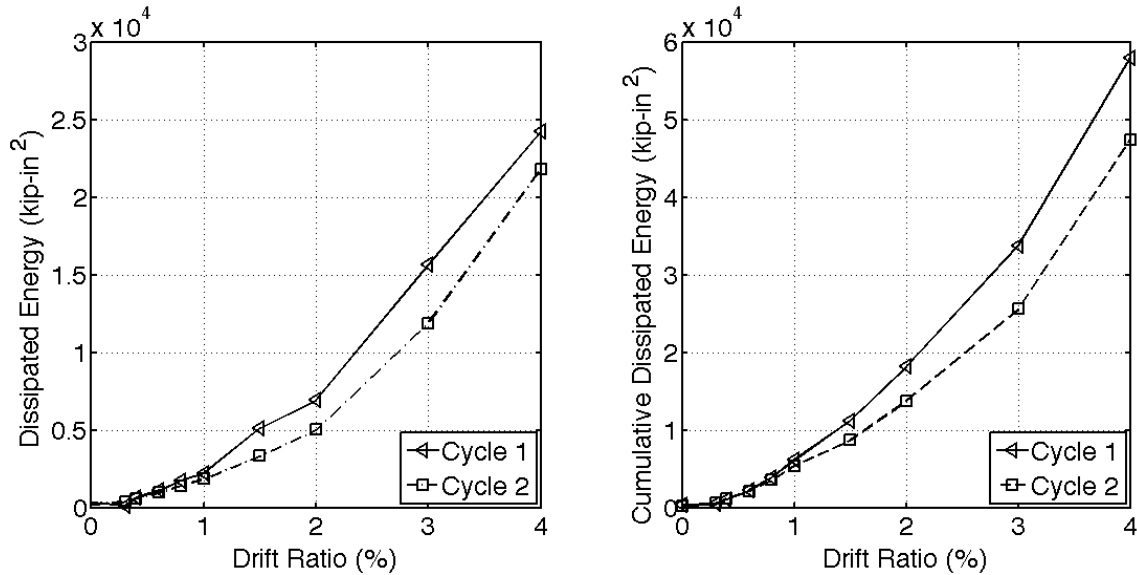


Figure 62: CM100 – dissipated energy at drift targets for each cycle

4.5 TEST RESULTS FOR CH60

Results for column CH60 are reported in this section. Specimen CH60 was reinforced with grade 60 ASTM A706 longitudinal and transverse bars with a high (H) T/Y ratio of 1.45. This specimen was designed as the benchmark for satisfactory behavior. As for all specimens, CH60 was tested under displacement-controlled quasi-static cyclic lateral loading. The recorded lateral displacement history is shown in Figure 63. An axial load of 242 kips was applied by the vertical actuators which together with the 10-kips self-weight of the top footing and testing frame resulted in an effective axial load of $15.2\% A_g f'_c$. The load was kept nearly constant throughout the test as shown in Figure 64.

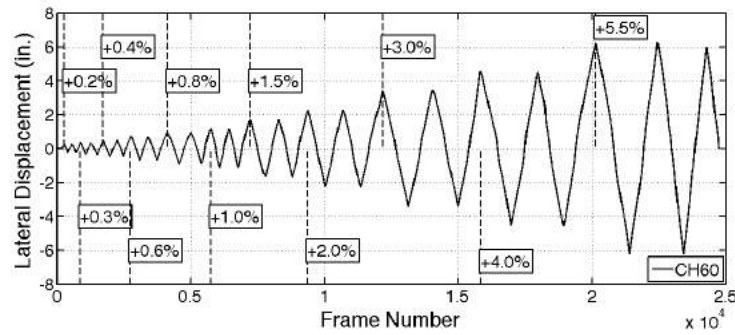


Figure 63: CH60 – measured lateral displacement at every captured frame

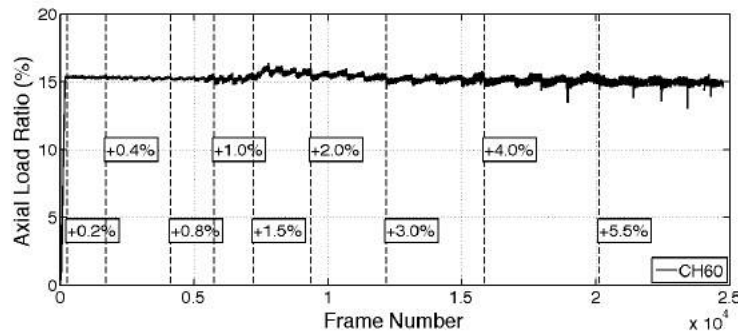


Figure 64: CH60 – applied axial load ratio at every captured frame

4.5.1 General Behavior

Prior to testing, no cracks were noticed on the specimen surface. The recorded lateral force versus drift ratio response of specimen CH60 is plotted in Figure 65. Table 16 summarizes the lateral force and drift values for all milestones for column CH60. The first flexural cracks were visible at the end of the first cycle to a drift ratio of +0.2% (Figure 65). These cracks corresponded to surface principal strains at the order of 0.002 (Figure 66). The initial flexural cracks propagated closer to the centerline of the column leading to the formation of first inclined cracks at the end of the first half-cycle to a drift ratio of +0.6% (Figure 66).

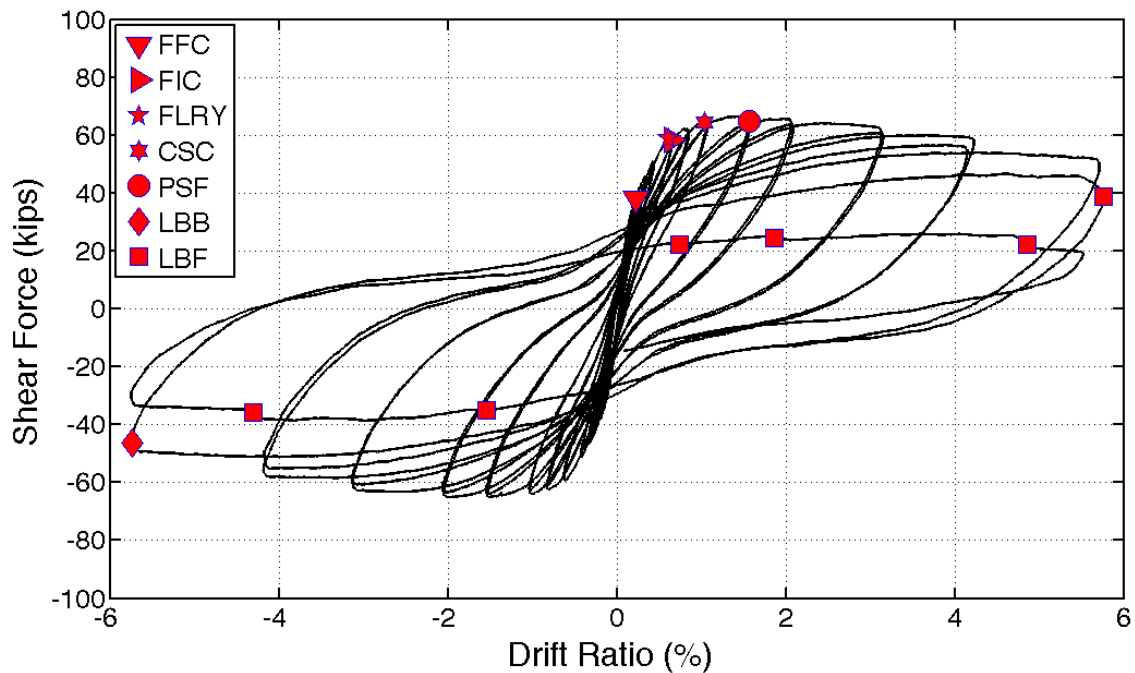


Figure 65: CH60 – lateral response

Table 16: CH60 - behavioral milestones

Milestone	Drift Ratio (%)	Lateral Load (kips)
First Flexural Crack	+0.2	+37.9
First Inclined Crack	+0.6	+58.9
First Long. Reinf. Yield	+0.6	+56.3
Cover Splitting Crack	+1.0	+63.7
Peak Shear Force	+1.5	+64.0
Long. Bar Buckling	-5.5	-46.3
Long. Bar Fracture	+5.5	+38.6

First yield in the longitudinal reinforcement was identified from strain gauge readings at the end of the first cycle to a drift ratio of +0.6%. As the column was pushed to the first cycle towards a drift ratio of +1.0%, the initial flexural cracks opened wider and additional cracks formed closer to the column mid-height (Figure 66). The maximum applied shear-force of 64.6 kips was recorded at the end of first cycle to a drift ratio of +1.5%. Beyond that drift cycle, the lateral load diminished slightly, driven by second order axial load effects and the accumulation of damage such as concrete spalling. Top and base moments versus lateral drift ratio are plotted in Figure 67. As can be seen in the figure, peak moment strength occurred at a drift ratio of 1.5%. Gradual degradation of moment strength occurred beyond that drift due to accumulation of damage in concrete. During the first cycle to a drift ratio of -5.5%, initiation of longitudinal bar buckling was observed and was associated with a gradual loss in the moment capacity during that half cycle (Figure 67).

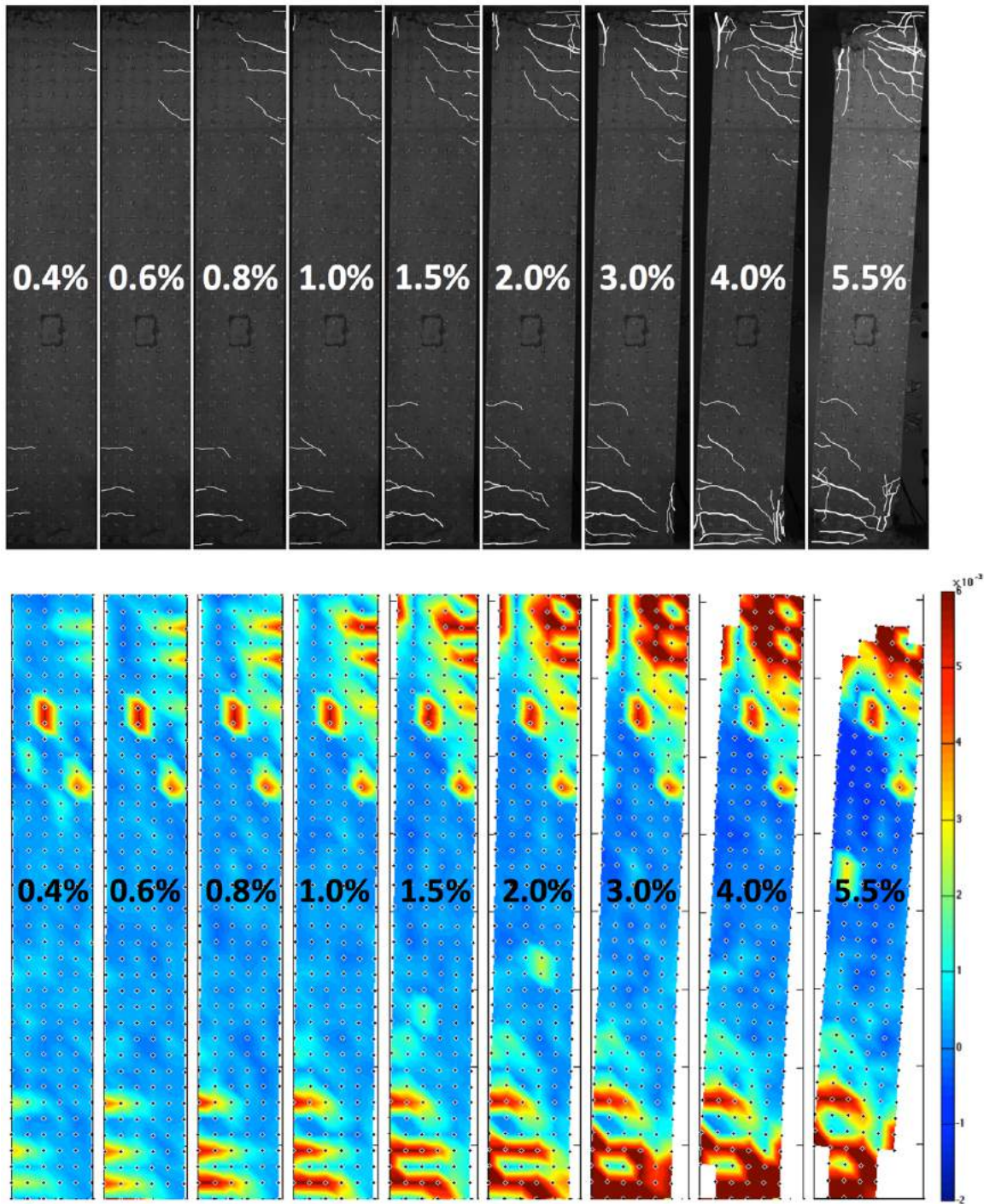


Figure 66: CH60 - cracking pattern (up) and measured principal strains (down) at drift targets

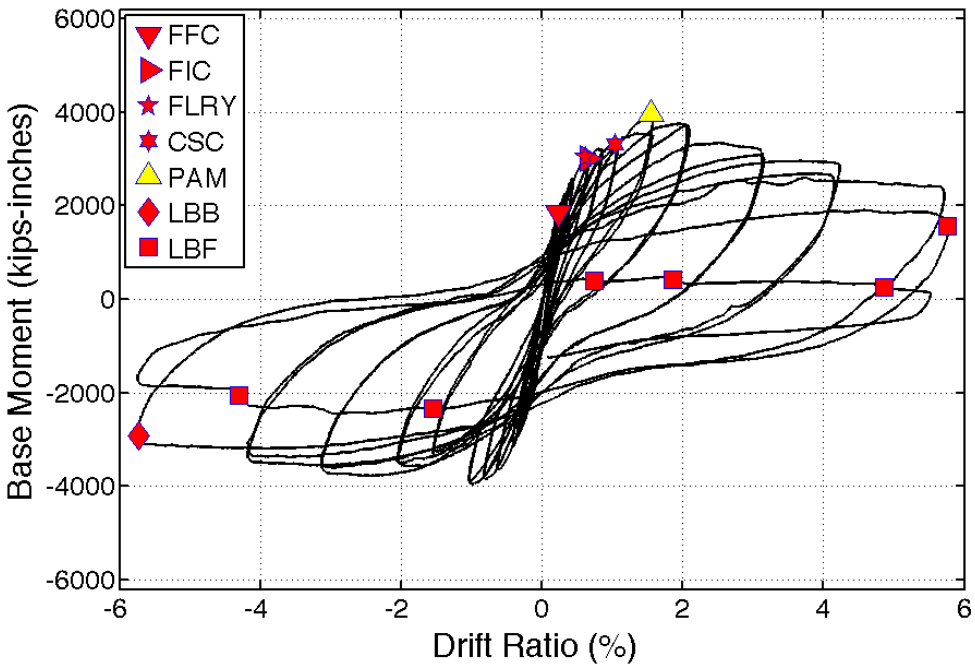
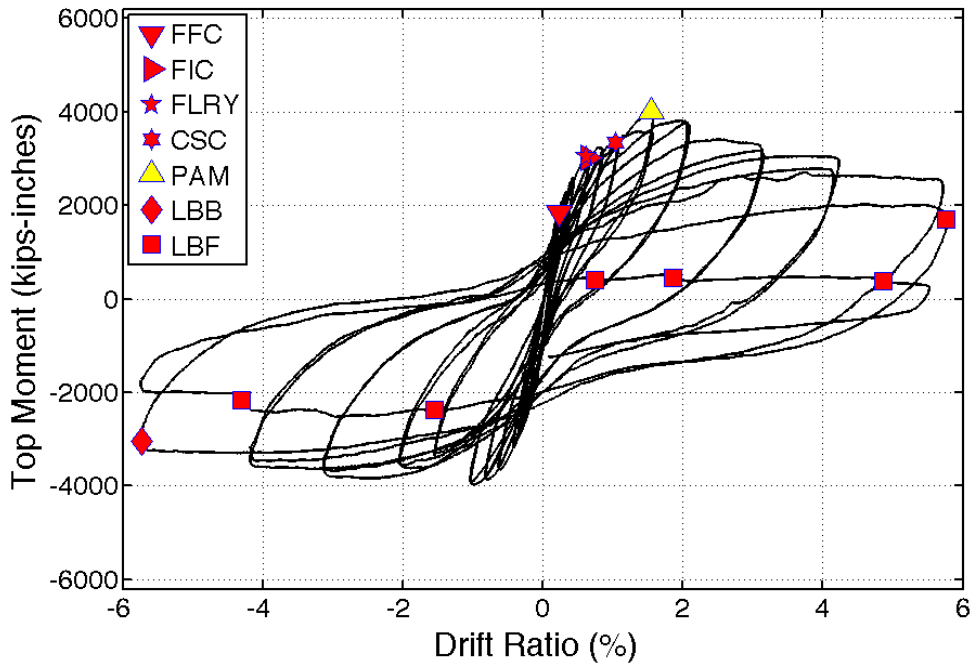


Figure 67: CH60 - base and top moment vs. drift ratio

As the column was pushed to drift ratios of 3.0%, 4.0%, and 5.5%, increasing crushing and spalling of the concrete cover was observed. The rotation in the plastic hinge region concentrated in four main flexural cracks, two in each column-end. These cracks were 11.5 inches from the ends of the specimen and reached 0.15 in. by the end of the first cycle to a drift ratio of 5.5%. At the same drift ratio, vertical cracks at the location of the longitudinal reinforcement propagated 22 in. from column ends, indicating de-bonding between the longitudinal bars and the surrounding concrete. These cracks initiated a drift ratio of 1.5%, which corresponded to a curbing of the rate of increase in longitudinal bars strains with increasing drift ratios. This behavior is discussed in more details in Section 4.5.3.

The lateral load resistance of the column remained stable and the column maintained axial load capacity past the first cycle to a drift ratio of +5.5% (Figure 68). During the second cycle to a drift ratio of +5.5%, the column experienced an 18% loss in peak moment resistance strength as compared to the previous half-cycle, due to significant buckling of longitudinal bars. By then, the cover concrete in the top and bottom plastic hinge regions had spalled to a distance of about 11.5 in. from column ends. As a result, on its way to completing two 5.5% drift cycles, one of the longitudinal bars fractured at the base of the column at a drift ratio of 3.6% (Figure 68; Figure 69). Just prior to first bar fracture, the column had lost more than 50% of its measured peak lateral moment resistance. The first bar fracture contributed to additional loss in lateral strength. The column was able to carry the prescribed axial load throughout the test without showing signs of significant axial deformation even after longitudinal reinforcement fracture. It is noteworthy that the middle bar fractured first. This bar was restrained by the 90-degree bend of a cross-tie, which had opened up significantly allowing the bar to buckle (Figure 69).

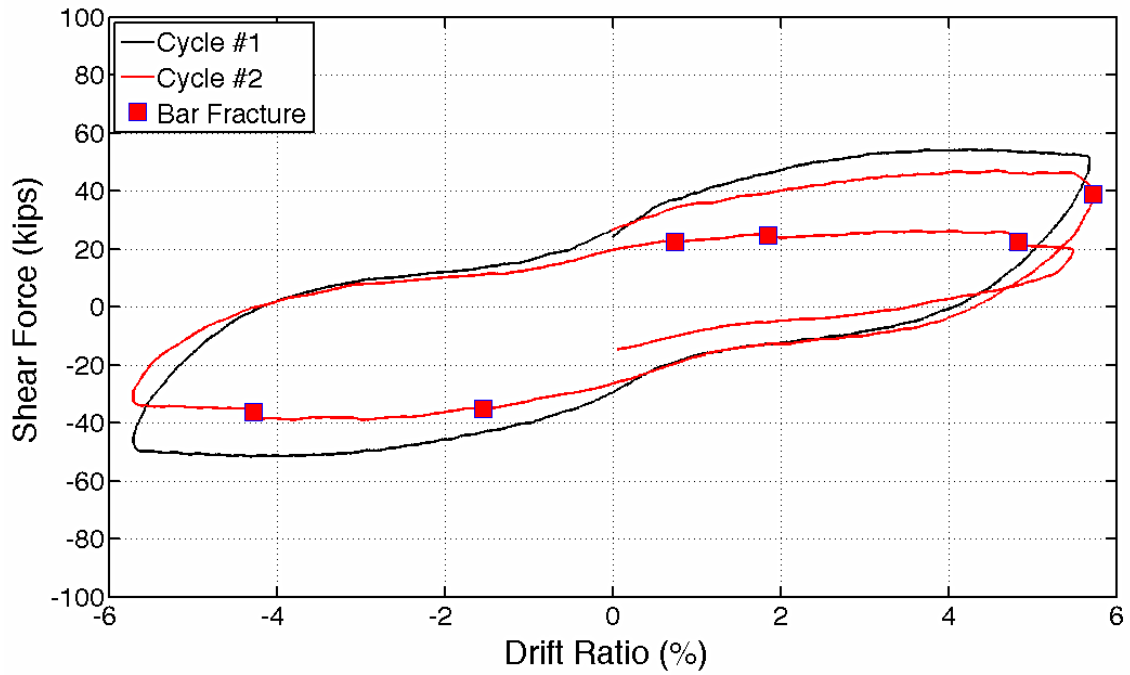


Figure 68: CH60 – last cycles response

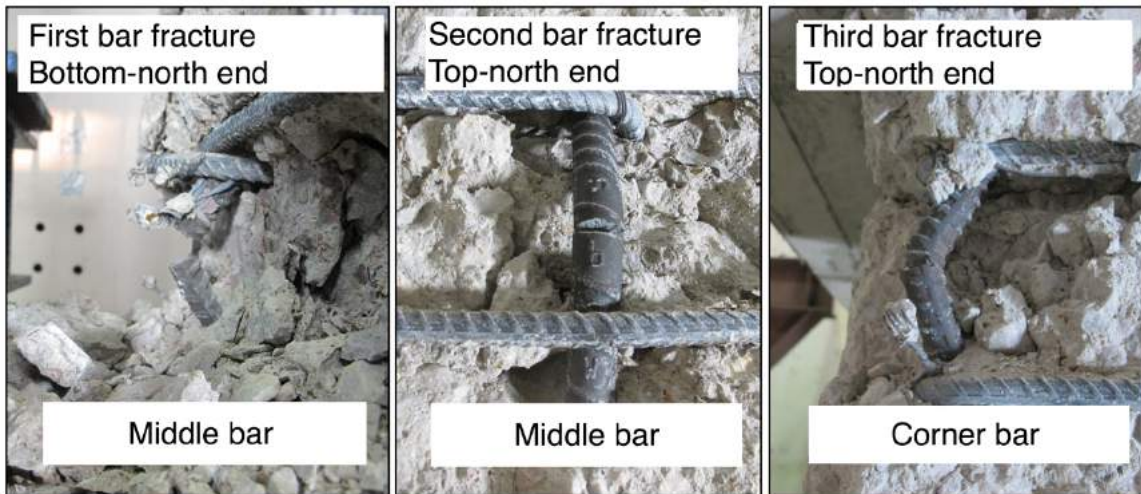


Figure 69: CH60 – picture of fractured and buckled bars

4.5.2 Deformation Components

Flexural deformations contributed most to the column lateral drift throughout the test (Table 17; Figure 70). At higher drifts, the relative weight of flexural deformations lowered as the bar-slip component increased from about 25% of the total drift at low drift levels, to about 35% in the post-yield cycles. Possibly, debonding of the longitudinal reinforcement from the surrounding concrete at larger levels of concrete damage resulted in this observed increase in recorded bar-slip contribution. This debonding of longitudinal bars due to concrete damage could have decoupled the bar deformations from measured concrete surface movements, from which bar-slip deformations were extracted. Shear deformations increased in absolute value, but remained relatively low at around 4% of total drift throughout the test. The low amount of shear deformations was due to the applied shear stresses being relatively low. Results for deformation components were not reliable after cycles to a drift ratio of 4.0%.

Table 17: CH60 - deformation components as percentage of total

Total	Flexure	Bar-slip	Shear
0.2%	72.8%	24.1%	3.1%
0.3%	72.2%	23.9%	3.8%
0.4%	71.4%	24.9%	3.7%
0.6%	65.2%	30.4%	4.4%
0.8%	60.4%	35.1%	4.5%
1.0%	59.7%	35.9%	4.4%
1.5%	60.7%	34.8%	4.5%
2.0%	62.1%	33.4%	4.5%
3.0%	63.2%	32.1%	4.6%
4.0%	63.2%	33.4%	4.3%

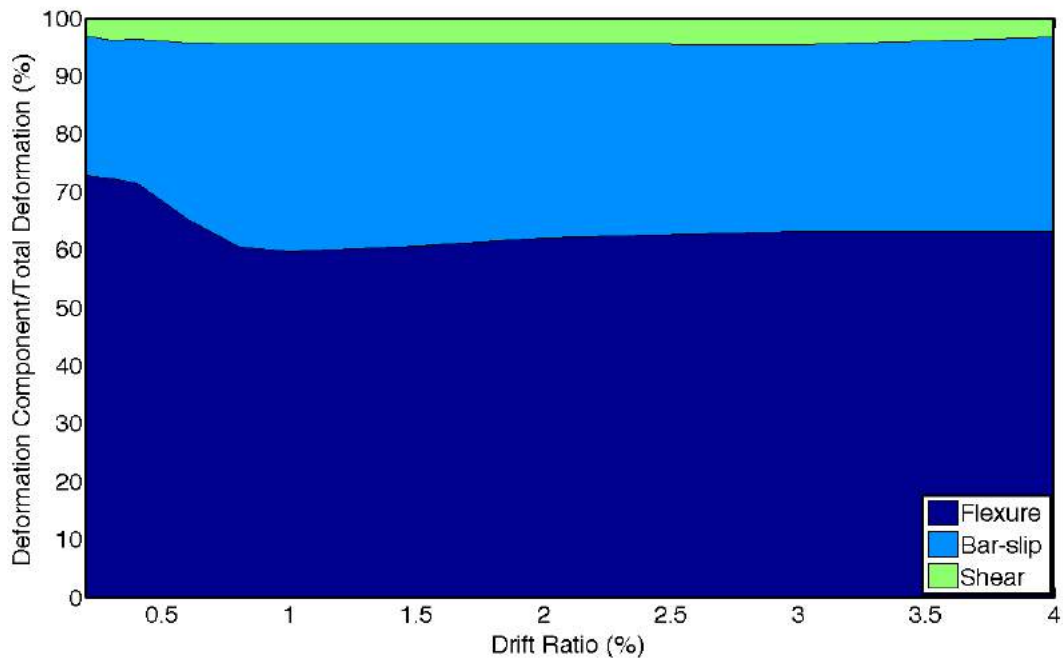


Figure 70: CH60 – deformation components

4.5.3 Strain History

Maximum strain demands were recorded at the interfaces between the column and footings. Figure 71 shows a typical strain versus lateral load response recorded on longitudinal bars at column ends. Figure 72 plots longitudinal bar tension strains at the end of each positive drift cycle target, measured at the top and bottom column interfaces with footings. The #6 bars used as longitudinal reinforcement in CH100 had a yield strain of 0.0024 as obtained from material testing. This strain was first reached at a drift ratio of 0.4% (Figure 72). However, the drift ratio of 0.6% was reported as the first yield, as an average between the available strain gauge recordings. After yield, the strain demands increased without significant increase in the lateral load. In general, strain demands on longitudinal bars were higher in the second cycle to the same drift target, with the difference increasing at higher drifts. This difference was however relatively small, and on the order of 5% of the strain value.

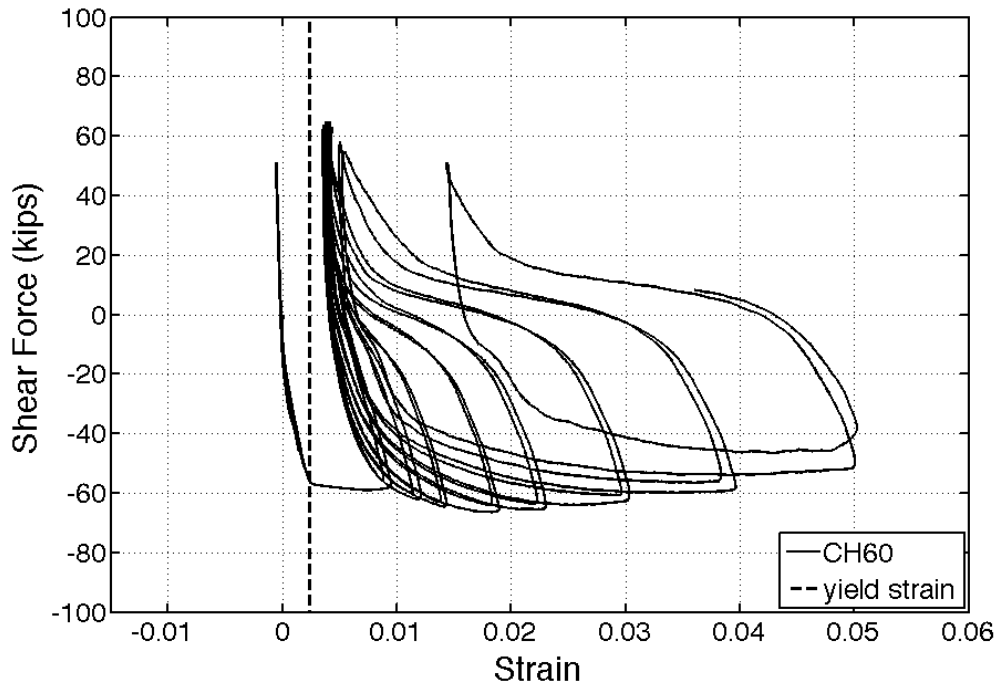


Figure 71: CH60 – strain gauge L4NW (bottom north-western corner) recording at the interface between the column and top footing

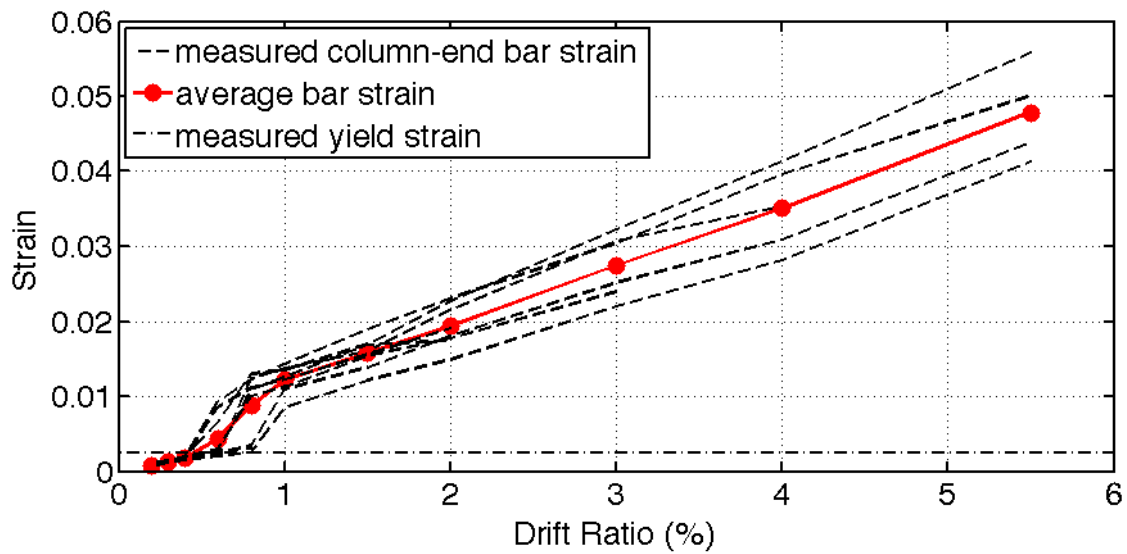


Figure 72: CH60 –column-end bar strain gauge recordings and calculated average

4.5.4 Strain Profile

Strain readings over the height of south-western longitudinal bar are given in Figure 73. As the column was pushed past the first yield to higher drift targets, the yielded length of the bar went up to 12 inches from the base of the column, as compared to 23 inches in specimen CH100.

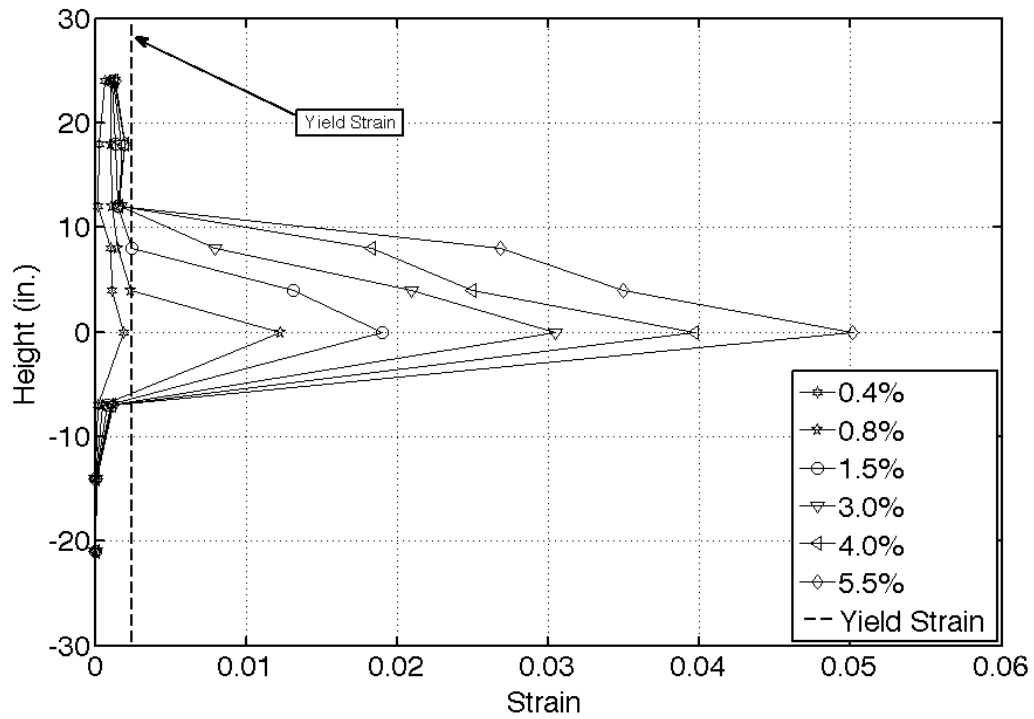


Figure 73: CH60 – longitudinal reinforcement strain demands over height at drift targets

4.5.5 Crack Widths

Data from the GVIS was used to monitor the widths of the major flexural cracks at first yield were monitored. These cracks were identified as having a width of 0.008 inches or larger at first yield. Considering that ACI 318-14 intends to limit crack widths to 0.016 inches during service loading, half of this value was used conservatively as a threshold at first yield for cracks of concern. Cracks within seven quadrilateral target elements were identified as satisfying the above- mentioned criteria, for each drift direction; three at the bottom half of the member, and four in the upper part (Figure 66). The number of cracks was the same for both directions of loading. During the first half cycle to a positive drift (column being pushed south, i.e. right in the pictures), flexural crack widths were measured in the bottom-south and top-north side of the member. Strain readings between the second elements in from the column vertical surfaces were used to calculate the reported cracks width values. This was done as the outermost targets in the plastic-hinge region were lost at high demands due to cover crushing. The average of these cracks is plotted in Figure 74 and identified as cracks occurring “Half Cycle 1”. The same procedure was followed for other positive and negative drift half cycles for each drift target. At first yield, at a drift ratio of 0.6%, the average of all cracks was 0.012 inches. These cracks opened wider as the member was pushed passed yield. At a drift ratio of 0.8% the average of these cracks was 0.015 inches which is similar to the average of the cracks measured in other columns at the same drift ratio. No significant difference in crack width was noticed between the successive half cycles in which the column was being pushed in the same direction. These critical cracks were all located within 16 inches from the ends of the member. As the column was pushed to higher drifts (past 1.0% drift ratio) two large flexural cracks formed at each end of the member, 12 inches from its ends. Figure 75 plots the width of one of

these cracks as measured throughout the test. This crack reached a maximum width of 0.2 inches by the end of the first cycle to a drift ratio of 5.5%, as compared to 0.15 inches for the other columns.

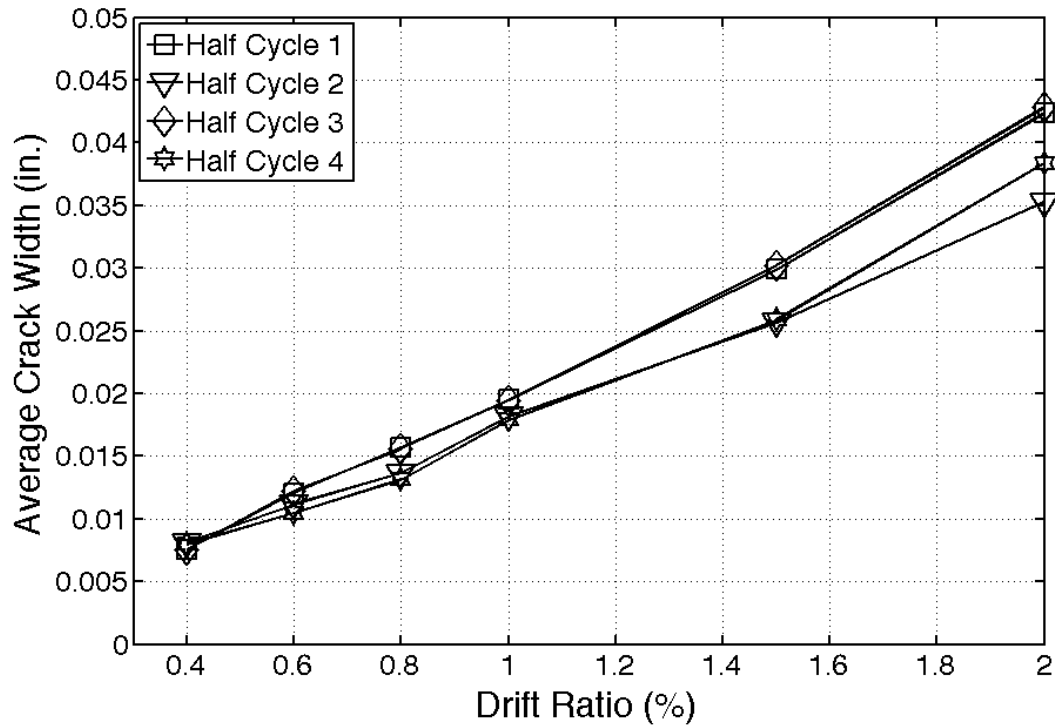


Figure 74: CH60 - average values of largest flexural crack widths at drift targets

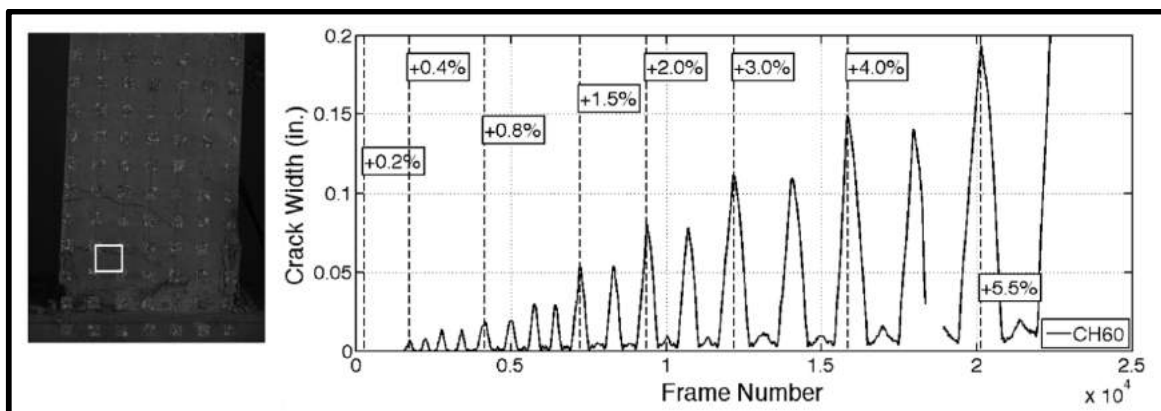


Figure 75: CH60 – width of one of the two largest flexural cracks

4.5.6 Buckling History

Buckling of the longitudinal reinforcement in CH60 was identified through the rotation measured from a row of targets at a distance of 9 inches from the ends of the column (Figure 76). These target rows were selected as they corresponded to the end location of the buckled bars. The rotation increased progressively with the increase in lateral drift ratio, indicating an increase in the concentration of rotations at column ends. No difference in rotation was noticed in consecutive cycles to the same drift ratio until after the member completed two full cycles to a drift ratio of 4.0%. An increase in curvature demand was recorded at the first cycle to a drift ratio of +5.5%, as compared to the cycles to 4.0% drift ratio. This was due to the increase in deformation demand, as well as slight buckling, as observed in Figure 77. The moment resistance was 22% lower at this point, as compared to the peak measured moment resistance. More significant buckling was observed in the following cycles (Figure 76; Figure 77). The first bar fracture was noted at the second cycle at a drift ratio of +5.5%. At the onset of the first bar fracture, moment resistance was 33% lower than the peak measured moment resistance.

Transverse reinforcement in column CH60 was spaced at 6 longitudinal bar diameters on center, as compared to 4.7 bar diameters in columns reinforced with grade 100 bars, which may explain why buckling initiated at a lower drift demands in CH60 than in members reinforced with grade 100 steel. Also, the damage in the cover concrete, which lead to the softening of the response was higher in CH60 as compared to other tested specimens.

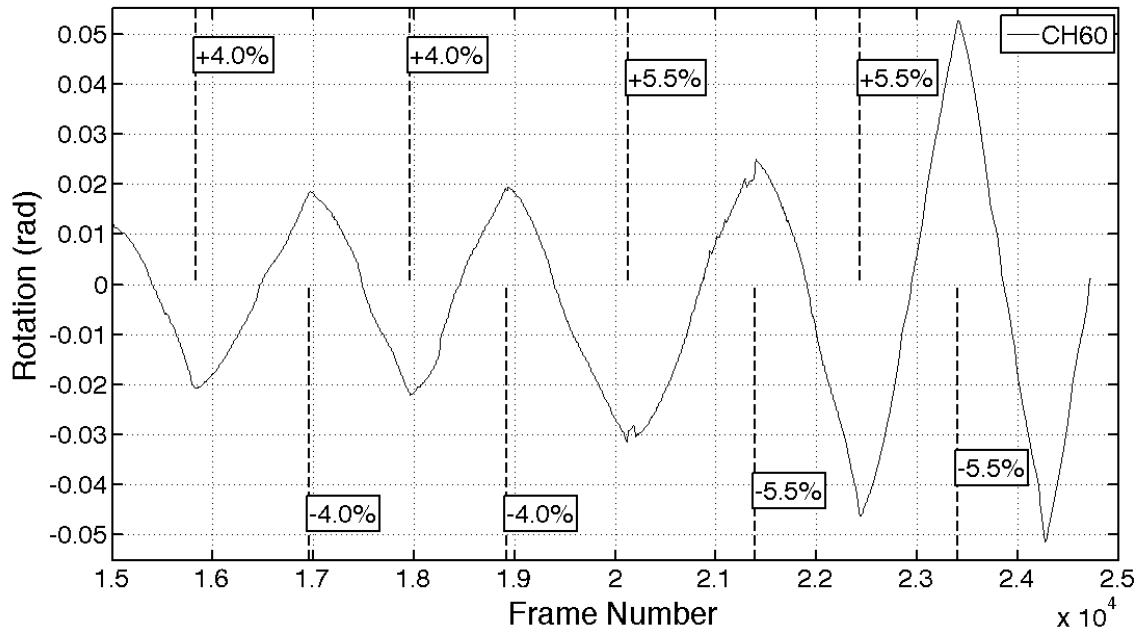


Figure 76: CH60 – rotation at a distance 9 inches from the base

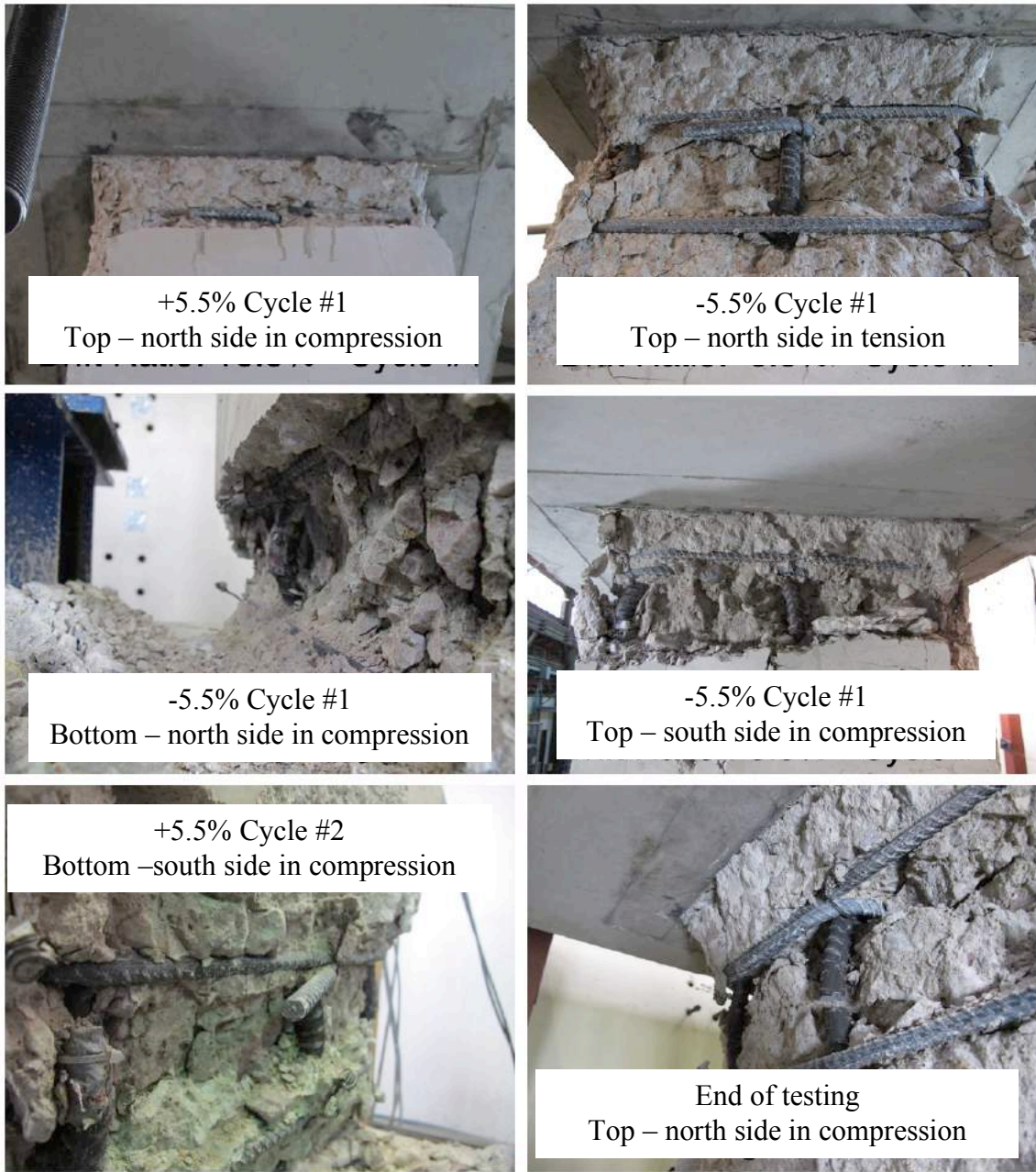


Figure 77: CH60 –longitudinal bar buckling

4.5.7 Energy Dissipation

The dissipated energy, defined as the area under the average top and bottom moment versus lateral drift relation, is plotted in Figure 78 for each cycle as moment strength is more representative of column sectional strength, as opposed to lateral-load strength that is influenced by second order deformation effects. The average top and bottom moment was used to compute the dissipated energy. Prior to first yielding (drift ratio targets up to 0.8%) the amount of dissipated energy was similar between the two cycles at each target drift. As the column was pushed to higher drifts and damage accumulated, the difference in energy dissipation between the cycles increased. The difference between two consecutive post-yield cycles to the same drift ratio was in the range of 3 to 20%. The difference in cumulative dissipated energy between cycles at the end of the 4% drift ratio cycles was 8.3%.

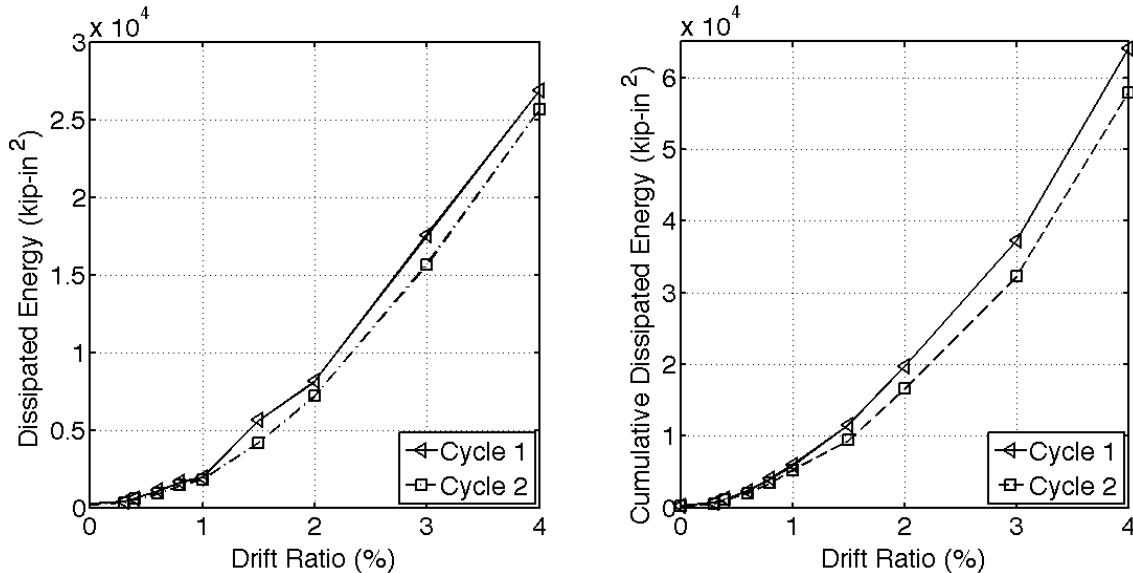


Figure 78: CH60 – dissipated energy at drift targets for each cycle

5. Discussion on Experimental Results

This chapter provides a comparative discussion between the recorded behaviors of the column specimens in light of the differences in the mechanical properties of the reinforcing steel bars (i.e., grade of reinforcement, shape of stress/strain curve, strain hardening, and steel ductility). The discussions focus on concerns related to the usage of grade 100 reinforcing bars in seismic designs. Recommendations about minimum mechanical properties for high-strength steel reinforcement to achieve acceptable seismic behavior in concrete columns are also discussed.

5.1 GENERAL BEHAVIOR

The different mechanical properties of the reinforcement in each column lead to members reaching major milestones at different drift ratios in many instances (Table 18). However, the major milestones were reached at similar drifts for columns CH100 and CL100, considering that the mechanical properties of the steel used in these specimens did not vary significantly. Longitudinal bars in both specimens yielded close to 100 ksi and had a distinct yield plateau. The major difference between the reinforcement used in these two members was the tensile-to-yield ratio (T/Y), which for the steel in CH100 was 1.27 and for the steel in CL100 was 1.16.

Table 18: Summary of behavioral milestones for all four specimens

	CH100		CL100		CM100		CH60	
	Drift Ratio (%)	Lateral Load (kips)	Drift Ratio (%)	Lateral Load (kips)	Drift Ratio (%)	Lateral Load (kips)	Drift Ratio (%)	Lateral Load (kips)
FFC [†]	+0.20	+40.2	+0.20	+38.2	0.20	+42.6	+0.20	+37.9
FIC	+0.61	+60.4	+0.61	+57.8	+0.60	+65.2	+0.61	+58.9
FLRY	+1.01	+69.2	+1.00	+78.4	+1.51	+87.5	+0.58	+56.3
CSC	+1.50	+72.8	+1.50	+79.4	+1.50	+87.5	+1.00	+63.7
PSF	-2.03	-81.9	-2.01	-80.8	-2.93	-97.5	+1.51	+64.0
LBB	+5.50	+64.3	+5.50	+64.0	-5.50	-80.6	-5.50	-46.3
FBF	-3.63	-55.6	+4.80	+58.6	+4.28	+74.1	+5.53	+40.0

[†] Abbreviations refer to the milestones in lateral response plots: FFC – First Flexural Crack; FLRY – First Longitudinal Reinforcement Yield; FIC – First Inclined Crack; CSC – Cover Splitting Crack; PSF – Peak Shear Force; LBB – Longitudinal Bar Buckling; FBF – First Bar Fracture

Figure 79 shows the measured response of these most directly comparable columns, CH100 and CL100. Filled markers correspond to milestones in CH100; hollow markers correspond to milestones in CL100. All the milestones occurred at nearly identical drifts in the two columns, besides the one corresponding to bar fracture and first longitudinal reinforcement yield, thus markers overlapped in Figure 79. First flexural and inclined cracking occurred at identical drift ratios for both columns, which can be expected as the measured concrete compressive strength was similar for both specimens (5.16 ksi for CL100 vs 5.21 ksi for CH100). The first yield occurred relatively early in the loading protocol for both specimens, since specimen design aimed to maximize the strain demands in the longitudinal reinforcement. First yield was recorded at the end of the first cycle to a drift ratio of +1.0% for both CH100 and CL100. Mechanical properties of the reinforcement did not dictate major differences between the overall lateral force versus lateral drift behaviors of the two specimens. The lower tensile to yield ratio of bars in column CL100 produced a slightly softer re-loading response in the inelastic range, but the column reached similar drift targets as CH100 before any bar fracture.

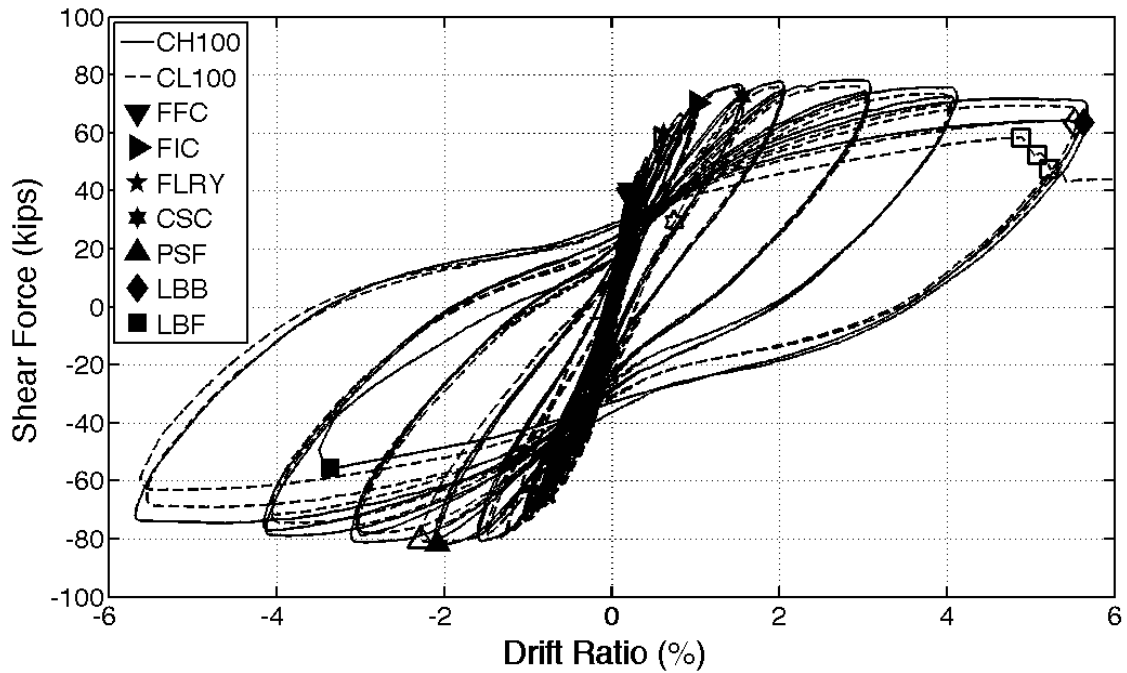


Figure 79: Lateral response of CH100 and CL100 with milestones (filled markers for CH100, hollow marker for CL100)

First yield in specimen CM100 was determined when the first longitudinal bar reached the assumed yield strain (0.63%), which was based on the 0.2% strain offset method for these bars that do not have a marked yield point. This led to CM100 having an apparent late first yield at a drift ratio of +1.5% (Table 18). In contrast to CM100, longitudinal reinforcement in CH60 yielded at a drift ratio of +0.6% (Table 18). First yield occurred earlier in the loading protocol of CH60 than in the specimens with grade 100 steel, due to the lower yield strain of the grade 60 bars (0.24%). The lower strength of the grade 60 #6 bars compared to the #6 grade 100 bars, also led to a lower lateral strength and lower applied shear stresses for CH60 than for columns reinforced with grade 100 bars.

As targeted shear stresses were relatively low in all columns, they only exhibited minor diagonal cracking (i.e., cracks having an inclination from horizontal greater than 25 degrees). The higher tensile strength of the steel used in CM100 contributed to higher shear stresses in the section. For this reason, specimen CM100 had longer inclined cracks which propagated further towards the centerline of the column than other columns. Transverse reinforcement did not yield in any of the specimens.

All specimens sustained a flexural mode of degradation characterized by concrete crushing, longitudinal bar buckling and eventually longitudinal bar fracture. Varying degrees of longitudinal bar buckling was observed in all specimens in the cycles prior to the one that resulted in the fracture of the first bar. Column CH60 reinforced with the conventional grade 60 bars and having hoops and cross-ties spaced at 6.0 longitudinal bar diameters ($6.0d_b$) sustained more significant bar buckling and earlier in the loading protocol (starting at first cycle to a drift ratio of +5.5%) compared with columns reinforced with grade 100 bars. Columns with grade 100 bars had hoops and cross-ties spaced at $4.7d_b$, which appears to have restrained the longitudinal reinforcement and confined the core concrete better than observed in CH60. CM100 showed the least sign of bar buckling and the buckling was observed to take place only in the last half cycle prior to first bar fracture. The lateral buckling amplitudes of bars in CM100 were also much smaller than those in other columns, with CH60 bars exhibiting the largest buckling amplitudes. The much higher strain hardening gradient of ASTM A1035 bars in CM100, compared with other bars, may have delayed the opening of cross-tie bends and maintained a higher tangent axial stiffness in the inelastic strain range of longitudinal bars, thus enhancing their buckling strength and performance compared with that of bars exhibiting a yield plateau.

All columns showed comparable lateral-load behavior and completed at least one full cycle to a drift ratio 5.5% prior to bar fracture. Column CH100 sustained bar fracture at a drift ratio of 3.2% as it was being pushed to the second cycle of -5.5% drift ratio. CL100 completed the 5.5% cycles and first bar fracture happened at a drift ratio of 4.8% as the column was being pushed to the first cycle of 7.0%. The first bar in CM100 fractured at 4.3% drift ratio as the column was being pushed towards its second cycle to a drift ratio of +5.5%. The first bar in CH60 fractured at the end of the second cycle to a drift ratio of +5.5%. The comparable drift capacities of all columns were observed despite their longitudinal bars having a wide range of uniform and fracture elongations, as well as varying hardening behaviors and manufacturing processes. Although there are no set targets for satisfactory seismic behavior, a stable response with limited lateral strength loss up to a drift ratio of 4% is generally considered to be an acceptable performance objective for collapse prevention at the Maximum Considered Earthquake (MCE) hazard level. All the columns tested satisfied that performance criteria and can therefore be considered to have valid materials and designs for regions of high seismicity. All columns lost significant lateral strength due to the fracture of longitudinal bars at various points during the cycles to the drift-ratio target of 5.5%. Bar fractures were due to a combination of buckling-induced strain demands and low-cycle fatigue. It is noteworthy that bar fractures were due mainly to low cycle fatigue and buckling and that the results presented herein only apply to bars having similar fatigue performance as those tested in this study. As demonstrated in Chase and Ghannoum (2015) grade 100 bars in production today have highly variable low-cycle fatigue performance.

5.2 MOMENT STRENGTH - ENVELOPE BEHAVIOR

5.2.1 Moment Strength

ACI 318-14 allows the use of a bilinear elastic-plastic behavior for reinforcement when designing for flexural strength of a section. A maximum usable concrete compressive strain of 0.003 is allowed in ACI 318-14, while the specified yield strength of the longitudinal bars (f_{ys}) is used to obtain the nominal moment strength (M_{ns}) and $1.25f_{ys}$ when calculating the probable moment strength (M_{prs}). The moment strength of each member calculated using the above assumptions and results are presented in Table 19. Additionally, the nominal (M_{nm}) and probable (M_{prm}) moment strengths were estimated using the measured yield strength of column bars, and are presented in Table 19. Table 20 presents the ratios of the maximum measured moments in the columns to the computed moment strengths. All computed values account for a concentric axial load of 15% of the gross sectional capacity.

For columns CH100, CL100, and CH60, the nominal and factored moment strengths were in close agreement with the yield strengths recorded experimentally; even when using the measured yield strength of the bars (Table 19; Table 20). The measured yield strength for column CM100 was however 24% higher than the computed nominal strength. The probable moment strengths, M_{prm} , of columns CH60, CH100, and CL100 were within 15% of the measured peak moment strengths. Due to the hardening behavior of the ASTM A1035 bars in CM100, its probable moment strength was underestimated by approximately 38% when using the specified yield strength of 100 ksi in the calculations and 24% when using the measured yield strength of the bars. Results therefore indicate that a factor higher than 1.25 may be warranted when estimating the probable moment strength of columns with A1035 longitudinal bars.

The nominal flexural capacity based on specified material properties (M_{ns}) of CH60 was evaluated to be 3220 kip-in, while for the columns reinforced with grade 100 reinforcement that strength was 18% larger at 3810 kip-in. This difference correlates well with the experimental peak moments of CH100 and CL100 that were about 18% stronger than that of column CH60. However, the measured yield moment of CH100 and CL100 were about 30% higher than that of column CH60.

Table 19: Flexural strength of columns evaluated using ACI 318-14 procedures and measured experimentally

Specimen	M_{ns}^{\S} (kip-in)	M_{nm} (kip-in)	ϕM_{ns} (kip-in)	ϕM_{nm} (kip-in)	M_{prs} (kip-in)	M_{prm} (kip-in)	M_{ye} (kip-in)	M_{ue} (kip-in)
CH100	3810	3810	3430	3430	4170	4200	4230	4800
CL100	3810	3910	3430	3520	4170	4150	3950	4570
CM100	3810	4160	3430	3740	4170	4620	4720	5760
CH60	3220	3300	2898	2970	3530	3950	3260	4080

M_{ns} – nominal moment capacity of the section calculated per ACI 318-14 procedures and specified steel yield strength; M_{nm} – nominal moment capacity of the section calculated per ACI 318-14 procedures and measured steel yield strength; ϕ – flexural strength reduction factor of 0.9 from ACI-318-14; M_{prs} – probable moment calculated from with ACI-318 procedures and 1.25 times the specified steel yield strength; M_{prm} – moment capacity calculated per ACI-318 procedures and ultimate measured steel strength; M_{ye} – moment at first yield from the experimental tests; M_{ue} – maximum measured moment from the experiments.

Table 20: Ratios of measured to calculated moment strengths

Specimen	M_{ue}/M_{ns}	M_{ue}/M_{nm}	$M_{ue}/\phi M_{ns}$	$M_{ue}/\phi M_{nm}$	M_{ue}/M_{prs}	M_{ue}/M_{prm}
CH100	1.11	1.11	1.23	1.23	1.15	1.14
CL100	1.04	1.01	1.15	1.12	1.10	1.10
CM100	1.24	1.13	1.38	1.26	1.38	1.24
CH60	1.01	0.99	1.13	1.10	1.16	1.03

Compression strains were measured between the outermost targets of the first and third rows from column ends (gauge length of 5.5 inches). At the applied peak moment, the measured compressive strains were on the order of 0.005 for CH100, 0.0055 for CL100, 0.0075 for CM100, and 0.0033 for CH60. At this point during the loading protocol the first bond splitting cracks had already formed. However, no observable spalling had taken place

in CH100, CL100, and CH60. Specimen CM100 had already spalled when the above-mentioned compressive strain was reached due to the large deformation demands at peak strength. These strain measurements indicate that adjusting the maximum useable compression strain for moment strength evaluation beyond the 0.0003 value in ACI 318-14 may be warranted for HSRB.

5.2.2 Envelope Response

The envelopes of the average top and bottom moments versus drift response averaged for the first negative half-cycle are presented for all columns in Figure 80. The response of the columns did not show significant strength degradation (Figure 80-left) up to the first cycle to a drift ratio of 5.5%, which corroborates the relatively low amount of damage observed up to that point. However, by the end of the first cycle to a drift ratio of 5.5%, buckling of longitudinal bars occurred in all columns, resulting in lateral-strength degradation. Column CH60 showed the largest relative degradation in strength prior to bar fracture, with its moment resistance dropping to 78% of the peak moment strength in the first cycle to a drift ratio of -5.5%. The observed moment strength degradation in column between drift ratios of 1 to 4% can be attributed to progressive crushing of concrete cover.

Columns CH60, CH100, and CL100 exhibited a similar moment versus drift response up to a drift ratio of 3%, when normalized with their nominal moment strength. Differences in transverse reinforcement spacing, steel grades and the T/Y ratios showed little influence on the responses. CH60 lost strength more rapidly at higher drifts than the columns reinforced with grade 100 bars even though grade 60 bars had a higher T/Y ratio. A possible explanation for this observation is that the wider spacing lower strength of the transverse reinforcement in CH60 provided less confinement to the concrete, which caused the concrete core to degrade more rapidly. The envelope response for columns CH100 and

CL100, which had the same reinforcement details but differing T/Y ratios, showed some difference in strength degradation, with CL100 being up to 10% weaker at the end of the first cycle to a drift ratio of 5.5% than CH100.

Column CM100 on the other hand exhibited a very different moment-strength envelope curve than the other three columns. The column showed significant hardening (or strength gains) up to a drift ratio of 4%. Beyond that drift, strength degradation initiated as in other columns and increased with bar buckling during the second cycle to a drift ratio of 5.5%. It appears that the hardening behavior of the ASTM A1035 bars in CM100 contributed to this hardening effect through both gains in strength of the longitudinal bars but also due to the hardening behavior of the transverse bars, which likely enhanced the confinement of the concrete core. Moreover, as discussed in Section 4.4.6, cross-ties in CM100 did not open up as much as they did in other columns, which limited the buckling amplitude of the longitudinal bars.

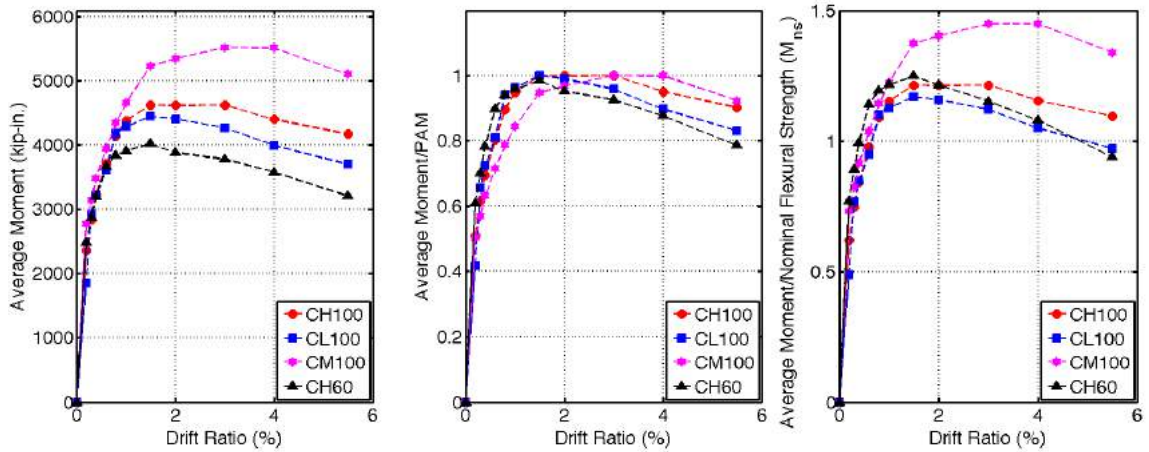


Figure 80: Average backbone of the response for each column

5.3 CYCLIC BEHAVIOR

Columns CH60, CL100, and CH100 exhibited a typical lateral force versus drift hysteretic response. When the columns were pushed laterally in one direction, flexural cracks opened at the tension faces. As the columns were unloaded and pushed back in the opposite direction, these cracks closed gradually as the tension faces went into compression. Prior to the yielding of longitudinal reinforcement in tension, hysteretic force-versus-drift loops were observed to be essentially linear in loading and unloading. This indicates that limited slip between the bars and the surrounding concrete occurred around the flexural cracks. When the columns were pushed past yielding of the longitudinal bars, then unloaded and pushed back in the opposite direction, flexural cracks closed gradually until the longitudinal bars reached zero stress at significant tensile strains. At that stage, the plastic strains in the bars kept the cracks open until sufficient compressive stresses were applied to zero their strains and close the cracks. This re-loading branch of the hysteresis loops corresponds with a less stiff force-drift response as the section stiffness is mainly determined by the longitudinal bars. Once cracks closed again, the section stiffness increased again during the re-loading branch. This typical behavior was observed in CH60 (Figure 81-CH60). Columns CH100 and CL100 exhibited a similar behavior as CH60 but with a much stiffer crack closing phase at the beginning of re-loading (Figure 81-CH100; CL100). This behavior is likely due to the higher strength of the grade 100 bars, which required a larger force to bring them to zero strain and close the cracks. Column CM100 on the other hand barely showed signs of that reduced re-loading stiffness during the crack closing phase. This behavior may be due to flexural cracks being smaller in CM100 compared with those of other columns, which would shorten the crack closing phase.

The second cycle to the same drift target dissipated less energy than the first cycle in all columns. As can be seen in Figure 82, this lower energy dissipation is mainly due to differences in the re-loading branch of the hysteretic behavior (Figure 82). In the first cycle to a certain drift target the rotation demands needed to open wider cracks, on the other hand in the second cycle, these cracks were already opened and less lateral force was needed for the member to accommodate the required rotation demands. The first cycle to the subsequent drift target followed closely the second cycle curve to the previous drift target.

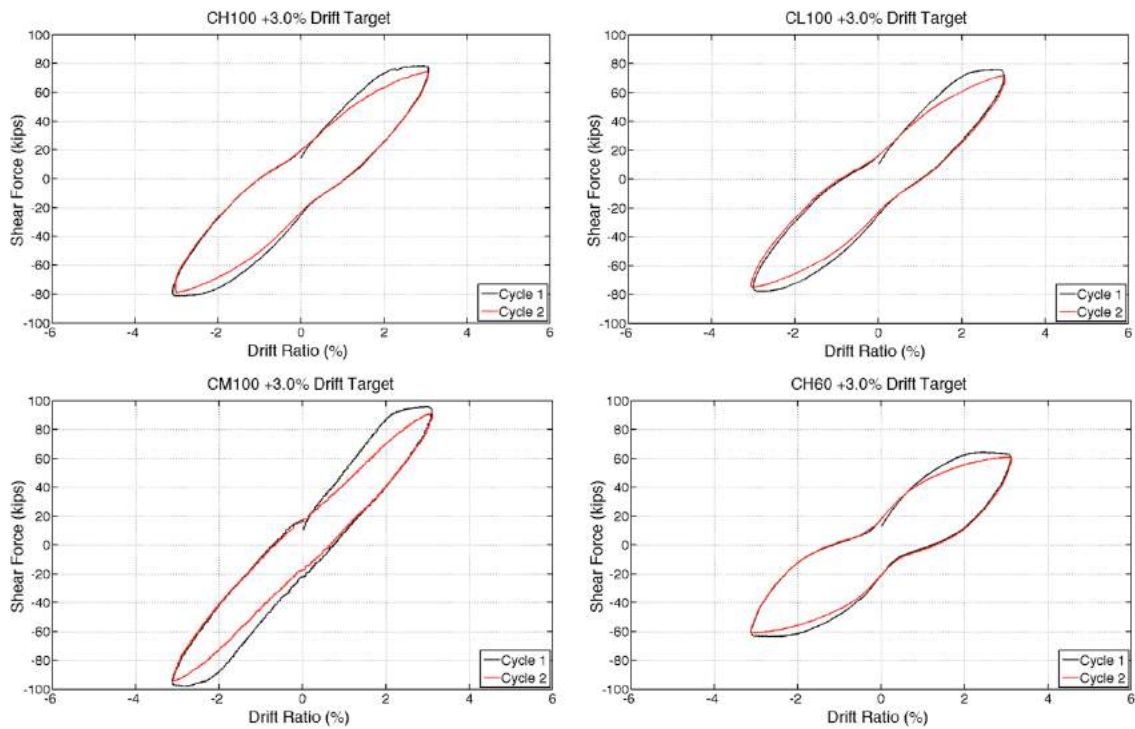


Figure 81: Hysteresis loops of columns pushed to a drift ratio of 3.0%

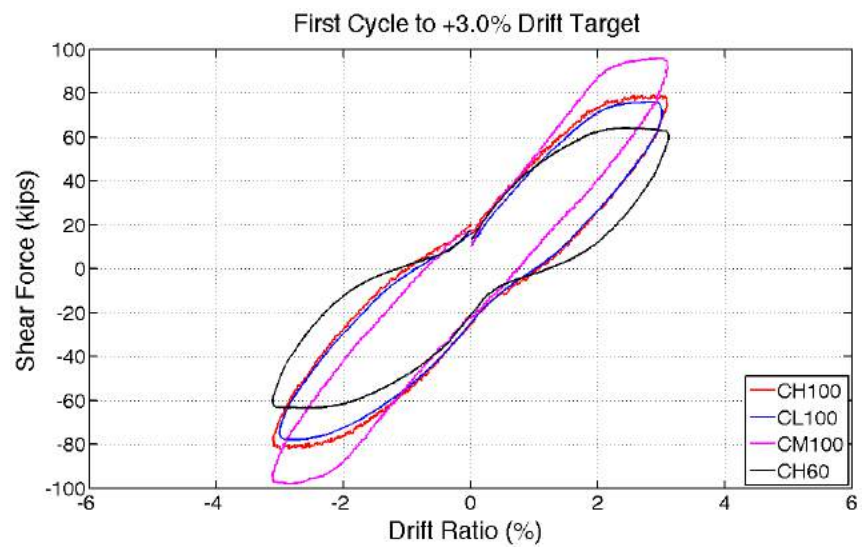


Figure 82: Hysteresis loops of all columns pushed to the first cycles to a drift ratio of 3.0%

Figure 83 gives the cumulative dissipated energy of each member up to a drift ratio of 4.0%. Cumulative energy was evaluated as the cumulative area under the average top and bottom moment versus drift ratio curve. The first and second cycles to the same drift target are separated for the discussion carried below. The amount of total energy dissipated in the first cycles was similar for all members, even though there were large differences in the moment strengths of the columns. However, the cumulative dissipated energy in the second cycles showed more pronounced differences, with CM100 dissipating 17% less energy by the end of the 4.0% drift cycles as compared to CH100.

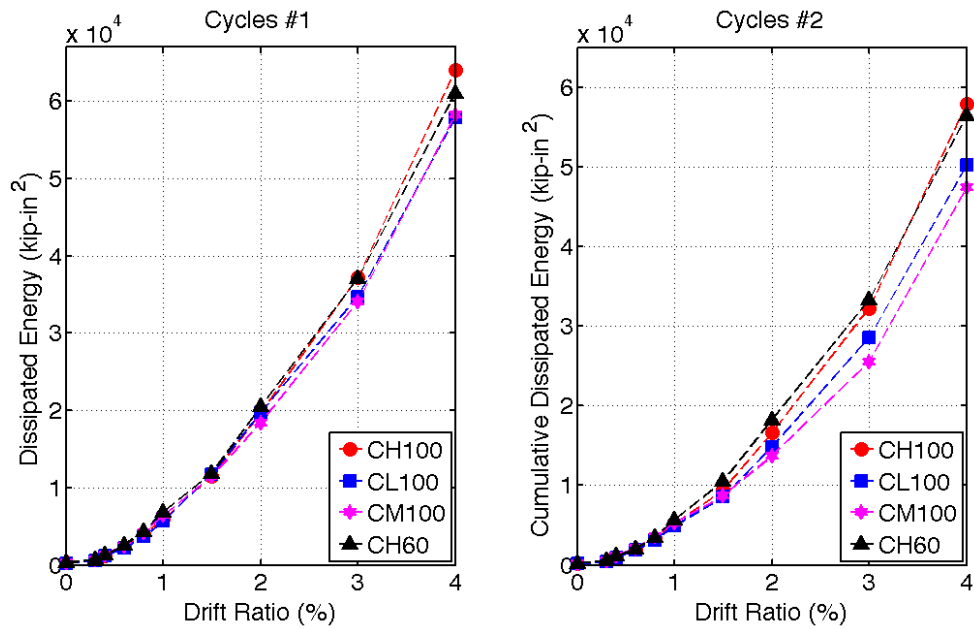


Figure 83: Cumulative dissipated energy at drift targets: first cycle (left); second cycle (right)

When normalized by the nominal moment strength of each member (M_{nm} or M_{ns}), CH60 is seen to have a much larger normalized energy dissipation capacity given a design strength than CH100, CL100 and especially CM100 (Figure 84). Columns reinforced with bars that had a defined yield plateau produced wider hysteresis loops, leading to CH60 having the highest amount of energy dissipation even given the lower strength of the bars. Comparing the energy dissipation between the columns with steel having a yield plateau, i.e., CH60, CH 100 and CL100, it can be seen that the T/Y ratio also affects the amount of energy dissipation. The higher T/Y ratio allows for larger amounts of energy dissipation. The lower amount of dissipated energy in CM100 can partly be attributed to the higher peak strength it exhibited given the same elastic stiffness as the other columns, and partly due to the unloading stiffness as seen in Figure 82. The high strain hardening gradient in column CM100 contributed to the increase in internal forces without increasing the dissipated energy proportionally (Figure 84). The lateral load versus lateral drift response of the CM100 can be idealized as linear to an effective yield point that is much higher than the estimated yield nominal strength. CM100 dissipated less energy per cycle to a given drift demand than the other columns with a lower effective yield force and drift, because of this higher effective yield force and associated higher effective yield drift. Conversely, because bars in CM100 reached their yield strains at larger drift demands, they sustained less inelastic strains at a given drift demand than bars in CH100 and CL100. This may have contributed to the CM100 having thinner hysteretic loops resulting in less dissipated energy.

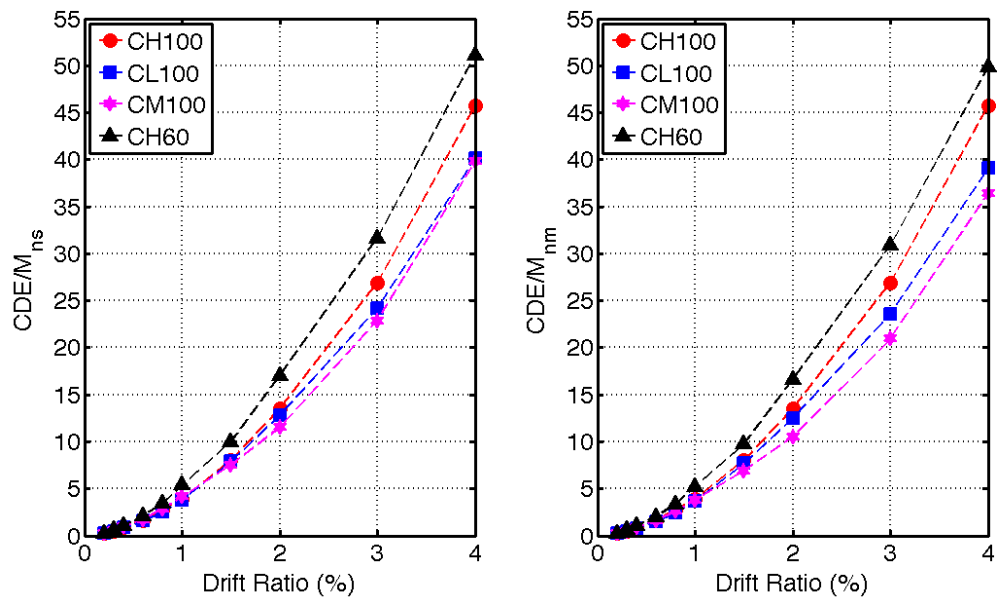


Figure 84: Cumulative dissipated energy (CDE) as a fraction of M_{ns} (left) and M_{nm} (right)

5.4 STRAIN DEMANDS AND PLASTICITY SPREAD

In seismically detailed concrete columns, loss of lateral strength can be expected from crushing of the concrete in the core and buckling or fracture of the longitudinal bars. When sufficient confinement is provided, as was the case for all columns in this study, the deformation capacity associated with a significant loss of lateral strength is often determined by the behavior of the longitudinal bars. In turn, the behavior of the longitudinal bars is highly governed by their mechanical properties, lateral restraint, and strain demands.

In this section, strain demands on the longitudinal bars of the column specimens are explored in more detail. Several mechanical properties of longitudinal bars can influence their strain demands, as well as their buckling and fracture behaviors, namely: 1. the existence of a yield plateau; 2. the length of the yield plateau; 3. the initial slope of strain hardening; 4. the tensile to yield strength (T/Y) ratio; and the fatigue life. In order to help with the discussion in this section, typical stress-strain curves of the four types of longitudinal bars used in the specimens are reproduced again from in Figure 85.

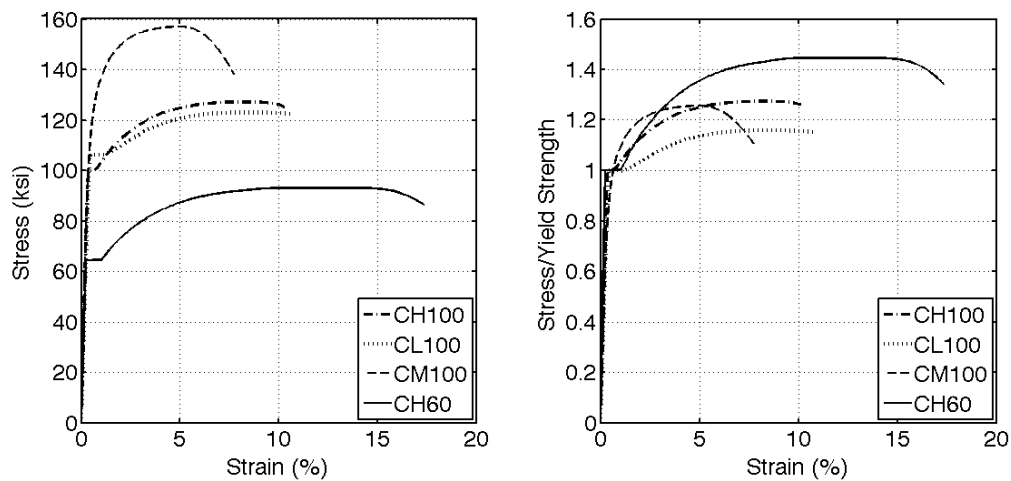


Figure 85: Typical stress-strain curve for longitudinal reinforcement used in each specimen

It is noteworthy that the strain values shown in Figure 85 were measured using a gauge length of 8 inches, while the strains measured on longitudinal bars in columns represent local strains and were measured with 1/5 in. strain gauges.

5.4.1 Maximum Strain Demands in the Longitudinal Bars

Figure 86 presents the average measured strains in longitudinal bars of all columns, measured at the top and bottom column interfaces with the adjacent footings. As can be seen in the figure, bars with a well-defined yield point and yield plateau exhibited a jump in strain demands right after yielding, whereas bars in CM100 that did not exhibit a well-defined yield point experienced a gradual increase in strain demands with increasing drift demands.

The strain gauges in CL100 were lost before reaching the +5.5% drift ratio. Projecting the strain at this drift target for CL100 by linear extension for the last slope of the strain-drift curve yields a strain of 0.076. The average measured strain at a drift ratio of 5.5% in column CH100 was significantly lower than that of CL100 and came in at 0.055. Thus, the longitudinal bars in CL100 are projected to have reached 89% of their uniform strain or 60% of their fracture elongation at a drift ratio of 5.5% prior to buckling. Longitudinal bars in CH100 reached 73% of their uniform strain or 48% of their fracture elongation at a drift ratio of 5.5% prior to buckling. The strain demands in CM100 increased gradually without showing jumps as in other columns, and were smaller than in other columns at drift ratios between 1.0% and 4.0%. However, at cycles which resulted in the failure of each member (to drift ratios of 5.5%) the strain demands in CM100 and CH100 were similar at 0.055. These strains are close to the uniform elongation values and 75% of the fracture elongation for the ASTM A1035 steel in CM100.

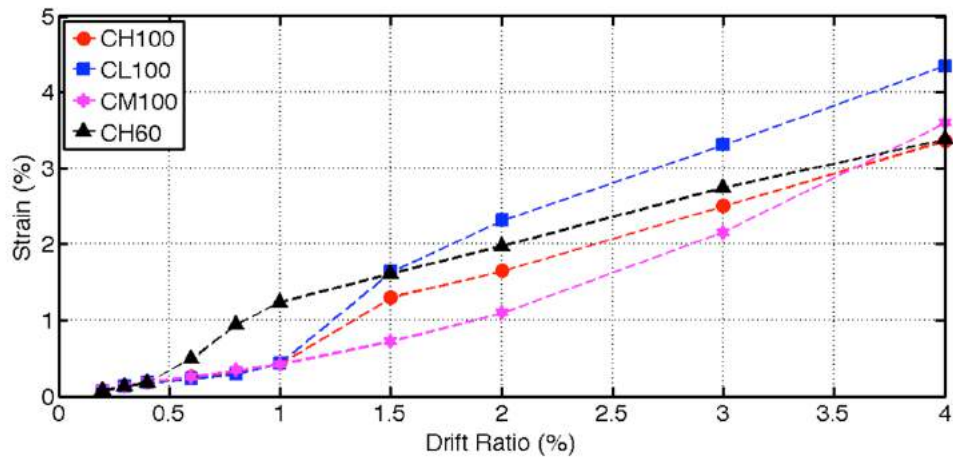


Figure 86: Average strain demands in longitudinal reinforcement at drift targets for all column

Strain demands for columns CH100 and CL100 are compared in Figure 87. This allows for the isolation of the effect of the tensile to yield strength (T/Y) ratio and yield plateau on strain demands. The main difference between the types of steel used in columns CH100 and CL100 was the T/Y ratio of their reinforcing bars. Longitudinal bars in these two columns experienced first yield at a drift ratio of about 1.0%. Prior to yield, strain demands were similar for both columns. Past yielding, the strain demands of bars in CL100 were significantly larger than those of bars in CH100. The main differences between the bars of the two columns was their T/Y ratio as well as the strain range over which a yield plateau occurs. Bars in CL100 had a lower T/Y ratio and longer yield plateau than those of column CH100. The length of the yield plateau was found to account for most of the difference in strain demands that bars in the two columns experienced at a drift ratio of 1.5%. This can be seen in Figure 88 in which the strain range of the yield plateau is subtracted from the after-yield measured strains (i.e., for data points at drift ratios of 1.5% and higher). Possibly the increase in strain without an increase in bar strength in the yield plateau phase concentrates strains at the critical crack, generating the observed jumps in strain demands just after yielding. Once strain hardening initiates at the end of the plateau, strains were able to redistribute away from the critical crack again and the rate of increase in strain demands with increasing drift reduced.

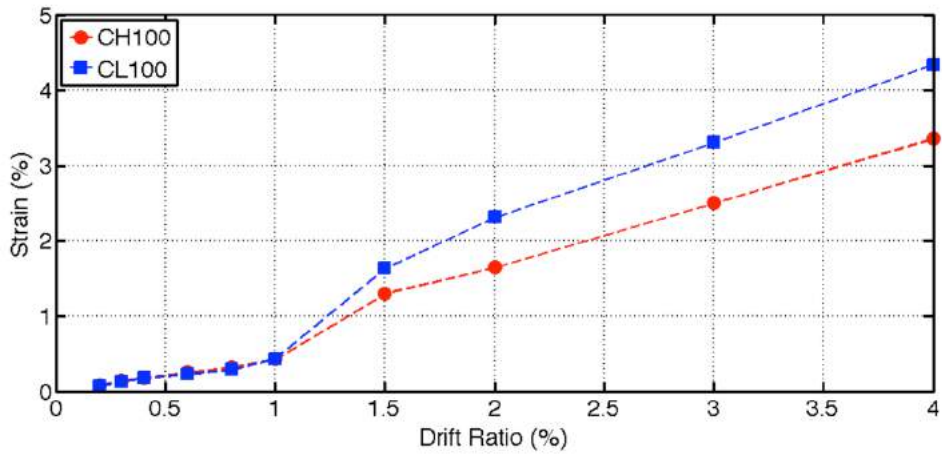


Figure 87: Average strain demands in longitudinal bars at column ends at various drift targets [CH100 & CL100]

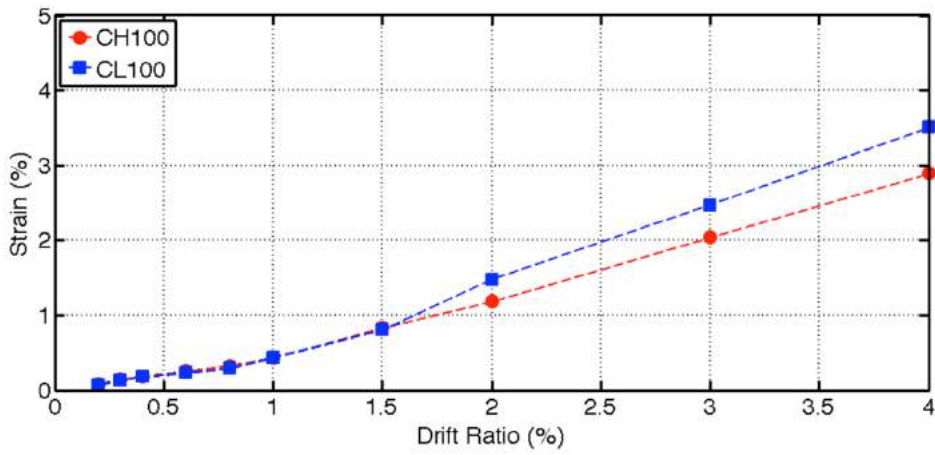


Figure 88: Average strain demands in longitudinal bars at column ends at various drift targets [CH100 & CL100]

Strains recorded in the bars at a drift ratio of 1.5% (~ 0.015 strain) correspond to strains just past the yield plateau in the stress-strain curves of the steel used in CH100 and CL100. The rate of strain increase was higher for CL100 after this point and more pronounced in the drift-ratio range of 1.5% to 2.0%. This could be attributed to a lower initial strain hardening tangent modulus for CL100 bars, which is related to the lower T/Y ratio.

The same pattern was seen when analyzing strain demands in the longitudinal bars of CH60 (Figure 89; Figure 90). The longitudinal reinforcement in CH60 yielded at a drift ratio of 0.6%, leading to these bars experiencing higher strains than reinforcement in columns with grade 100 at low drift levels (between drift ratios of 0.6% and 1.5%). The yield plateau strain range also appeared to influence the strains from a drift ratio of 0.6% to 1.5% as can be seen in Figure 90 in which the strain range of the yield plateau is subtracted from the after-yield measured strains from the recorded strain demands. Strain increases with respect to drift beyond a drift ratio of 1.5% in the bars of CH60 were depressed by the steep strain hardening tangent modulus and the high T/Y ratio (Figure 89) compared with those for column CH100 and CL100 (Figure 90).

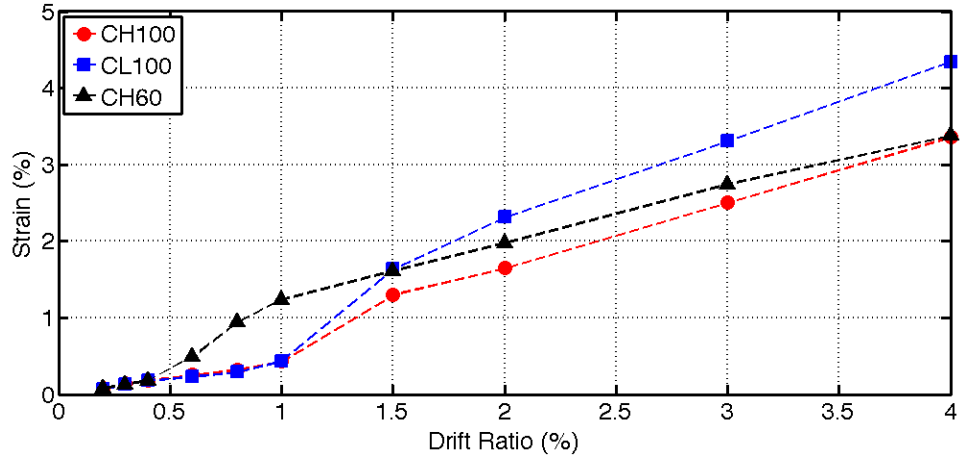


Figure 89: Average strain demands in longitudinal reinforcement at drift targets [CH100; CL100 & CH60]

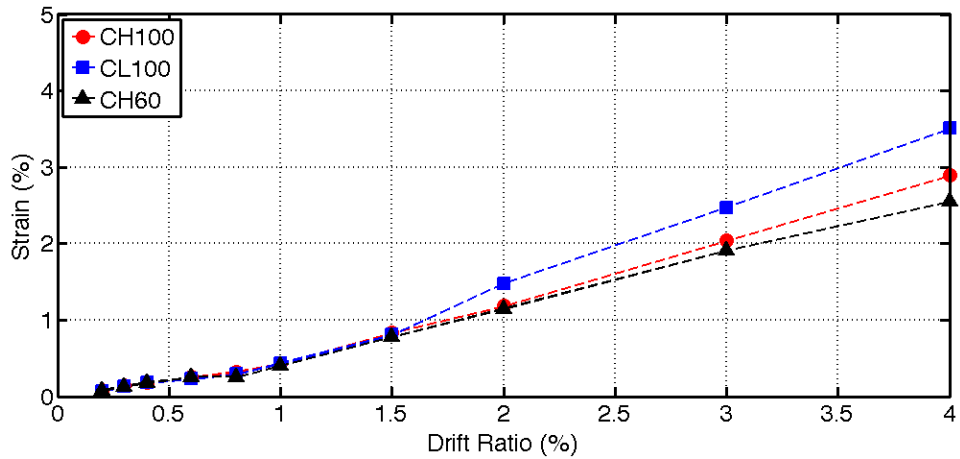


Figure 90: Average strain demands after removing the length of the yield plateau at drift ratios beyond yield (0.6% for CH60 and 1.5% for CH100 and CL100) [CH100; CL100 & CH60]

5.4.2 Strains over Height in the Longitudinal Bars

The ability of inelastic strains in longitudinal bars to spread away from the critical flexural cracks reduces the strain concentrations and demands at those cracks. Parameters extrinsic to the bars themselves that influence strain values in longitudinal bars include the axial load ratio and shear stresses (Limantono, 2016). While the axial load ratio was the same between all four tested specimens, shear stresses in specimen CH60 were significantly lower due to the lower flexural strength of the section compared with those reinforced with grade 100 bars. Bar properties that could influence strain concentrations at cracks include: 1. the existence of a yield plateau; 2. the length of the yield plateau; 3. the tangent modulus during strain hardening; and 4. the tensile to yield strength (T/Y) ratio.

Plots in Figure 91 to Figure 93 show the distance from column end over which inelastic tensile strains spread in the longitudinal bars of the specimens. The un-filled markers show the height up to which inelastic strains spread in individual longitudinal bars. The distance up to which inelastic strains spread in a certain bar was calculated by linear interpolation between the farthest strain gauge from column end recording a strain larger than the measured yield strain (Table 7) and the adjacent gauge with a strain recording that remained in the elastic range. In Figures 1 to 3, the solid lines with filled markers represent the average distance inelastic strains spread from either column end, for all longitudinal bars in a given column with reliable strain gauge readings.

Figure 91 compares the spread of inelastic strains in specimens CL100 and CH100. The longitudinal bars in these two specimens had nearly the same yield strength and a distinct yield plateau. The bars in these columns had different yield plateau lengths, initial strain hardening slopes, and T/Y ratios. Thus, comparing the behavior of these two columns can give an indication on how these bars properties affect plasticity spread. Specimen

CL100 showed higher strain concentrations at its ends, with inelastic strains in the bars spreading over a shorter length as compared to CH100. The distance over which inelastic strains spread increased with increasing drift ratios in both columns. Inelastic strains in CH100 were recorded up to a distance of 21.2 inches for column end on average at a drift ratio of 5.5%, as compared to 18 inches in CL100. At one bar, inelastic strains spread up to 23.5 inches in CH100, while in CL100 they didn't go beyond 21 inches. The length of the yield plateau for the reinforcement used in CL100 was 0.84% (strain) as compared to 0.47% for the bars used in CH100. This, together with a lower strain-hardening tangent modulus may have produced the shorter plasticity spread in CL100.

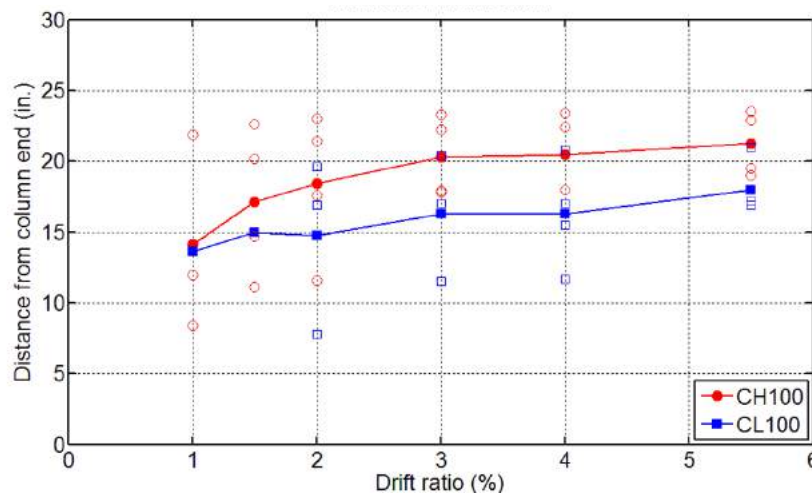


Figure 91: Spread of inelastic strains on the longitudinal bars of CH100 and CL100

In Figure 92, results from specimen CH60 are added to the previous plot. The distance over which inelastic strains spread in the longitudinal bars of CH60 was on average similar to, but lower than those in CH100. Specimen CH60 being reinforced with grade 60 #6 bars, had a smaller flexural strength and associated shear demands than columns reinforced with grade 100 bars. As such, this column may have experienced less

tension shift in its bars (Section 4.5.1), which can have a beneficial effect on spreading bars strain demands (Limantono, 2016). At larger drifts, however, the larger T/Y ratio and associated strain hardening tangent modulus of the grade 60 bars brought strain demands in those bars in closer agreement with those of the grade 100 bars having the lower T/Y ratio of column CH100. Plastic strains in CH100 spread on average up to a distance of 21.2 inches from column ends or 1.18 of the height of the section ($h=18\text{ in.}$), while for CH60 they spread up to 20.2 inches on average or $1.12h$. In CL100, inelastic strains were limited to a height of 18 inches on average, equal to the section height. These findings are corroborated by the observed crack pattern described in Chapter 4 that showed two major cracks in the plastic hinge region of CH60, similar to the ones observed in CH100.

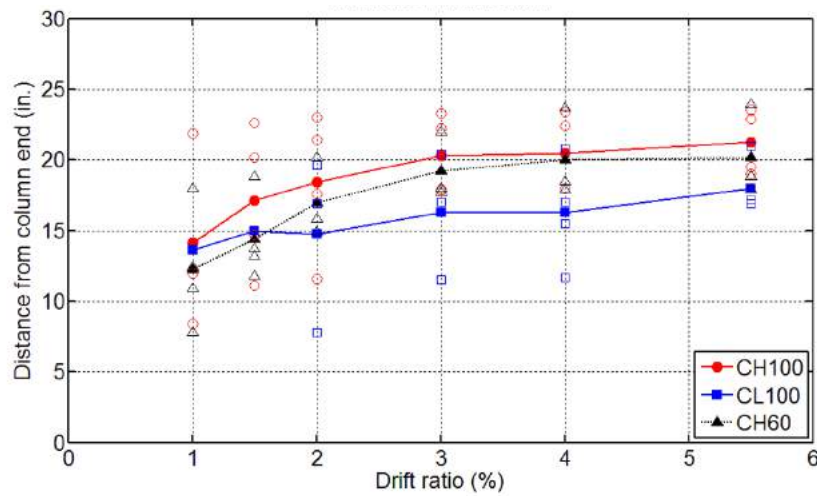


Figure 92: Spread of inelastic strains on the longitudinal bars of CH100, CL100, and CH60

As seen in Figure 93a, the plastic hinge length over which inelastic bar strains were recorded in specimen CM100 reached 20.6 in. or $1.14h$. The elastic strain limit used in Figure 3a was calculated using the 0.2% offset methods, which was equal to a strain of 0.006 as reported in Table 7. However, it was found that the reported plasticity spread was sensitive to the choice of elastic strain limit for the A1035 bars in CM100, which do not exhibit a clear yielding point. In Figure 93b, the yield strain for bars in CM100 was taken as the average measured strain during bar tension tests at the specified yield stress of the bars of 100 ksi. That average strain was 0.0039. For this definition of yield strain, inelastic strains spread on average up to 24.3 inches from the ends of column CM100, or $1.33h$. At one bar, the height over which these strains spread was 27 inches, or $1.5h$. These findings also corroborate the crack pattern observed in specimen CM100 described in Chapter 4.

While increased spreading of strain demands is beneficial for enhancing a member's deformation capacity, the observed length over which inelastic bar demands were recorded in CH60, CH100, and CM100 exceeded slightly the length prescribed in ACI 318-14 of 18 inches over which higher amounts of transverse reinforcement is required at the column ends to satisfy Special Moment Frame requirements.

The plastic hinge length over which inelastic strains were measured seems to level off at lower drifts for members with a lower T/Y ratio, i.e. CH100 and CL100. The spread in plasticity is more gradual with respect to drift demand in members with higher T/Y ratios, as observed in members CM100 and CH60. This could be attributed to the lower tangent modulus during strain hardening in the steel with the lower T/Y ratios.

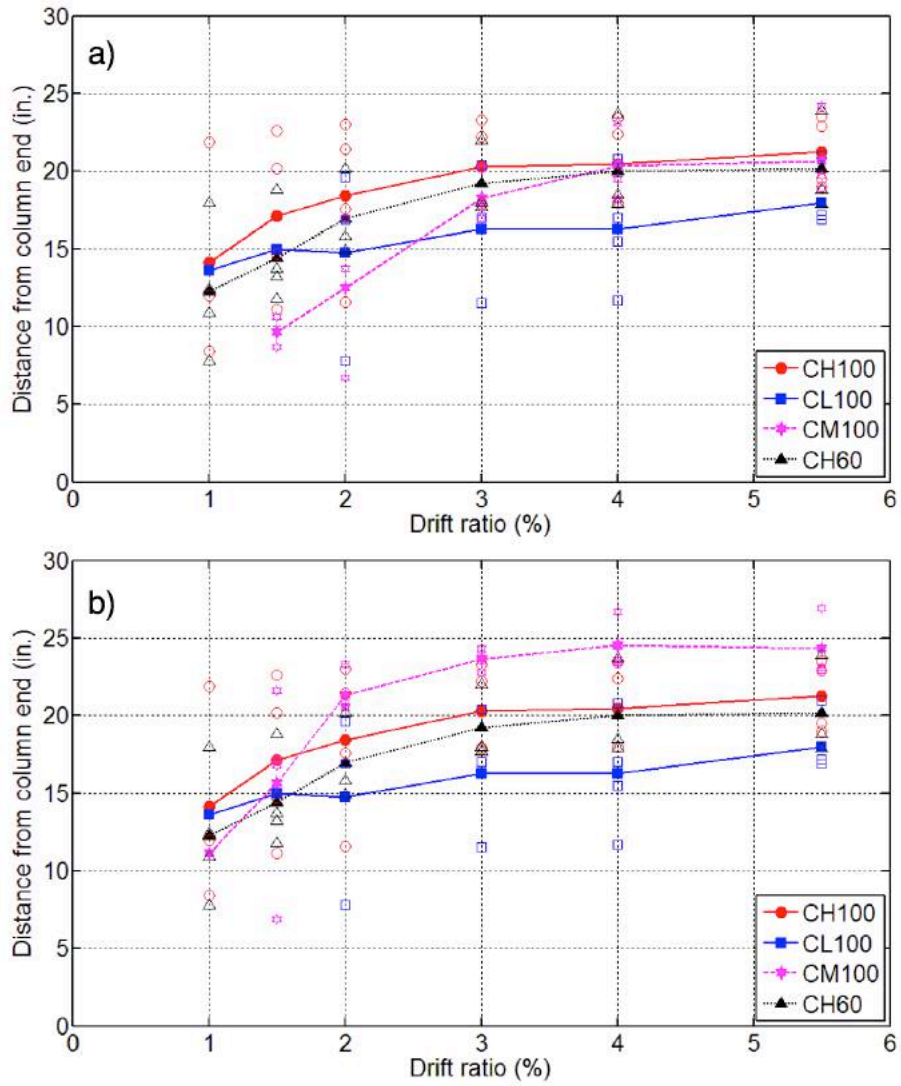


Figure 93: Spread of inelastic strains on the longitudinal bars of all specimens: a) yield strain in CM100 calculated with 0.2% offset rule; b) yield strain in CM100 taken at a stress of 100 ksi

Figure 94 presents the average measured tensile strains in the longitudinal reinforcement over the height of each member at different drift ratios. The strains were averaged for all top and bottom longitudinal bar strain readings. In Figure 4, positive distance values represent distances within the column span, while negative distance values represent locations within the column foundations. Similar observations on plasticity spread as the ones made above can be concluded from this plot. Bars with higher T/Y ratios were able to spread inelastic strain farther into the column span compared with those having a lower T/Y ratio. A draw-back in strain demands with increasing distance from column end was observed for CL100 at a drift ratio of 2.0%. This was attributed to the crack pattern observed in this specimen. One large crack formed at a distance of 8.5 inches from each column end (see Section 4.3.1).

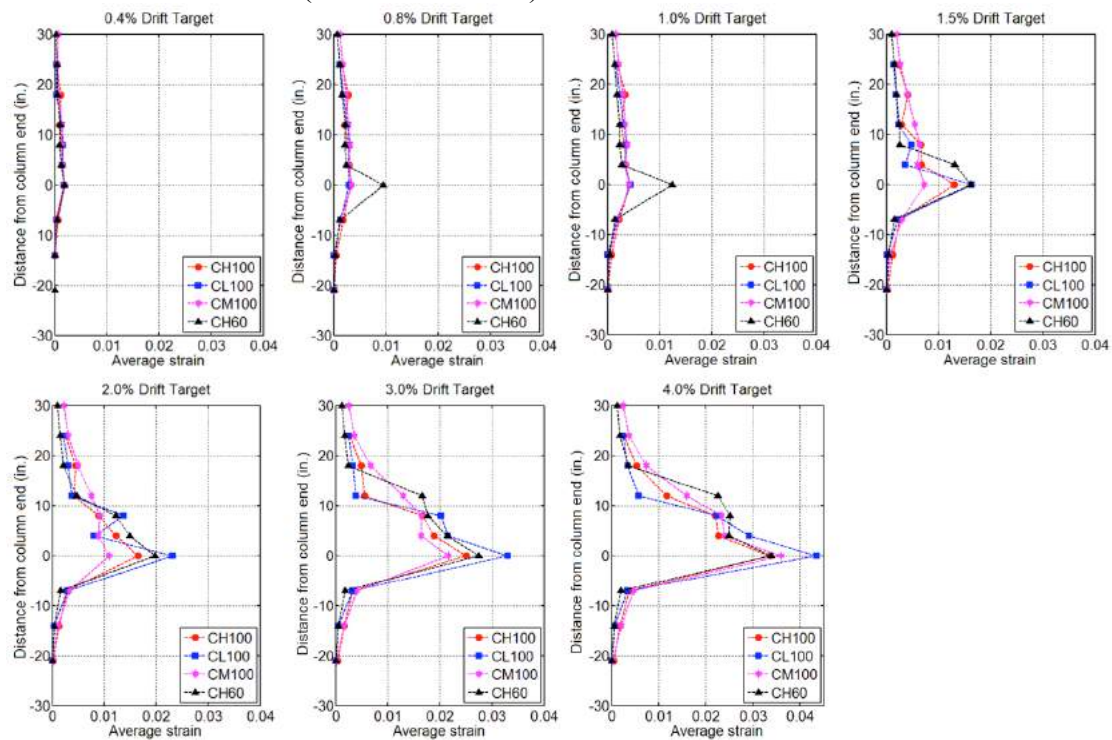


Figure 94: Average strain in longitudinal reinforcement over column and foundation spans at different drift ratios

6. Summary and Conclusions

6.1 SUMMARY

High-strength reinforcing bars (HSRB) with yield strength of 80 ksi and higher are currently under development in the U.S. for seismic as well as non-seismic applications. However, the HSRB being developed have varying mechanical properties. None of these bars are able to match the benchmark mechanical properties of the benchmark grade 60 bars, with each high-strength variant diverging from benchmark behavior in different ways. Structural engineers and steel mills are currently trying to strike the best balance between needed and feasible properties for high-strength reinforcing bars.

A targeted structural testing program was carried out to uncover any major issues in the performance of HSRB in concrete members, as well as provide necessary data to set material specifications for HSRB. The experiments conducted in this study were designed to push the new HSRB to large strain demands in concrete columns. Of particular interest was quantifying the effects of the shape of the stress-strain curve and the tensile-to-yield (T/Y) strength ratio of high-strength longitudinal bars on the behavior of concrete columns and the strain demands in the longitudinal bars.

Four columns were tested cyclically under a constant axial load of about 15% of the gross axial capacity. Concrete strength was around 5 ksi for all columns. The column specimens were:

- CH100: reinforced with grade 100 (i.e., having a yield strength of 100 ksi or higher) longitudinal and transverse bars having a relatively high tensile-to-yield (T/Y) ratio for that grade, and produced using the micro-alloying process.

- CL100: reinforced with grade 100 longitudinal and transverse bars having a relatively low T/Y ratio for that grade, and produced primarily using the quenching and tempering process.
- CM100: reinforced with grade 100 longitudinal and transverse bars satisfying the ASTM A1035 standard, and produced using the MMFX proprietary process.
- CH60: reinforced with grade 60 longitudinal and transverse bars satisfying the ASTM A706 standard and having a typical T/Y ratio for this grade.

Reinforcing bars in columns CH100, CL100, and CH60 exhibited well-defined yield points, yield plateau over varying strain ranges, and varying tangent moduli in their inelastic range of behavior. Reinforcing bars in CM100 on the other hand exhibited a rounded stress-strain relation without a distinct yield point. These A1035 bars also exhibited a significantly higher hardening tangent modulus than bars in the other columns prior to reaching their tensile strength.

All specimens sustained a flexural mode of degradation characterized by concrete crushing, longitudinal bar buckling, and eventually longitudinal bar fracture.

6.2 CONCLUSIONS

➤ *Global Behavior*

All columns showed comparable drift capacities and completed at least one full cycle to a drift ratio of 5.5% prior to bar fracture. The comparable drift capacities of all columns were observed despite their longitudinal bars having a wide range of uniform and fracture elongations, as well as varying hardening behaviors and manufacturing processes. Although there are no set targets for satisfactory seismic behavior, a stable response with limited lateral strength loss up to a drift ratio of 4% is generally considered to be an acceptable performance objective for collapse prevention at the Maximum Considered

Earthquake (MCE) hazard level. All the columns tested satisfied that performance criteria and can therefore be considered to have valid materials and designs for regions of high seismicity.

All columns lost significant lateral strength due to the fracture of longitudinal bars at various points during the cycles to the drift-ratio target of 5.5%. Bar fractures were due to a combination of buckling-induced strain demands and low-cycle fatigue.

➤ ***Effects of Bar Mechanical Properties on Drift Capacity***

The uniform and fracture elongations of longitudinal bars did not have a determining role in the drift capacity of the columns tested. The uniform elongation of the longitudinal bars varied from a minimum of 4.9% in CM100 to a maximum of 11.8% in CH60, while all columns exhibited comparable drift capacities.

Since buckling of the longitudinal bars always preceded their fracture, the buckling propensity of longitudinal bars combined with their high-strain demand, or low-cycle fatigue behavior appear to have played a critical role in determining the drift capacity of the well-confined concrete columns at first longitudinal bar fracture. Buckling is believed to have induced large localized strain demands in the bars that added rapidly to the fatigue damage induced by prior strain demands. Bar buckling and fracture is the expected mode of strength degradation in well-confined concrete columns satisfying the requirements for Special Moment Frames of ACI 318-14, particularly for columns under low to moderate axial loads. Therefore, factors affecting both degradation modes must be adequately understood and controlled to achieve acceptable seismic drift capacity in columns reinforced with HSRB.

➤ ***Effects of Reinforcing Bar Mechanical Properties and Detailing on Buckling***

Two factors were found to influence the buckling behavior of the longitudinal bars in this study: i) the spacing of the hoops, and 2) the hardening behavior of the longitudinal and transverse bars. The spacing of the hoops that braced the grade 100 bars was reduced, since the #6 higher strength longitudinal bars were to carry significantly higher loads than the #6 grade 60 bars, while still having the same flexural rigidity as the grade 60 bars. Grade 60 bars were laterally braced by transverse hoops at a spacing of six longitudinal-bar diameters ($6.0d_b$), while grade 100 bars were braced at $4.7d_b$. Longitudinal bars buckled at around the same drift demands in all columns in this study. Therefore, the adjusted hoop spacing in the columns with grade 100 bars was able to offset the detrimental effects of the higher bar strength and their buckling propensity. Using a larger hoop spacing for grade 100 bars up to those currently permitted in ACI 318-14 for grade 60 bars (i.e., $6.0d_b$) is therefore not advised, as that would likely produce worse drift capacities for columns reinforced with grade 100 bars than for those reinforced with grade 60 bars.

ASTM A1035 grade 100 longitudinal bars braced using A1035 grade 100 hoops and cross-ties exhibited much less pronounced buckling than grade 100 bars having a yield plateau and a shallower stress/strain hardening slope. This was attributed to the higher buckling capacity in the inelastic hardening range of the A1035 bars compared with that of other grade 100 bars having shallower inelastic tangent modulus of elasticity. Additionally, A1035 cross-ties did not open up as much at their bends during testing as other grade 100 bars did, thereby restraining longitudinal bars more effectively. By sustaining significantly less buckling amplitudes than other grade 100 bars, A1035 bars likely incurred less strain concentrations due to buckling. Results therefore indicate that the rounded hardening shape

of the stress-strain curve of A1035 bars may have offset any detrimental effects on column deformation capacity that their lower elongation capacities may have had.

➤ ***Effects of Bar Mechanical Properties on Plasticity Spread***

Columns CH100 and CL100 had the same design and were both reinforced with grade 100 bars with similar stress-strain shapes, but with differing tangent modulus during strain hardening and tensile-to-yield strength (T/Y) ratios. Thus, these two column tests isolated the effects of mechanical properties of grade 100 bars on column behavior. Results from these two columns indicated that using longitudinal bars with a higher T/Y ratio results in greater spread of inelastic deformations and strains away from the section of peak moment demand. Column CH60, which had bars with a well-defined yield point but a higher T/Y ratio than the grade 100 bars, experienced similar spreads of inelastic bar strains as bars in CH100. The lower shear stresses in CH60 compared to the columns with grade 100 bars may have limited the beneficial effects of the tension shift phenomenon on plasticity spread in CH60.

By the end of testing, inelastic strains in the longitudinal bars of CH100 had spread on average up to 21.2 inches or 1.18 times the section height ($h=18$ in.) from the location of peak moment. Inelastic strains spread up to similar average distance for all longitudinal bars of CH60, or up to 20.2 inches. In CL100, inelastic strains were limited to a height of 18 inches on average, or h .

The lack of a well-defined yielding point and a relatively steep inelastic hardening tangent modulus produced a different strain distribution behavior for CM100 than in other columns. The measured strains in the longitudinal bars indicated that the inelastic demands spread over a significantly larger distance from column ends in CM100 than in other

columns. The length over which inelastic bar strains (i.e. strains higher than strain corresponding to a stress in the bar of 100 ksi) were recorded to reach on average 24.3 in. or $1.33h$ in CM100, with one longitudinal bars spreading its inelastic strain up to 27 inches or $1.5h$ from column end.

While increased spreading of strain demands is beneficial for reducing strain concentrations and enhancing member deformation capacity, the observed length over which inelastic bar demands were recorded in CH60, CH100, and particularly CM100 exceeded the length prescribed in ACI 318-14 (18 inches) over which larger amounts of transverse reinforcement is required at column ends satisfy Special Moment Frame requirements.

➤ ***Effects of Bar Mechanical Properties on Bar Strain Demands***

Prior to first yield, peak tension strain demands in longitudinal bars were similar for all columns. Columns CH100, CL100 and CH60 experienced jumps in the peak tension strain demands of longitudinal bars just after yielding. Possibly the increase in strain without an increase in bar strength in the yield plateau phase concentrated strains at the critical crack, generating the observed jumps in strain demands just after yielding. Once strain hardening initiated at the end of the plateau, bars were able to redistribute strains away from the critical crack and the rate of increase in strain demands with increasing drift was observed to reduce. No such strain jumps occurred in the longitudinal bars of CM100, which did not exhibit a yield plateau. Strain demands in the longitudinal bars of CM100 therefore remained significantly lower than those of bars in other columns at moderate drift ratio ranges (1.5% to 3%).

The grade 60 longitudinal bars in CH60 yielded at the lowest drift ratio of 0.6% due to their lower yield strain. The jump in strain demands just after yielding drove bars in column CH60 to experience higher strains at lower drifts than the bars in other columns. Columns CH100 and CL100 experienced the strain jumps at a drift ratio of 1.0%. Their strain demands increased at that drift well beyond the strain in the bars of CM100.

The length of the yield plateau was found to account for most of the difference in strain demands that bars in columns CH100, CL100 and CH60 experienced just after first yield or at a drift ratios below 2%. After this point, the T/Y ratio of the longitudinal reinforcement defined the rate of increase of tensile strain demands with respect to column drift, with a higher T/Y leading to lower strains at higher drift targets. The higher rate of increase in strains with respect to drifts in bars of CL100 resulted in those bars having the largest strain demands at a drift ratio of 4.0%, even though the grade 60 bars in CH60 had larger strain demands at lower drifts.

➤ ***Effects of Bar Mechanical Properties on Cracking***

Flexural cracking patterns corroborated the observations on plasticity spread and strain demands on longitudinal bars. Column CM100, in which plasticity spread farthest and strain demands were lowest on the longitudinal bars, sustained a larger number of narrower flexural cracks that spread farther away from the regions of peak moment. Column CH60 exhibited wider critical cracks at moderate drift levels than other columns. This corroborates the findings of higher strain demands in the longitudinal bars of CH60 at those drift levels compared with other columns.

➤ ***Effects of Bar Mechanical Properties on Moment Strength***

ACI 318-14 provisions for moment strength were more conservative in estimating the moment strength of members reinforced with grade 100 steel than for CH60. The measured peak concrete compressive strains in column CH60 reinforced with grade 60 bars at peak moment strength was 0.0033, which is close the allowed strain values of 0.003 stipulated in ACI 318-14 for evaluating moment strength. Measured concrete compressive strains at peak moment strength were however significantly larger than 0.003 and exceeded 0.005 in columns reinforced with grade 100 bars. Test results therefore suggest that an increase beyond the 0.003 value in ACI 318-14 for the usable concrete compression strain may be warranted to achieve improved estimates of moment strength for members with HSRB.

Probable moment strengths estimated using 1.25 the specified yield strength of longitudinal bars, as per ACI 318-14, resulted in reasonable estimates of peak moment strength for columns CH100, CL100 and CH60. For those columns, the estimated probable moment strengths were consistently lower than the peak measure moment strength by 10 to 15%. Due to the hardening behavior of the ASTM A1035 bars in CM100, its probable moment strength was underestimated by approximately 38% when using the specified yield strength of 100 ksi in the calculations and 24% when using the measured yield strength of the bars. Results therefore indicate that a factor higher than 1.25 may be warranted when estimating the probable moment strength of columns with A1035 longitudinal bars.

➤ ***Effects of Bar Mechanical Properties on Column Energy Dissipation***

The amount of total energy dissipated in the first cycles to the drift targets was similar for all members, even though there were large differences in the moment strengths of the columns. However, the cumulative dissipated energy in the second cycles showed more pronounced differences, with CM100 dissipating 17% less energy during the second cycle to the 4.0% drift target as compared to CH100. When normalized by the nominal moment strength of each member, CH60 was seen to have a significantly larger normalized energy dissipation capacity given a design strength than CH100, CL100 and especially CM100. The lower amount of dissipated energy in CM100 can partly be attributed to the higher peak strength it exhibited given that it had the same elastic stiffness as the other columns, and partly due to the a less steep unloading lateral stiffness. Bars with a higher T/Y ratio resulted in larger energy dissipation.

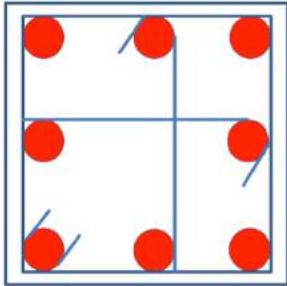
➤ ***Low-Cycle Fatigue Life of Bars***

As demonstrated in Chase and Ghannoum (2015), grade 100 bars under development today possess highly variable low-cycle fatigue performance. Therefore, the drift-capacity conclusions made in this study only apply to bars having similar low-cycle fatigue performance as those tested in this study.

Appendix A

Appendix A1: Design Calculations and checks (per ACI 318-14) for columns in Special Moment Frames

Columns Reinforced with Grade 100 Steel – CH100, CL100, CM100



$$\begin{aligned}
 cv &:= 1 \text{ in} & db &:= 0.75 \cdot \text{in} & dt &:= 0.5 \text{ in} \\
 fc &:= 5 \text{ ksi} & Ab &:= db^2 \cdot \frac{3.14}{4} & At &:= dt^2 \cdot \frac{3.14}{4} \\
 l_w &:= 108 \cdot \text{in} & f_{yl} &:= 104 \text{ ksi} & f_{yt} &:= 105 \text{ ksi} \\
 E &:= 29000 \text{ ksi} \\
 E_c &:= 57000 \cdot \frac{\sqrt{fc \cdot 1000 \text{ ksi}}}{1000} = 4.031 \times 10^3 \cdot \text{ksi}
 \end{aligned}$$

1. Checks from ACI 318-14

18.7.2.1 Shortest cross sectional dimension: >12 in b := 18 in h := 18 in
 18.7.2.1 Short to long dimension ratio > 0.4

$$\frac{b}{h} = 1 \quad d := h - cv - dt - \frac{db}{2} = 16.125 \cdot \text{in}$$

18.7.4 Area of longitudinal reinforcement:

$$\begin{aligned}
 A_{min} &:= 0.01 \cdot b \cdot h = 3.24 \cdot \text{in}^2 \\
 A_{max} &:= 0.06 \cdot b \cdot h = 19.44 \cdot \text{in}^2 & A_{st} &:= 8 \cdot Ab = 3.532 \cdot \text{in}^2
 \end{aligned}$$

18.7.5 Transverse Reinforcement

$$l_0 := \max\left(18 \text{ in}, \frac{l_w}{6}, d\right) = 18 \cdot \text{in}$$

18.7.5.2 Spacing of crossties or legs of rectilinear hoops:

$$\begin{aligned}
 hx_{max} &:= 14 \text{ in} \\
 hx &:= \frac{(b - 2cv - dt)}{2} = 7.75 \cdot \text{in}
 \end{aligned}$$

18.7.5.3 Spacing of transverse reinforcement:

$$s_0 := \min\left[6 \cdot db, 4 \text{ in} + \frac{(14 \text{ in} - hx)}{2}, \frac{h}{4}\right] = 4.5 \cdot \text{in}$$

Chosen spacing: $s_v := 3.5 \text{ in}$

Forces in each reinforcing layer:

$$F1 := \begin{cases} \frac{\epsilon s3}{|\epsilon s3|} \cdot f_{yl} \cdot A1 & \text{if } |\epsilon s1| > \frac{f_{yl}}{E} \\ \epsilon s1 \cdot E \cdot A1 & \text{otherwise} \end{cases} = 117.852 \cdot \text{kip}$$

$$F2 := \begin{cases} \frac{\epsilon s3}{|\epsilon s3|} \cdot f_{yl} \cdot A2 & \text{if } |\epsilon s2| > \frac{f_{yl}}{E} \\ \epsilon s2 \cdot E \cdot A2 & \text{otherwise} \end{cases} = -53.826 \cdot \text{kip}$$

$$F3 := \begin{cases} \frac{\epsilon s3}{|\epsilon s3|} \cdot 1.25 f_{yl} \cdot A3 & \text{if } |\epsilon s3| > \frac{f_{yl}}{E} \\ \epsilon s3 \cdot E \cdot A3 & \text{otherwise} \end{cases} = -172.209 \cdot \text{kip}$$

Compression force from concrete: $F_c := 0.85 \cdot \beta \cdot f_c \cdot b \cdot c = 361.08 \cdot \text{kip}$

$$F := F1 + F2 + F3 + F_c = 252.897 \cdot \text{kip}$$

$$M_{pr} := F_c \cdot \left(\frac{-\beta \cdot c}{2} + \frac{h}{2} \right) + F1 \cdot \left(-d1 + \frac{h}{2} \right) + F2 \cdot \left(-d2 + \frac{h}{2} \right) + F3 \cdot \left(-d3 + \frac{h}{2} \right) = 4.609 \times 10^3 \cdot \text{kip} \cdot \text{in}$$

Mpr from OpenSees:

$$M_{pr} := 4490 \text{kip} \cdot \text{in}$$

$$\gamma := \frac{F}{b \cdot h \cdot f_c} = 0.156$$

Shear: $\lambda := 1$

$$V_e := \frac{2M_{pr}}{l} = 83.148 \cdot \text{kip}$$

$$V_{n\text{required}} := \frac{V_e}{0.75} = 110.864 \cdot \text{kip}$$

$$\tau := \frac{\frac{V_e}{\text{kip}} \cdot 1000}{\frac{b}{\text{in}} \cdot \frac{d}{\text{in}} \cdot \sqrt{\frac{f_c}{\text{ksi}} \cdot 1000}} = 4.051$$

Check ACI 21.6.5.2 Shall we account for V_c ?

- a) Induced shear force represents more than one-half of the shear strength
- b) Factored axial load:

$$F = 252.897 \cdot \text{kip} \quad \sigma := b \cdot h \cdot \frac{f_c}{20} = 81 \cdot \text{kip}$$

Axial compression is more than 5% of the capacity, thus we should consider V_c .

$$V_c := 2 \cdot \left(1 \text{ksi} + \frac{F \cdot 1000}{2000 \cdot b \cdot h} \right) \cdot \lambda \cdot \sqrt{\frac{f_c \cdot 1000}{\text{ksi}}} \cdot b \cdot \frac{\left(h - c_v - d_t - \frac{d_b}{2} \right)}{1000} = 57.067 \cdot \text{kip}$$

$$V_{s\text{required}} := V_{n\text{required}} - V_c = 53.797 \cdot \text{kip}$$

$$V_{s\text{provided}} := 3 \cdot A_t \cdot f_{yt} \cdot \frac{(h - c_v)}{s} = 300.263 \cdot \text{kip}$$

$$A_{v\text{required}} := \frac{V_{s\text{required}} \cdot s}{f_{yt} \cdot \left(h - c_v - d_t - \frac{d_b}{2} \right)} = 0.111 \cdot \text{in}^2$$

$$V_{n\text{provided}} := V_c + V_{s\text{provided}} = 357.33 \cdot \text{kip}$$

$$A_{v\text{provided}} := 3 \cdot A_t = 0.589 \cdot \text{in}^2$$

$$\omega_w := \frac{A_{v\text{required}}}{A_{v\text{provided}}} = 0.189$$

Detailing

Minimum Hook Lengths:

For longitudinal reinforcement hooks: 90* hook length: $l_{b1} := 12 \cdot d_b = 9 \cdot \text{in}$

180* hook length: $l_{b2} := 4 \cdot d_b = 3 \cdot \text{in}$

For tie hooks: $l_v := 6 \cdot d_t = 3 \cdot \text{in}$

Minimum Bend Diameters:

For longitudinal reinforcement: $\theta_l := 6 \cdot d_b = 4.5 \cdot \text{in}$

For ties: $\theta_v := 4 \cdot d_t = 2 \cdot \text{in}$

Confined concrete

1. Confining Pressure

$$bc := b - 2 \cdot cv - 2 \cdot \frac{dt}{2} = 15.5 \cdot \text{in} \quad hc := bc = 15.5 \cdot \text{in}$$
$$frx := \frac{3 \cdot At \cdot fyt}{s \cdot bc} = 1.14 \cdot \text{ksi} \quad fry := frx = 1.14 \cdot \text{ksi}$$

2. Effective Area

$$wi := \frac{bc - 2 \cdot cv - 2 \cdot dt - 3 \cdot db}{2} = 5.125 \cdot \text{in}$$
$$Aineff := \frac{8 \cdot wi^2}{6} = 35.021 \cdot \text{in} \cdot (\text{in}) \quad s1 := s - 2 \cdot \frac{dt}{2} = 3 \cdot \text{in}$$
$$Aeff := (bc \cdot hc - Aineff) \left(1 - \frac{s1}{2 \cdot bc}\right) \cdot \left(1 - \frac{s1}{2 \cdot hc}\right) = 167.429 \cdot \text{in} \cdot \text{in}$$
$$Acc := hc \cdot bc - 8 \cdot Ab = 236.718 \cdot \text{in} \cdot \text{in}$$

3. Effective confinement coefficient

$$ke := \frac{Aeff}{Acc} = 0.707$$

4. Effective lateral confining pressure

$$freff := ke \cdot frx = 0.806 \cdot \text{ksi} \quad \frac{freff}{fc} = 0.161 \text{ ----->>>>>}$$
$$fcc := 1.85 \cdot fc = 9.25 \cdot \text{ksi}$$

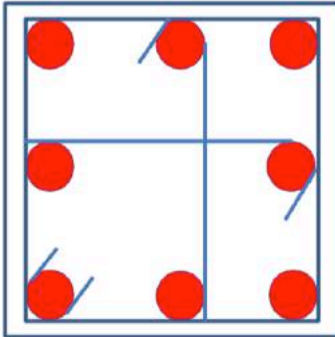
5. Strain at ultimate stress

$$\epsilon_{cc} := \epsilon_{co} \cdot \left[1 + 5 \cdot \left(\frac{fcc}{fc} - 1\right)\right] = 0.011 \quad \epsilon_{co} := 0.002 \quad \text{Ref: Mander et al}$$

6. Maximum strain capacity of confined concrete

$$\rho_s := \frac{At \cdot bc \cdot 6}{Acc \cdot s} = 0.022$$
$$\epsilon_{cmax} := 0.004 + 0.1 \cdot \frac{\rho_s \cdot f_{yl}}{fc} = 0.05$$

Column Reinforced with Grade 60 Steel - CH60



$$\begin{aligned}
 c_v &:= 1 \text{ in} & d_b &:= 0.75 \cdot \text{in} & d_t &:= 0.5 \text{ in} \\
 f_c &:= 5.0 \text{ ksi} & A_b &:= d_b^2 \cdot \frac{3.14}{4} & A_t &:= d_t^2 \cdot \frac{3.14}{4} \\
 l_w &:= 108 \cdot \text{in} & f_{yl} &:= 64 \text{ ksi} & f_{yt} &:= 65 \text{ ksi} \\
 & & E &:= 29000 \text{ ksi} & & \\
 E_c &:= 57000 \cdot \frac{\sqrt{f_c \cdot 1000 \text{ ksi}}}{1000} = 4.031 \times 10^3 \cdot \text{ksi}
 \end{aligned}$$

1. Checks from ACI 318-14

18.7.2.1 Shortest cross sectional dimension: >12 in

$$b := 18 \text{ in} \quad h := 18 \text{ in}$$

18.7.2.1 Short to long dimension ratio > 0.4

$$\frac{b}{h} = 1 \quad d := h - c_v - d_t - \frac{d_b}{2} = 16.125 \cdot \text{in}$$

18.7.4 Area of longitudinal reinforcement:

$$A_{min} := 0.01 \cdot b \cdot h = 3.24 \cdot \text{in}^2$$

$$A_{max} := 0.06 \cdot b \cdot h = 19.44 \cdot \text{in}^2 \quad A_{st} := 8 \cdot A_b = 3.532 \cdot \text{in}^2$$

18.7.5 Transverse Reinforcement

$$l_0 := \max\left(18 \text{ in}, \frac{l}{6}, d\right) = 18 \cdot \text{in}$$

18.7.5.2 Spacing of cross-ties or legs of rectilinear hoops:

$$h_{xmax} := 14 \text{ in}$$

$$h_x := \frac{(b - 2c_v - d_t)}{2} = 7.75 \cdot \text{in}$$

18.7.5.3 Spacing of transverse reinforcement:

$$s_0 := \min\left[6 \cdot d_b, 4 \text{ in} + \frac{(14 \text{ in} - h_x)}{2}, \frac{h}{4}\right] = 4.5 \cdot \text{in}$$

$$\text{Chosen spacing: } s_w := 4.5 \text{ in}$$

b) Cross sectional area:

$$Ash1 := 0.3 \cdot s \cdot (b - 2cv) \cdot \frac{(b \cdot h) - (b - 2cv)(h - 2cv)}{(b - 2cv)(h - 2cv)} \cdot \frac{fc}{fyt} = 0.441 \cdot \text{in}^2$$

$$Ash2 := 0.09 \cdot s \cdot (b - 2 \cdot cv) \cdot \frac{fc}{fyt} = 0.498 \cdot \text{in}^2$$

$$Ash := \max(Ash1, Ash2) = 0.498 \cdot \text{in}^2 \quad Ashprovided := 3 \cdot At = 0.589 \cdot \text{in}^2$$

2. Calculate M_{pr} :

Longitudinal bar layer position relative to the top concrete fiber of the section, and area per layer:

$$d1 := cv + \frac{db}{2} = 1.375 \cdot \text{in} \quad A1 := 3 \cdot Ab = 1.325 \cdot \text{in}^2$$

$$d2 := d1 + \frac{(h - 2 \cdot d1)}{2} = 9 \cdot \text{in} \quad A2 := 2 \cdot Ab = 0.883 \cdot \text{in}^2$$

$$d3 := d2 + \frac{(h - 2 \cdot d1)}{2} = 16.625 \cdot \text{in} \quad A3 := 3 \cdot Ab = 1.325 \cdot \text{in}^2$$

Concrete compression block parameter: $\beta := 0.85 - 0.05 \cdot \left(-4 + \frac{fc}{\text{ksi}} \right) = 0.8$
(ratio of max stress to avg stress)

Assume NA depth: $c := 5.3 \text{in}$

Assume strain at top fiber concrete is (conservative): $\epsilon_{cu} := 0.004$

Assuming plain sections remain plain, the strain in each reinforcing layer is:

$$\epsilon_{s1} := \epsilon_{cu} \cdot \frac{(c - d1)}{c} = 2.962 \times 10^{-3}$$

$$\epsilon_{s2} := \epsilon_{cu} \cdot \frac{(c - d2)}{c} = -2.792 \times 10^{-3}$$

$$\epsilon_{s3} := \epsilon_{cu} \cdot \frac{(c - d3)}{c} = -8.547 \times 10^{-3}$$

Forces in each reinforcing layer:

$$F1 := \begin{cases} \frac{\epsilon_{s1}}{|\epsilon_{s1}|} \cdot f_{yl} \cdot A1 & \text{if } |\epsilon_{s1}| > \frac{f_{yl}}{E} \\ \epsilon_{s1} \cdot E \cdot A1 & \text{otherwise} \end{cases} = 84.78 \cdot \text{kip}$$

$$F2 := \begin{cases} \frac{\epsilon_{s2}}{|\epsilon_{s2}|} \cdot f_{yl} \cdot A2 & \text{if } |\epsilon_{s2}| > \frac{f_{yl}}{E} \\ \epsilon_{s2} \cdot E \cdot A2 & \text{otherwise} \end{cases} = -56.52 \cdot \text{kip}$$

$$F3 := \begin{cases} \frac{\epsilon_{s3}}{|\epsilon_{s3}|} \cdot 1.25 f_{yl} \cdot A3 & \text{if } |\epsilon_{s3}| > \frac{f_{yl}}{E} \\ \epsilon_{s3} \cdot E \cdot A3 & \text{otherwise} \end{cases} = -105.975 \cdot \text{kip}$$

Compression force from concrete: $F_c := 0.85 \cdot \beta \cdot f_c \cdot b \cdot c = 324.36 \cdot \text{kip}$

$$F := F1 + F2 + F3 + F_c = 246.645 \cdot \text{kip}$$

$$M_{pr} := F_c \cdot \left(\frac{-\beta \cdot c}{2} + \frac{h}{2} \right) + F1 \cdot \left(-d1 + \frac{h}{2} \right) + F2 \cdot \left(-d2 + \frac{h}{2} \right) + F3 \cdot \left(-d3 + \frac{h}{2} \right) = 3.686 \times 10^3 \cdot \text{kip} \cdot \text{in}$$

Mpr from OpenSees:

$$M_{pr} := 3525 \text{ kip} \cdot \text{in}$$

$$\gamma := \frac{F}{b \cdot h \cdot f_c} = 0.152$$

Shear: $\lambda := 1$

$$V_e := \frac{2M_{pr}}{l} = 74.074 \cdot \text{kip}$$

$$V_{nrequired} := \frac{V_e}{0.75} = 98.765 \cdot \text{kip}$$

$$\tau := \frac{\frac{V_e}{\text{kip}} \cdot 1000}{\frac{b}{\text{in}} \cdot \frac{d}{\text{in}} \cdot \sqrt{\frac{f_c}{\text{ksi}} \cdot 1000}} = 3.609$$

Check shall we account for V_c ?

- a) Induced shear force represents more than one-half of the shear strength
- b) Factored axial load:

$$F = 246.645 \cdot \text{kip} \quad \sigma := b \cdot h \cdot \frac{f_c}{20} = 81 \cdot \text{kip}$$

Axial compression is more than 5% of the capacity, thus we are allowed to consider V_c .

$$V_c := 2 \cdot \left(1 \text{ksi} + \frac{F \cdot 1000}{2000 \cdot b \cdot h} \right) \cdot \lambda \cdot \sqrt{\frac{f_c \cdot 1000}{\text{ksi}}} \cdot b \cdot \frac{\left(h - c_v - d_t - \frac{d_b}{2} \right)}{1000} = 56.671 \cdot \text{kip}$$

$$V_{srequired} := V_{nrequired} - V_c = 42.094 \cdot \text{kip}$$

$$V_{sprovided} := 3 \cdot A_t \cdot f_{yt} \cdot \frac{(h - c_v)}{s} = 144.571 \cdot \text{kip}$$

$$A_{vrequired} := \frac{V_{srequired} \cdot s}{f_{yt} \cdot \left(h - c_v - d_t - \frac{d_b}{2} \right)} = 0.181 \cdot \text{in}^2$$

$$V_{nprovided} := V_c + V_{sprovided} = 201.242 \cdot \text{kip}$$

$$A_{vprovided} := 3 \cdot A_t = 0.589 \cdot \text{in}^2$$

$$\omega_v := \frac{A_{vrequired}}{A_{vprovided}} = 0.307$$

Detailing

Minimum Hook Lengths:

For longitudinal reinforcement hooks: 90° hook length: $l_{b1} := 12 \cdot d_b = 9 \cdot \text{in}$
 180° hook length: $l_{b2} := 4 \cdot d_b = 3 \cdot \text{in}$
 For tie hooks: $l_v := 6 \cdot d_t = 3 \cdot \text{in}$

Minimum Bend Diameters:

For longitudinal reinforcement: $\theta_l := 6 \cdot d_b = 4.5 \cdot \text{in}$
 For ties: $\theta_v := 4 \cdot d_t = 2 \cdot \text{in}$

Confined concrete

1. Confining Pressure

$$bc := b - 2 \cdot cv - 2 \cdot \frac{dt}{2} = 15.5 \cdot \text{in} \quad hc := bc = 15.5 \cdot \text{in}$$

$$frx := \frac{3 \cdot At \cdot fyt}{s \cdot bc} = 0.549 \cdot \text{ksi} \quad fry := frx = 0.549 \cdot \text{ksi}$$

2. Effective Area

$$wi := \frac{bc - 2 \cdot cv - 2 \cdot dt - 3 \cdot db}{2} = 5.125 \cdot \text{in}$$

$$Aineff := \frac{8 \cdot wi^2}{6} = 35.021 \cdot \text{in} \cdot \text{in} \quad s1 := s - 2 \cdot \frac{dt}{2} = 4 \cdot \text{in}$$

$$Aeff := (bc \cdot hc - Aineff) \left(1 - \frac{s1}{2 \cdot bc}\right) \left(1 - \frac{s1}{2 \cdot hc}\right) = 155.684 \cdot \text{in} \cdot \text{in}$$

$$Acc := hc \cdot bc - 8 \cdot Ab = 236.718 \cdot \text{in} \cdot \text{in}$$

3. Effective confinement coefficient

$$ke := \frac{Aeff}{Acc} = 0.658$$

4. Effective lateral confining pressure

$$freff := ke \cdot frx = 0.361 \cdot \text{ksi} \quad \frac{freff}{fc} = 0.072 \quad \text{----->>>>>$$

$$fcc := 1.46 \cdot fc = 7.3 \cdot \text{ksi}$$

5. Strain at ultimate stress

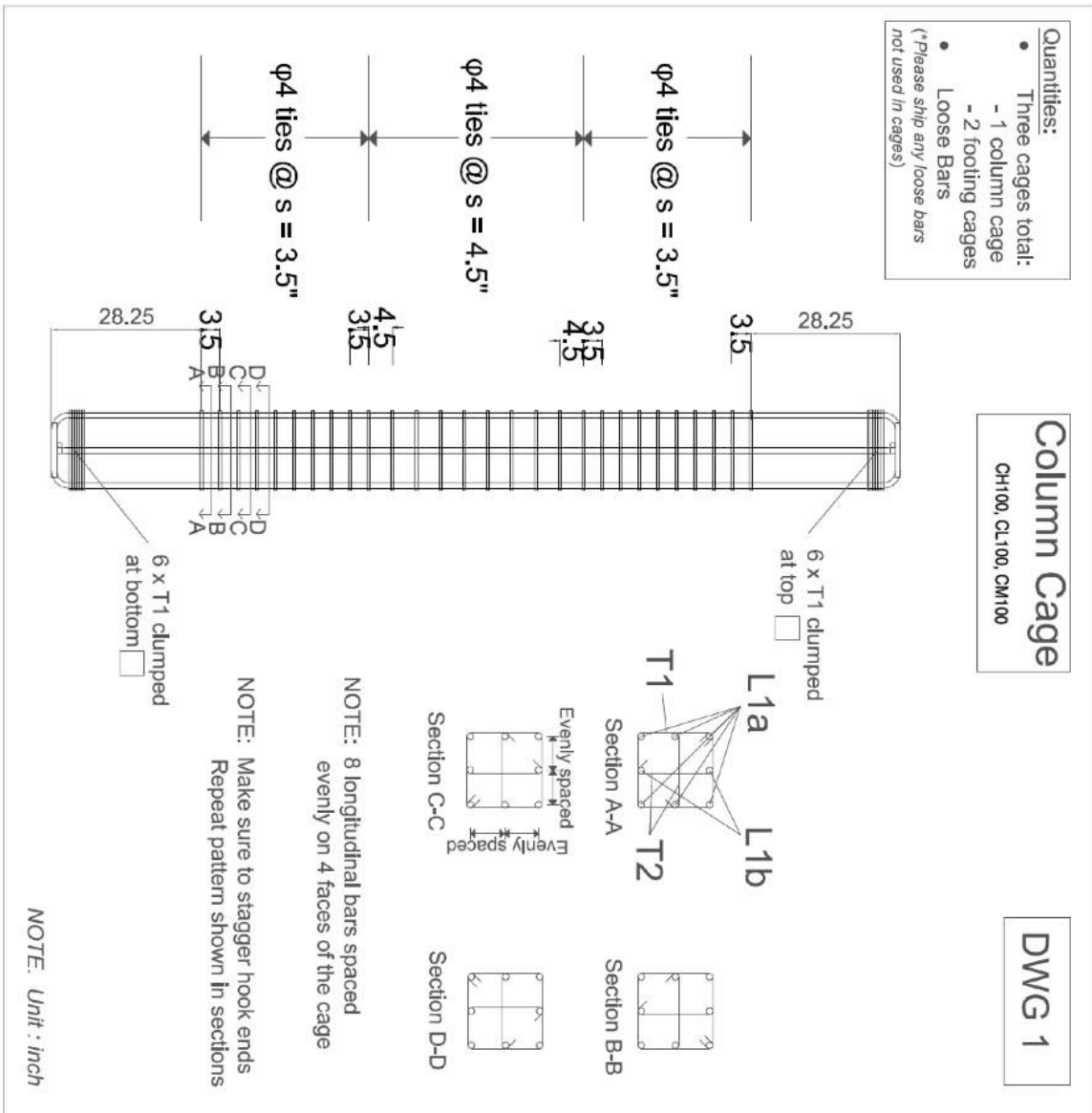
$$\epsilon_{cc} := \epsilon_{co} \left[1 + 5 \cdot \left(\frac{fcc}{fc} - 1\right)\right] = 6.6 \times 10^{-3} \quad \epsilon_{co} := 0.002 \quad \text{Ref: Mander et al}$$

6. Maximum strain capacity of confined concrete

$$\epsilon_{cmax} := 0.004 + 0.1 \cdot \frac{\rho_s \cdot fy1}{fc} = 0.026$$

$$\rho_s := \frac{At \cdot bc \cdot 6}{Acc \cdot s} = 0.017$$

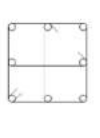
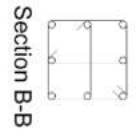
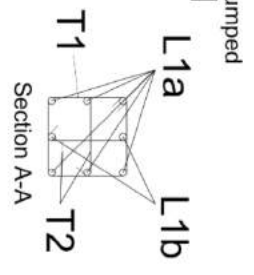
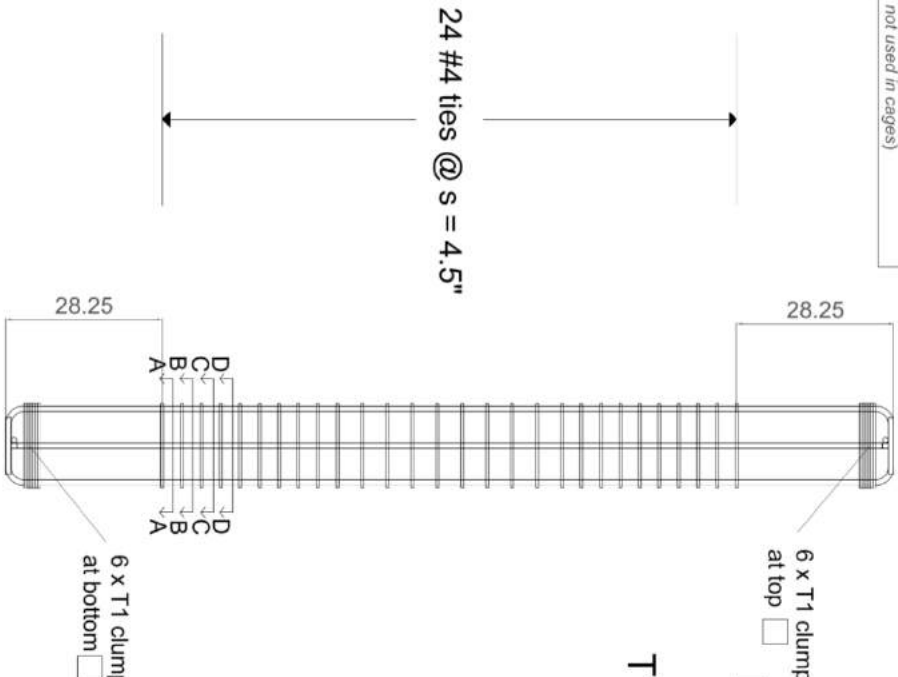
Appendix A2: Detailed drawings of the specimens



Column Cage CH60

DWG 1b

- Quantities:
- Three cages total:
 - 1 column cage
 - 2 footing cages
 - Loose Bars
- (*Please strip any loose bars not used in cages)



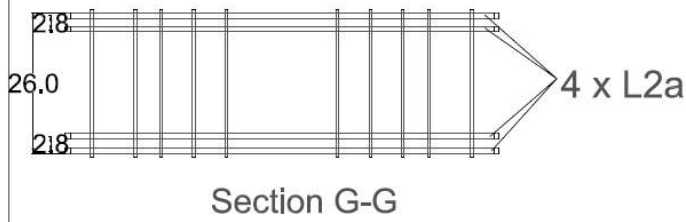
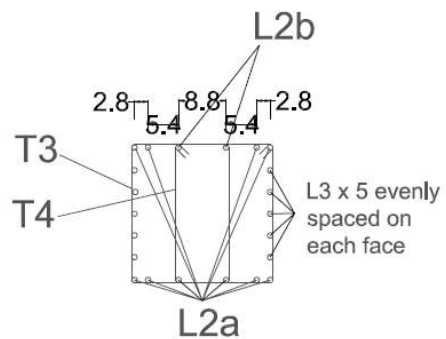
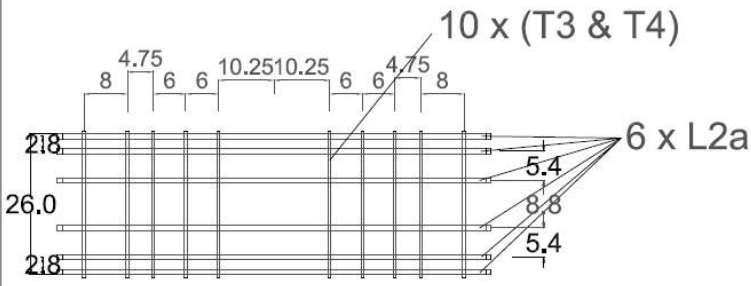
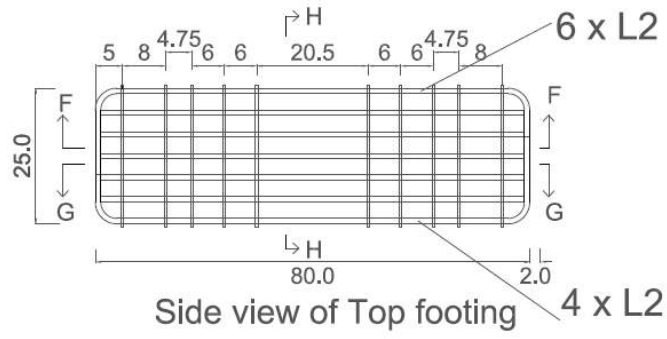
NOTE: Make sure to stagger hook ends
Repeat pattern shown in sections

NOTE: Unit : inch

- Quantities:**
- Three cages total:
 - 1 column cage
 - 2 footing cages
 - Loose Bars
 (*Please ship any loose bars not used in cages)

Footing Cages
Quantity = 2

DWG 2



NOTE: Make sure to stagger hook ends

NOTE. Unit : inch

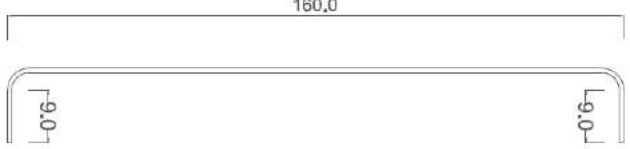
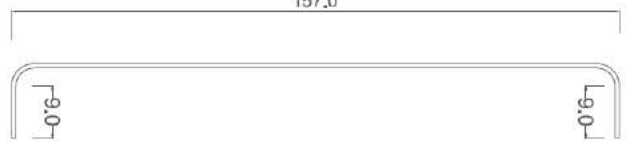
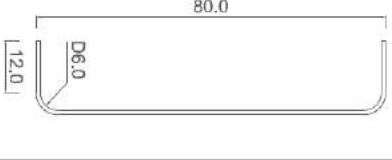
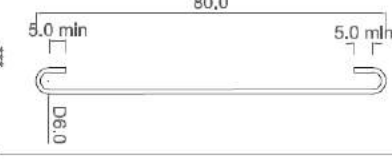
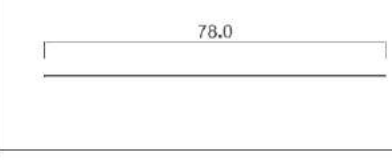
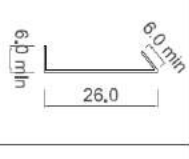
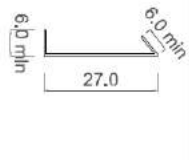
DWG 3

Tolerances:
 T1, T2 +/- 1/4 "
 All others +/- 1/2 "

Bar schedule

GR60 Bars A706 or A615
 GR100 Bars Special Grade

Note: Unit : Inch
 T1, T2, CP1 must be from same heat
 L1a, L1b, and CP2 must be from same heat

L1a	L1b	L2a	L2b	L3	L4	L5
						
<p>NOTE: Bend inside diameter = 3.0" for #4 bars Bend inside diameter = 4.5" for #6 bars As specified - for other bars</p>						

*** Please ship any loose bars not used in cages.

NOTE: Unit : Inch

203

DWG 4

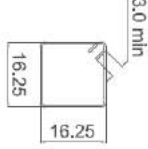
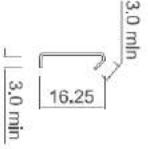
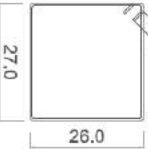
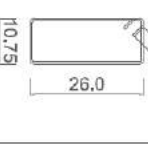
Tolerances:
 T1, T2 + $-1/4$ "
 All others + $-1/2$ "

Bar schedule

GR60 Bars A706 or A615
 GR100 Bars Special Grade

Note: Unit : Inch

T1, T2, CP1 must be from same heat
 L1a, L1b, and CP2 must be from same heat

T1	T2	T3	T4				
#4 Gr 100 bar x 40	#4 Gr 100 bar x 80	#4 Gr 60 ties x 20	#4 Gr 60 ties x 20				
							

NOTE. Bend inside diameter = 3.0" for #4 bars

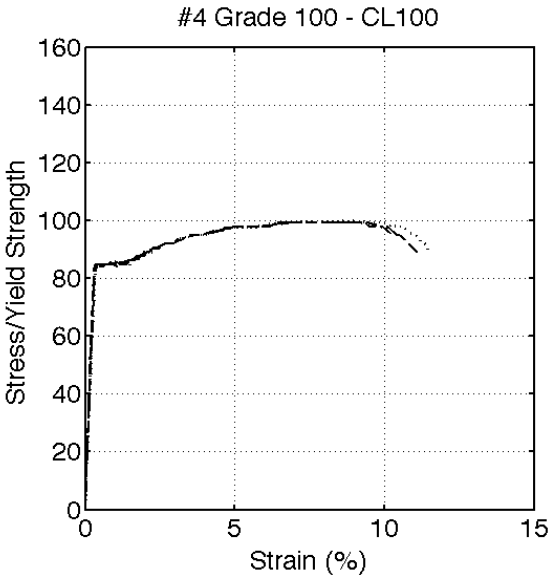
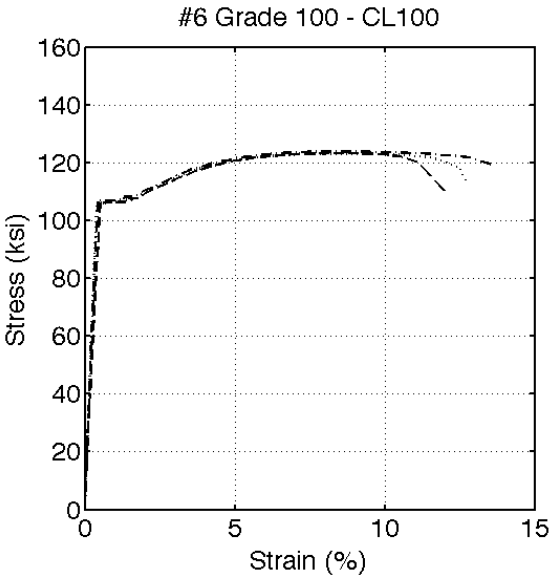
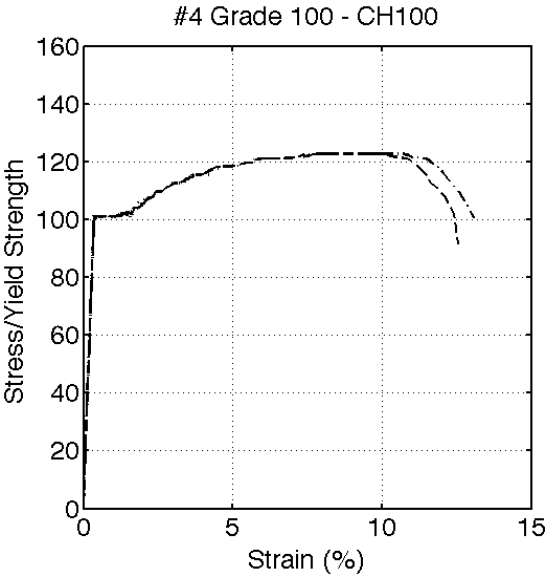
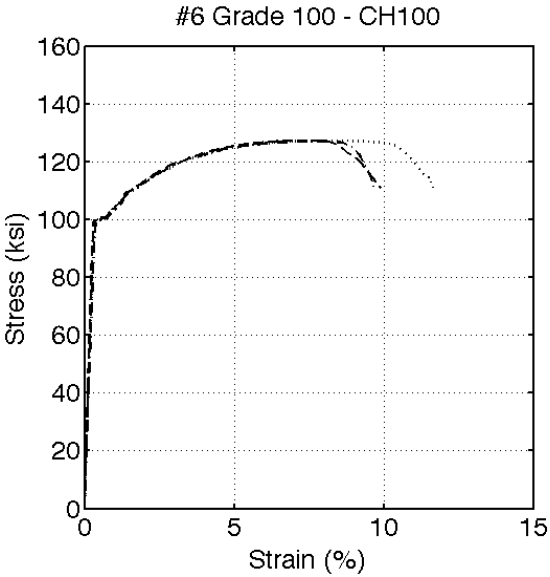
NOTE: Unit : Inch

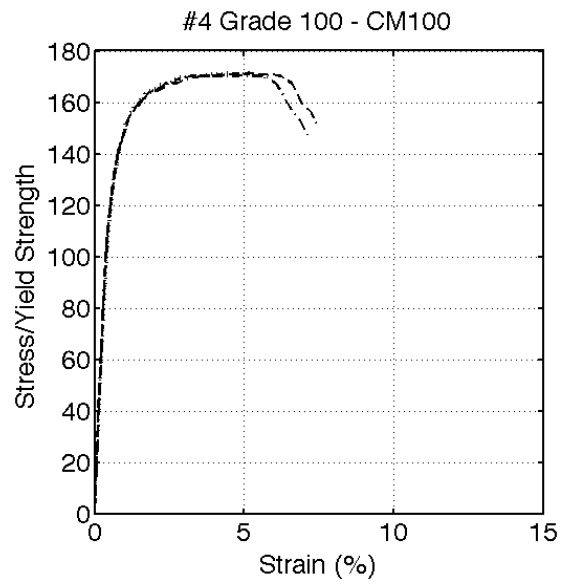
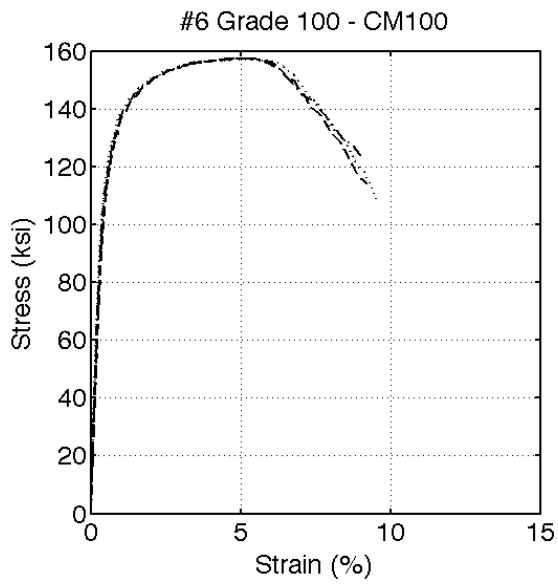
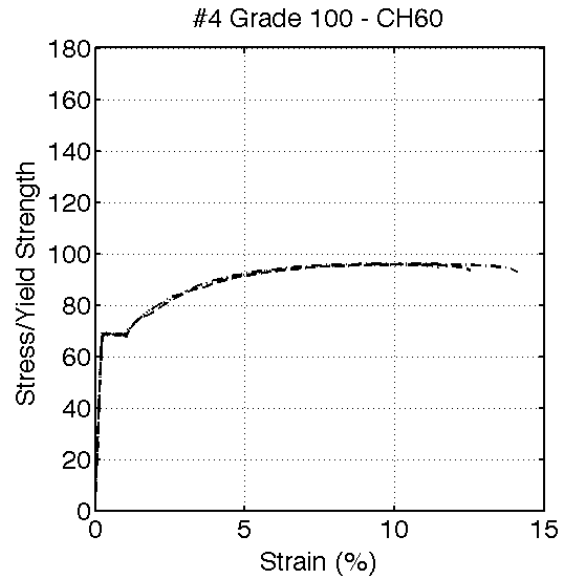
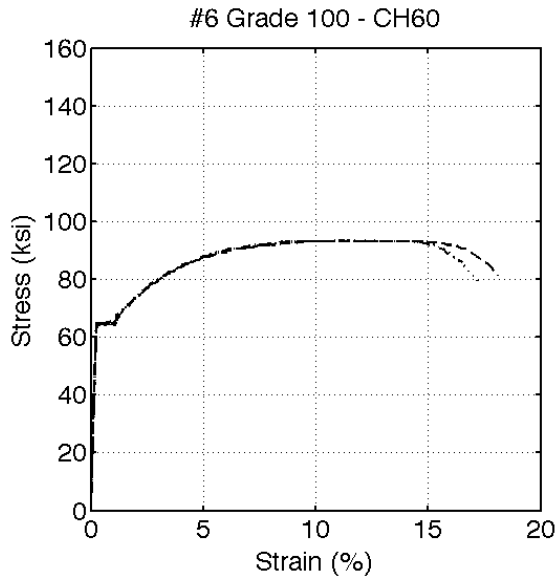
Appendix B

Appendix B1: Concrete cylinders' from columns - compressive strength

		Cylinder 1	Cylinder 2	Cylinder 3	Average
CH100	7 days	4.13	3.93	3.96	4.01
	14 days	4.88	4.67	4.57	4.71
	21 days	4.99	4.86	4.69	4.85
	28 days	5.27	5.10	5.15	5.17
	Day of the test	5.17	5.24	5.21	5.21
CL100	7 days	3.85	4.09	4.01	3.98
	14 days	4.79	4.53	4.67	4.66
	21 days	5.04	5.07	5.05	5.05
	28 days	5.20	4.90	5.31	5.13
	Day of the test	5.30	5.08	5.11	5.16
CM100	7 days	5.00	4.80	4.88	4.89
	14 days	N/A	N/A	N/A	N/A
	21 days	N/A	N/A	N/A	N/A
	28 days	5.56	5.44	5.48	5.49
	Day of the test	5.60	5.50	5.63	5.58
CH60	7 days	3.34	3.41	3.29	3.35
	14 days	4.23	4.12	4.18	4.18
	21 days	4.36	4.31	4.41	4.36
	28 days	4.45	4.41	4.47	4.48
	Day of the test	4.48	4.69	4.54	4.57

Appendix B2: Steel tensile test results





Bar Size	Specimen	Trial Number	Yield Strength (ksi)	Tensile Strength (ksi)	Tensile to Yield Ratio	Elastic Modulus (ksi)	Uniform Elongation (%)	Fracture Elongation (%)
#6	CH100	1	99.965	127.049	1.271	29,920	7.425	9.754
		2	99.802	127.242	1.275	30,170	8.179	11.653
		3	100.149	127.354	1.272	33,950	7.123	9.875
	CL100	1	106.866	123.884	1.159	25,150	8.883	12.702
		2	106.134	123.089	1.160	26,240	8.571	12.698
		3	106.261	123.234	1.160	20,374	8.412	12.016
	CM100	1	122.961	157.378	1.280	27,230	4.884	10.164
		2	124.977	157.392	1.259	28,480	4.957	9.700
		3	124.540	157.387	1.264	24,570	4.915	9.459
	CH60	1	64.472	93.355	1.448	25,640	11.401	16.920
		2	64.387	93.396	1.451	26,200	11.716	17.531
		3	64.390	93.199	1.447	27,000	12.174	18.351
#4	CH100	1	101.069	122.698	1.214	28,349	9.282	13.263
		2	101.082	N/A	N/A	28,740	N/A	N/A
		3	101.024	122.683	1.214	28,266	8.752	12.400
	CL100	1	84.387	99.331	1.177	25,986	8.010	11.276
		2	84.726	99.970	1.180	24,461	8.298	11.959
		3	84.677	99.351	1.173	28,346	7.810	11.379
	CM100	1	141.518	170.412	1.204	22,590	4.468	8.170
		2	141.656	171.735	1.212	21,890	4.519	8.007
		3	138.375	171.279	1.238	25,400	5.012	9.696
	CH60	1	66.602	96.150	1.444	30,400	0.102	0.153
		2	N/A	N/A	N/A	N/A	N/A	N/A
		3	67.800	94.694	1.397	30,900	0.010	0.140

Appendix C

Applied base shear and axial load were computed by enforcing large-deformation equilibrium on the test frame using the recorded actuator loads and displacements. A free body diagram of the applied forces is shown in figure below. Column forces applied to the frame are assumed to be point loads applied from a single point on the actuator. The locations of the actuator's ends were measured prior to the test, in order for the initial angles to be tared accordingly. Potentiometers measured the movement of the frame needed to interpolate the angle differences and the resulting forces.

$$\theta_N = \sin^{-1} \left(\frac{\Delta_H + \Delta_{H0N}}{\Delta_{VN} + \Delta_{V0N}} \right)$$

$$\theta_S = \sin^{-1} \left(\frac{\Delta_H + \Delta_{H0S}}{\Delta_{VS} + \Delta_{V0S}} \right)$$

$$\theta_H = \sin^{-1} \left(\frac{\Delta_{Vframe} + \Delta_{H0}}{\Delta_{Hact} + \Delta_{H0act}} \right)$$

$$V = H \cdot \cos\theta_H + V_N \cdot \sin\theta_N + V_S \cdot \sin\theta_S$$

$$P = H \cdot \sin\theta_H + V_N \cdot \cos\theta_N + V_S \cdot \cos\theta_S$$

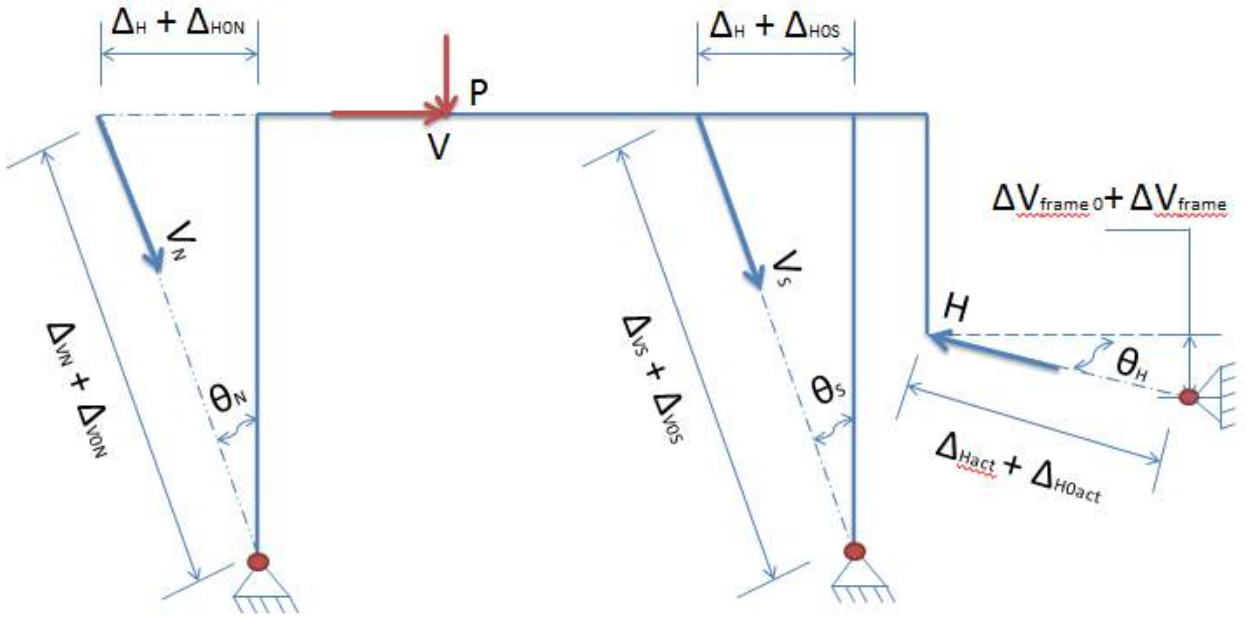
Δ_H = Horizontal displacement of the column

Δ_{VN} = Vertical movement of the north actuator

Δ_{VS} = Vertical movement of the south actuator

Δ_{Vframe} = Vertical movement of the steel frame

Δ_{Hact} = Movement of horizontal actuator



References

American Concrete Institute (ACI) Committee 318 (1956), "Building Code Requirement for Reinforced Concrete (ACI 318-56)", American Concrete Institute, Detroit, MI.

American Concrete Institute (ACI) Committee 318 (1971), "Building Code Requirement for Reinforced Concrete (ACI 318-71)", American Concrete Institute, Detroit, MI.

American Concrete Institute (ACI) Committee 318 (2014), "Building Code Requirements for Reinforced Concrete (ACI 318-14)," American Concrete Institute, Farmington Hills, MI

American Concrete Institute (ACI), 2010, Design Guide for the Use of ASTM A1035/A1035M Grade 100 Steel Bars for Structural Concrete, ACI ITG-6R-10, American Concrete Institute, Farmington Hills, Michigan.

Aoyama, H., 2001, "Design of Modern Highrise Reinforced Concrete Structures", Imperial College Press, London, United Kingdom.

ASTM A1035 / A1035M-16, Specification for Deformed and Plain, Low-Carbon, Chromium, Steel Bars for Concrete Reinforcement, ASTM International, West Conshohocken, PA, 2016, www.astm.org

ASTM A370-16, Standard Test Methods and Definitions for Mechanical Testing of Steel Products, ASTM International, West Conshohocken, PA, 2016, www.astm.org

ASTM A615 / A615M-16, Standard Specification for Deformed and Plain Carbon-Steel Bars for Concrete Reinforcement, ASTM International, West Conshohocken, PA, 2016, www.astm.org

ASTM A706 / A706M-16a, Standard Specification for Deformed and Plain Low-Alloy Steel Bars for Concrete Reinforcement, ASTM International, West Conshohocken, PA, 2016, www.astm.org

ASTM C39 / C39M-16, Standard Test Method for Compressive Strength of Cylindrical Concrete Specimens, ASTM International, West Conshohocken, PA, 2016, www.astm.org

ASTM E8 / E8M-16a, Standard Test Methods for Tension Testing of Metallic Materials, ASTM International, West Conshohocken, PA, 2016, www.astm.org

Baker, A.L.L. (1956), "Ultimate Load Theory Applied to the Design of Reinforced and Prestressed Concrete Frames," Concrete Publications Ltd., London.

Baker, A.L.L. and Amarakone, A.M.N. (1964), "Inelastic Hyperstatic Frame Analysis," Proceedings International Symposium on the Flexural Mechanics of Reinforced Concrete, ACI SP-12, Miami, pp. 85-142.

Baker, A., and Amarakone, A., 1965, "Inelastic hyperstatic frames analysis." ACI Special Publication, No. 12, pp. 85-142.

Barbosa A. R., and Link T., Seismic Performance of High-Strength Steel RC Bridge Columns," ASCE Journal of Bridge Engineering, 2015.

Berry, M., Lehman D. E., and Lowes L. N. (2008), "Lumped-Plasticity Models for Performance Simulation of Bridge Columns", ACI Structural Journal, V. 105, No. 3, May-June, pp. 270-279. 2015,

Berry, P. B., Eberhardt M. O (2008), "Performance Modelling Strategies for Modern Reinforced Concrete Bridge Columns", PEER Report

Brown, Jeff, Kunnath, Sashi K. "Low-Cycle Fatigue Failure of Reinforcing Steel Bars." *ACI Materials Journal* 6.110, 2004, 457-65.

Caifu, Y., 2010, "Development of high strength construction rebars," Proceedings, International Seminar on Production and Application of High Strength Seismic Grade Rebar Containing Vanadium, Central Iron & Steel Research Institute, Beijing, China.

Cheng M. Y., and Gduquoio M. B., "Cyclic Behavior of Reinforced Concrete Flexural Members using High-Strength Flexural Reinforcement." *ACI Structural Journal*, 111 (4), July-August 2014.

Corley, W. G., 1966, "Rotational capacity of reinforced concrete beams," Proceedings of the American Society of Civil Engineers, ST 5, 121-146.

Erasmus, L., and Pussegoda, N., 1978, "Safe bend radii for deformed reinforcing bar to avoid failure by strain age embrittlement," *New Zealand Engineering*, Vol. 33, No. 8, pp. 170-177.

Federal Emergency Management Agency (FEMA), "Interim Testing Protocols for Determining the Seismic Performance Characteristics of Structural and Nonstructural Components." FEMA-461, Federal Emergency Management Agency, Washington, DC, 2007, 138.

Gladman, T., 'The physical metallurgy of microalloyed steels'; London, Institute of Materials, 1997.

Grimaldi A., Rinaldi, Z. "Influence of the Steel Properties on the Ductility of R.C. Structures". 12WCEE World Conf. on Earthquake Engineering, Auckland New Zealand, January 2000.

Limantono, A., A. "Modeling Strain Demands in Longitudinal Steel bars of Concrete Columns." Thesis, University of Texas at Austin, 2016.

Macchi, G., Pinto, P.E., Sanpaolesi, L., "Ductility requirements for reinforcement under Eurocodes," *Structural Engineering International*, 6.4, 1996, 249-54.

Mattock, A.H. (1964), "Rotational Capacity of Hinging Regions in Reinforced Concrete Beams," *Proceedings International Symposium on the Flexural Mechanics of Reinforced Concrete*, ACI SP-12, Miami, pp. 143-181.

Mattock, A.H. (1967), Discussion of "Rotational Capacity of Hinging Regions in Reinforced Concrete Beams," by Corley, W.G., *Journal of the Structural Division, ASCE*, V. 93, No. ST2, Apr., pp. 519-522.

MMFX Technologies Corporation, "Material Properties and Design Considerations MMFX2 (ASTM A1035/AASHTO MP18)," *MMFX Product Information*, December 2012, 36 pp.

NEHRP Consultants Joint Venture, "Use of High-Strength Reinforcement for Earthquake Resistant Concrete Structures," *NIST GCR 13-917-30*, Applied Technology Council, Redwood City, CA, 2013.

Panagiotakos, T. B., Fardis, M. N. "Deformations of Reinforced Concrete Members at Yielding and Ultimate.", *ACI Structural Journal*, 98 (2), Marh-April 2001, 135 - 148

Park, R. and Paulay, T., *Reinforced Concrete Structures*, Wiley, 1975,

Paulay T., and Priestley M. J. N. (1992), "Seismic Design of Reinforced Concrete and Masonry Structures", John Wiley & Sons, Inc

Restrepo, J. I., Seible, F., Stephan, B., Schoettler, J. "Seismic Testing of Bridge Columns Incorporating High-Performance Materials." *ACI Structural Journal*, 103 (4), July-August 2006, 496 – 504.

Restrepo-Posada, J.I., Dodd, L., Park, R., Cooke, N. "Variables Affecting Cyclic Behavior of Reinforcing Steel." *J. Struct. Eng.*, 120(11), 1994, 3178–3196.

Restrepo-Posada, J.I., 1992, Seismic Behaviour of Connections Between Precast Concrete Elements, Ph.D. Thesis, University of Canterbury, Christchurch, New Zealand.

Rautenberg, J.M., 2011, Drift Capacity of Concrete Columns Reinforced with High Strength Steel, Ph.D. Thesis, Purdue University, West Lafayette, Indiana.

Rautenberg, J.M., Pujol, S., Tavallali, H., Lepage, A., 2012, "Reconsidering the use of high-strength reinforcement in concrete columns", *Engineering Structures*, No. 37, pp. 135-142.

Rautenberg, J.M., Pujol, S., Tavallali, H., Lepage, A., 2013, "Drift Capacity of Concrete Columns Reinforced with High Strength Steel", *ACI Structural Journal*, Vol. 110, No. 2, pp. 307-318.

Slavin, C.M., Ghannoum, W.M., "Defining Structurally Acceptable Properties of High- Strength Steel Bars through Material and Column Testing, PART I: MATERIAL TESTING REPORT," (05-14), Charles Pankow Foundation, August 2015, pp. 135.

Sokoli, D., and Ghannoum, W.M., "High-strength Reinforcement in Columns under High Shear Stresses," *ACI Structural Journal*, 113 (3), 2016.

Sokoli, D. "Seismic Performance of Concrete Columns Reinforced with High Strength Steel." Thesis. University of Texas at Austin, 2014.

Sokoli, D., Shekarchi, W., Buenrostro, E., Ghannoum, W.M., "Advancing behavioral understanding and damage evaluation of concrete members using high-resolution digital image correlation data," *Earthquakes and Structures*, V. 7, No. 5, pp. 609-26, November 2014.

Tallavali, H., Lepage, A., Rautenberg, J. M., Pujol, S., 2014, Concrete beams reinforced with high-strength steel subjected to displacement reversals." *ACI Structural Journal*, Vol. 111, No. 5, pp. 1037-1047.

Wight, J. K., *Reinforced Concrete Mechanics and Design 7th Edition*, Pearson Education, Inc, 2016.